SYNTHESIS AND EVALUATION OF FLUORESCENT TOOLS FOR STUDIES OF CANCER BIOLOGY

By

Zhe (Gavin) Gao

Submitted to the graduate degree program in Medicinal Chemistry and the Graduate Faculty of the University of Kansas in partial fulfillment of the requirements for the degree of Doctor of Philosophy.

_____

Chairperson Dr. Blake R. Peterson

_____

Dr. Michael Rafferty

_____

Dr. Thomas Prisinzano

_____

Dr. Paul Hanson

_____

Dr. Jeffrey Krise

Date Defended: May 10, 2019

The Dissertation Committee for Zhe (Gavin) Gao

certifies that this is the approved version of the final dissertation:

SYNTHESIS AND EVALUATION OF FLUORESCENT TOOLS

FOR STUDIES OF CANCER BIOLOGY

_____

Chairperson Dr. Blake R. Peterson

Date Approved: May 10, 2019

ABSTRACT

A key enabling technology in biological sciences involves fluorescent probes. These probes are typically small molecules, proteins, or nucleic acids that either possess intrinsic fluorescence or are linked to a fluorophore that emits photons and can be detected by techniques such as fluorescence spectroscopy, imaging, or flow cytometry. In early-stage drug discovery projects, fluorescent probes can be used to sort and differentiate particular types of cells, conduct high-throughput screening campaigns, and image subcellular compartments. In this dissertation, I describe the use of fluorescent probes to study microtubules and mitochondria in living cells. These structures and organelles are of substantial interest in fundamental cellular biology and as targets of anticancer agents. One of these projects is focused on the anticancer agent Paclitaxel (Taxol). This small molecule that binds microtubules and is one of the most effective treatment for patients with breast, ovarian, and lung cancers. Remarkably, although Taxol can shrink slow-growing tumors in some patients, this drug spares rapidly proliferating cells such as bone marrow cells. This inconsistency has been termed the proliferation rate paradox and is not well understood. To probe the mechanism of action of Taxol, we designed and synthesized a drug-like fluorescent probe termed PB-Gly-Taxol. This compound recapitulates many aspects of the biological properties of Taxol in cells, and provides a new tool to study proliferation rate paradox. In a second project, I describe the discovery of a small molecule termed 2,7-difluoropyronin B that accumulates in hyperpolarized mitochondria of cancer cells. When irradiated with visible blue light, this probe depolarizes mitochondrial membranes, offering a new chemical tool for photochemical control over mitochondrial biology.

ACKNOWLEDGMENTS

First of all, I would like to thank my advisor, Dr. Blake R. Peterson, for his mentorship and guidance during my time here in KU. I sincerely appreciate his support on both my research and academic endeavors. I would also like to thank my committee members Dr. Michael Rafferty, Dr. Thomas Prisinzano, Dr. Paul Hanson, and Dr. Jeffrey Krise for their year-long contributions to my research projects. Additionally, I would like to thank the entire Department of Medicinal Chemistry for their support. It's my honor to be part of this great academic family.

I also thank the group members of the Peterson Lab who have contributed to the work presented in this dissertation, particularly Dr. Molly Lee, Dr. Zachary Woydziak and his lab members Brandon Walls and Fadel Boumelhem. Additionally, I thank past and present Peterson group members, especially Dr. Chamani Perera, Dr. David Hymel, Dr. Matt Meinig, Ning Yang and Dr. Kelsey Knewtson for thoughtful discussions and help in the lab.

Finally, I want to thank my parents, Yiqin Gao and Yuping Ji for their continuous support throughout my graduate career.

TABLE OF CONTENTS

Table of Contents

Table of Figures

Table of Schemes

Chapter 1 - Introduction

1.1 Fluorescent probes for studies of cancer and other biological systems

Cancer is a major cause of human death. According to the World Health Organization (WHO), an estimated 9.6 million people died from cancer in 2018, with one in six deaths due to cancer. In 2015, patients in the USA paid approximately $80.2 billion for medical treatment, according to the Agency for Healthcare Research and Quality (AHRQ). This huge financial burden is projected to reach at least $158 billion in the US by 2020, according to the National Institutes of Health (NIH). As a consequence, every year billions of dollars are invested on medical research both in academia and industry, and the annual total budget of the National Cancer Institute (NCI) is ~ $5 billion. However, despite this large investment, scientific advances for the treatment of cancer are challenging because this condition is an extensive collection of diseases that are characterized by abnormal cell proliferation. More than 100 types of cancer have been identified, including breast cancer, prostate cancer, lung cancer and colon cancer, to name the most common types. Due to the innate complexity of this disease, it is difficult but crucial to study the different mechanisms of cancer initiation and progression and discover drugs and improved treatments.

A great deal of research on cancer biology involves the use of chemical probes. In general, a probe is a molecule that specifically interacts with an analyte of interest in a biological system such as cells in culture or an animal model. The analyte is usually a biomolecule such as a protein or nuclei acid. A fluorescent probe is a chemical probe with intrinsic fluorescence or is tagged with a fluorophore that emits fluorescent photons that

can be detected by techniques such as confocal microscopy or flow cytometry. Some fluorescent proteins are also used in this way, but compared to fluorescent proteins, fluorescent small molecule probes can in many cases be readily synthesized, are more chemically and optically stable, and may be less likely to perturb biological systems under investigation.

1.2 The use of fluorescent probes for cell sorting

Isolating and sorting a specific cell population from a heterogonous mixture is very important method in biological research, clinical diagnosis, and drug discovery. This approach offers a tool for scientists to pinpoint the mechanism of diseases and find potent therapeutic treatment for patients. For example, the first FDA-approved CellSearch blood test aids in the treatment of metastatic cancer patients by capturing, isolating and enumerating circulating tumor cells (CTC), a rare cell derived from a solid tumor that is capable of spreading throughout the body.[1]

1.2.1 Fluorescence-activated cell sorting

Many cell sorting technologies have been developed including magnetic-activated cell sorting (MACS) and fluorescence-activated cell sorting (FACS). Although MACS devices are significantly cheaper than FACS, MACS often retains non-labeled cells with the desired target cells, and it may poorly capture target cells far from the field source due to non-linear magnetic forces, limiting its application.[2] The first commercial FACS instrument was invented in 1969 by Dr. Herzenberg and his colleagues.[3] FACS is now

considered the gold standard for separating cells through the use of fluorescent dyes, fluorescent labeled antibodies, or genetically modified proteins bearing a fluorescent tag.

Early applications of FACS relied on small-molecule fluorescent dyes to sort cells based on the observation of unique biological properties. For example, one of the most widely used cell separation methods uses the small molecule propidium iodide (PI, **1** in Figure 1.1) to differentiate dead cells from living ones.[4] This assay is based on the ability of PI to enter cells with disrupted membranes, but this dye is excluded from cells with intact membranes. Once PI enters a cell, it intercalates into DNA in the nucleus and upon excitation, it emits red fluorescent photons. The resulting differences in cellular fluorescence can be used to separate dead from living cells. This method has been applied to numerous studies of cytotoxicity and membrane leakage in cancer biology. Another dye named 7-amino-actinomycin D (7-AAD, **2** in Figure 1.1) is also frequently utilized in these assays. The emission spectrum of 7-ADD is red-shifted compared to that of PI, reducing its spectral overlap with other green fluorophores in multi-color experiments.[5] Recently, to more accurately distinguish living from dying or dead cells, a combination of three fluorescent reagents, including 4'-6-diamidino-2-phenylindole (DAPI, **3**), tetramethylrhodamine methyl ester (TMRM, **4**) and fluorescein isothiocyanate(FITC, **5**)-conjugated Annexin V (Annex V^{FITC}) have been used together (Structures are shown in Figure 1.1).[6] Like PI and 7-AAD, DAPI binds to DNA and does not efficiently cross intact cell membranes, rendering it selective towards dead cells. TMRM is utilized to measure the mitochondrial membrane potential, an important indicator of the health of mitochondria, and TMRM accumulates specifically in active mitochondria of living cells. Annex V^{FITC} is a fluorescent protein that binds to phosphatidylserine exposed on the outer

leaflet of the plasma membrane during early apoptosis. Through the use of these three dyes, cells can be sorted into populations of living cells (DAPI-/ TMRM+/ Annex V^{FITC}-), apoptotic cells (DAPI-/ TMRM-/ Annex V^{FITC}+), and necrotic cells (DAPI+/ TMRM-/ Annex V^{FITC}+). Another frequently used dye is Hoechst 33342 (**6** in Figure 1.1), which has been applied to stain and isolate the side population (SP) of cancer cells.[7] These SP cells make up only a small percentage of cancer cells, but they feature upregulated ATP-binding cassette (ABC) transporter proteins. Hoechst 33342 is a known substrate of efflux pumps, making it an excellent tool to isolate SP cells.

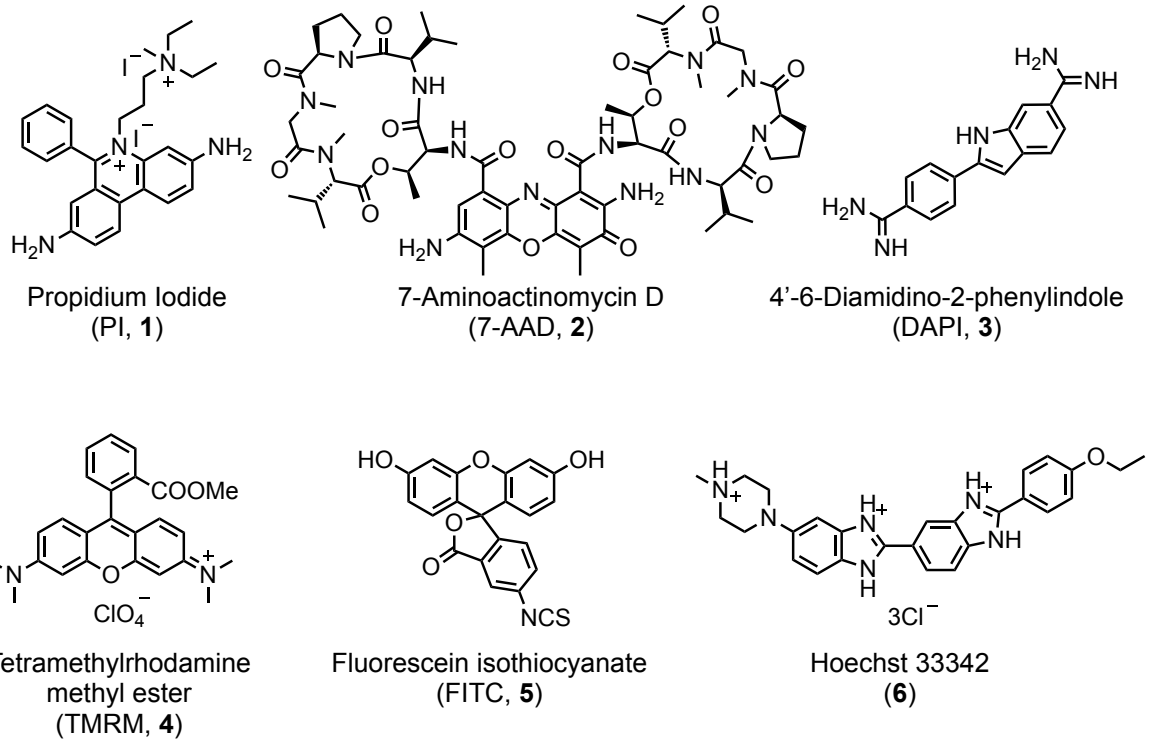

Figure 1.1. Examples of small-molecule fluorescent dyes used in cell sorting and flow cytometry.

1.2.2 Identification of fluorescent probes used for cell sorting

There are two major approaches to develop specific fluorescent dyes for use in cell sorting. One method starts with screening a library of structurally diverse fluorophores

against cells of interest and an isogenic counterpart, followed by a validation assay. This method has been termed the diversity-oriented fluorescence library approach (DOFLA)[8]. By screening a DOFL, many unique dyes have been discovered that identify specific cell types, including pluripotent stem cells,[9] microglia,[10] myocytes,[11] and α and β cells from pancreatic islets.[12, 13] One recent example of using DOFLA to establish a FACS method was the identification of a fluorescent probe named TiY (**7** in Figure 1.2) that specifically labels tumor initiating cells (TICs) in non-small cell lung cancer.[14] TICs are a subpopulation of cancer cells with high renewal capabilities that are associated with relapse and metastasis.[15] To develop a TIC-specific fluorescent probe, thousands of compounds from a DOLF were screened against a pair of cell lines: TS32 cells with high tumor sphere forming ability and 32A cells in which the growth factor from media was removed to serve as an isogenic counterpart. Secondary screening was additionally performed using TS10 cells derived from another lung cancer patient, and LuEpi as normal lung epithelial cells. Less than 10 compounds out of thousands screened exhibited profound selectivity towards TS32 and TS10 over 32A and LuEpi cells. Among them, TiY was the most efficacious dye. Interestingly, it forms a covalently bond to vimentin, a biomarker protein found in the cytosol that is associated with formation of tumor spheroids.

Another method to develop fluorescent probes for cell sorting is based on the rational design of a fluorescent substrate that can identify target cells that express a greater quantity of a specific enzyme compared to other cells. One classic example is BODIPY aminoacetaldehyde (BAAA, **8** in Figure 1.2), a substrate of aldehyde dehydrogenase 1 (ALDH1) that has been used to isolate cancer stem cells (CSC) that express ALDH1 at high levels. BAAA was constructed by conjugating the ALDH1

substrate aminoacetaldehyde with the fluorophore BODIPY. This green fluorescent substrate freely diffuses across cell membranes, but upon enzymatic reaction by ALDH1, it is converted into the corresponding acid, which is trapped in cells due to the generation of a negative charge. A high fluorescence intensity correlates to cells with high content of ALDH1, allowing their differentiation of cells with low levels of ALDH1. This method was initially reported for fractionation of primitive human hematopoietic stem cells (HSCs), a cell population with high fluorescence intensity and low light scattering, from blood samples by flow cytometry.[16] After its commercialization by STEMCELL Technologies and rebranding as ALDEFLUOR, it has been applied to detect stem cells in many tissues, including those from prostate, lung, breast, skeletal muscle, and colon.[17] Recently, to allow multicolor-based detection of CSCs with green fluorescent probes, a spectrally orthogonal red fluorescent substrate for ALDH named AldeRed 588-A (**9** in Figure 1.2)[18] was synthesized by conjugating the aldehyde moiety to a red fluorophore BODIPY 576/589. AldeRed 588-A exhibits specific uptake by cell lines expressing high levels of ALDH, K562 and L1210/cpa, compared to controls treated with the ALDH-inhibitor diethylaminobenzaldehyde (DEAB). AldeRed 588-A has been used to isolate human hematopoietic stem cells with high expression of ALDH from a heterogeneous mixture of blood cells, similar to ALDEFLUOR.

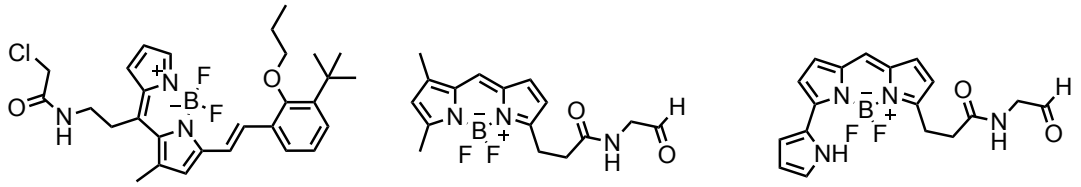

TiY (**7**) | BODIPY aminoacetaldehyde (BAAA, **8**) | AldeRed 588-A (**9**)

Figure 1.2. Examples of fluorescent probes for cell sorting discovered by screening and rational design.

1.3 The use of fluorescent probes in screening

Screening is a primary tool used to identify hit compounds with a desired biological activity in early-stage drug discovery. Advances in robotics have allowed the development of automated screening of large libraries of structurally diverse compounds, a method known as high throughput screening (HTS).[19] The readout of this type of screening is often fluorescence from fluorescent dyes or proteins, such as direct measurements of fluorescence intensity, fluorescent polarization (FP), Förster resonance energy transfer (FRET), and other related signals.[19, 20] These screening assays are usually performed in 96, 384, or 1536-microwell plate formats, and instruments used for the detection of these signals include flow cytometers, plate readers, and high-throughput microscopes. The efficacy or potency of hit compounds can be represented by EC_{50} (concentration of compound needed to achieve 50% maximum efficacy), IC_{50} (concentration of compound needed to achieve 50% maximum inhibition), K_d (dissociation constant, ligand concentration needed to bind half of the protein) and K_i (dissociation constant of inhibitors, an experimental condition-independent parameter as compared to IC_{50}[21]). The Ki can be derived from the IC_{50} by the Cheng-Prusoff equations shown in Figure 1.3, where the first equation is for inhibitor-enzyme interactions and the second one is for ligand-receptor interactions. A more general Cheng-Prusoff equation can be used where [A] is the concentration of agonist and [A50] is the agonist concentration causing 50% maximum response.[22]

$$K_{\mathrm{i}} = \frac{\mathrm{IC}_{50}}{1+[S]/K_m}, K_{\mathrm{i}} = \frac{\mathrm{IC}_{50}}{1+[L]/K_d}$$

$$K_i = \frac{IC_{50}}{(2 + ([A]/[A_{50}])^n)^{1/n} - 1}$$

Figure 1.3. Cheng-Prusoff equations for analysis of competitive inhibition and binding.

The sensitivity and performance of a screening assay is evaluated by its S:N (signal to noise), S:B (signal to background ratio), SW (signal window) and Z' factor, which are defined by the equations shown in Figure 1.4.

$$S{:}N = \frac{\mu_{max} - \mu_{min}}{\sigma_{min}}, S{:}B = \frac{\mu_{max}}{\mu_{min}}$$

$$SW = \frac{\mu_{max} - \mu_{min} - 3(\sigma_{max} + \sigma_{\min})}{\sigma_{max}}, Z' = 1 - \frac{3(\sigma_{max} + \sigma_{\min})}{|\mu_{max} - \mu_{min}|}$$

Figure 1.4. Equations used to determine assay sensitivity and performance (μ is the mean signal, σ is standard deviation of the signal).

1.3.1 Screening using fluorescence intensity

Fluorescence intensity provides one of the simplest methods for screening. Addition of test compounds is simply followed by measurement of fluorescence. This can be quantified by instruments such as flow cytometers, fluorescent plate readers, or microscopes. An example of a fluorescence-ON assay involves the identification of p-glycoprotein (P-gp) inhibitors using the HTS-compatible probe calcein acetoxymethyl ester (Calcein AM, commercialized as the Vybrant Multidrug resistance assay, **10** in Figure 1.5).[23] P-gp is an ABC transporter located on cellular plasma membranes that pumps out a variety of small molecule substrates. This transporter is frequently overexpressed by cancer cells and causes resistance to anti-cancer agents. Inhibition of P-gp provides a potential method to overcome resistance. Calcein, the hydrolyzed product of calcein AM, is a substrate of P-gp. It barely accumulates in cells expressing P-

gp, resulting in very low fluorescence. However, in the presence of a P-gp inhibitor, calcein accumulates in the cytosol, leading to a large increase in fluorescence, which can be quantified to evaluate the efficacy of inhibitors.[24] This assay has been applied to screen the Prestwick Chemical Library, and led to the discovery of three novel P-gp inhibitors.[25] A fluorescent imaging-based HTS has also been used in this way to identify four new P-gp inhibitors from a kinase inhibitor library.[26]

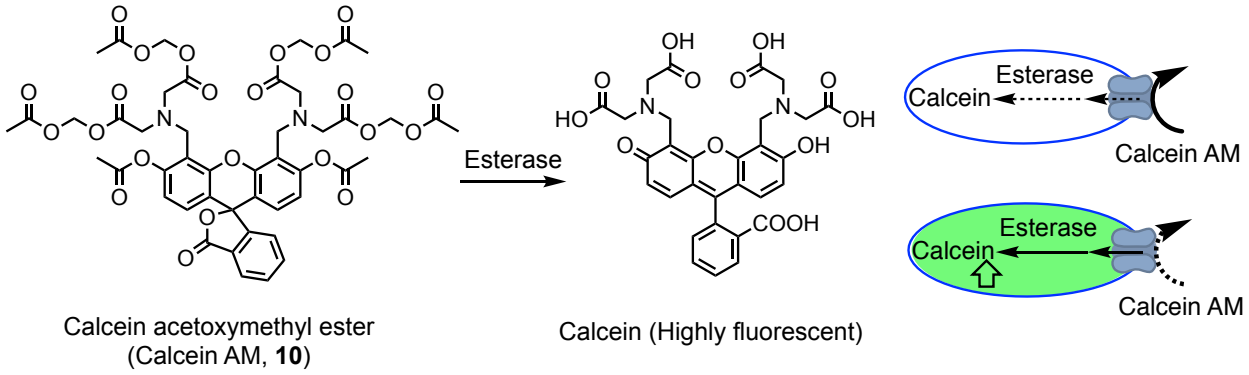

Figure 1.5. Principle of the Calcein AM assay of P-gp.

Another class of fluorescent probes lose fluorescence upon addition of test compounds. An example of this type of assay involves a substrate tagged with a fluorophore and a nearby quencher. Because of the quencher, this probe is initially non-fluorescent. Upon the cleavage by the enzyme, the dissociation of the quencher and fluorophore results in the emission of fluorescence. When an inhibitor is present, it can block the activity of the enzyme, causing an overall decrease of fluorescence compared to control. This reduction in fluorescence can be quantified as a function of concentration of the inhibitor to provide an IC_{50} value. Recently, a fluorogenic probe termed EP (**11** in Figure 1.6) was synthesized and used to screen a fragment library containing 1460 compounds. The goal was to identify potential inhibitors of ER aminopeptidase associated

with antigen processing (ERAAP), since downregulation of ERAAP leads to enhanced immune response to tumors. This EP probe is a modified substrate of ERAAP, where the N-terminus was linked to dinitrophenol (DNP) as a quencher and the C-terminus was tagged with the fluorophore BODIPY. The intact EP has low fluorescence due to quenching by the neighboring DNP, but upon addition of ERAAP, EP is hydrolyzed into two molecules, leading to emission of fluorescence from BODIPY. After a primary screen and validation, one fragment compound was found to be an irreversible inhibitor of ERAAP with the lowest IC_{50} (23 μM) reported to date.[27]

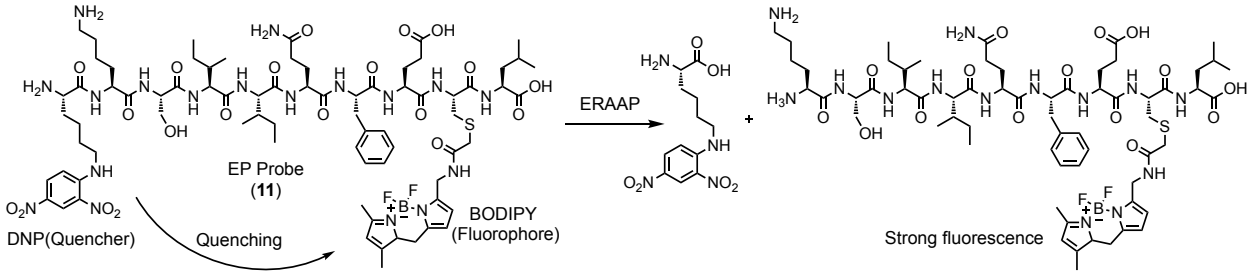

Figure 1.6. Screening for ERAAP inhibitors based on a fluorogenic EP probe.

Screening of fluorogenic probes of specific enzymes has not only been limited to peptide substrates but has also been applied to nucleic acids. One such example is OGR1 (**12** in Figure 1.7), a probe designed for determination of 8-oxoguanine glycosylase 1 (OGG1) activity and screening of OGG1 inhibitors.[28] OGG1 is the chief eukaryotic repair enzyme known to remove 8-oxoguanine by excising it from the sugar backbone of damaged double stranded DNA (dsDNA). 8-oxoguanine is also known to be a fluorescence quencher. To take advantage of this specific cleavage by OGG1 and the unique fluorescence quenching effect of 8-oxoguanine, the fluorescent nucleobase analogue tCo was installed in close proximity to the quencher 8-oxoguanine. Since 8-oxoguanine decreases the fluorescence of tCo, very little fluorescence is detected when

the backbone is intact, whereas in the presence of OGG1, 8-oxoguanine is cleaved from DNA, causing a 60-fold increase in the fluorescence of tCo. After HTS of 25,975 compounds followed by a validation assay, 22 compounds were confirmed as OGG1 inhibitors. Among them, one hit, a tetrahydroquinoline sulfonamide derivative, was subjected to further structural optimization, leading to an inhibitor named SU0268, with 59 nM IC_{50} value for OGG1.[29]

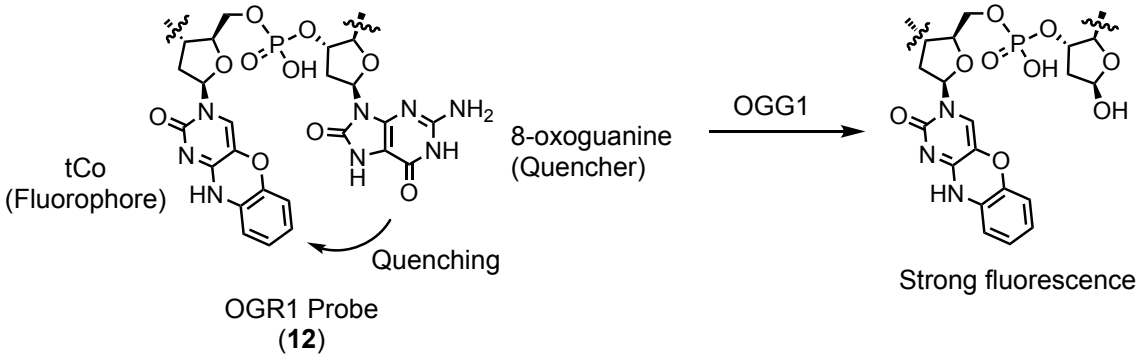

Figure 1.7 Screening OGG1 inhibitors based on a fluorogenic OGR1 probe.

However, measurement of fluorescence intensity can suffer from interference by compounds that exhibit intrinsic fluorescence and autofluorescence from biological samples, both of which can cause false positive results. To prevent these artifacts, a secondary screen of positive hits from the primary screen is usually be applied. Another solution involves using a far-red fluorescent probe for the readout to avoid spectral overlap with commonly used green or blue probes and biological autofluorescence.

1.3.2 Screening by Förster resonance energy transfer (FRET)

To minimize interference and increase the signal window, Förster resonance energy transfer (FRET) is another powerful technology for screening library compounds against proteins of interest. This fluorescence phenomenon was discovered by Theodor

Förster in 1948.[30] FRET probes are usually composed of two fluorophores that are placed in close proximity to each other, with one serving as a donor and the other an acceptor. Upon excitation at the donor's λ_{max}, energy is transferred to the acceptor when it is in close proximity, resulting in emission by the acceptor instead of the donor. According to the PubChem BioAssay database, FRET-based screening has been used to identify more than 70 target proteins, including kinases, other enzymes and receptors. One method to design a FRET pair involves using the tryptophan residue from the protein of interest as the donor and a fluorescent ligand as the acceptor. This method is only possible if a tryptophan residue is part of or close to the binding site. For example, tryptophan can be paired with MANT-uracil (**13** in Figure 1.8) at the binding site of cereblon to screen for inhibitors. MANT-uracil is a fluorescent ligand of the protein cereblon, a substrate of E3 ubiquitin ligase and a major binding partner of thalidomide, a drug currently used to treat myeloma. Due to the close proximity of tryptophan to bound MANT-uracil in the binding pocket of cereblon, the energy from exciting tryptophan at 295 nm is transferred to the fluorescent ligand MANT-uracil, which emits fluorescence at 440 nm. MANT-uracil alone is excited to a much lesser extent by 295 nm light. The FRET signal increases with titration of MANT-uracil to cereblon in a dose dependent manner and yields a binding curve after blank correction. Inhibitors such as thalidomide compete away MANT-uracil, resulting in a dose-dependent decrease in FRET signal that can be quantified to calculate the IC_{50} and Ki.[31]

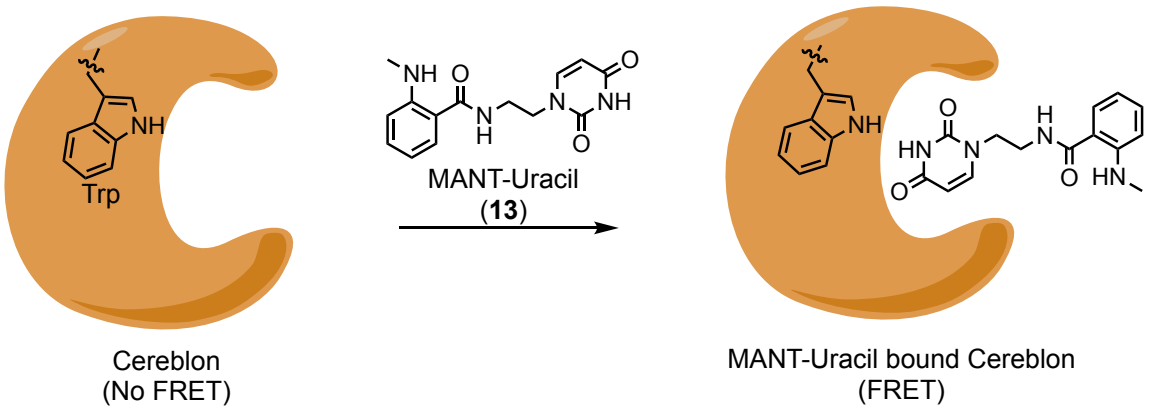

Figure 1.8 A FRET-based assay designed for screening of cereblon inhibitors.

1.3.3 Screening by fluorescence polarization

After its first theoretical description in 1926, fluorescence polarization (FP) has provided a powerful tool for studying interactions between ligands of proteins and nucleic acids. More recent applications of FP to HTS during in the 1990s profoundly facilitated drug discovery.[32] In this method, the fluorescent probe used is often called the tracer. When a fluorescent sample is excited by polarized light, emission intensity is collected parallel and perpendicular to the excitation light plane, represented as $F_{\parallel}$ and $F_{\perp}$. The polarization of the sample is defined as $(F_{\parallel} - F_{\perp})/(F_{\parallel} + F_{\perp})$. As shown in Figure 1.9, when only a small molecule tracer is present, its fast rotation yields low polarization. However, when a macromolecule such as protein or nucleic acid is bound to the tracer, the resulting complex tumbles much slower and emits highly polarized light. Therefore, the change in polarization reflects the interaction of tracer with the macromolecule. Upon addition of a test compound as a competitor, the tracer is liberated, causing a decreased polarization value. This difference in polarization can be quantified and fit to provide a dose-response curve. The IC_{50} and Ki of the ligand can be determined from this data. Because FP is a homogenous assay that does not require a washing step, FP assays have been widely

applied in industry and academia to screen drug candidates against target macromolecules. According to the PubChem BioAssay database, common targets investigated with this method include kinases, ion channels, nuclear receptors, G-protein coupled receptors (GPCRs), epigenetic regulators, proteases, transcription factors, secreted proteins, and phosphodiesterases, .

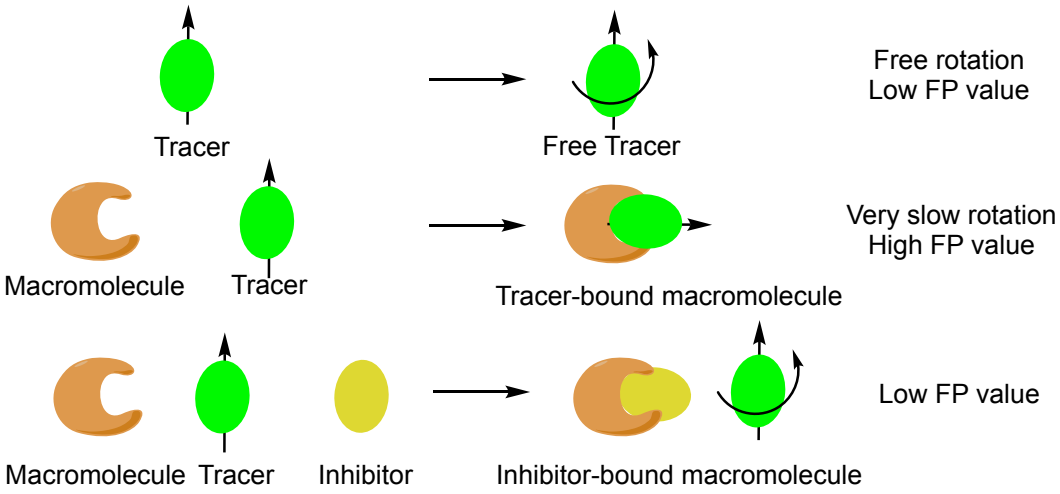

Figure 1.9. The principle of fluorescence polarization and its use in competition assays.

If the ligand of interest itself emits detectable fluorescence, it may be directly used as tracer. However, in most cases, the tracer is synthesized by conjugating a ligand to a fluorophore. For instance, three BH3 peptides labeled with fluorescein were used to generate the tracers f-Bad (NLWAAQRYGRELRRMSDK(Fluor.)FVD), f-Bak (GQVGRQLAIIGDK(Fluor.)INR) and f-Bax ((Fluo.)QDASTKKLSECLKRIGDELDS).[33] These three BH3 peptides bind the target protein Bcl-XL, and FP assays with Bcl-XL were used to calculate the affinity and signal window. f-Bad was found to have the highest affinity (21 nM) and an acceptable signal window (120 mP). The stability of f-Bad over time and the effect of increasing amounts of DMSO was tested to confirm the robustness of this assay. A competitive assay was validated by comparing the affinity of published

ligands with ligands measured with this assay. The Z' factor was found to range from 0.7 to 0.88, indicating that this FP assay would be excellent for HTS. A library of 370,400 compounds was screened by Abbott (now AbbVie), followed by a secondary assay involving affinity selection/mass spectrometry. From this study, 29 compounds with an affinity of better than 100 μM were obtained.[34] Abbvie later utilized this approach to find a hit compound that inhibits myeloid cell leukemia 1 (MCL-1), a BCL-2 family protein associated with tumor initiation, at a single digit micromolar concentration.[35] An academic group in Spain used this same method to screen the Prestwick Chemical Library of 880 small molecules.[36] They identified the antimalarial agent quinacrine as a weak inhibitor of Bcl-XL.

The methods previously discussed primarily depend on the existence of a known substrate or ligand of a protein target. However, for enzymes that are not well-characterized, it is challenging to design fluorescent probes based on a known substrate. To identify inhibitors of those enzymes, a fluorescence polarization technology for competitive activity-based protein profiling, named Fluopol-ABPP has been developed to address the problem.[37] This technology uses a reactive fluorescent probe that covalently binds the active site of an enzyme of interest. Before addition of this probe to an enzyme pre-dispensed in multi-well plates, a test compound is pre-incubated with the enzyme. As shown in Figure 1.10A, inhibitors will block the active site of the enzyme and prevent the reaction of the covalent probe with the enzyme, leading to a low FP value. Inactive compounds unable to occupy the active site cause the enzyme to be labelled with fluorescent probe, resulting in high FP signal. Low FP signals indicate potent inhibitors. For example, a reactive fluorophosphate rhodamine probe (**14** in Figure 1.10B) was used

to screen a library on 384-well plates to identify inhibitors of the cancer-associated retinoblastoma-binding protein-9 (RBBP9). This primary screening identified 35 hits out of 18,974 small molecules screened. After secondary proteomic assays, the alkaloid emetine was identified as a selective inhibitor of RBBP9 with an IC_{50} of 7.8 μM. This same method was applied to the discovery of thioltransferase glutathione S-transferase omega 1(GSTO1) inhibitors, in which phenyl sulfonate rhodamine was used as the reactive fluorescent probe (**15** in Figure 1.10B). Primary screening lead to 38 hits out of 2,000 compounds, followed by a secondary selectivity assay that was used to identify a potent GSTO1 inhibitor (IC_{50} = 120 nM). Additionally, a rhodamine conjugated F-amidine (RFA, **16** in Figure 1.10B) has been used to screen a 1,280-compound LOPAC library and identify ruthenium red (Ki of 17 μM) as the first inhibitor of apoenzyme protein arginine deiminases (PADs).[38]

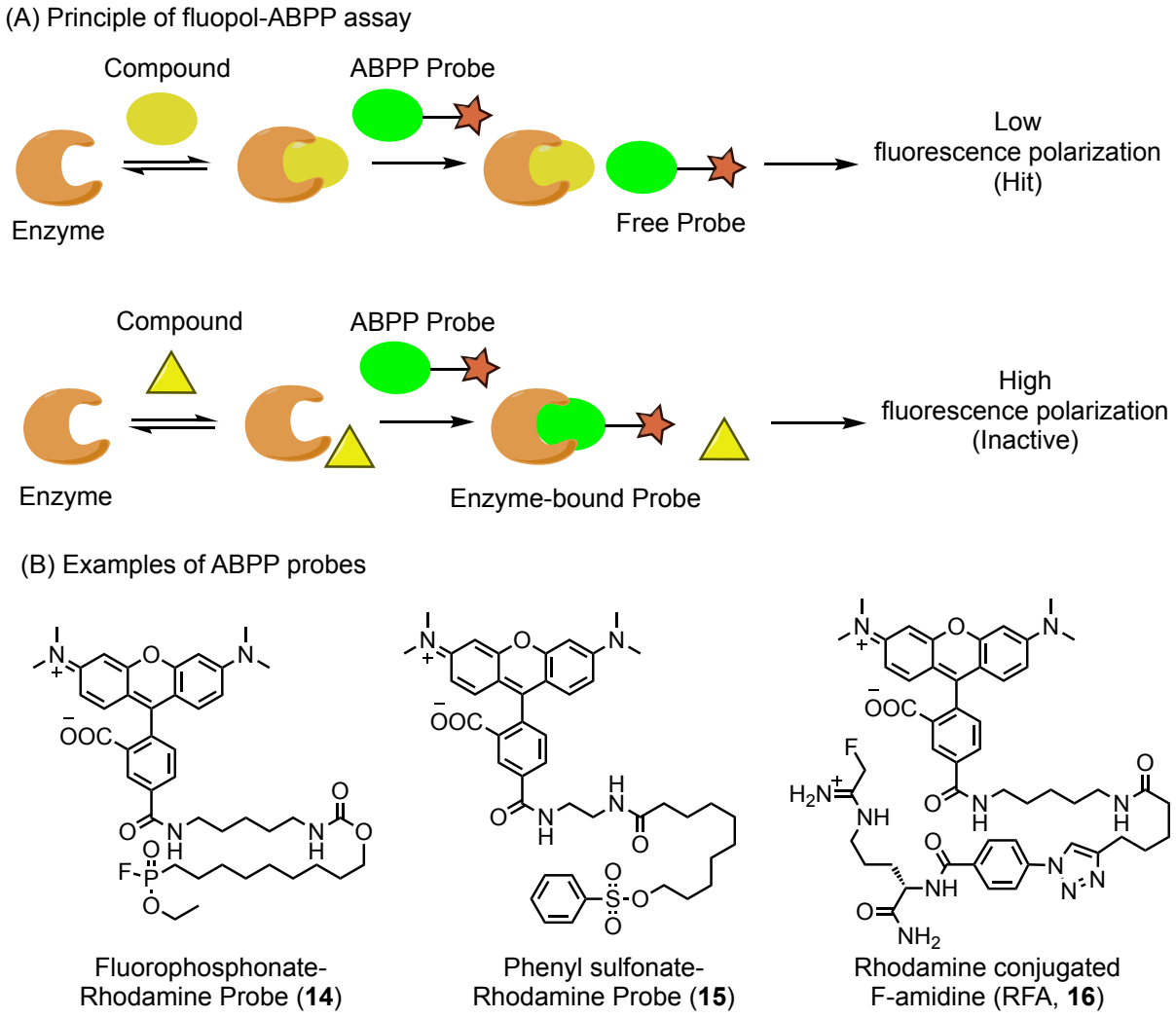

Figure 1.10 Schematic description of fluopol-ABPP assay (A) and the structures of typical fluorescent probes used in this assay (B).

1.4 Fluorescence-based imaging of subcellular compartments as a tool for drug discovery

1.4.1 Mitochondria

Mitochondria are organelles found in most eukaryotic cells. Key functions of these organelles include ATP production via oxidative phosphorylation, calcium regulation, and lipid oxidation. These normal functions of mitochondria depend on the integrity of the structures of the outer membrane, the inner membrane, the intermembrane space

between the inner and outer membranes, and the cristae formed by folding of the inner membrane and the matrix within the inner membrane. The electron transport chain (ETC) located in this inner membrane is essential for the transfer electrons and protons during energy production. Pumping protons out of the matrix creates a proton gradient (ΔpH) and electric potential ($\Delta\Psi_m$) across the mitochondrial inner membrane, where the pH in the matrix is close to 8, generating a more positively charged environment in mitochondria. Compared to the plasma membrane potential ($\Delta\Psi_m$ = -70 mV), the mitochondrial membrane potential is much larger ($\Delta\Psi_m$ = -120 mV), especially in cancer cells ($\Delta\Psi_m$ = -180 mV), where increased oxidative phosphorylation is needed to meet the needs of rapid proliferation. These properties often cause lipophilic cations to accumulate in mitochondria to a greater extent than other organelles or the cytosol. This unique feature allows the development of fluorescent probes that target mitochondria. Three major scaffolds of mitochondria-targeted dyes are the rhodamines, carbocyanines and triphenylphosphonium (TPP), all of which contain lipophilic aromatic rings with positively charged amines or phosphates.

Ever since the first report of the ability of rhodamine 123 (**17** in Figure 1.11) to selectively stain mitochondria of gerbil fibroma cells, rhodamines have been extensively studied as mitochondrial probes.[39] Other rhodamine-based dyes that specifically label mitochondria are rhodamine 6G (**18** in Figure 1.11),[40] rhodamine B (**19** in Figure 1.11),[41] and tetramethylrosamine (**20** in Figure 1.11).[42] Recently, the Peterson lab reported two novel hydrophobic rhodamines termed HRB and HR101 (**21** and **22** in Figure 1.11) that are capable of labeling and visualizing mitochondrial dynamics in living C. elegans.[43] All of the mitochondrial dyes previously described can be used to label living cells because

of their dependence on a functional mitochondrial membrane potential. Fixed (dead) cells that lack this potential do not selectively take up these dyes. To overcome this limitation, MitoTracker probes have been developed that stain active mitochondria but are retained after cellular fixation.[44, 45] MitoTracker probes are structurally related to rhodamine, but include a reactive chloromethyl group on the southern benzene ring. This chloromethyl group is believed to react with thiol groups of cysteine residues and become covalently conjugated to mitochondrial proteins, resulting in retention even after cell fixation. MitoTracker Orange and MitoTracker Red (**23** and **24** in Figure 1.11) emit red-shifted (> 550 nm) fluorescence. Their spectral orthogonality to green and blue fluorophores makes them compatible with multicolor assays. To further increase selectivity and reduce background signals, reduced forms of MitoTracker probes have been synthesized.[45] These probes, including MitoTracker Orange CM-H_2TMRos and MitoTracker Red CM-H_2XRos (**25** and **26** in Figure 1.11), are non-fluorescent due to disruption of the conjugated ring system. They become fluorescent after penetration into active mitochondria, oxidation, and become trapped in these organelles. Like their oxidized form, they are suitable for analysis of fixed cells by confocal microscopy.[46] Recently, silicon rhodamine, an analogue of rhodamine with silicon instead of oxygen in the xanthene middle ring, has gained popularity due to its excellent brightness and high photostability.[47] By screening a synthetic pool of ten analogues, a silicon rhodamine based fluorescent probe named SiR-Mito-8 (**27** in Figure 1.11) was identified as a specific mitochondrial dye.[48] Selectivity for mitochondria was shown to be associated with the hydrophobicity of the fluorophore, where more hydrophobic compounds (clogP > 5.5) tend to target mitochondria more effectively.

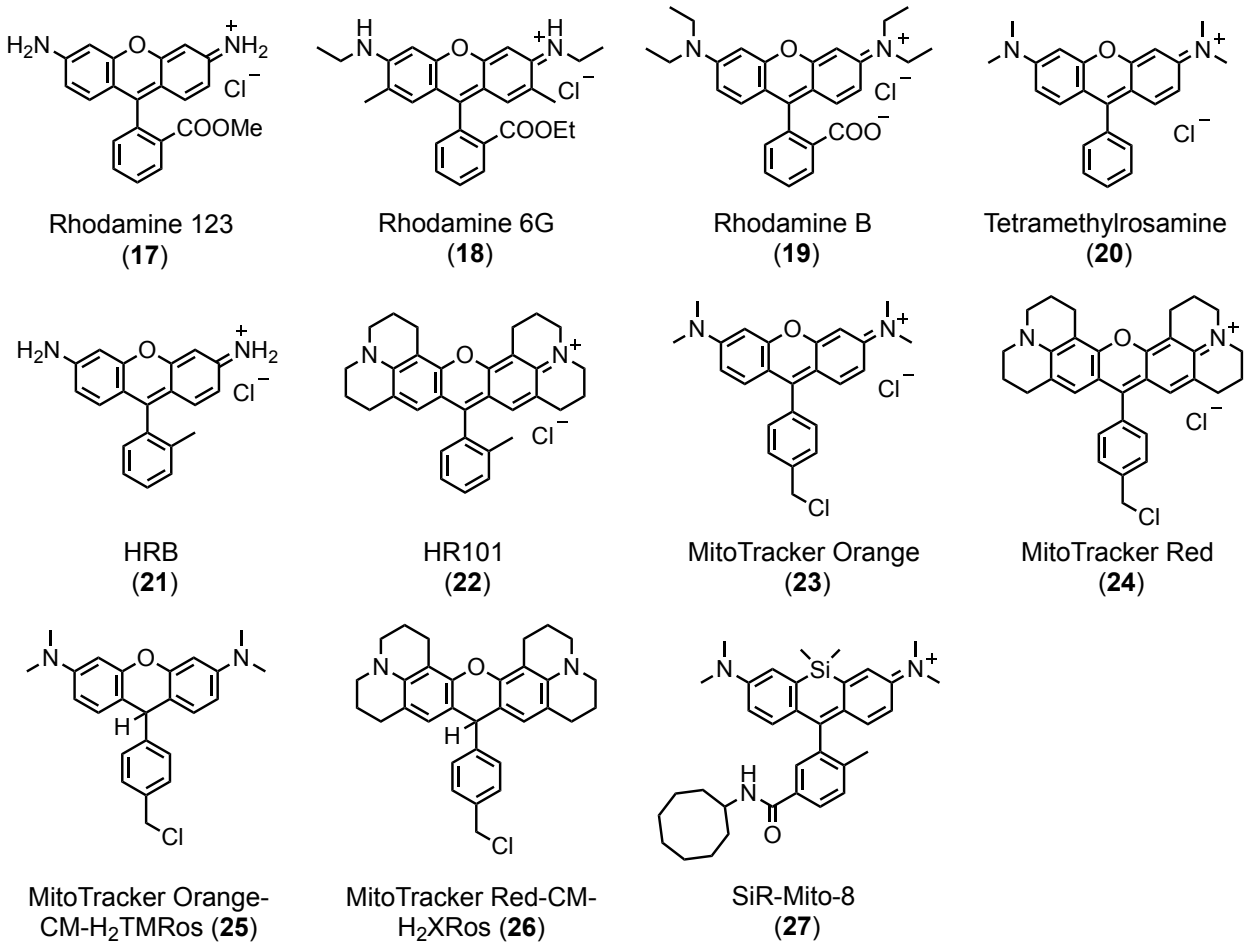

Figure 1.11. Rhodamines that selectively label mitochondria in living cells.

Most carbocyanine dyes with short alkyl chains, such as oxacarbocyanine $DiOC_6(3)$ and $DiOC_2(3)$ (**28** and **29** in Figure 1.12), stain mitochondria of eukaryotic cells at low concentrations (~ 0.1 μg/ml).[49] However, caution is needed when using these dyes at high concentrations because they are capable of staining other membranes such as those of the endoplasmic reticulum.[50, 51] Indocarbocyanine $DiIC_1(5)$ (**30** in Figure 1.12) is a far red probe that is sensitive to the mitochondrial membrane potential. It accumulates in active mitochondria, but it diffuses into the cytosol if depolarization occurs, providing a method to detect depolarization of these organelles. Thiacarbocyanine $DiSC_3(5)$ (**31** in Figure 1.12) is another far red probe that accumulates in mitochondria. However, this

compound inhibits complex 1 of the electron transport chain (ETC) and increases generation of reactive oxygen species (ROS), making it very cytotoxic.[52] Similar to other MitoTracker probes, MitoTracker Deep Red FM (**32** in Figure 1.12)[53-55] possess a chloromethyl group, making them compatible with both living and fixed cells. Due to its far red emission ($\lambda_{max,em}$ = 665 nm), MitoTracker Deep Red FM has been widely used in colocalization assays with other fluorophores or fluorescent proteins to determine selectivity for localization in mitochondria.[54, 56-58] The green fluorophore MitoTracker Geen FM (**33** in Figure 1.12) provides another mitochondrial dye that can be used in colocalization assays.[59, 60] Unlike rhodamine 123, this green dye accumulates in mitochondria regardless of the membrane potential, and it is thought to selectively react with mitochondrial proteins.[61] As a consequence, it has been used to determine the mass of mitochondria.[62, 63] A dual emission probe termed JC-1 (**34** in Figure 1.12) provides an approach to sensitively measure the mitochondrial membrane potential.[64, 65] JC-1 exists as monomers at low concentrations and emits green fluorescence. However, at high concentrations it aggregates and emits red fluorescence. In healthy or polarized mitochondria, JC-1 accumulates at high concentrations and therefore predominantly forms J-aggregates that emit more red than green fluorescence. Upon depolarization of mitochondria, the J-aggregates diffuse away from mitochondria into the cytosol, leading to increasing amounts of monomers that emit only green fluorescence. The ratio of red to green fluorescence can be quantified and correlated with the mitochondrial membrane potential, but JC-1 is known to exhibit poor water solubility.[66] More recently, JC-10, a similar potential-sensitive fluorescent probe, was developed to address this solubility issue.

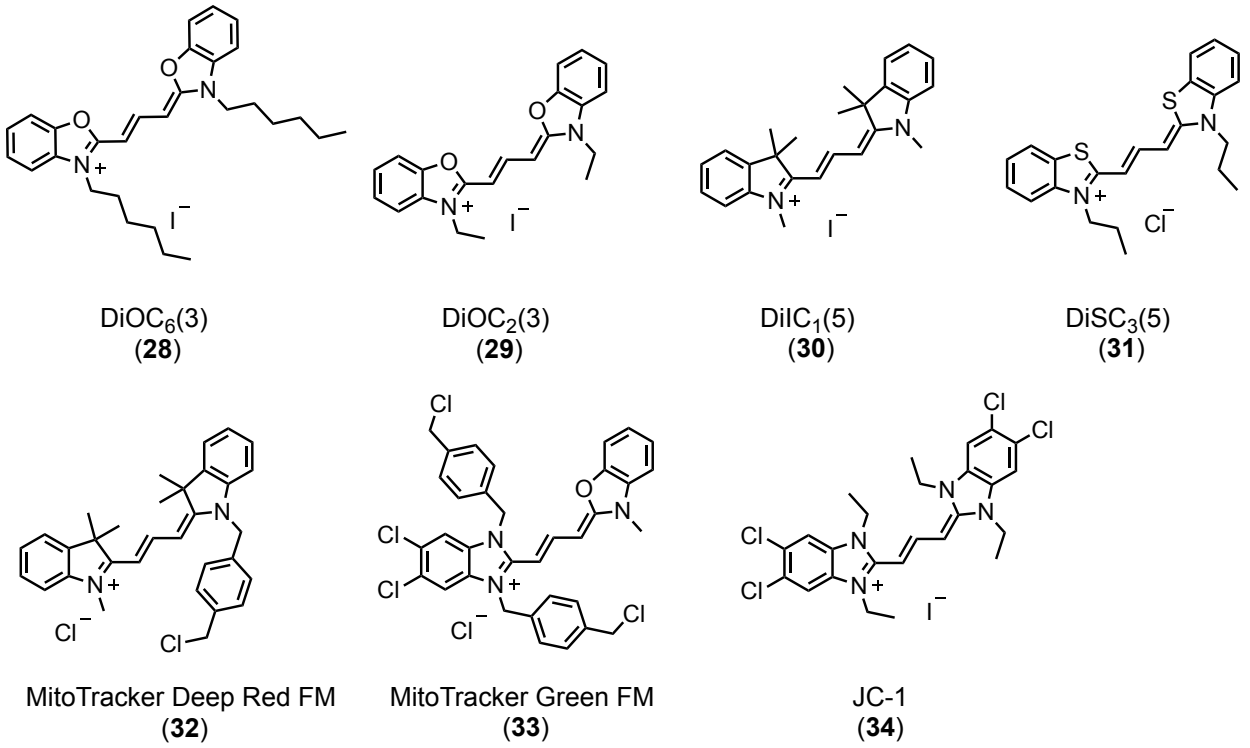

Figure 1.12. Fluorescent carbocyanines that accumulate in mitochondria.

Triphenylphosphonium (TPP) has long been known as a mitochondria-targeting moiety.[67] Conjugation of fluorophores with different emission profiles to TPP via a linker can be used to design mitochondria-targeted fluorescent probes. The coupling of TPP to BODIPY green, BODIPY red, or Cy5.5 has provided the TPP-based mitochondrial dyes TPP-Green, TPP-Red, and TPP-NIR (**35, 36** and **37** in Figure 1.13).[68] These probes can visualize mitochondria in cancer cells but are not particularly sensitive to the membrane potential. Attempts have been made to construct more potential-dependent probes by direct conjugation of TPP to BODIPY (**38** in Figure 1.13). Although this probe is sensitive to the membrane potential, it only partially accumulates in mitochondria.[69] Linking TPP to fluorescein via a decyl chain leads to MitoFluo (**39** in Figure 1.13), a green fluorophore suitable for mitochondria imaging with protonophoric activity.[70]

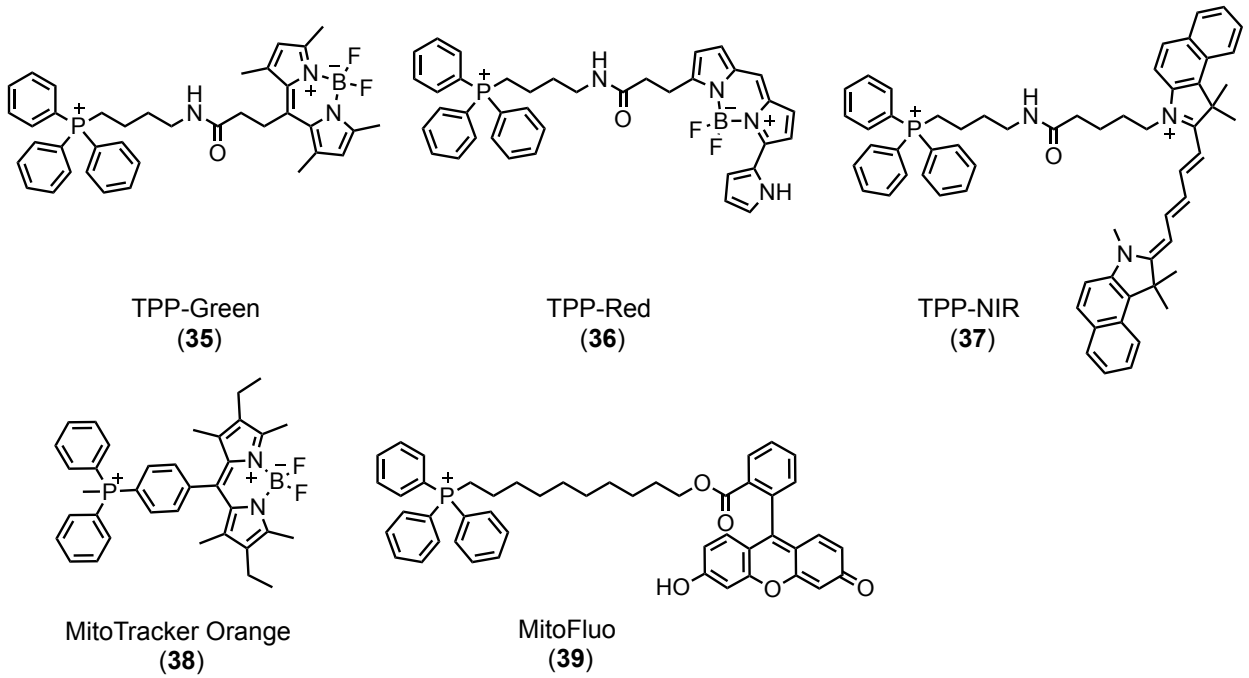

Figure 1.13. TPP-based fluorescent probes for staining of mitochondria.

Other positively charged lipophilic fluorescent probes that accumulate in mitochondria include Pyronin Y,[71] MitoBlue,[72] and FPB (**40, 41** and **42** in Figure 1.14).[73]

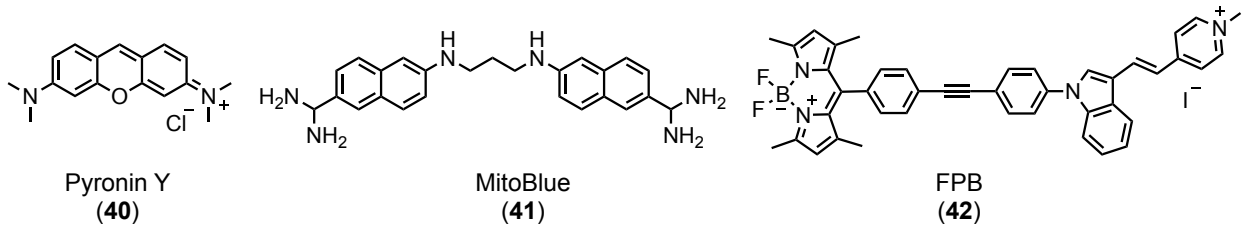

Figure 1.14. Mitochondrial probes based on other fluorescent scaffolds.

1.4.2 Microtubules as targets for the discovery of probes and drugs

Microtubules are a major component of the cytoskeleton of eukaryotic cells. They contribute to the structure and shape of cells. They also play crucial roles in mitosis and the transport of vesicles and organelles. Microtubules are long, hollow cylinders formed by tubulin proteins, composed of heterodimers of α-tubulin and β-tubulin. Many anti-

cancer agents selectively bind to these proteins, and fluorescent analogues of anticancer agents can be used to image microtubules in cells.

Most fluorescent probes of microtubules are based on fluorescent taxoids. Taxoids, compounds related to the anticancer drug Taxol (paclitaxel, **43** in Figure 1.15), stabilize microtubules by binding to β-tubulin. Some of the earliest fluorescent probes of microtubules comprise conjugates of the dyes fluorescein or Oregon Green linked to the 7-OH of Taxol though L-Ala or β-Ala linkers and are termed Flutax-1[74] and Flutax-2[75] (**44** and **45** in Figure 1.15). Both of these dyes have been extensively studied as fluorescent taxoids for imaging of microtubules in cells and for studies of binding to tubulin. TubulinTracker Green (ThermoFisher Scientific, **46** in Figure 1.15) is an acetylated derivative of Flutax-2 that exhibits enhanced cellular permeability. After entering cells, this non-fluorescent probe requires hydrolysis by esterases to generate the fluorescent product Flutax-2. Hexaflutax (**47** in Figure 1.15)[76] is an analogue of Flutax-2 with a longer alkyl linker. This compound was previously used to establish the existence of a new accessible kinetic site on the microtubule surface that binds Taxol. Fchitax-3 (**48** in Figure 1.15)[77] is a derivative of Flutax-2 that stains cellular microtubules, centrosomes, and mitotic spindles. Moreover, it exhibits increased potency against resistant cells that overexpress the efflux pump P-glycoprotein.

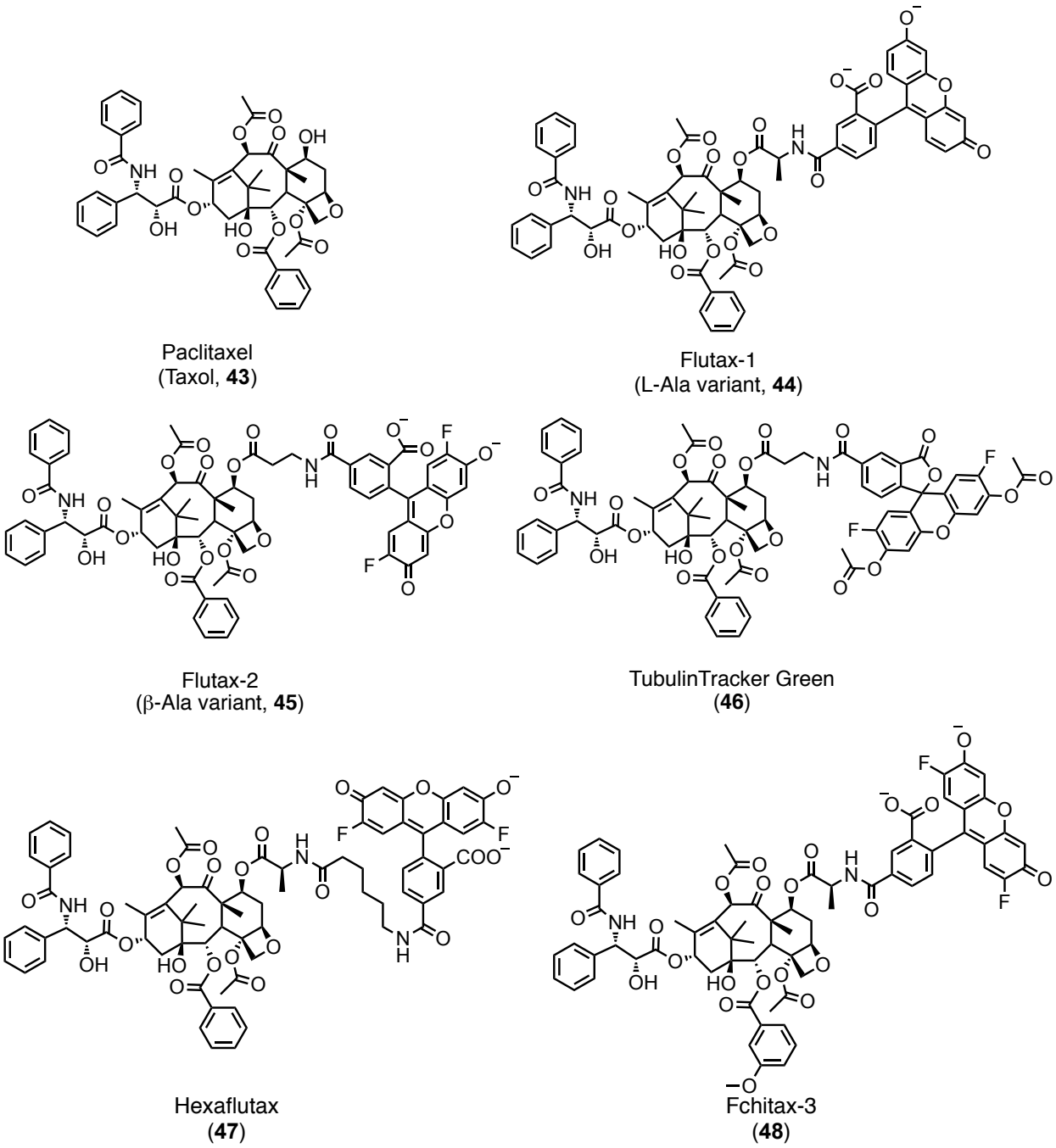

Figure 1.15. Structures of Taxol (paclitaxel) and fluorescent analogues.

Replacement of the N-benzoyl group of the side chain on paclitaxel by a BODIPY propionyl substituent yields BODIPY FL Paclitaxel (**49** in Figure 1.16), a fluorescent taxoid capable of producing fluorescent microtubules in solution that are stable for a week at room temperature.[78] However, this compound is generally not suitable for imaging

microtubules in living cells. To overcome this limitation, a photoactivatable BODIPY paclitaxel (**50** in Figure 1.16)[79] was recently reported that attaches a boron-alkylated BODIPY to the 7-OH of Taxol via a β-Ala linker. The weakly fluorescent alkyl BODIPY can be converted into the strongly fluorescent methoxyl BODIPY upon irradiation. As expected, this BODIPY paclitaxel exhibits a 3-fold enhancement of fluorescence after photoactivation and can be used to visualize both *in vitro* assembled and intracellular microtubules using super-resolution microscopy. Another strategy to stain intracellular microtubules using the BODIPY fluorophore is to assemble the fluorescent probe (**53** in Figure 1.16) *in situ* with a click reaction.[80] The two reactants used are non-fluorescent Taxol-TCO and weakly fluorescent Tetrazine-BODIPY (**51** and **52** in Figure 1.16). Trans-cyclooctene (TCO) reacts rapidly with this tetrazine in water,[81] and cells treated with Taxol-TCO followed by Tetrazine-BODIPY were reported to yield strong microtubule fluorescence, with minimal fluorescence background observed in controls only treated with the individual components.

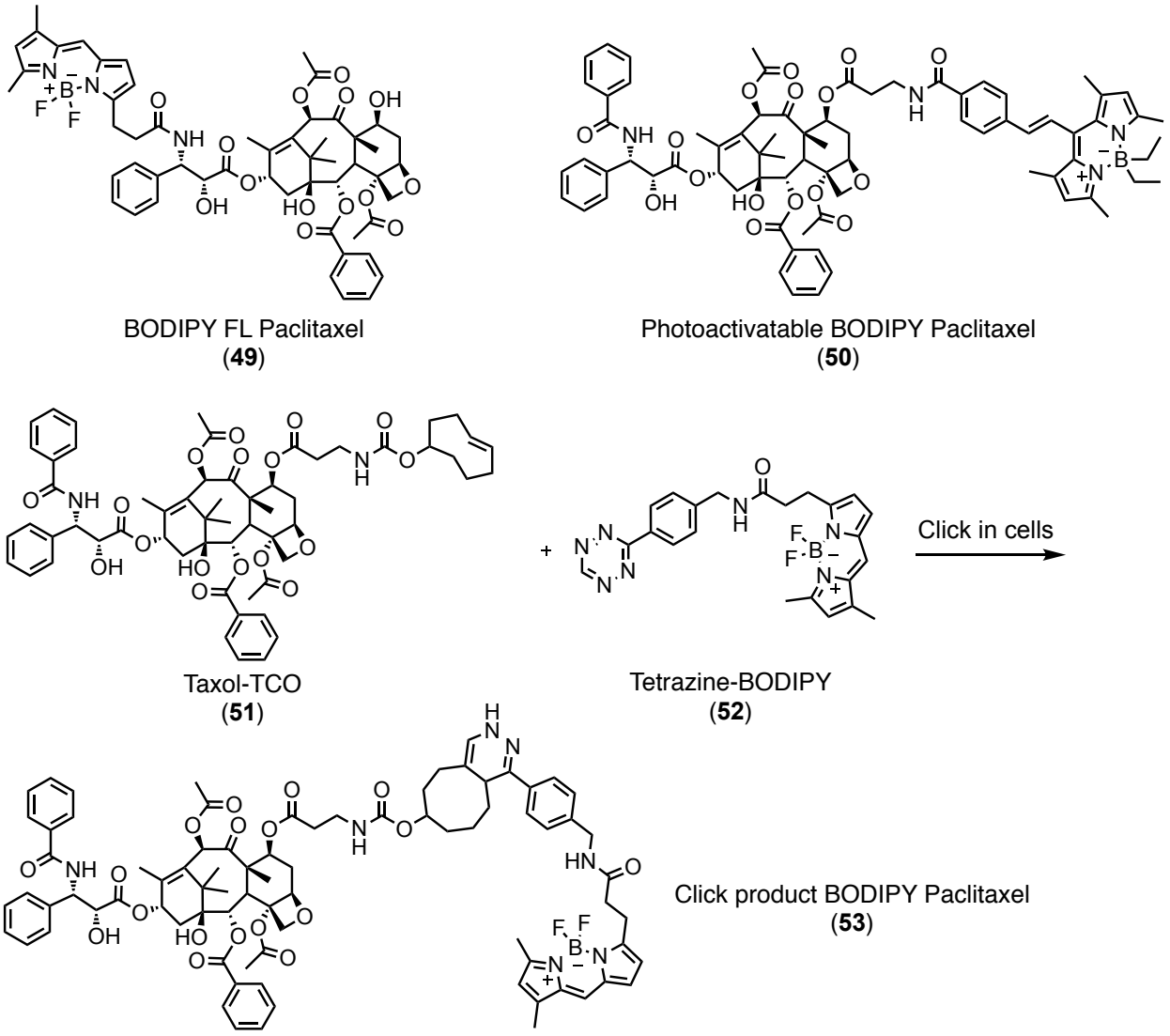

BODIPY FL Paclitaxel (**49**)

Photoactivatable BODIPY Paclitaxel (**50**)

Taxol-TCO (**51**)

Tetrazine-BODIPY (**52**)

Click product BODIPY Paclitaxel (**53**)

Figure 1.16 Fluorescent BODIPY related taxoids.

The silicon-rhodamine-based fluorescent taxoid SiR-tubulin (**54** in Figure 1.17)[82] was constructed by connecting this fluorophore to the side-chain 3'-NH_2 of Taxol. However, unlike BODIPY FL Paclitaxel, SiR-tubulin is able to image microtubules in living cells by super-resolution microscopy. The background signal of SiR-tubulin in cells is low, so a washing step was not required. This low background is a consequence of SiR-tubulin existing in equilibrium as a non-fluorescent spirolactone and a fluorescent zwitterion.

Initially, this compound predominately exists as the spirolactone. However, upon binding to the polar surface of microtubules, it shifts to the zwitterion, resulting in a 10-fold increase in fluorescence. The same group also developed the first larotaxel-based fluorescent probe of microtubules named 580CP-LTX (**55** in Figure 1.17),[83] which is synthesized by coupling carborhodamine 580CP to the 3'-position of larotaxel via an 8-aminooctanoic acid linker.

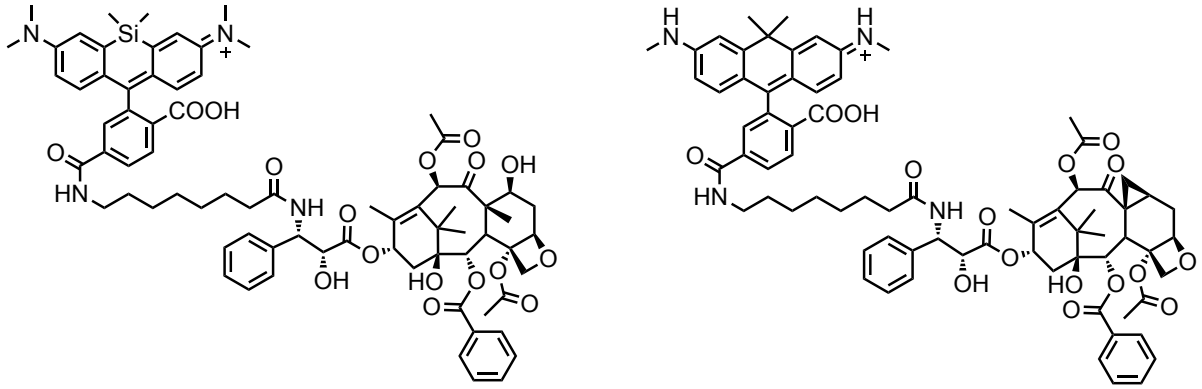

Figure 1.17. Other fluorescent probes for labeling of cellular microtubules.

1.5 Outline of this dissertation

My research in the Peterson lab at KU Med. Chem. has focused on the study of fluorescent probes targeting proteins and cellular organelles and their application in cancer biology. Chapter 2 describes the synthesis and evaluation of a fluorescent analogue of Taxol that selectively targets microtubules and functions as a sensitive substrate of P-gp. Chapter 3 describes the identification of a fluorescent pyronin that enables rapid depolarization of mitochondrial membrane potential upon irradiation with visible blue light.

1.6 References

1. Cristofanilli, M.; Budd, T.; Ellis, M. J.; Stopeck, A.; Matera, J.; Miller, C.; Reuben, J. M.; Doyle, G. V.; Allard, W. J.; Terstappen, L. W. M. M.; Hayes, D. F. Circulating tumor cells, disease progression and survival in metastatic breast cancer. *N. Engl. J. Med.* **2004,** 351, 781-791.

2. Shields, C. W. t.; Ohiri, K. A.; Szott, L. M.; Lopez, G. P. Translating microfluidics: Cell separation technologies and their barriers to commercialization. *Cytometry B Clin. Cytom.* **2017,** 92, 115-125.

3. Hulett, H. R.; Bonner, W. A.; Barrett, J.; Herzenberg, L. A. Cell sorting: automated separation of mammalian cells as a function of intracellular fluorescence. *Science* **1969,** 166, 747-749.

4. Crowley, L. C.; Scott, A. P.; Marfell, B. J.; Boughaba, J. A.; Chojnowski, G.; Waterhouse, N. J. Measuring Cell Death by Propidium Iodide Uptake and Flow Cytometry. *Cold Spring Harb. Protoc.* **2016,** 2016, 647-651.

5. Rabinovitch, P. S.; Torres, R. M.; Engel, D. Simultaneous cell cycle analysis and two-color surface immunofluorescence using 7-amino-actinomycin D and single laser excitation: applications to study of cell activation and the cell cycle of murine Ly-1 B cells. *J. Immunol.* **1986,** 136, 2769-2775.

6. Wallberg, F.; Tenev, T.; Meier, P. Analysis of Apoptosis and Necroptosis by Fluorescence-Activated Cell Sorting. *Cold Spring Harb. Protoc.* **2016,** 2016, 347-352.

7. Goodell, M. A. Stem cell identification and sorting using the hoechst 33342 side population (SP). *Curr. Protoc. Cytom.* **2002,** 9.18, 1-11.

8. Yun, S. W.; Kang, N. Y.; Park, S. J.; Ha, H. H.; Kim, Y. K.; Lee, J. S.; Chang, Y. T. Diversity oriented fluorescence library approach (DOFLA) for live cell imaging probe development. *Acc. Chem. Res.* **2014,** 47, 1277-1286.

9. Im, C. N.; Kang, N. Y.; Ha, H. H.; Bi, X.; Lee, J. J.; Park, S. J.; Lee, S. Y.; Vendrell, M.; Kim, Y. K.; Lee, J. S.; Li, J.; Ahn, Y. H.; Feng, B.; Ng, H. H.; Yun, S. W.; Chang, Y. T. A fluorescent rosamine compound selectively stains pluripotent stem cells. *Angew. Chem. Int. Ed. Engl.* **2010,** 49, 7497-7500.

10. Leong, C.; Lee, S. C.; Ock, J.; Li, X.; See, P.; Park, S. J.; Ginhoux, F.; Yun, S. W.; Chang, Y. T. Microglia specific fluorescent probes for live cell imaging. *Chem. Commun. (Camb.)* **2014,** 50, 1089-1091.

11. Kim, Y. K.; Lee, J. S.; Bi, X.; Ha, H. H.; Ng, S. H.; Ahn, Y. H.; Lee, J. J.; Wagner, B. K.; Clemons, P. A.; Chang, Y. T. The binding of fluorophores to proteins depends on the cellular environment. *Angew. Chem. Int. Ed. Engl.* **2011,** 50, 2761-2763.

12. Kang, N. Y.; Lee, S. C.; Park, S. J.; Ha, H. H.; Yun, S. W.; Kostromina, E.; Gustavsson, N.; Ali, Y.; Chandran, Y.; Chun, H. S.; Bae, M.; Ahn, J. H.; Han, W.; Radda, G. K.; Chang, Y. T. Visualization and isolation of Langerhans islets by a fluorescent probe PiY. *Angew. Chem. Int. Ed. Engl.* **2013,** 52, 8557-8560.

13. Lee, J. S.; Kang, N. Y.; Kim, Y. K.; Samanta, A.; Feng, S.; Kim, H. K.; Vendrell, M.; Park, J. H.; Chang, Y. T. Synthesis of a BODIPY library and its application to the development of live cell glucagon imaging probe. *J. Am. Chem. Soc.* **2009,** 131, 10077-10082.

14. Lee, Y. A.; Kim, J. J.; Lee, J.; Lee, J. H. J.; Sahu, S.; Kwon, H. Y.; Park, S. J.; Jang, S. Y.; Lee, J. S.; Wang, Z.; Tam, W. L.; Lim, B.; Kang, N. Y.; Chang, Y. T. Identification

of Tumor Initiating Cells with a Small-Molecule Fluorescent Probe by Using Vimentin as a Biomarker. *Angew. Chem. Int. Ed. Engl.* **2018,** 57, 2851-2854.

15. Qureshi-Baig, K.; Ullmann, P.; Haan, S.; Letellier, E. Tumor-Initiating Cells: a criTICal review of isolation approaches and new challenges in targeting strategies. *Mol. Cancer* **2017,** 16, 40-56.

16. Storms, R. W.; Trujillo, A. P.; Springer, J. B.; Shah, L.; Colvin, O. M.; Ludeman, S. M.; Smith, C. Isolation of primitive human hematopoietic progenitors on the basis of aldehyde dehydrogenase activity. *Proc. Natl. Acad. Sci. U.S.A.* **1999,** 96, 9118-9123.

17. Dolle, L.; Boulter, L.; Leclercq, I. A.; van Grunsven, L. A. Next generation of ALDH substrates and their potential to study maturational lineage biology in stem and progenitor cells. *Am. J. Physiol. Gastrointest. Liver Physiol.* **2015,** 308, G573-G578.

18. Minn, I.; Wang, H.; Mease, R. C.; Byun, Y.; Yang, X.; Wang, J.; Leach, S. D.; Pomper, M. G. A red-shifted fluorescent substrate for aldehyde dehydrogenase. *Nat. Commun.* **2014,** 5, 3662.

19. Inglese, J.; Johnson, R. L.; Simeonov, A.; Xia, M.; Zheng, W.; Austin, C. P.; Auld, D. S. High-throughput screening assays for the identification of chemical probes. *Nat. Chem. Biol.* **2007,** 3, 466-479.

20. Hall, M. D.; Yasgar, A.; Peryea, T.; Braisted, J. C.; Jadhav, A.; Simeonov, A.; Coussens, N. P. Fluorescence polarization assays in high-throughput screening and drug discovery: a review. *Methods Appl. Fluoresc.* **2016,** 4, 022001.

21. Tonge, P. J. Quantifying the Interactions between Biomolecules: Guidelines for Assay Design and Data Analysis. *ACS Infect. Dis.* **2019**.

22. Leff, P.; Dougall, I. G. Further concerbs over Cheng-Prusoff analysis. *Trends Pharmacol. Sci.* **1993,** 14, 89-91.

23. U.S. patent No. 5,872,014.

24. Homolya, L.; Holló, Z.; Mechetner, E. B.; Sarkadi, B. A new method for quantitative assessment of P-glycoprotein-related multidrug resistance in tumour cells. *Br. J. Cancer.* **1996,** 73, 849-855.

25. Ivnitski-Steele, I.; Larson, R. S.; Lovato, D. M.; Khawaja, H. M.; Winter, S. S.; Oprea, T. I.; Sklar, L. A.; Edwards, B. S. High-throughput flow cytometry to detect selective inhibitors of ABCB1, ABCC1, and ABCG2 transporters. *Assay Drug Dev. Technol.* **2008,** 6, 263-276.

26. Ansbro, M. R.; Shukla, S.; Ambudkar, S. V.; Yuspa, S. H.; Li, L. Screening compounds with a novel high-throughput ABCB1-mediated efflux assay identifies drugs with known therapeutic targets at risk for multidrug resistance interference. *PLoS ONE* **2013,** 8, e60334.

27. Zhang, J.; Yang, S. J.; Gonzalez, F.; Yang, J.; Zhang, Y.; He, M.; Shastri, N.; Murthy, N. A peptide-based fluorescent probe images ERAAP activity in cells and in high throughput assays. *Chem. Commun. (Camb.)* **2018,** 54, 7215-7218.

28. Edwards, S. K.; Ono, T.; Wang, S.; Jiang, W.; Franzini, R. M.; Jung, J. W.; Chan, K. M.; Kool, E. T. In Vitro Fluorogenic Real-Time Assay of the Repair of Oxidative DNA Damage. *Chembiochem.* **2015,** 16, 1637-1646.

29. Tahara, Y. K.; Auld, D.; Ji, D.; Beharry, A. A.; Kietrys, A. M.; Wilson, D. L.; Jimenez, M.; King, D.; Nguyen, Z.; Kool, E. T. Potent and Selective Inhibitors of 8-Oxoguanine DNA Glycosylase. *J. Am. Chem. Soc.* **2018,** 140, 2105-2114.

30. Förster, T. Zwischenmolekulare energiewanderung und fluoreszenz. *Ann. Phys.* **1948,** 437, 55-75.

31. Boichenko, I.; Deiss, S.; Bar, K.; Hartmann, M. D.; Hernandez Alvarez, B. A FRET-Based Assay for the Identification and Characterization of Cereblon Ligands. *J. Med. Chem.* **2016,** 59, 770-774.

32. Lea, W. A.; Simeonov, A. Fluorescence polarization assays in small molecule screening. *Expert Opin. Drug Discov.* **2011,** 6, 17-32.

33. Zhang, H.; Nimmer, P.; Rosenberg, S. H.; Ng, S. C.; Joseph, M. Development of a high-throughput fluorescence polarization assay for Bcl-x *Anal. Biochem.* **2002,** 307, 70-75.

34. Qian, J.; Voorbach, M. J.; Huth, J. R.; Coen, M. L.; Zhang, H.; Ng, S. C.; Comess, K. M.; Petros, A. M.; Rosenberg, S. H.; Warrior, U.; Burns, D. J. Discovery of novel inhibitors of Bcl-xL using multiple high-throughput screening platforms. *Anal. Biochem.* **2004,** 328, 131-138.

35. Bruncko, M.; Wang, L.; Sheppard, G. S.; Phillips, D. C.; Tahir, S. K.; Xue, J.; Erickson, S.; Fidanze, S.; Fry, E.; Hasvold, L.; Jenkins, G. J.; Jin, S.; Judge, R. A.; Kovar, P. J.; Madar, D.; Nimmer, P.; Park, C.; Petros, A. M.; Rosenberg, S. H.; Smith, M. L.; Song, X.; Sun, C.; Tao, Z. F.; Wang, X.; Xiao, Y.; Zhang, H.; Tse, C.; Leverson, J. D.; Elmore, S. W.; Souers, A. J. Structure-guided design of a series of MCL-1 inhibitors with high affinity and selectivity. *J. Med. Chem.* **2015,** 58, 2180-2194.

36. Orzaez, M.; Mondragon, L.; Garcia-Jareno, A.; Mosulen, S.; Pineda-Lucena, A.; Perez-Paya, E. Deciphering the antitumoral activity of quinacrine: Binding to and inhibition of Bcl-xL. *Bioorg. Med. Chem. Lett.* **2009,** 19, 1592-1595.

37. Bachovchin, D. A.; Brown, S. J.; Rosen, H.; Cravatt, B. F. Identification of selective inhibitors of uncharacterized enzymes by high-throughput screening with fluorescent activity-based probes. *Nat. Biotechnol.* **2009,** 27, 387-394.

38. Lewallen, D. M.; Bicker, K. L.; Madoux, F.; Chase, P.; Anguish, L.; Coonrod, S.; Hodder, P.; Thompson, P. R. A FluoPol-ABPP PAD2 high-throughput screen identifies the first calcium site inhibitor targeting the PADs. *ACS Chem. Biol.* **2014,** 9, 913-921.

39. Johnson, L. V.; Walsh, M. L.; Chen, L. B. Localization of mitochondria in living cells with rhodamine 123. *Proc. Natl. Acad. Sci. U.S.A.* **1979,** 77, 990-994.

40. Horikoshi, T.; Yoshioka, T.; Kubota, Y.; Yanagisawa, K. Fluorescent dye monitoring of mitochondrial changes associated with malignant cell transformation. *Cell Struct. Funct.* **1987,** 12, 525-537.

41. Deng, X.; Yin, X.; Allan, R.; Lu, D. D.; Maurer, C. W.; Haimovitz-Friedman, A.; Fuks, Z.; Shaham, S.; Kelesnick, R. Ceramide biogenesis is required for radiation-induced apoptosis in the germ line of c. elegans. *Science* **2008,** 322, 110-115.

42. U.S. Patent, No 5,686,261.

43. Mottram, L. F.; Forbes, S.; Ackley, B. D.; Peterson, B. R. Hydrophobic analogues of rhodamine B and rhodamine 101: potent fluorescent probes of mitochondria in living C. elegans. *Beilstein J. Org. Chem.* **2012,** 8, 2156-2165.

44. Poot, M.; Zhang, Y. Z.; Krämer, J. A.; Wells, K. S.; Jones, L. J.; Hanzel, D. K.; Lugade, A. G.; Singer, V. L.; Haugland, R. P. Analysis of mitochondrial morphology and function with novel fixable fluorescent stains. *J. Histochem. Cytochem.* **1996,** 44, 1363-1372.

45. U.S. Patent, No. 5,686,261.

46. Jayaraman, S. Flow cytometric determination of mitochondrial membrane potential changes during apoptosis of T lymphocytic and pancreatic beta cell lines: comparison of tetramethylrhodamineethylester (TMRE), chloromethyl-X-rosamine (H2-CMX-Ros) and MitoTracker Red 580 (MTR580). *J. Immunol. Methods* **2005,** 306, 68-79.

47. Grimm, J. B.; Brown, T. A.; Tkachuk, A. N.; Lavis, L. D. General Synthetic Method for Si-Fluoresceins and Si-Rhodamines. *ACS Cent. Sci.* **2017,** 3, 975-985.

48. Sung, J.; Rho, J. G.; Jeon, G. G.; Chu, Y.; Min, J. S.; Lee, S.; Kim, J. H.; Kim, W.; Kim, E. A New Infrared Probe Targeting Mitochondria via Regulation of Molecular Hydrophobicity. *Bioconjug. Chem.* **2019,** 30, 210-217.

49. Johnson, L. V.; Walsh, M. L.; Bockus, B. J.; Chen, L. B. Monitoring of relative mitochondrial membrane potential in living cells by fluorescence microscopy. *J. Cell Biol.* **1981,** 88, 526-535.

50. Terasaki, M.; Reese, T. S. Characterization of endoplasmic reticulum by co-localization of BiP and dicarbocyanine dyes. *J. Cell Sci.* **1992,** 101, 315-322.

51. Terasaki, M. Fluorescent labeling of endoplasmic reticulum. *Methods Cell Biol.* **1989,** 29, 125-135.

52. Kadigamuwa, C. C.; Mapa, M. S. T.; Wimalasena, K. Lipophilic Cationic Cyanines Are Potent Complex I Inhibitors and Specific in Vitro Dopaminergic Toxins with Mechanistic Similarities to Both Rotenone and MPP+. *Chem. Res. Toxicol.* **2016,** 29, 1468-1479.

53. Shim, S. H.; Xia, C.; Zhong, G.; Babcock, H. P.; Vaughan, J. C.; Huang, B.; Wang, X.; Xu, C.; Bi, G. Q.; Zhuang, X. Super-resolution fluorescence imaging of organelles in

live cells with photoswitchable membrane probes. *Proc. Natl. Acad. Sci. U.S.A.* **2012,** 109, 13978-13983.

54. Mezaki, Y.; Yamaguchi, N.; Yoshikawa, K.; Miura, M.; Imai, K.; Itoh, H.; Senoo, H. Insoluble, speckled cytosolic distribution of retinoic acid receptor alpha protein as a marker of hepatic stellate cell activation in vitro. *J. Histochem. Cytochem.* **2009,** 57, 687-699.

55. Carlini, L.; Manley, S. Live intracellular super-resolution imaging using site-specific stains. *ACS Chem. Biol.* **2013,** 8, 2643-2648.

56. Meinig, J. M.; Peterson, B. R. Anticancer/antiviral agent Akt inhibitor-IV massively accumulates in mitochondria and potently disrupts cellular bioenergetics. *ACS Chem. Biol.* **2015,** 10, 570-576.

57. Zhou, R.; Yazdi, A. S.; Menu, P.; Tschopp, J. A role for mitochondria in NLRP3 inflammasome activation. *Nature* **2011,** 469, 221-225.

58. Li, X.; Zhang, R.; Guo, L.; Zhang, H.; Meng, F.; Yang, R.; Li, C.; Liu, Z.; Yu, X. Co-localization coefficients of a target-switchable fluorescent probe can serve as an indicator of mitochondrial membrane potential. *Anal. Chem.* **2018**.

59. Soultanakis, R. P.; Melamede, R. J.; Berpalov, I. A.; Wallace, S. S.; Beckman, K. B.; Ames, B. N.; Taatjes, D. J.; Janssen-Heininger, Y. M. W. Fluorescene detection of 8-oxoguanine in nuclear and mitochondrial DNA of cultured cells using a recombinant Fab and confocal scanning laser microscopy. *Free Radic. Biol. Med.* **2000,** 28, 987-998.

60. Zheng, Z.; Zhang, T.; Liu, H.; Chen, Y.; Kwok, R. T. K.; Ma, C.; Zhang, P.; Sung, H. H. Y.; Williams, I. D.; Lam, J. W. Y.; Wong, K. S.; Tang, B. Z. Bright Near-Infrared Aggregation-Induced Emission Luminogens with Strong Two-Photon Absorption,

Excellent Organelle Specificity, and Efficient Photodynamic Therapy Potential. *ACS Nano* **2018,** 12, 8145-8159.

61. Presley, A. D.; Fuller, K. M.; Arriaga, E. A. MitoTracker Green labeling of mitochondrial proteins and their subsequent analysis by capillary electrophoresis with laser-induced fluorescence detection. *J. Chromatogr. B* **2003,** 793, 141-150.

62. Mitra, K.; Wunder, C.; Roysam, B.; Lin, G.; Lippincott-Schwartz, J. A hyperfused mitochondrial state achieved at G1-S regulates cyclin E buildup and entry into S phase. *Proc. Natl. Acad. Sci. U.S.A.* **2009,** 106, 11960-11965.

63. Puleston, D. Detection of Mitochondrial Mass, Damage, and Reactive Oxygen Species by Flow Cytometry. *Cold Spring Harb Protoc* **2015,** 2015, pdb prot086298.

64. Smiley, S. T.; Reers, M.; Mottola-Hartshorn, C.; Lin, M.; Chen, A.; Smith, T. W.; Steele, G. D.; Chen, L. B. Intracellular heterogeneity in mitochondrial membrane potentials revealed by a J-aggregate-forming lipophilic cation JC-1. *Proc. Natl. Acad. Sci. U.S.A.* **1991,** 88, 3671-3675.

65. Reers, M.; Smith, T. W.; Chen, L. B. J-aggregate formation of a carbocyanine as a quantitative fluorescent indicator of membrane potential. *Biochemistry* **1991,** 30, 4480-4486.

66. Sakamuru, S.; Li, X.; Attene-Ramos, M. S.; Huang, R.; Lu, J.; Shou, L.; Shen, M.; Tice, R. R.; Austin, C. P.; Xia, M. Application of a homogenous membrane potential assay to assess mitochondrial function. *Physiol. Genomics.* **2012,** 44, 495-503.

67. Zielonka, J.; Joseph, J.; Sikora, A.; Hardy, M.; Ouari, O.; Vasquez-Vivar, J.; Cheng, G.; Lopez, M.; Kalyanaraman, B. Mitochondria-Targeted Triphenylphosphonium-Based

Compounds: Syntheses, Mechanisms of Action, and Therapeutic and Diagnostic Applications. *Chem. Rev.* **2017,** 117, 10043-10120.

68. Yuan, H.; Cho, H.; Chen, H. H.; Panagia, M.; Sosnovik, D. E.; Josephson, L. Fluorescent and radiolabeled triphenylphosphonium probes for imaging mitochondria. *Chem. Commun. (Camb.)* **2013,** 49, 10361-10363.

69. Nigam, S.; Burke, B. P.; Davies, L. H.; Domarkas, J.; Wallis, J. F.; Waddell, P. G.; Waby, J. S.; Benoit, D. M.; Seymour, A. M.; Cawthorne, C.; Higham, L. J.; Archibald, S. J. Structurally optimised BODIPY derivatives for imaging of mitochondrial dysfunction in cancer and heart cells. *Chem. Commun. (Camb.)* **2016,** 52, 7114-7117.

70. Denisov, S. S.; Kotova, E. A.; Plotnikov, E. Y.; Tikhonov, A. A.; Zorov, D. B.; Korshunova, G. A.; Antonenko, Y. N. A mitochondria-targeted protonophoric uncoupler derived from fluorescein. *Chem. Commun. (Camb.)* **2014,** 50, 15366-15369.

71. Cowden, R. R.; Curtis, S. K. Supravital experiments with pyronin Y, a fluorochrome of mitochondria and nucleic acids. *Histochemistry* **1983,** 77, 535-542.

72. Sanchez, M. I.; Martinez-Costas, J.; Mascarenas, J. L.; Vazquez, M. E. MitoBlue: a nontoxic and photostable blue-emitting dye that selectively labels functional mitochondria. *ACS Chem. Biol.* **2014,** 9, 2742-2747.

73. He, H.; Li, D. W.; Yang, L. Y.; Fu, L.; Zhu, X. J.; Wong, W. K.; Jiang, F. L.; Liu, Y. A novel bifunctional mitochondria-targeted anticancer agent with high selectivity for cancer cells. *Sci. Rep.* **2015,** 5, 13543.

74. Souto, A. A.; Acuna, A. U.; Andreu, J. M.; Barasoain, I.; Abal, M.; Amat-Guerri, F. New fluorescent water-soluble taxol derivatives. *Angew. Chem. Int. Ed. Engl.* **1995,** 34, 2710-2712.

75. Diaz, J. F.; Strobe, R.; Engelborghs, Y.; Souto, A. A.; Andreu, J. M. Molecular recognition of taxol by microtubules. Kinetics and thermodynamics of binding of fluorescent taxol derivatives to an exposed site. *J. Biol. Chem.* **2000,** 275, 26265-26276.

76. Diaz, J. F.; Barasoain, I.; Souto, A. A.; Amat-Guerri, F.; Andreu, J. M. Macromolecular accessibility of fluorescent taxoids bound at a paclitaxel binding site in the microtubule surface. *J. Biol. Chem.* **2005,** 280, 3928-3937.

77. Li, X.; Barasoain, I.; Matesanz, R.; Diaz, J. F.; Fang, W. S. Synthesis and biological activities of high affinity taxane-based fluorescent probes. *Bioorg. Med. Chem. Lett.* **2009,** 19, 751-754.

78. Melan, M. A. Use of flurochrome-tagged taxol to produce fluorescent microtubules in solution. *BioTechniques* **1998,** 25, 188-192.

79. Wijesooriya, C. S.; Peterson, J. A.; Shrestha, P.; Gehrmann, E. J.; Winter, A. H.; Smith, E. A. A Photoactivatable BODIPY Probe for Localization-Based Super-Resolution Cellular Imaging. *Angew. Chem. Int. Ed. Engl.* **2018,** 57, 12685-12689.

80. Devaraj, N. K.; Hilderbrand, S.; Upadhyay, R.; Mazitschek, R.; Weissleder, R. Bioorthogonal turn-on probes for imaging small molecules inside living cells. *Angew. Chem. Int. Ed. Engl.* **2010,** 49, 2869-2872.

81. Patterson, D. M.; Nazarova, L. A.; Prescher, J. A. Finding the right (bioorthogonal) chemistry. *ACS Chem. Biol.* **2014,** 9, 592-605.

82. Lukinavicius, G.; Reymond, L.; D'Este, E.; Masharina, A.; Gottfert, F.; Ta, H.; Guther, A.; Fournier, M.; Rizzo, S.; Waldmann, H.; Blaukopf, C.; Sommer, C.; Gerlich, D. W.; Arndt, H. D.; Hell, S. W.; Johnsson, K. Fluorogenic probes for live-cell imaging of the cytoskeleton. *Nat. Methods* **2014,** 11, 731-733.

83. Lukinavicius, G.; Mitronova, G. Y.; Schnorrenberg, S.; Butkevich, A. N.; Barthel, H.; Belov, V. N.; Hell, S. W. Fluorescent dyes and probes for super-resolution microscopy of microtubules and tracheoles in living cells and tissues. *Chem. Sci.* **2018,** 9, 3324-3334.

Chapter 2 - Fluorescent mimics of paclitaxel that selectively bind microtubules and sensitively detect efflux by P-glycoprotein

2.1 Introduction

Paclitaxel (Taxol, 2-1, structure shown in Figure 2-1) is a natural product isolated from the bark extract of yew tree *Taxus brevifolia*.[1] It is been approved by FDA for treatment of various cancers, including ovarian, breast and lung cancers.[2] Its widely acceptable mechanism of action for killing cancer involves binding of Taxol to the β subunit of the protein tubulin, which along with α-tubulin, forms microtubules in cells (Figure 2.1 shows a crystal structure of tubulin bound to the Taxol analogue Taxotere and assembly of microtubules).[3] Hydrolysis of GTP to GDP provides a driving force for assembly of microtubules from dimers of alpha and beta tubulin.[4, 5] These microtubules continuously participate in dynamic growth and shrinkage.[6] Taxol stabilizes polymerized microtubules, inhibiting the these dynamics of tubulin polymerization.[7] This can cause mitotic arrest and cell death by apoptosis.[6, 8]

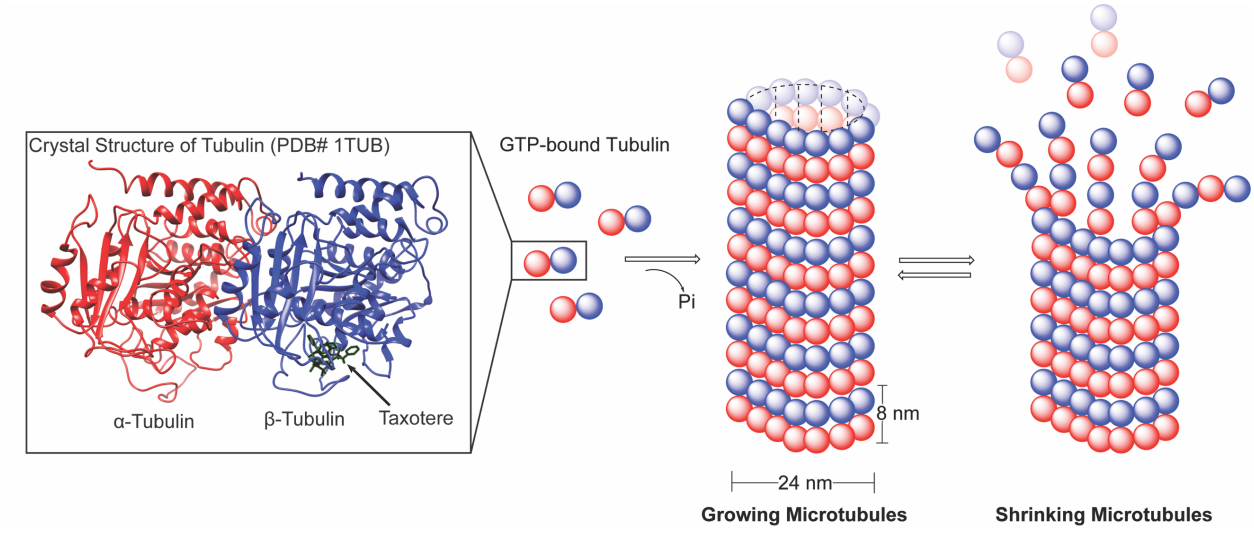

Figure 2.1 Crystal structure of tubulin protein binding with Taxotere and dynamics of microtubules formed by tubulin

However, in human patients, the anticancer activity of Taxol is not fully consistent with an antimitotic mechanism of action.[9, 10] In vivo, Taxol can shrink slow growing solid tumors, such as breast cancers that have a doubling time of approximately 147 days.[10] In these same patients, this drug has limited effect on rapidly dividing cells such as bone marrow myeloid progenitor cells, which double every 3 days. Thus, is unclear how Taxol selectively melts slow-growing tumors while sparing other rapidly dividing cells. This inconsistency has been termed the proliferation rate paradox.[9]

To probe the mechanisms underlying the proliferation rate paradox, we hypothesized that a fluorescent mimic of Taxol that could be detected by confocal microscopy and quantified by flow cytometry could be beneficial. Many fluorescent taxoids have been reported, including commercially available Flutax-1, Flutax-2 and BODIPY-Taxol (structures are shown in Figure 2-2).[11-25] Among them, Flutax-2 is one of the most extensively investigated fluorescent mimics. Structurally related compounds were first described by Nicolaou and co-workers.[17] Flutax-2 is composed of Taxol linked at its 7-position to the bright green fluorophore Oregon Green (OG) with a β-alanine. The term Flutax-2 has also been used to describe related compounds with an L-Ala linker. These probes have been widely used to study the binding mode of Taxol to microtubules,[11, 12] assessing efflux by P-glycoprotein,[26] and analysis of tau-microtubule interactions.[27] The BODIPY fluorophore has also been linked to Taxol.[23-25] However, these BODIPY derivatives are not generally considered suitable for labeling intracellular tubulin in living cells.

The partitioning of a charged compound between organic and buffered aqueous solutions can be represented in log units and defined as $LogD_{pH}$.[28, 29] This can be a crucial physicochemical property for construction of fluorescent probes that penetrate cellular membranes. High experimental LogD values, and calculated cLogD values, are generally associated with higher permeability across lipid membranes. For the most drug-like fluorescent mimics of Taxol, the fluorophore should perturb the properties of Taxol to the lowest possible extent. In Flutax-2, OG exists as a polar dianion at physiological pH (pH = 7.4),[30] causing a large increase of polarity of almost 1000 fold ($cLogD_{7.4}$ = 0.0 for Flutax-2 vs $cLogD_{7.4}$ = 2.9 for Taxol). This loss of lipophilicity suggests that Flutax-2 will be less cell permeable than Taxol, and this high polarity might cause low cytotoxicity in cells compared with Taxol. Consequently, Flutax-2 does not closely mimic Taxol in physicochemical properties and cellular activity.

To obtain a more drug-like fluorescent mimic of Taxol, a smaller and less polar fluorophore might be beneficial. For this application, we choose to incorporate the coumarin-derived fluorophore Pacific Blue (PB).[31] Molly Lee of the Peterson laboratory developed a synthetic method to prepare PB on gram scale starting from inexpensive 2,3,4,5-tetrafluorobenzoic acid.[32] Additionally, PB can be excited at 405 nm with a violet laser found on many confocal microscopes and flow cytometers. As a new approach to create fluorescent mimics of Taxol, we designed three PB-Taxol analogues with different amino acid-derived linkers, PB-Gly-Taxol, PB-βAla-Taxol and PB-GABA-Taxol (structures shown in Figure 2-1). Because modification of the 7-OH of Taxol can preserve high affinity for microtubules,[33] these three PB-Taxols were linked at this position. More importantly, the cLogD of a designed Taxol derivative linked to PB via the simplest amino

acid (glycine) bearing one methylene group (PB-Gly-Taxol, **2-5**, $cLogD_{7.4}$= 2.0) is close to the parent compound Taxol ($cLogD_{7.4}$ = 2.9). The binding affinity, cytotoxicity, and efflux profiles of these compounds were evaluated by confocal laser scanning microscopy and flow cytometry. In these studies, the synthesis and determination of binding affinity were conducted by Dr. Molly Lee.

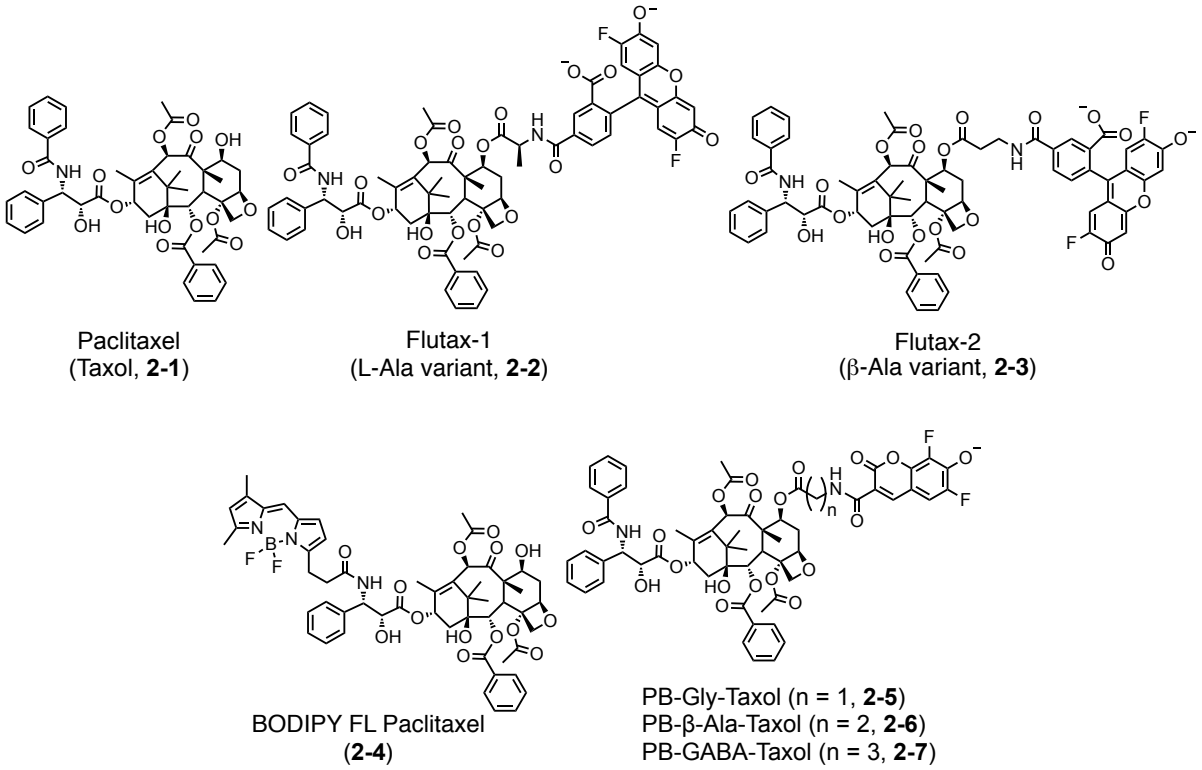

Figure 2.2 Structures of Paclitaxel, commercially available fluorescent taxoids, and novel PB-Taxoids.

2.2 Synthesis of PB-Taxols

The PB-Taxols were prepared in four major steps as shown in Scheme 2.1. Protection of Taxol with TBSCl under basic conditions selectively modified the 2'-OH with TBS without reactivity at the 7-OH.[34] After protection, Fmoc-amino acid linkers were conjugated to the 7-OH of TBS-protected Taxol (**2-8**) by classical EDC coupling to obtain

intermediates (**2-9**, **2-10**, and **2-11**). Cleavage of the Fmoc group with 20% piperidine in DMF, followed by reaction with the active ester PB-NHS provided the corresponding TBS-protected PB-Taxols (**2-12**, **2-13**, **2-14**). The TBS group was deprotected using TBAF in THF to generate the desired PB-Taxols (**2-5**, **2-6**, **2-7**).

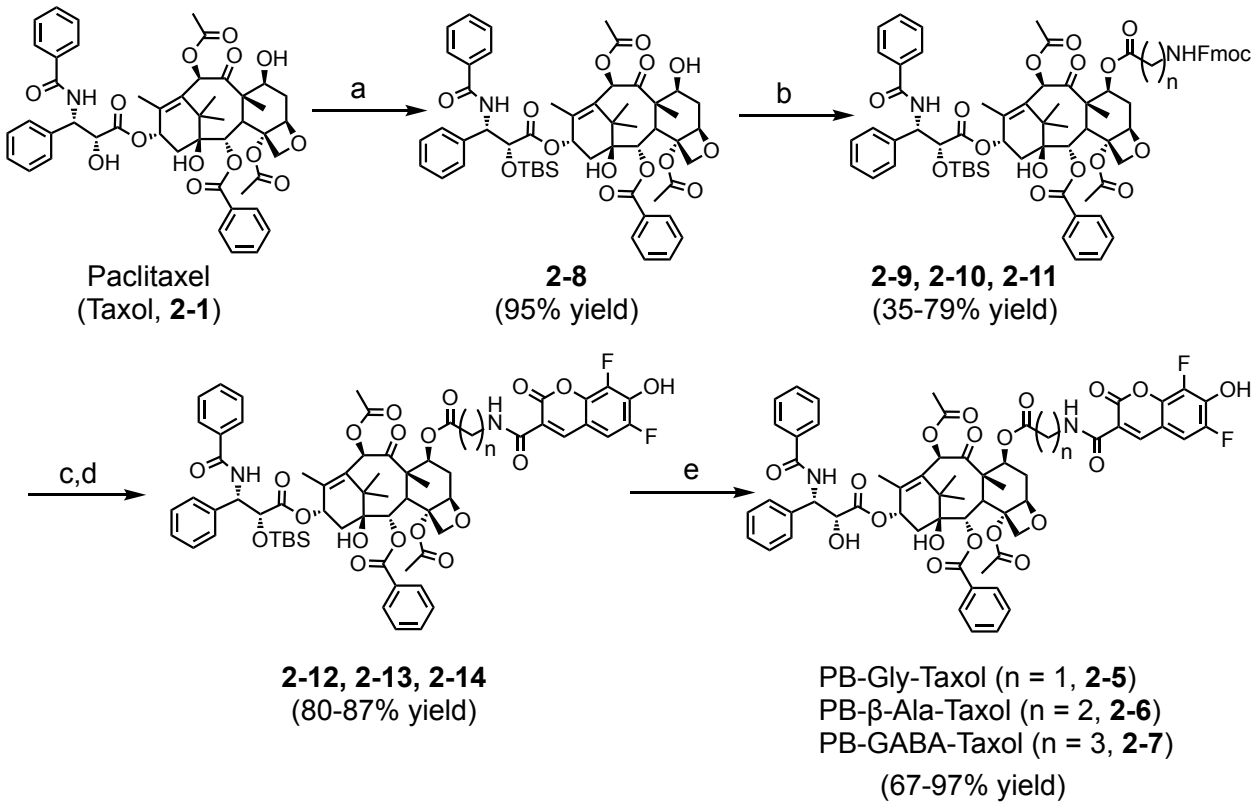

Scheme 2.1 Synthesis of PB-Taxoids. Reagents and conditions: a) TBDMSCl, imidazole, DMF. b) Fmoc-aa-OH, EDC, DMAP, DCM/DMF. c) Piperidine, DMF. d) PB-NHS, DIEA, DMF. e) TBAF (1 M), THF.

The most widely used fluorescent taxoid is Flutax-2. To compare novel taxoids with this compound, we synthesized Flutax-2 from intermediate **2-10** and Oregon Green NHS, followed by cleavage of the protecting group (Scheme 2.2).

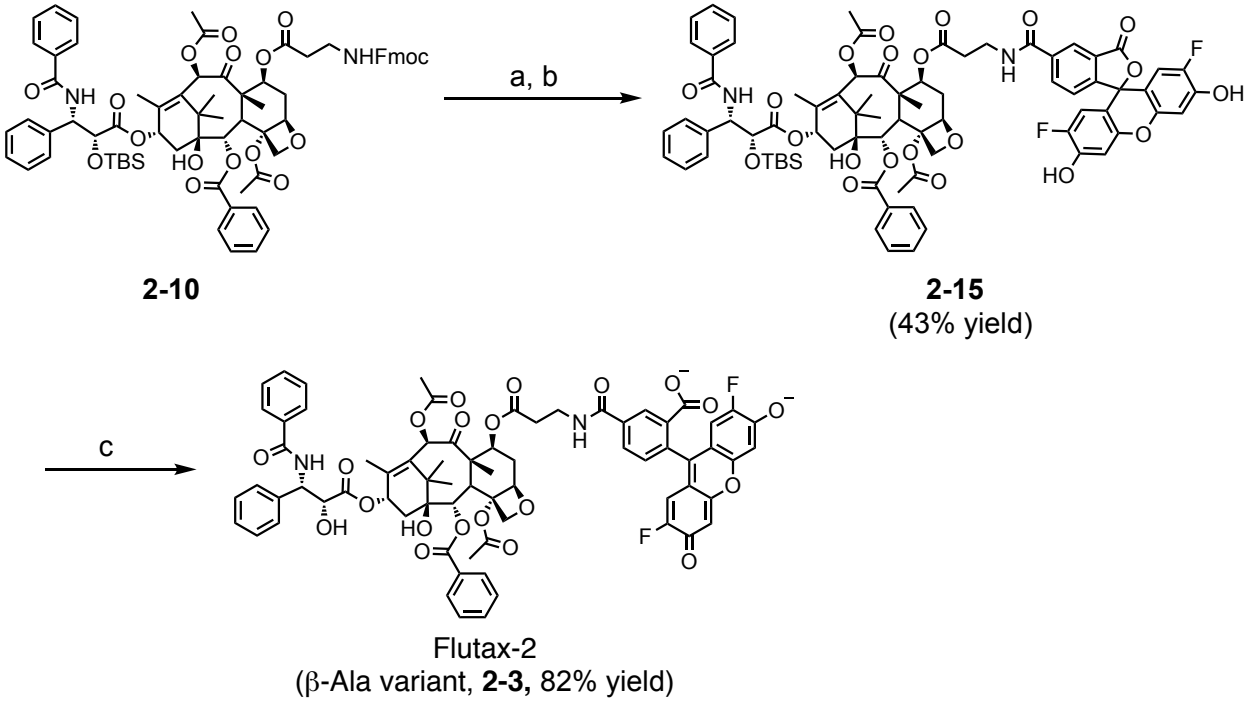

2-10

2-15
(43% yield)

Flutax-2
(β-Ala variant, **2-3,** 82% yield)

Scheme 2.2 Synthesis of Flutax-2. Reagents and conditions: a) Piperidine, DMF. b) OG-NHS, DIEA, DMF. c) TBAF, THF.

2.3 Photophysical properties of PB-Taxoids

To examine the photophysical properties of PB-Taxoids, absorption and emission spectra were obtained in 10% DMSO / PBS, with the inclusion of 0.5% Triton X-100 to limit aggregation. As shown in Figure 2.3, all three fluorescent taxoids exhibit similar absorption and emission spectra and can be readily excited with a violet laser at 405 nm, allowing imaging by confocal microscopy and analysis by flow cytometry. In contrast, Flutax-2 is red shifted compared to the PB-Taxoids and is best excited at 488 nm. In addition, the extinction coefficients of these compounds were determined to allow normalization of concentration by absorbance spectroscopy. Their extinction coefficients (ε = 24300 $M^{-1}cm^{-1}$ for PB-Gly-Taxol, ε = 23300 $M^{-1}cm^{-1}$ for PB-βAla-Taxol, ε = 24100 $M^{-1}cm^{-1}$ for PB-GABA-Taxol) are similar to the parent fluorophore PB (ε = 29500 $M^{-1}cm^{-1}$).[32]

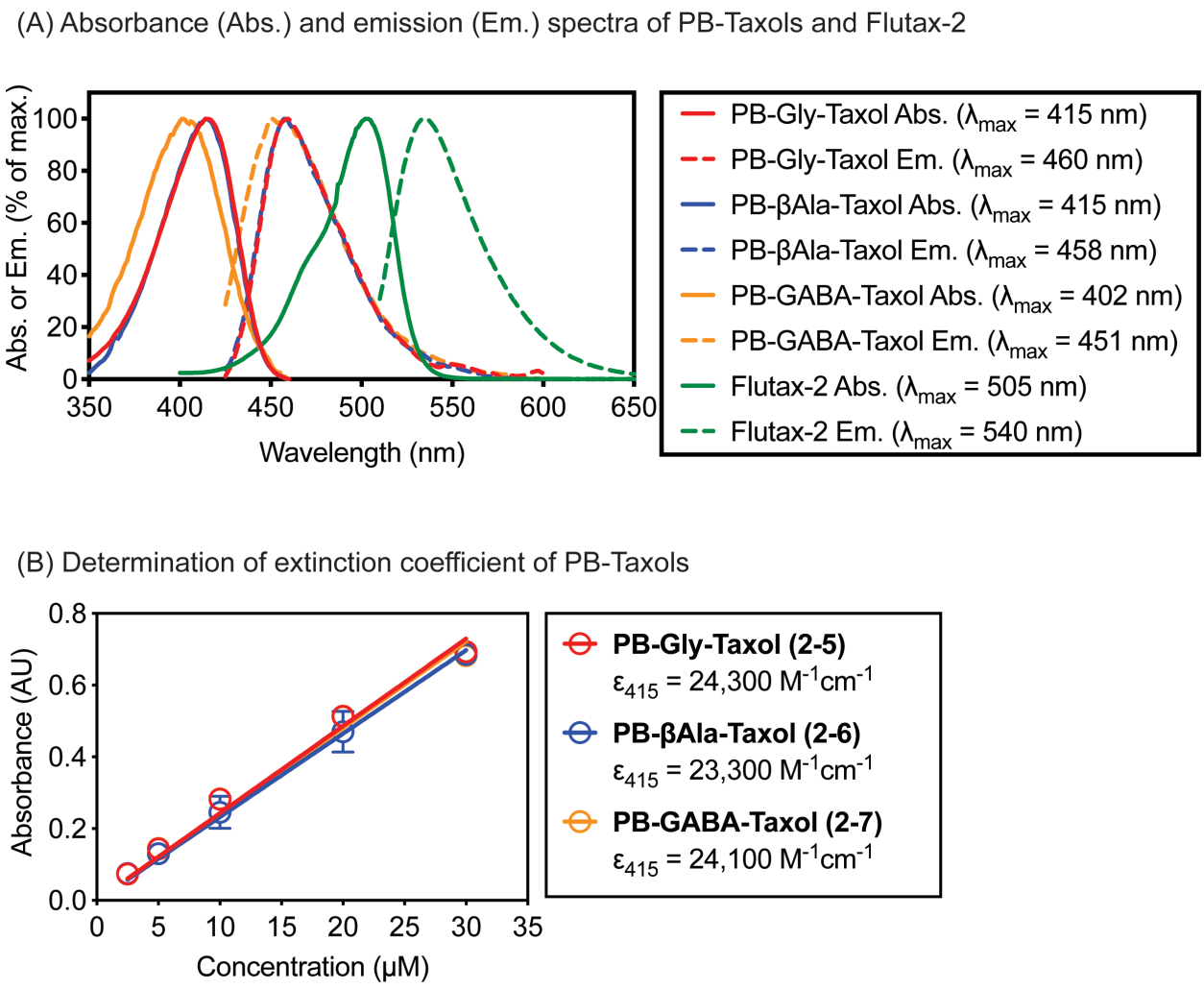

Figure 2.3 Photophysical properties of fluorescent compounds. (A) Normalized absorbance (Abs., 10 μM) and emission (Em., 10 nM) spectra of PB-Gly-Taxol (**2-5**), PB-βAla-Taxol (**2-6**), PB-GABA-Taxol (**2-7**), and Flutax-2 (**2-3**). (B) Determination of extinction coefficients of the PB-Taxoids.

2.4 Determination of binding affinity for tubulin

Computational docking of the PB-Taxoids, Flutax-2, and Taxol to a recent cryo-EM structure of β-tubulin (PDB 3J6G)[5] using Autodock Vina[35] was used to compare possible modes of binding This modeling suggest that PB-Taxoids will bind tubulin similarly to Taxol. The fluorophore PB can potentially occupy a pocket close to the Taxol

binding site, suggesting it may favor binding (Figure 2.4). However, this approach was not able to readily predict differences in affinity of the different PB-Taxoids.

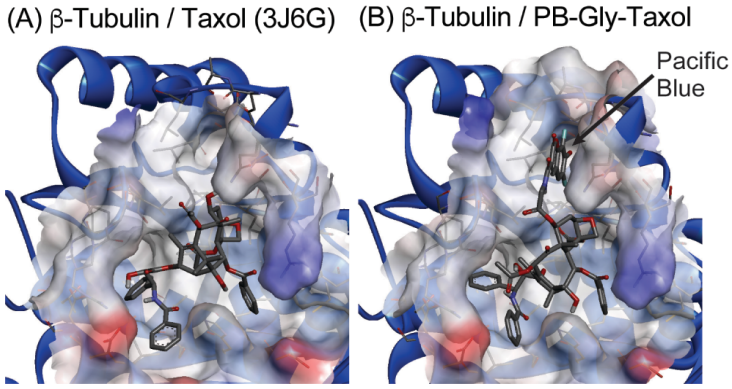

Figure 2.4 Comparison of a published crystal structure of Taxol bound to β-tubulin with a model of PB-Gly-Taxol docked to the apo-protein. The core structure of PB-Gly-Taxol sits in the Taxol-binding pocket, whereas the PB side chain can fit into an adjacent pocket on the protein surface.

To experimentally determine the binding affinities of PB-Taxoids for microtubules in vitro, we performed a fluorescence enhancement assay using crosslinked microtubules in aqueous GAB buffer (10 mM Phosphate, 1 mM EDTA, 1 mM GTP, 3.4 M glycerol, pH = 6.5). These studies revealed that PB-Gly-Taxol exhibited the lowest apparent K_d of 34 ± 6 nM, followed by PB-βAla-Taxol (K_d = 63 ± 8 nM) and PB-GABA-Taxol (K_d = 265 ± 54 nM), indicating that the length of spacer between Taxol core structure and PB plays a crucial role in binding to microtubules. The shortest linker was found to be optimal, and the longer and more flexible spacers were detrimental to binding. Compared to the binding affinity of Flutax-2 (L-Ala, K_d = 14 nM) quantified by changes in fluorescence anisotropy,[36] PB-Gly-Taxol was the most similar in affinity.

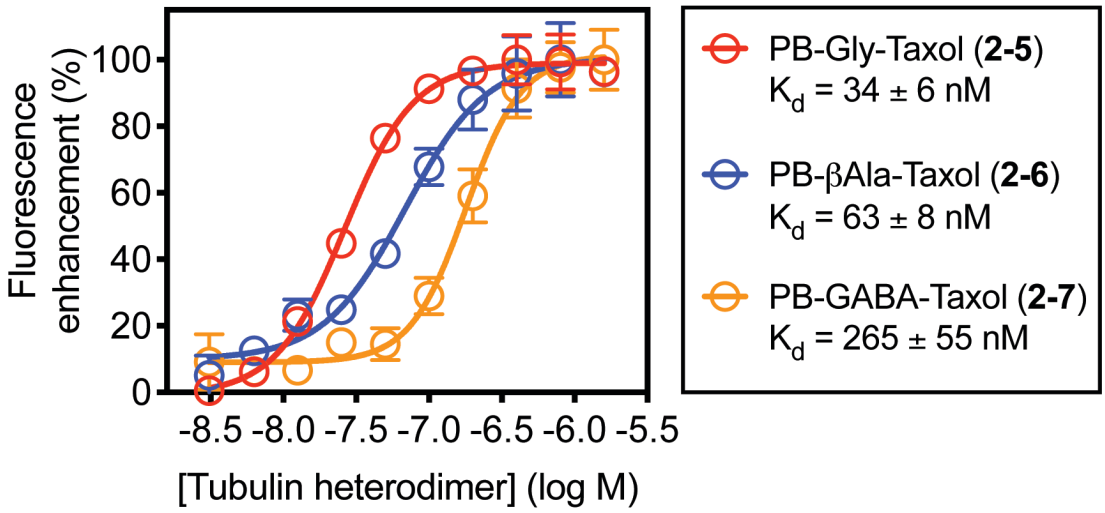

Figure 2.5 Determination of the binding affinities of PB-Taxoids (25 nM) to crosslinked microtubules by enhancement of fluorescence. Experiments were conducted in aqueous GAB buffer (pH 6.5). PB was excited at 405 nm and emitted photons were collected at and above 450 nm.

2.5 Cytotoxicity of PB-Taxoids towards cancer cell lines

Binding of Taxol to microtubules is known to be correlated with cytotoxicity in rapidly dividing cancer cells. Higher binding affinity usually aligns with higher cytotoxicity. To examine whether PB-Taxoids follow the same pattern, the toxicity of these compounds towards HeLa cervical carcinoma cells after 48 h were measured by flow cytometry. Propidium iodide (PI) was applied to stain dead cells and separate them from live ones. The count of live cells as a function of concentration was plotted in Prism 7 software to generate dose-response curves. The drug concentration where 50% of cells were dead was defined as the IC_{50}. Compared with Taxol (IC_{50} = 7 nM), PB-Gly-Taxol (IC_{50} = 120 nM) proved to be the most toxic of the three PB-Taxoids. PB-βAla-Taxol (IC_{50} = 1630 nM) and PB-GABA-Taxol (IC_{50} = 2090 nM) were found to be relatively non-toxic. These IC_{50} values were correlated with the observed apparent K_d values. Interestingly, the toxicity of Flutax-2 (IC_{50} = 1750 nM) was low despite its high affinity for tubulin in vitro, suggesting that the OG fluorophore has a profound effect on the biological properties of Taxol. This

loss of toxicity from OG might be a result of low permeability and lower accumulation in cells.

Taxol is known to be a substrate of P-glycoprotein (P-gp).[37] This efflux pump, found on the plasma membrane, is mainly responsible for the elimination of xenobiotics.[38] To examine whether PB-Taxols are similar to Taxol as efflux substrates, cells were co-treated with verapamil, a known P-gp inhibitor.[39] If PB-Taxols are substrates of P-gp, additional cellular uptake of PB-Taxols was predicted to be observed, potentially resulting in increased cellular fluorescence and cytotoxicity. After co-treatment with 25 μM of verapamil, a concentration that is nontoxic to HeLa cells (Figure 2.6), but sufficient enough to inhibit P-gp, we found that cytotoxic dose-response curves of PB-Taxols were shifted to the left compared to cells without verapamil (Figure 2.7). The IC_{50} values of Taxol, PB-Gly-Taxol, PB-βAla-Taxol and PB-GABA-Taxol decreased by approximately 2-fold, 2-fold, 5-fold and 3.6-fold, respectively. More importantly, Flutax-2, a known P-gp substrate,[26] exhibited the lowest cytotoxicity (IC_{50} = 1310 nM) in the presence of verapamil, suggesting it does not closely mimic Taxol in that respect.

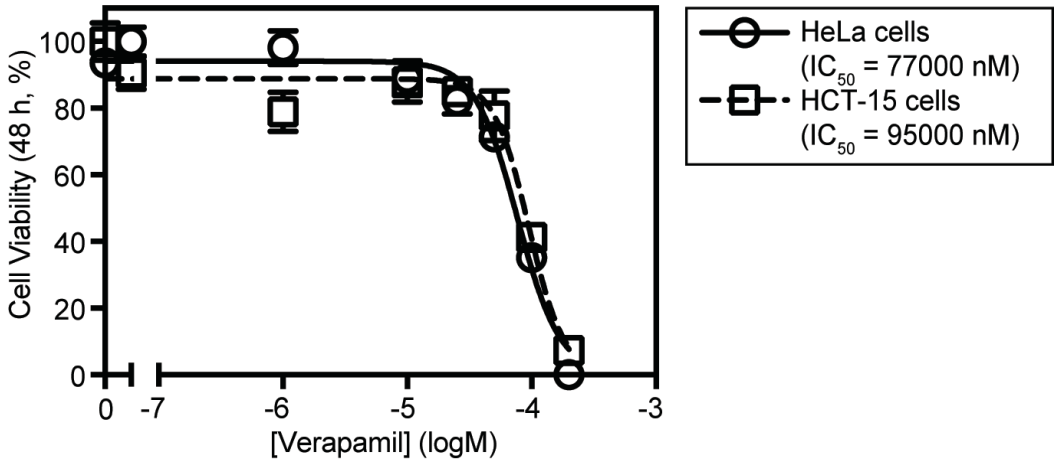

Figure 2.6 Analysis of cytotoxicity of verapamil in HeLa and HCT-15 cells over 48 h. Cellular viability was measured by flow cytometry.

(A) Cytotoxicity of compounds towards HeLa cells

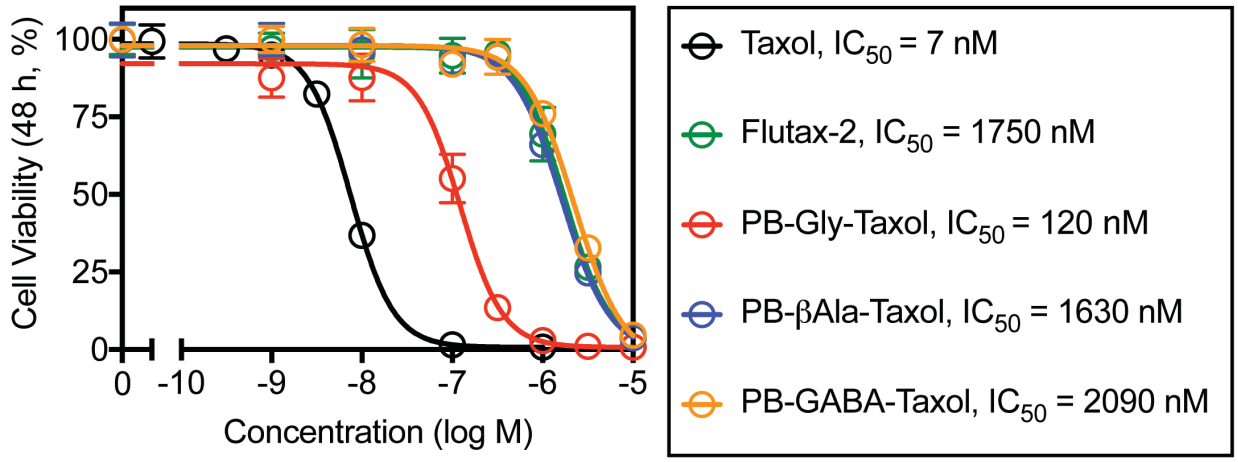

(B) Cytotoxicity of compounds towards HeLa cells in the presence of verapamil (25 μM)

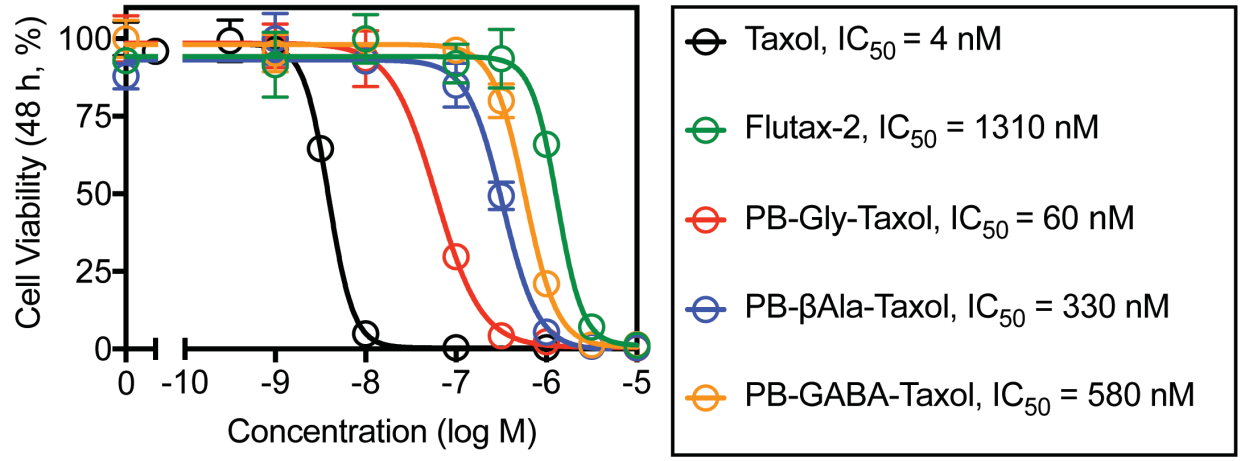

Figure 2.7 Analysis of cytotoxicity in HeLa cells. Cells were treated with compounds in the absence (A) or presence (B) of verapamil (25 μM) for 48 h. Cell viability was measured by flow cytometry.

The HeLa cell line is known to express low levels of P-gp[40] compared to the HCT-15 cell line. Consequently, the cytotoxicity of PB-Taxols in HCT-15 cells with or without verapamil was similarly evaluated. Similar to the trend observed in HeLa cells, PB-Gly-Taxol (IC_{50} = 3760 nM) exhibited the greatest cytotoxicity compared to Taxol (IC_{50} = 120 nM), followed by PB-βAla-Taxol (IC_{50} > 10000 nM) and PB-GABA-Taxol (IC_{50} > 20000

nM). The addition of 25 μM verapamil increased the cytotoxicity of Taxol, PB-Gly-Taxol, PB-βAla-Taxol and PB-GABA-Taxol by 40-fold, 42-fold, 34-fold and 27-fold, respectively.

(A) Cytotoxicity of compounds towards HCT15 cells

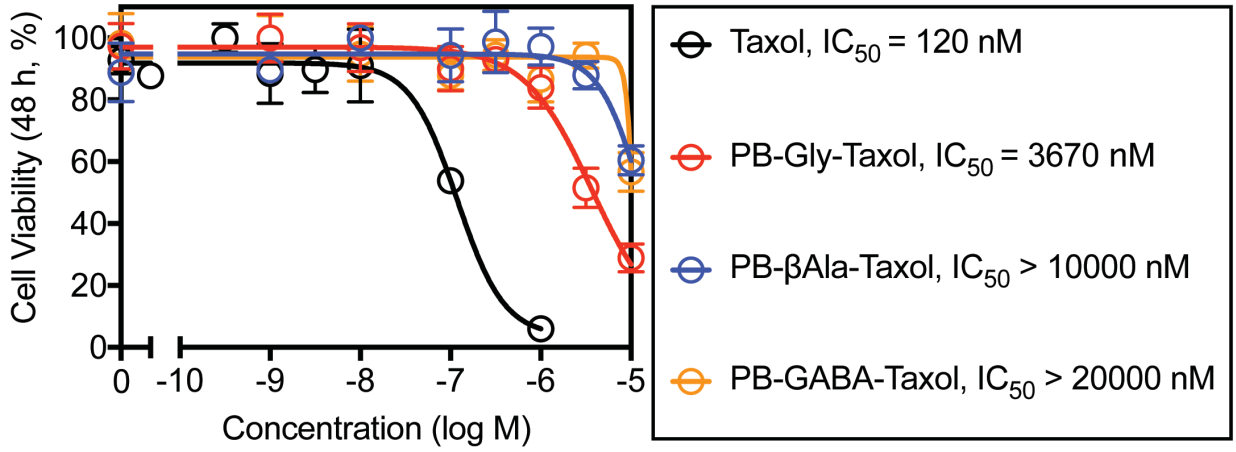

(B) Cytotoxicity of compounds towards HCT15 cells in the presence of verapamil (25 μM)

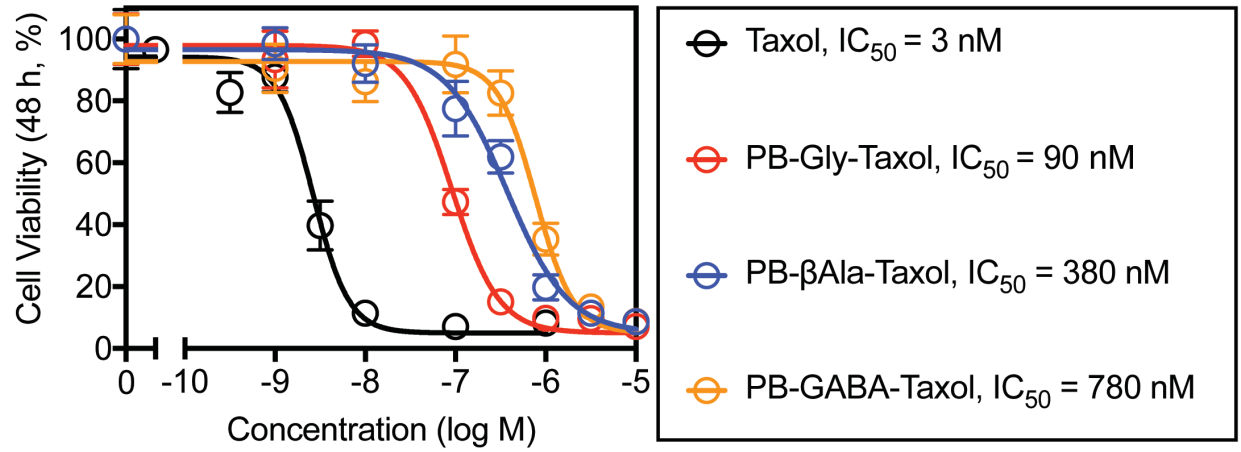

Figure 2.8 Analysis of cytotoxicity in HCT15 cells. Cells were treated with compounds in the absence (A) or presence (B) of verapamil (25 μM) for 48 h. Cell viability was measured by flow cytometry.

In contrast to Flutax-2 and the other PB-Taxols, PB-Gly-Taxol was found to exhibit the greatest toxicity and represent the closest fluorescent mimic of Taxol. Moreover, the effects of verapamil parallel the effect of this P-gp inhibitor on the toxicity of Taxol. For these reasons, we focused most of our further studies on this particular fluorescent probe.

2.6 Localization of PB-Taxoids in live cancer cells by confocal microscopy

To visualize the localization of PB-Taxoids in live cells, confocal laser scanning microscopy was employed. These studies revealed that after treatment with PB-Gly-Taxol for 1 h, cellular fluorescence can be observed in a network of cytoplasmic filaments, consistent with association with microtubules. The addition of verapamil increased the brightness of this fluorescence in live HeLa cells in a dose-dependent manner (Figure 2.9).

(A) Treatment of HeLa cells with PB-Gly-Taxol (**2-5**, 1 μM, 1 h)

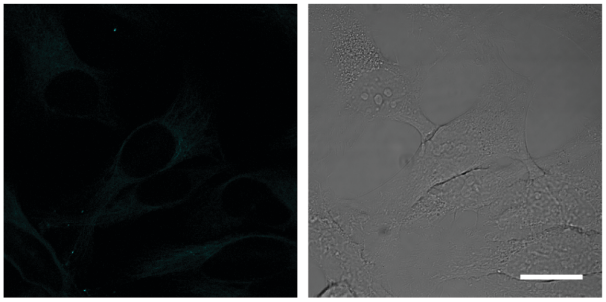

(B) Treatment of HeLa cells with PB-Gly-Taxol (**2-5**, 1 μM, 1 h) and verapamil (1 μM)

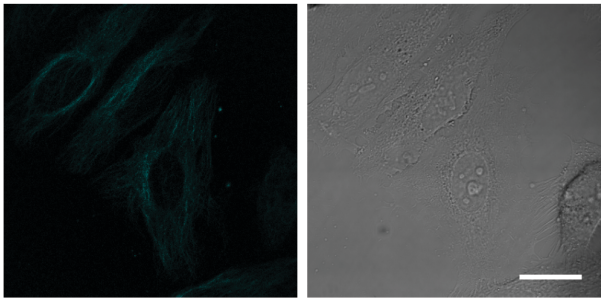

(C) Treatment of HeLa cells with PB-Gly-Taxol (**2-5**, 1 μM, 1 h) and verapamil (10 μM)

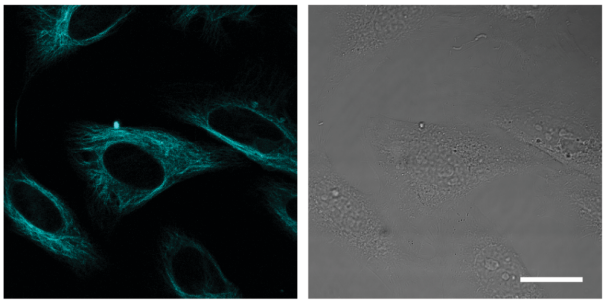

(D) Treatment of HeLa cells with PB-Gly-Taxol (**2-5**, 1 μM, 1 h) and verapamil (25 μM)

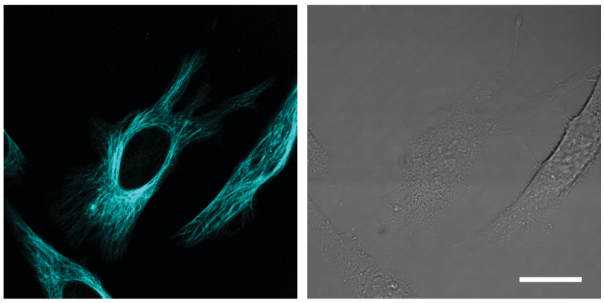

(E) Treatment of HeLa cells with PB-Gly-Taxol (**2-5**, 1 μM, 1 h) and verapamil (100 μM)

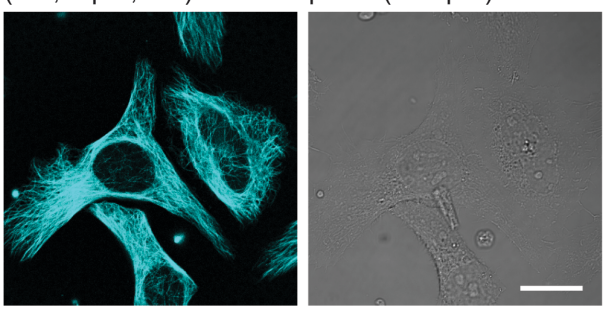

(F) Structure of (±) verapamil

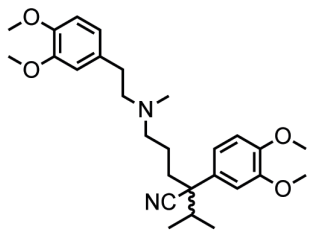

Figure 2.9 Dose-dependent effects of verapamil on the uptake of PB-Gly-Taxol in live HeLa cells. Images were taken by confocal laser scanning microscopy (Ex. 405 nm, Em. 425-500 nm) after 1 h incubation at 37 °C with increasing concentration of verapamil (0, 1, 10, 25, 100 μM, A to E). Scale bar = 25 microns. The structure of racemic verapamil is shown in F.

To confirm the stained intracellular structrues are microtubules, a fluorescence colocalization assay was performed. Since the emission spectra of Flutax-2 and PB-Gly-Taxol are mutually orthogonal, HeLa cells were co-treated with Flutax-2 and PB-Gly-Taxol. After incubation for 1 h, PB-Gly-Taxol colocalizes very well with Flutax-2 shown in Figure 2.10, confirming binding to microtubules. However, PB-Gly-Taxol only stains microtubule, whereas Flutax-2 accumulates in other structures previously reported to be associated with the Golgi apparatus.[16]

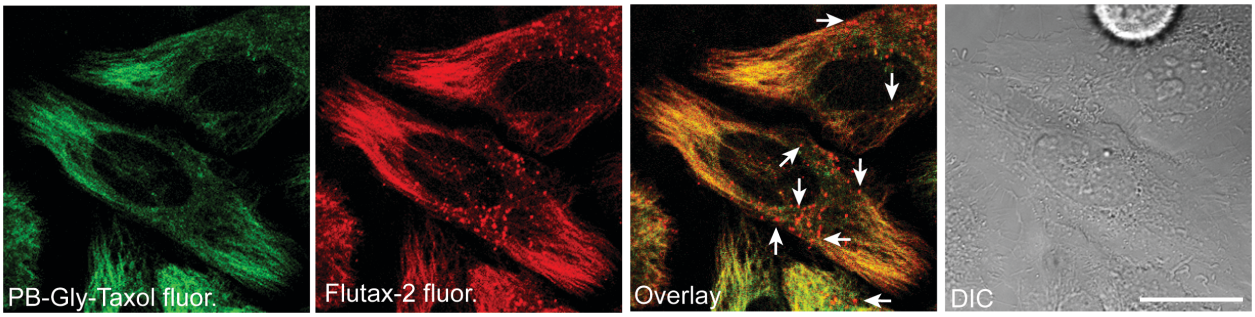

Figure 2.10 Confocal laser scanning and DIC microscopy of HeLa cells treated with PB-Gly-Taxol (1 μM), Verapamil (25 μM) and Flutax-2 (5 μM) for 1 h at 37 °C. Scale bar = 25 microns.

2.7 PB-Gly-Taxol is a P-gp substrate as evidenced by confocal microscopy

Overexpression of P-gp frequently confers resistance to the antiproliferative effect of Taxol.[41] To further confirm that PB-Gly-Taxol is a P-gp substrate, we transfected PC-3 cells that do not express P-gp[42] with a plasmid (pHaMDR-EGFP)[43] encoding P-gp fused to enhanced green fluorescent protein (EGFP). After 48 h, cells that were successfully transfected exhibited fluorescence (false colored red in Figure 2.11) on the plasma

membrane distinct from adjacent non-transfected cells that don't express P-gp. After treatment with the spectrally orthogonal PB-Gly-Taxol for 1 h, the cells expressing P-gp exhibited little uptake of PB-Gly-Taxol (false colored green in Figure 2.11), whereas cells that did not express P-gp could be seen to strongly accumulate PB-Gly-Taxol on microtubules. This dramatic difference indicates that P-gp efficiently promotes efflux of PB-Gly-Taxol. Additionally, co-treatment with PB-Gly-Taxol and verapamil reversed this effect by inhibiting the efflux of PB-Gly-Taxol. This rescue of function depends on the concentration of verapamil. At 25 μM, cells with high expression of P-gp maintain some efflux of PB-Gly-Taxol. However, at 100 μM verapamil, most cells are stained with PB-Gly-Taxol even cells that express high levels of P-gp. This evidence strongly supports the hypothesis that PB-Gly-Taxol is an efficient substrate of P-gp.

(A) Treatment of HCT-15 cells transiently transfected with P-gp-EGFP with PB-Gly-Taxol (**2-5**, 1 μM, 1 h)

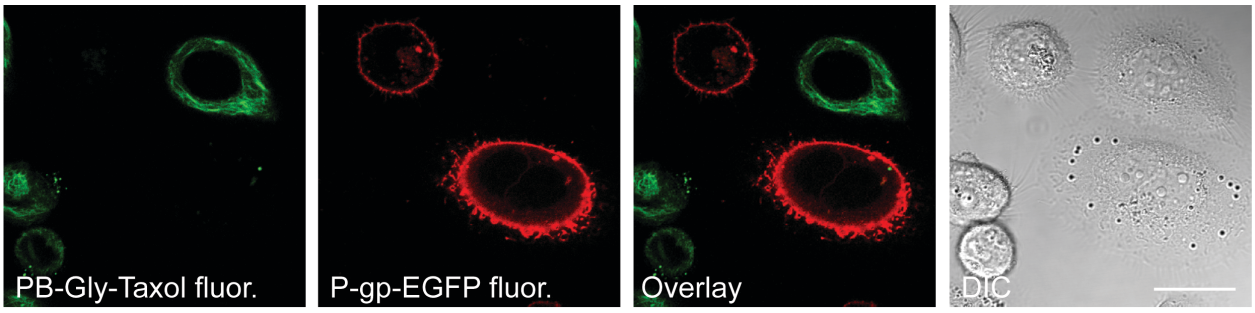

(B) Treatment of HCT-15 cells transiently transfected with P-gp-EGFP with PB-Gly-Taxol (**2-5**, 1 μM) and verapamil (25 μM, 1 h)

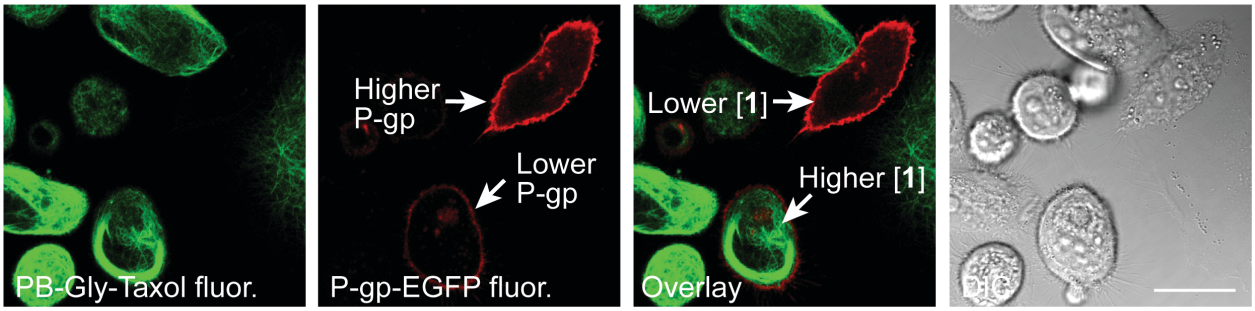

(C) Treatment of HCT-15 cells transiently transfected with P-gp-EGFP with PB-Gly-Taxol (**2-5**, 1 μM) and verapamil (100 μM, 1 h)

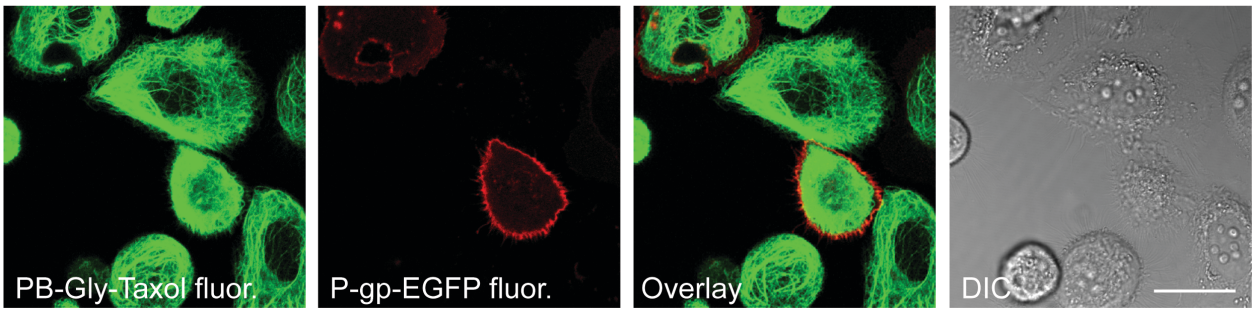

Figure 2.11 Confocal laser scanning and DIC micrographs of living PC3 cells transiently transfected with P-gp-EGFP and treated with PB-Gly-Taxol without (A) and with (B, C) verapamil. In panel B, the effects of lower and higher expression of P-gp in transfected cells treated with verapamil (25 μM) are highlighted. In panel C, treatment with a higher concentration of verapamil (100 μM) results in greater inhibition of efflux by P-gp. Scale bar = 25 microns.

2.8 PB-Taxoids are highly sensitive substrates of P-gp

To further investigate the sensitivity of PB-Gly-Taxol as a P-gp substrate, we compared this compound with the widely used P-gp substrate rhodamine 123 (Rho123).[44]

Rho123 is a green fluorophore that becomes localized in mitochondria. It additionally binds to a putative R site (named after Rho123) of P-gp. With addition of the P-gp inhibitor verapamil, Rho123 accumulate to a greater extent in mitochondria, resulting an increased fluorescence that can be detected by confocal microscopy and flow cytometry. After treatment of P-gp expressing HeLa cells with Rho123 or PB-Gly-Taxol for 1 h, we observed increased binding to mitochondria or microtubules by confocal microscopy upon addition of 25 μM verapamil. However, substantial differences were observed between these two probes. Using the same microscope settings (laser power and gain), the uptake of PB-Gly-Taxol was observed to increase dramatically whereas the change of cellular fluorescence with Rho123 was modest. A similar pattern was observed in P-gp-overexpressing HCT15 cells (Figure 2.12).

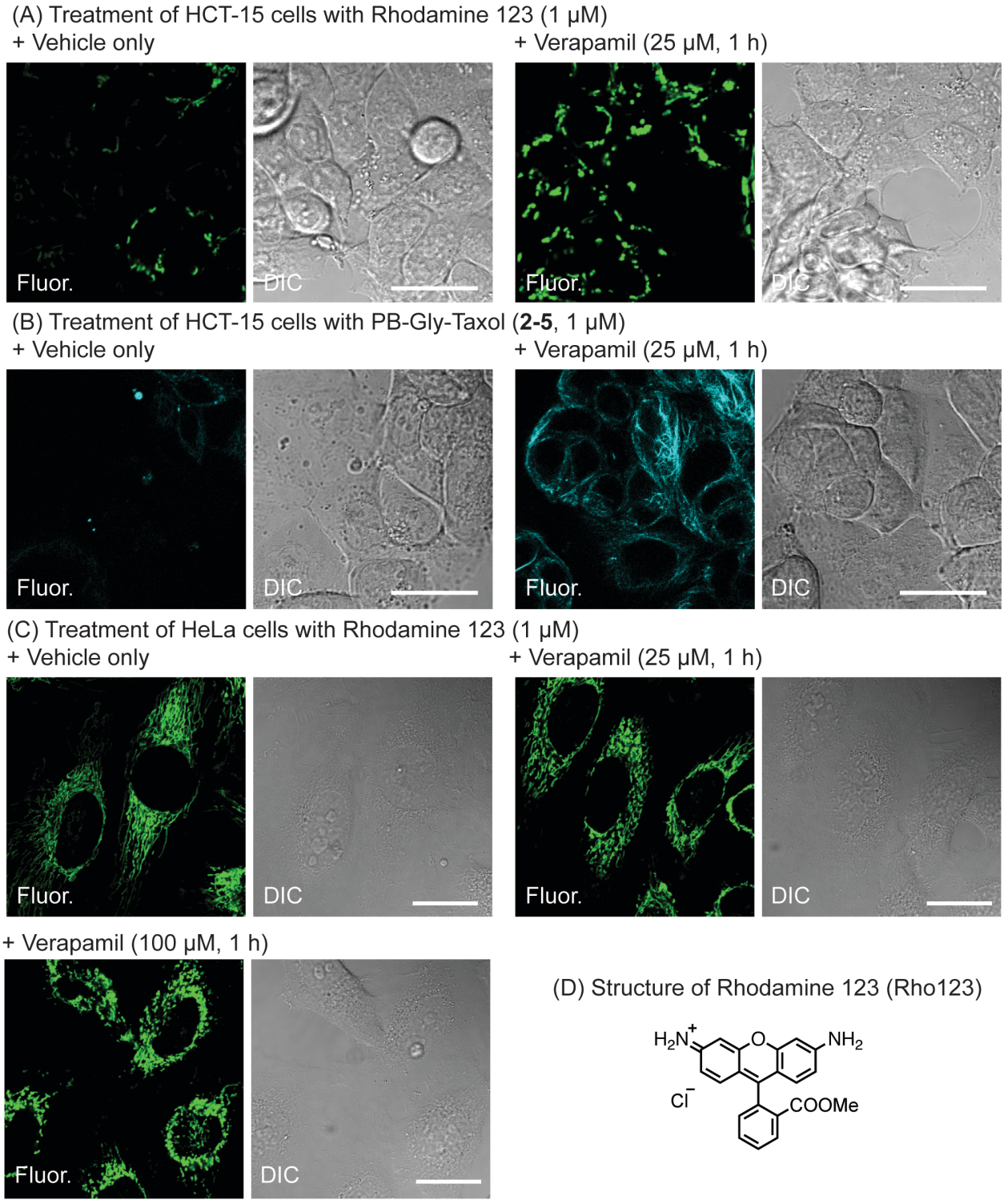

Figure 2.12 Confocal laser scanning and DIC microscopy of HCT15 cells treated with P-gp substrate Rho123 (A, C) or PB-Gly-Taxol (B) for 1 h 37°C. Scale bar = 25 microns. The structure of Rho123 is shown in D.

To quantify these changes of fluorescence intensity, we used flow cytometry to measure the fluorescence of each dye and calculate the fold change upon addition of 25 μM or 100 μM verapamil. In HCT15 cells, the fluorescence of Rho123 increased by 3-fold with either 25 μM or 100 μM verapamil while the fluorescence of PB-Gly-Taxol increases by 7-fold with 25 μM and 15-fold with 100 μM verapamil. In HeLa cells, the fluorescence of Rho123 remains the same upon addition of 25 μM or 100 μM verapamil. We conclude that Rho123 is unable to detect P-gp at the low levels expressed by HeLa cells. In contrast, the fluorescence of PB-Gly-Taxol increases by 10-fold with 25 μM and 23-fold with 100 μM verapamil, indicating it is a much more sensitive P-gp substrate than Rho123.

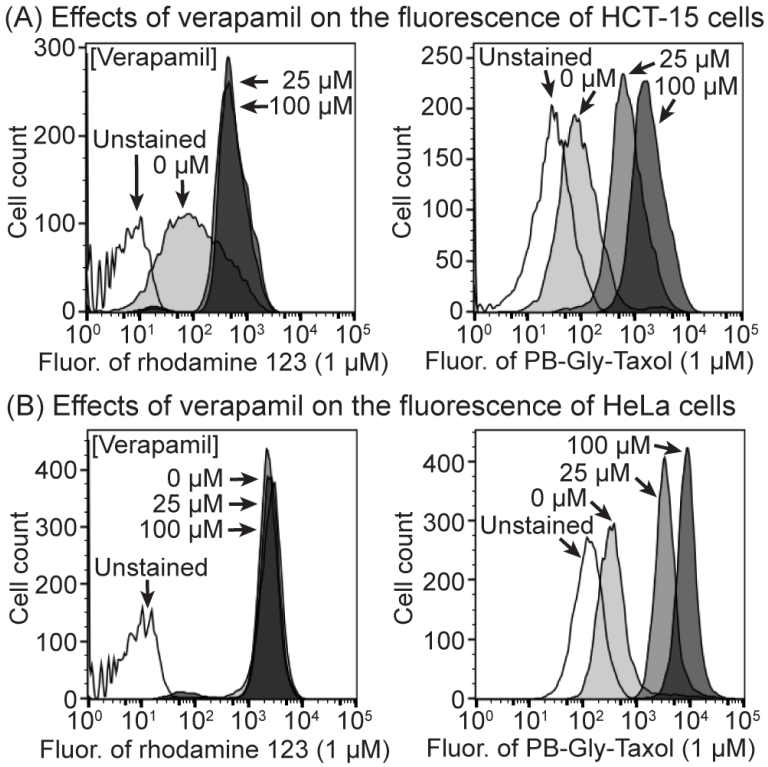

Figure 2.13 Quantitative analysis of fluorescence changes of Rho123 (1 μM) or PB-Gly-Taxol (1 μM) in HeLa cells (A) and HTC15 cells (B) upon addition of verapamil (0 μM, 25 μM, 100 μM) for 1 h at 37 °C.

2.9 Conclusions

Unlike Flutax-2, which exhibits low toxicity that does not closely mimic Taxol due to modification with the OG fluorophore, PB-Gly-Taxol recapitulates more of the tubulin binding, cytotoxicity, and efflux properties of parent drug Taxol. In brief, PB-Gly-Taxol binds microtubules with double digit nanomolar affinity, and it has the highest binding affinity among the three PB-Taxols studied. This high binding affinity data is correlated with enhanced cytotoxicity in both the HeLa and HCT-15 cancer cell lines. Additionally, in contrast to the commercially available Flutax-2, PB-Gly-Taxol stains microtubules in cells with high specificity as imaged by confocal microscopy. Similar to Taxol, PB-Gly-Taxol accumulates in a dose-dependent manner in HeLa cells upon addition of the P-gp inhibitor verapamil. This observation was supported by a transfection of PC3 cells with a plasmid encoding MDR-EGFP. Moreover, PB-Gly-Taxol is a much more sensitive than Rhodamine 123 as a P-gp substrate in cancer cell lines. In future studies, because PB-Gly-Taxol represents a close mimic of many of the biological properties of Taxol, we hypothesize that it might provide as a novel tool the study proliferation rate paradox associated with this important anticancer drug.

2.10 Experimental Section

General experimental section. Chemicals were from Sigma Aldrich, Acros Organics, Alfa Aesar, Oakwood Chemical, or Chem-Impex International. ^{1}H and ^{13}C NMR spectra were acquired on an Avance AVIII 500 MHz instrument. Chemical shifts (δ) are reported in ppm referenced to $CDCl_3$ (7.26 ppm for ^{1}H and 77.2 ppm for ^{13}C) or DMSO-d_6 (2.50 ppm for ^{1}H, 39.5 ppm for ^{13}C). ^{1}H coupling constants (J_{HH}, Hz) and ^{13}C coupling constants (J_{CF}, Hz) are reported as: chemical shift, multiplicity (s = singlet, d = doublet, t = triplet, m

= multiplet, dd = doublet of doublets, ddd = doublet of doublet of doublets, dq = doublet of quartets, dt = doublet of triplets, ddt = doublet of doublet of triplets), coupling constant, and integration. High Resolution Mass Spectra (HRMS) were obtained at the Mass Spectrometry Laboratory at the University of Kansas on a Micromass LCT Premier. Thin layer chromatography (TLC) used EMD aluminum-backed (0.20 mm) silica plates (60 F-254). Flash chromatography used ICN silica gel (200-400 mesh). TLC plates were visualized with a UV lamp. Preparative HPLC was performed with an Agilent 1200 instrument equipped with a Hamilton PRP-1 reverse phase column (250 mm length, 21.2 mm ID, 7 µm particle size) with detection of absorbance at 215, 254, 370, and 488 nm. All non-aqueous reactions were carried out using flame- or oven-dried glassware under an atmosphere of dry argon or nitrogen. Tetrahydrofuran (THF), dichloromethane (CH_2Cl_2), and *N*,*N*-dimethylformamide (DMF) were purified via filtration through two columns of activated basic alumina under an atmosphere of argon using a solvent purification system from Pure Process Technology (GlassContour). Absorbance spectra were obtained using a semimicro (1.4 mL) UV quartz cuvette (Sigma-Aldrich, Z27667-7) on an Agilent 8452A diode array spectrometer. Molar extinction coefficients (ε), used to determine concentrations by absorbance, were measured in PBS (10 mM Na_2HPO_4, 137 mM NaCl, 2.7 mM KCl, 1.8 mM KH_2PO_4, pH 7.4) containing 10% DMSO and 0.5% Triton X-100 and calculated from Beer's Law plots of absorbance λ_{max} versus concentration (Figure S1). Linear least squares fitting of the data (including a zero intercept) was used to determine the slope (ε). Fluorescence spectra were acquired using a SUPRASIL ultra-micro quartz cuvette (PerkinElmer, B0631079) on a Perkin-Elmer LS55 Fluorescence

Spectrometer (10 nm slit width). Values for $cLogD_{pH7.4}$ were calculated with MarvinView (v. 16.7.25.0, ChemAxon LogP method).

Cell culture: HeLa cells, obtained from ATCC (CCL-2), were cultured in Dulbecco's Modified Eagle Medium (DMEM, Sigma D6429). PC-3 cells (a gift from Dr. Matthew Levy, Albert Einstein College of Medicine) were cultured in DMEM/Ham's F-12 medium (Sigma 8437). HCT-15 cells (ATCC CCL-225, a gift from Dr. Liang Xu, University of Kansas) were cultured in RPMI-1640 medium (Sigma R8758). Media was supplemented with fetal bovine serum (FBS, 10%), penicillin (100 units/mL), and streptomycin (100 µg/mL). Cells were maintained in a humidified 5% CO_2 incubator at 37 °C.

Transient transfection of PC-3 cells with pHaMDR-EGFP: PC-3 cells in DMEM/Ham's F-12 medium were seeded onto an 8-well cover glass slide (Ibidi µ-Slide, 300 µL, 20,000 cells/well) and allowed to proliferate for 16 h at 37 °C. Plasmid pHaMDR-EGFP (2 µg, a gift from Dr. Michael M. Gottesman, National Cancer Institute) was incubated at 22 °C with the DNA transfection reagent X-tremeGENE HP (2 µL, Roche) in serum-free DMEM medium (200 µL). After 30 min, the DNA complex (20 µL) was added to each well. The cells were further incubated at 37 °C for 48 h. After transfection, the cells were washed with complete medium, further treated with probes, and imaged by confocal microscopy.

Confocal microscopy: Cells were added to an 8-well cover glass slide (Ibidi µ-Slide, 300 µL, 20,000 cells/well) and allowed to proliferate for 24 h prior to addition of compounds. Compounds in DMSO stock solutions were serially diluted 1,000-fold in complete medium

(final concentration of 0.1% DMSO) prior to addition to cells. Cells were treated with compounds at 37 °C for one hour before imaging with a Leica SPE2 confocal laser-scanning microscope (63X oil-immersion objective). Taxol-PB analogues were excited with a 405 nm laser and emitted photons were collected from 425-500 nm. Flutax-2, EGFP, and rhodamine 123 were excited with a 488 nm laser and emitted photons were collected from 500-600 nm.

Analysis of cytotoxicity: Cells were seeded on a 96-well plate in complete medium at 8,000 cells / 200 μL per well 16 h prior to treatment. All compounds were serial diluted in DMSO and added to complete medium to achieve a 1:1000 dilution factor (0.1% DMSO in each well). The original media was removed from all wells by aspiration and replaced with the treatment media (200 μL) at the concentrations indicated. Plates were incubated for 48 h at 37 °C and cells were analyzed in triplicate. Following this incubation period, the media was aspirated and wells were washed with PBS (phosphate-buffered saline, pH 7.4). Wells were further treated with trypsin EDTA solution (50 μL) at 37 °C for 5 min (HeLa cells) or 10 min (HCT-15 cells) followed by complete medium (100 μL) containing propidium iodide (PI, 4.5 μM). The total cell-count for each well was determined by flow cytometry, using an Accuri C6 flow cytometer, and staining with propidium iodide was used to identify populations of live cells. Counts of viable cells for each treatment, determined in triplicate, were used to generate dose-response curves. These curves were fitted by non-linear regression with an inhibitor vs. response variable slope 4-parameter model (GraphPad Prism 7) to determine IC_{50} values. Based on curve fitting, standard errors for all cytotoxic IC_{50} values were < 5%.

Analysis of cellular efflux by flow cytometry: Trypsinized HCT-15 or HeLa cells (200,000 cells/200 µL per Eppendorf tube) were incubated in suspension with PB-Gly-Taxol (HeLa, 1 µM; HCT-15, 1 µM), Rho123 (HeLa, HCT-15, 1 µM), and either DMSO (0.2%) or verapamil (25 µM or 100 µM, 0.2% DMSO) for 1 h at 37 °C. After incubation, cells were centrifuged at 2000 rpm for 2 min. The supernatant was removed, cells were washed with cold PBS, and pelleted again by centrifugation. The PBS was removed, and cells were resuspended in cold PBS (2% BSA), and placed on ice prior to flow cytometry. Analysis was performed on a BD FACS Aria Fusion instrument equipped with 405 and 488 nm lasers. 10,000 cells were counted for each sample and each condition was tested in triplicate. Photons emitted by PB-Gly-Taxol were collected after passing through a Pacific Blue filter (450 / 40 nm) and photons emitted by rhodamine 123 were collected after passing through a FITC filter (530 / 30 nm). Cell populations were gated based on untreated cells.

Preparation of cross-linked microtubules: Following a previously published protocol[15], microtubules were stabilized against disassembly for use in binding studies. Briefly, tubulin (50 µM, cytoskeleton Inc., cat# MT001-A, from bovine brain) in GAB buffer (10 mM phosphate, 1 mM EDTA, 1 mM GTP, 3.4 M glycerol, pH 6.5) was incubated at 37 °C for 30 min to allow assembly of microtubules. Glutaraldehyde (20 mM) was added, and the solution was incubated at 37 °C for 10 min to achieve cross-linking. The reaction was quenched by the addition of $NaBH_4$ (to 60 mM) on ice.

Determination of affinities of PB-Taxoids for tubulin by fluorescence enhancement:

Fluorescence intensity data was acquired using a Corning 96-well solid black polystyrene microplate on a Packard Fusion Microplate Reader equipped with excitation (405 / 30 nm) and emission filters (450 nm LP) for Pacific Blue. The concentration of tubulin heterodimers was determined by absorbance at 280 nm in GAB buffer (pH 6.5) using ε = 115,000 M^{-1} cm^{-1}. Different concentrations of cross-linked microtubules, chosen to span a range of at least 20% to 80% complexation, were incubated with fixed concentrations of **2-5, 2-6, 2-7** (25 nM) in GAB buffer (pH 6.5) at 22 °C with shaking for 1 h. These fixed probe concentrations were chosen to be below the predicted K_d values to assure equilibrium binding measurements. Measurements of fluorescence (I_{sample}) were recorded for each sample. Average fluorescence (I_{mt}) intensities of the background signal of microtubules alone were calculated by averaging three sample intensities for each concentration of tubulin in microtubules. Average fluorescence (I_f) intensities of the free ligand were calculated by averaging three sample intensities of the Pacific Blue probe in GAB. Background-subtracted fluorescence (I) signals were calculated as: $I = I_{sample} - I_{mt}$

The change in fluorescence intensity for each sample was calculated by subtracting the average (n=6) fluorescence of the free ligand (If). This change was plotted against the concentration of tubulin, and curve-fitting using a one-site specific binding model (GraphPad Prism 7) was used to calculate dissociation constants (Kd). Addition of Taxol (10 μM) as a competitor completely inhibited the increase in fluorescence of PB-Taxols upon binding, indicating a specific interaction of PB-Taxols at the Taxol-binding site (data not shown).

General synthesis procedure A: Synthesis of paclitaxel derivatives **2-9, 2-10, 2-11**. Fmoc-amino acid derivatives (4 eq), *N*-(3-dimethylaminopropyl)-N′-ethylcarbodiimide hydrochloride (EDC, 4 eq.), and 4-dimethylaminopyridine (DMAP, 0.5 eq) were stirred in anhydrous CH_2Cl_2 : DMF (v/v = 2/1, 22 °C, 15 min). The TBS-protected paclitaxel derivative **2-8** was added, and the reaction mixture was stirred for 16 h. The mixture was diluted with CH_2Cl_2 (75–175 mL) and washed with saturated aqueous NH_4Cl (50–100 mL x 1), water (25–50 mL x 1) and satd. aqueous NaCl (25–50 mL x 1). The organic layer was collected, dried over anhydrous Na_2SO_4 and purified by silica column chromatography (eluent: 97:3 CH_2Cl_2/MeOH).

General synthesis procedure B: Synthesis of PB-Taxols (**2-5, 2-6, 2-7**). Tetra-*N*-butylammonium fluoride in THF (TBAF, 1.0 M, 2 eq.) was added to a solution of **2-12, 2-13,** or **2-14** (1 eq.) in THF (0.5 mL) and stirred at 22 °C for 90 min. The reaction was concentrated under reduced pressure, the residue was dissolved in DMSO (1.5 mL), and the product purified by preparative RP-HPLC (gradient: H_2O:CH_3CN (9:1) to (0:100) with added TFA (0.1%) over 20 min; elution time = 16–17 min). Pure fractions were collected, combined, and solvent removed by lyophilization.

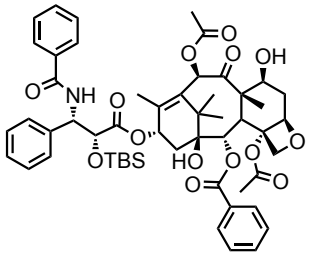

2-8

(2a*R*,4*S*,4a*S*,6*R*,9*S*,11*S*,12*S*,12b*S*)-9-(((2*R*,3*S*)-3-Benzamido-2-((*tert*-butyldimethylsilyl)oxy)-3-phenylpropanoyl)oxy)-12-(benzoyloxy)-4,11-dihydroxy-4a,8,13,13-tetramethyl-5-oxo-3,4,4a,5,6,9,10,11,12,12a-decahydro-1*H*-7,11-methanocyclodeca[3,4]benzo[1,2-*b*]oxete-6,12b(2a*H*)-diyl diacetate (2-8). This compound was synthesized by modifying a previously reported (*J. Am. Chem. Soc.* **2007,** *129*, 11653-11661) procedure. To a solution of paclitaxel (**2-1**, 500 mg, 0.59 mmol) in anhydrous DMF (2.1 mL) at 22 °C was added imidazole (208 mg, 3.06 mmol) and *tert*-butyldimethylchlorosilane (542 mg, 3.61 mmol). After stirring for 16 h, the mixture was diluted with CH_2Cl_2 (175 mL) and washed with saturated aqueous NH_4Cl (100 mL x 1), water (50 mL x 1) and satd. aqueous NaCl (50 mL x 1). The organic layer was collected, dried over anhydrous Na_2SO_4 and concentrated. The residue was triturated with hexane to afford **2-8** as a white solid (536 mg, 95%). ^{1}H NMR (500 MHz, $CDCl_3$) δ 8.18-8.10 (d, *J* = 8.0 Hz, 2H), 7.74 (d, *J* = 8.0 Hz, 2H), 7.64-7.45 (m, 4H), 7.45-7.36 (m, 4H), 7.33-7.30 (m, 3H), 7.07 (d, *J* = 8.9 Hz, 1H), 6.34-6.24 (m, 2H), 5.78-5.63 (m, 2H), 5.04-4.92 (m, 1H), 4.73-4.61 (m, 1H), 4.44 (dd, *J* = 11.0, 6.6 Hz, 1H), 4.33 (d, *J* = 8.5 Hz, 1H), 4.22 (d, *J* = 8.5 Hz, 1H), 3.82 (d, *J* = 7.0 Hz, 1H), 2.63-2.52 (m, 4H), 2.48 (broad s, 1H), 2.40 (dd, *J* = 15.3, 9.5 Hz, 1H), 2.23 (s, 3H), 2.17-2.06 (m, 1H), 1.97-1.84 (m, 4H), 1.77 (broad s, 1H), 1.69 (s, 3H), 1.24 (s, 3H), 1.13 (s, 3H), 0.80 (s, 9H), –0.08 (s, 3H), –0.29 (s, 3H); ^{13}C NMR (126 MHz, $CDCl_3$) δ 203.9, 171.5, 171.4, 170.3, 167.2, 167.0, 142.6, 138.4, 134.2, 133.8, 133.0, 132.0, 130.4, 129.2, 128.93, 128.89, 128.86, 128.1, 127.1, 126.6, 84.6, 81.3, 79.3, 76.6, 75.7, 75.3, 75.2, 72.3, 71.5, 58.6, 55.8, 45.6, 43.4, 35.9, 35.7, 26.9, 25.7, 23.2, 22.4, 21.00, 18.3, 15.1, 9.8, –5.1, –5.7; HRMS (ESI-) m/z 990.4047 (M-H$^+$, $C_{53}H_{65}NO_{14}SiNa$ requires 990.4072).

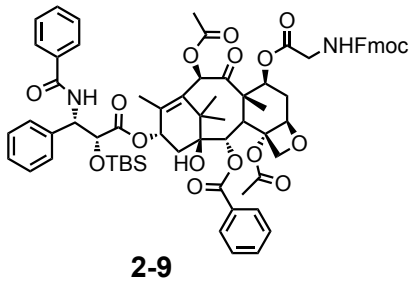

2-9

(2a*R*,4*S*,4a*S*,6*R*,9*S*,11*S*,12*S*,12b*S*)-4-(((((9*H*-Fluoren-9-yl)methoxy)carbonyl)glycyl)oxy)-9-(((2*R*,3*S*)-3-benzamido-2-((*tert*-butyldimethylsilyl)oxy)-3-phenylpropanoyl)oxy)-12-(benzoyloxy)-11-hydroxy-4a,8,13,13-tetramethyl-5-oxo-3,4,4a,5,6,9,10,11,12,12a-decahydro-1*H*-7,11-methanocyclodeca[3,4]benzo[1,2-*b*]oxete-6,12b(2a*H*)-diyl diacetate (2-9). Following general procedure A, Fmoc-Gly-OH (119 mg, 0.4 mmol) and **2-8** (97 mg, 0.1 mmol) yielded **2-9** (43 mg, 35%) as a white solid. ^{1}H NMR (500 MHz, $CDCl_3$) δ 8.16 (m, 2H), 7.84-7.74 (m, 4H), 7.71-7.61 (m, 3H), 7.60-7.30 (m, 16H), 7.11 (d, *J* = 11.0 Hz, 1H), 6.29 (t, *J* = 11.0 Hz, 1H), 6.23 (s, 1H), 5.84-5.68 (m, 3H), 5.54 (m, 1H), 5.07-4.97 (m, 1H), 4.70 (d, *J* = 2.5 Hz, 1H), 4.48-4.35 (m, 3H), 4.30 (t, *J* = 9.5 Hz, 1H), 4.23 (d, *J* = 10.5 Hz, 1H), 4.17-4.08 (m, 1H), 3.99 (d, *J* = 9.0 Hz, 1H), 3.91-3.81 (m, 1H), 2.71-2.52 (m, 4H), 2.51-2.38 (m, 1H), 2.32-3.11 (m, 4H), 2.00 (s, 3H), 1.96-1.89 (m, 1H), 1.85 (s, 3H), 1.25 (s, 3H), 1.19 (s, 3H), 0.83 (s, 9H), –0.01 (s, 3H), –0.27 (s, 3H); ^{13}C NMR (126 MHz, $CDCl_3$) δ 202.0, 171.6, 170.1, 170.0, 169.8, 167.2, 167.0, 156.9, 144.2, 144.0, 141.4, 141.38, 141.35, 138.3, 134.2, 133.9, 132.4, 132.0, 130.4, 129.1, 128.94, 128.91, 128.2, 127.79, 127.78, 127.2, 127.1, 126.5, 125.5, 125.4, 120.1, 84.0, 81.1, 78.7, 76.5, 75.8, 75.2, 74.5, 72.1, 71.5, 67.4, 56.2, 55.8, 47.3, 47.0, 43.5, 43.2, 35.7, 33.4, 26.5, 25.7, 23.1, 21.5, 21.1, 18.3, 14.8, 11.0, –5.1, –5.7; HRMS (ESI+) m/z 1269.4939 ($M+Na^+$, $C_{70}H_{78}N_2O_{17}SiNa$ requires 1269.4968).

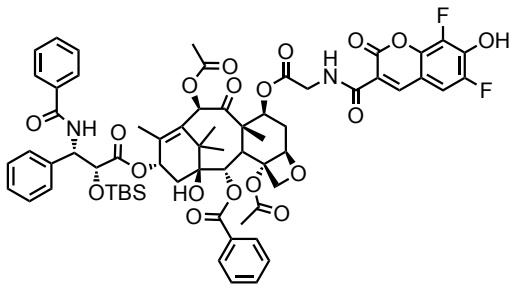

2-12

(2a*R*,4*S*,4a*S*,6*R*,9*S*,11*S*,12*S*,12b*S*)-9-(((2*R*,3*S*)-3-Benzamido-2-((*tert*-butyldimethylsilyl)oxy)-3-phenylpropanoyl)oxy)-12-(benzoyloxy)-4-(((6,8-difluoro-7-hydroxy-2-oxo-2*H*-chromene-3-carbonyl)glycyl)oxy)-11-hydroxy-4a,8,13,13-tetramethyl-5-oxo-3,4,4a,5,6,9,10,11,12,12a-decahydro-1*H*-7,11-methanocyclodeca[3,4]benzo[1,2-*b*]oxete-6,12b(2a*H*)-diyl diacetate (2-12). To a solution of piperidine (20%) in DMF (2 mL) was added **2-9** (14 mg, 0.011 mmol). The mixture was stirred at 22 °C for 10 min followed by complete removal of piperidine under reduced pressure. To this crude intermediate in DMF (0.5 mL) was added Pacific Blue-NHS ester (5 mg, 0.015 mmol), and DIEA (6 µL, 0.034 mmol). After stirring for 16 h, the reaction was concentrated under reduced pressure. The crude product was dissolved in DMSO (2 mL) and purified by preparative reverse phase HPLC (gradient: 90/10 H_2O/MeCN to 100% MeCN over 20 min with 0.1% TFA added; retention time = 19 min) to yield **2-12** (12 mg, 85%) as a yellow solid. ^{1}H NMR (500 MHz, $CDCl_3$) δ 9.07 (t, *J* = 6.0 Hz, 1H), 8.71 (d, *J* = 1.3 Hz, 1H), 8.13-8.06 (m, 2H), 7.78-7.71 (m, 2H), 7.61-7.28 (m, 10H), 7.14 (d, *J* = 9.0 Hz, 1H), 7.09 (dd, *J* = 9.3, 1.3 Hz, 1H), 6.28 (t, *J* = 9.2 Hz, 1H), 6.20 (s, 1H), 5.81-5.62 (m, 3H), 5.02-4.98 (m, 1H), 4.67 (d, *J* = 2.1 Hz, 1H), 4.40-4.26 (m, 2H), 4.24-4.14 (m, 2H), 3.96 (d, *J* = 7.0 Hz, 1H), 2.73-2.52 (m, 4H), 2.40 (dd, *J* = 15.3, 9.4 Hz, 1H), 2.32-2.15 (m, 4H), 2.00-1.85 (m, 4H), 1.79 (s, 3H), 1.58 (broad s, 1H), 1.23 (s, 3H),

1.14 (s, 3H), 0.78 (s, 9H), –0.04 (s, 3H), –0.31 (s, 3H); ^{13}C NMR (126 MHz, $CDCl_3$) δ 201.8, 171.6, 170.2, 170.1, 169.2, 167.8, 166.9, 161.9, 159.6, 148.9 (dd, *J* = 243.9, 3.5 Hz), 147.8, 141.4, 140.9 (d, *J* = 10.7 Hz), 139.6 (m), 138.8 (dd, *J* = 244.4, 5.0 Hz), 138.1, 138.0, 134.0, 133.9, 132.6, 132.1, 130.3, 129.1, 129.0, 128.89, 128.87, 128.2, 127.1, 126.5, 116.5, 110.3 (d, J = 9.1 Hz), 109.9 (dd, *J* = 20.0, 2.4 Hz), 84.1, 81.1, 78.7, 76.5, 75.6, 75.1, 74.5, 72.6, 71.5, 56.0, 55.9, 47.0, 43.5, 42.1, 35.6, 33.3, 26.6, 25.6, 23.1, 21.6, 21.0, 18.3, 14.8, 11.0, –5.1, –5.9, HRMS (ESI+) m/z 1271.4191 ($M+Na^+$, $C_{65}H_{70}N_2O_{19}SiNa$ requires 1271.4208).

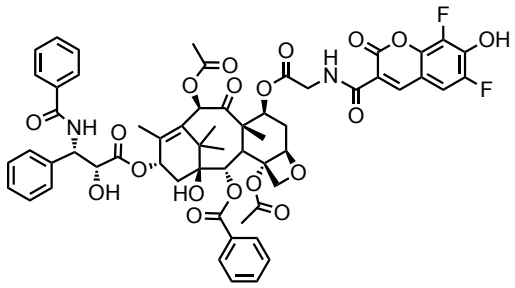

PB-Gly-Taxol
2-5

(2a*R*,4*S*,4a*S*,6*R*,9*S*,11*S*,12*S*,12b*S*)-9-(((2*R*,3*S*)-3-Benzamido-2-hydroxy-3-phenylpropanoyl)oxy)-12-(benzoyloxy)-4-(((6,8-difluoro-7-hydroxy-2-oxo-2*H*-chromene-3-carbonyl)glycyl)oxy)-11-hydroxy-4a,8,13,13-tetramethyl-5-oxo-3,4,4a,5,6,9,10,11,12,12a-decahydro-1*H*-7,11-methanocyclodeca[3,4]benzo[1,2-*b*]oxete-6,12b(2a*H*)-diyl diacetate (PB-Gly-Taxol, 2-5). Following general procedure B, **2-12** (10 mg, 0.008 mmol) yielded compound **1** (6 mg, 67%) as a yellow solid. ^{1}H NMR (500 MHz, $CDCl_3$) δ 9.09 (t, *J* = 6.0 Hz, 1H), 8.79 (d, *J* = 1.0 Hz, 1H), 8.16-8.07 (m, 2H), 7.82-7.75 (m, 2H), 7.68-7.60 (m, 1H), 7.56-7.34 (m, 10H), 7.23 (dd, *J* = 9.0, 2.0 Hz, 1H), 7.12 (d, *J* = 9.0 Hz, 1H), 6.23-6.14 (m, 2H), 5.82 (dd, *J* = 9.0, 2.5 Hz, 1H), 5.69-5.61 (m, 2H), 5.00-4.94 (m, 1H), 4.82 (d, *J* = 2.5 Hz, 1H), 4.40-4.28 (m, 2H), 4.24-4.13 (m, 2H),

3.95-3.88 (d, *J* = 7.0 Hz, 1H), 2.72-2.58 (m, 1H), 2.44-2.29 (m, 4H), 2.27 (s, 3H), 1.97-1.88 (m, 2H), 1.82 (s, 3H), 1.80 (s, 3H), 1.24 (s, 3H), 1.17 (s, 3H); HRMS (ESI-) m/z 1133.3340 ($M-H^+$, $C_{59}H_{55}F_2N_2O_{19}$ requires 1133.3367).

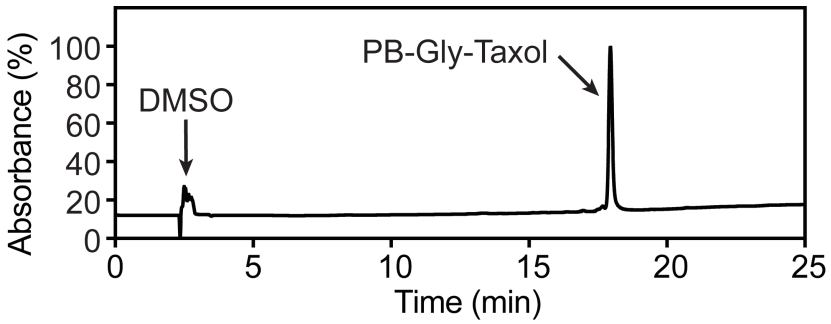

Figure 2.12 Analytical HPLC profile of PB-Gly-Taxol (**2-5**) after preparative HPLC. Retention time = 18.0 min monitored by UV absorbance at 254 nm. Purity >96% by HPLC.

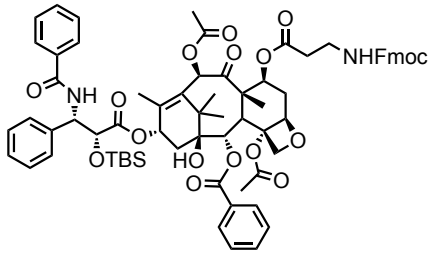

2-10

(2a*R*,4*S*,4a*S*,6*R*,9*S*,11*S*,12*S*,12b*S*)-4-((3-((((9*H*-Fluoren-9yl)methoxy)carbonyl)amino)propanoyl) oxy)-9-(((2*R*,3*S*)-3-benzamido-2-((*tert*-butyldimethylsilyl)oxy)-3-phenylpropanoyl)oxy)-12 (benzoyloxy)-11-hydroxy-4a,8,13,13-tetramethyl-5-oxo-3,4,4a,5,6,9,10,11,12,12a-decahydro-1*H*-7,11-methanocyclodeca[3,4]benzo[1,2-*b*]oxete-6,12b(2a*H*)-diyl diacetate (2-10). Following general procedure A, Fmoc-β-Ala-OH (643 mg, 2.06 mmol) and **2-8** (500 mg, 0.52 mmol) yielded **2-10** (440 mg, 68%) as a white solid. ^{1}H NMR (500 MHz, $CDCl_3$) δ 8.17-8.11 (m, 2H), 7.79-7.73 (m, 4H), 7.68-7.57 (m, 3H), 7.57-7.26 (m, 15H), 7.08 (d, *J* = 8.5 Hz, 1H), 6.31 (s, 1H), 6.27 (t, *J* = 9.5 Hz, 1H), 5.83 (t, *J* = 6.0 Hz, 1H), 5.77-5.59 (m, 3H), 4.98 (dd, *J* = 9.6, 2.0 Hz, 1H), 4.68 (d, *J*

= 2.2 Hz, 1H), 4.45-4.30 (m, 3H), 4.25-4.18 (m, 2H), 3.99 (d, *J* = 6.8 Hz, 1H), 3.58-3.42 (m, 2H), 2.64-2.50 (m, 6H), 2.44 (dd, *J* = 15.2, 9.4 Hz, 1H), 2.21-2.12 (m, 1H), 2.10 (s, 3H), 1.99 (s, 3H), 1.93-1.85 (m, 1H), 1.84 (s, 3H), 1.23 (s, 3H), 1.18 (s, 3H), 0.80 (s, 9H), –0.03 (s, 3H), –0.30 (s, 3H); ^{13}C NMR (126 MHz, $CDCl_3$) δ 202.4, 171.6, 171.4, 170.1, 169.8, 167.1, 156.6, 144.20, 144.19, 141.4, 141.3, 138.4, 134.2, 134.0, 132.7, 132.0, 130.4, 129.1, 129.0, 128.9, 128.1, 127.8, 127.2, 127.1, 126.5, 125.3, 120.0, 84.0, 81.0, 78.8, 76.5, 75.5, 75.2, 74.6, 71.7, 71.4, 66.7, 56.2, 55.8, 47.4, 46.8, 43.4, 36.2, 35.8, 34.4, 33.6, 26.5, 25.7, 23.2, 21.6, 20.9, 18.3, 14.8, 11.1, –5.0, –5.7; HRMS (ESI+) m/z 1283.5148 ($M+Na^+$, $C_{71}H_{80}N_2O_{17}SiNa$ requires 1283.5124).

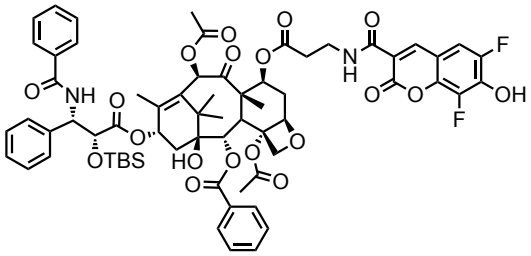

2-13

(2a*R*,4*S*,4a*S*,6*R*,9*S*,11*S*,12*S*,12b*S*)-9-(((2*R*,3*S*)-3-Benzamido-2-((*tert*-butyldimethylsilyl)oxy)-3-phenylpropanoyl)oxy)-12-(benzoyloxy)-4-((3-(6,8-difluoro-7-hydroxy-2-oxo-2*H*-chromene-3-carboxamido)propanoyl)oxy)-11-hydroxy-4a,8,13,13-tetramethyl-5-oxo-3,4,4a,5,6,9,10,11,12,12a -decahydro-1*H*-7,11-methanocyclodeca[3,4]benzo[1,2-*b*]oxete-6,12b(2a*H*)-diyl diacetate (2-13). 2-10 (100 mg, 0.079 mmol) was stirred for 10 min at 22 °C in piperidine / DMF (1:5, 2 mL). Piperidine was completely removed under reduced pressure, and Pacific Blue-NHS ester (32 mg, 0.094 mmol) and DIEA (69 µL, 0.397 mmol) in DMF (2 mL) were added. After stirring for 16 h, the reaction was concentrated under reduced pressure. Silica chromatography (eluent: 290:9:1 CH_2Cl_2/MeOH/AcOH) yielded **2-13** (80 mg, 80%) as a

yellow solid. ^{1}H NMR (500 MHz, $CDCl_3$) δ 8.94 (t, *J* = 6.0 Hz, 1H), 8.71 (d, *J* = 1.3 Hz, 1H), 8.16-8.08 (m, 2H), 7.79-7.72 (m, 2H), 7.61-7.54 (m, 1H), 7.54-7.28 (m, 10H), 7.17-7.09 (m, 2H), 6.28 (t, *J* = 9.5 Hz, 1H), 6.25 (s, 1H), 5.76-5.64 (m, 3H), 5.03-4.96 (m, 1H), 4.68 (d, *J* = 2.0 Hz, 1H), 4.35 (d, *J* = 8.5 Hz, 1H), 4.21 (d, *J* = 8.5 Hz, 1H), 3.98 (d, *J* = 6.5 Hz, 1H), 3.80-3.63 (m, 2H), 2.73-2.60 (m, 3H), 2.59 (s, 3H), 2.42 (dd, *J* = 15.3, 9.4 Hz, 1H), 2.20-2.15 (m, 1H), 2.14 (s, 3H), 1.98 (s, 3H), 1.96-1.88 (m, 1H), 1.83 (s, 3H), 1.76 (broad s, 1H), 1.30-1.23 (m, 1H), 1.22 (s, 3H), 1.16 (s, 3H), 0.80 (s, 9H), –0.02 (s, 3H), –0.31 (s, 3H); ^{13}C NMR (126 MHz, $CDCl_3$) δ 202.1, 171.6, 171.2, 170.1, 169.3, 167.5, 167.0, 161.5, 159.9, 149.1 (dd, *J* = 243.81, 3.78 Hz), 147.5, 141.1, 140.8 (d, *J* = 8.82 Hz), 139.8(m), 139.2(dd, *J* = 243.18, 8.82 Hz), 138.2, 134.1, 133.9, 132.7, 132.1, 130.3, 129.1, 128.94, 128.89, 128.1, 127.2, 126.5, 116.8, 110.3 (d, *J* = 9.35 Hz), 109.8 (dd, *J* = 20.16, 3.38 Hz), 84.2, 81.1, 78.8, 76.6, 75.4, 75.2, 74.6, 71.8, 71.4, 56.1, 55.9, 47.0, 43.5, 35.7, 35.4, 34.1, 33.4, 26.5, 25.7, 23.2, 21.5, 20.9, 18.3, 14.8, 11.1, –5.0, –5.7; HRMS (ESI+) m/z 1263.4574 ($M+H^+$, $C_{66}H_{73}F_2N_2O_{19}Si$ requires 1263.4545).

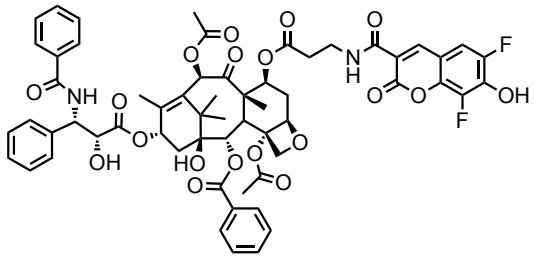

PB-βAla-Taxol
2-6

(2a*R*,4*S*,4a*S*,6*R*,9*S*,11*S*,12*S*,12b*S*)-9-(((2*R*,3*S*)-3-Benzamido-2-hydroxy-3-phenylpropanoyl)oxy)-12-(benzoyloxy)-4-((3-(6,8-difluoro-7-hydroxy-2-oxo-2*H*-chromene-3-carboxamido)propanoyl) oxy)-11-hydroxy-4a,8,13,13-tetramethyl-5-oxo-3,4,4a,5,6,9,10,11,12,12a-decahydro-1*H*-7,11-

methanocyclodeca[3,4]benzo[1,2-*b*]oxete-6,12b(2a*H*)-diyl diacetate (PB-βAla-Taxol, 2-6). To a solution of **2-13** (50 mg, 0.040 mmol) in anhydrous THF (1 mL) at 22 °C was added a solution of TBAF in THF (1.0 M, 84 µL, 0.084 mmol). After stirring for 90 min, the mixture was concentrated and purified by silica column chromatography (1:9:290 AcOH/MeOH/DCM) to afford **2-6** as a yellow solid (44 mg, 97%). ^{1}H NMR (500 MHz, $CDCl_3$) δ 9.03 (t, *J* = 6.0 Hz, 1H), 8.76 (s, 1H), 8.10 (d, *J* = 7.0 Hz, 2H), 7.77 (d, *J* = 7.0 Hz, 2H), 7.65-7.58 (m, 1H), 7.55-7.30 (m, 10H), 7.21 (dd, *J* = 9.1, 1.7 Hz, 2H), 6.21-6.13 (m, 2H), 5.80 (dd, *J* = 8.5, 2.0 Hz, 1H), 5.66 (d, *J* = 7.0 Hz, 1H), 5.61 (dd, *J* = 10.5, 7.0 Hz, 1H), 4.95 (dd, *J* = 9.3, 1.8 Hz, 1H), 4.81 (d, *J* = 2.5 Hz, 1H), 4.32 (d, *J* = 8.5 Hz, 1H), 4.19 (d, *J* = 8.5 Hz, 1H), 3.91 (d, *J* = 7.0 Hz, 1H), 3.81-3.61 (m, 2H), 2.75-2.66 (m, 1H), 2.66-2.56 (m, 2H) 2.37 (s, 3H), 2.35-2.27 (m, 2H) 2.12 (s, 3H), 1.94-1.80 (m, 2H), 1.86-1.76 (m, 6H), 1.20 (s, 3H), 1.15 (s, 3H); HRMS (ESI-) m/z 1147.3541 ($M-H^+$, $C_{60}H_{57}F_2N_2O_{19}$ requires 1147.3524).

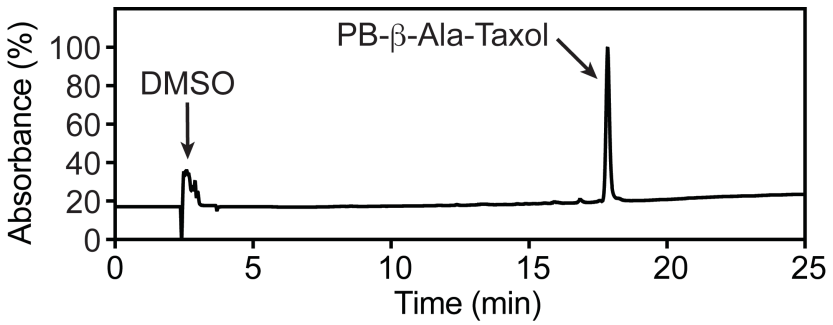

Figure 2.13 Analytical HPLC profile of PB-β-Ala-Taxol (**2-6**) after preparative HPLC. Retention time = 17.9 min monitored by UV absorbance at 254 nm. Purity >98% by HPLC.

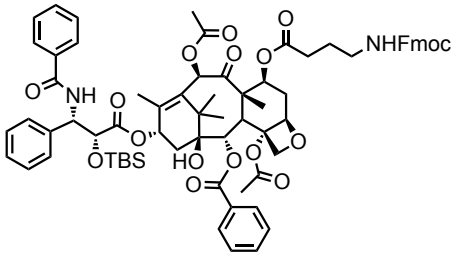

2-11

(2a*R*,4*S*,4a*S*,6*R*,9*S*,11*S*,12*S*,12b*S*)-4-((4-((((9*H*-Fluoren-9-yl)methoxy)carbonyl)-amino)butanoyl)oxy)-9-(((2*R*,3*S*)-3-benzamido-2-((*tert*-butyldimethylsilyl)oxy)-3-phenylpropanoyl)oxy)-12-(benzoyloxy)-11-hydroxy-4a,8,13,13-tetramethyl-5-oxo-3,4,4a,5,6,9,10,11,12,12a-decahydro-1*H*-7,11-methanocyclodeca[3,4]benzo[1,2-*b*]oxete-6,12b(2a*H*)-diyl diacetate (2-11). Following general procedure A, 4-(Fmoc-amino)butyric acid (130 mg, 0.4 mmol) and **2-8** (97 mg, 0.1 mmol) yielded **2-11** (100 mg, 79%) as a white solid. ^{1}H NMR (500 MHz, $CDCl_3$) δ 8.17-8.10 (m, 2H), 7.80-7.72 (m, 4H), 7.65-7.57 (m, 3H), 7.59-7.47 (m, 3H), 7.46-7.29 (m, 11H), 7.08 (d, *J* = 9.0 Hz, 1H), 6.32-6.20 (m, 2H), 5.82-5.66 (m, 3H), 5.59 (dd, *J* = 10.6, 7.0 Hz, 1H), 4.98 (dd, *J* = 9.7, 2.0 Hz, 1H), 4.67 (d, *J* = 2.0 Hz, 2H), 4.46-4.40 (m, 2H), 4.38-4.32 (m, 1H), 4.26-4.16 (m, 2H), 3.96 (d, *J* = 6.8 Hz, 1H), 3.42-3.12 (m, 2H), 2.67-2.53 (m, 4H), 2.49-2.39 (m, 2H), 2.32-2.23 (m, 1H), 2.22-2.12 (m, 1H), 2.06 (s, 3H), 1.97 (s, 3H), 1.87-1.80 (m, 4H), 1.75-1.69 (m, 3H), 1.22 (s, 3H), 1.17 (s, 3H), 0.80 (s, 9H), –0.03 (s, 3H), –0.30 (s, 3H); ^{13}C NMR (126 MHz, $CDCl_3$) δ 201.9, 172.4, 171.6, 170.3, 170.0, 167.2, 167.0, 156.7, 144.2, 141.5, 141.4, 141.2, 138.3, 134.2, 133.9, 132.6, 132.0, 130.4, 129.1, 128.94, 128.90, 128.1, 127.8, 127.7, 127.19, 127.16, 127.13, 126.5, 125.2, 125.1, 120.1, 84.1, 81.1, 78.7, 76.5, 75.6, 75.2, 74.6, 71.6, 71.4, 66.3, 56.2, 55.8, 47.5, 47.0, 43.5, 39.4, 35.7, 33.5, 30.0, 26.5, 25.7, 23.8, 23.2, 21.5, 20.9, 18.3, 14.8, 11.1, –5.0, –5.7.; HRMS (ESI+) m/z 1297.5265 ($M+Na^+$, $C_{72}H_{82}N_2O_{17}SiNa$ requires 1297.5281).

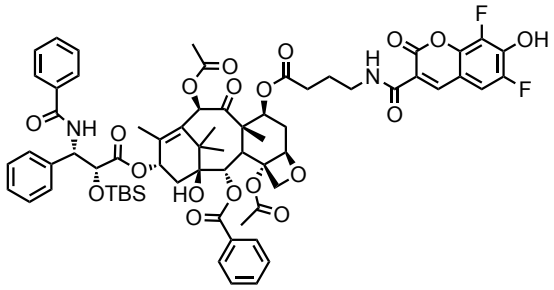

2-14

(2a*R*,4*S*,4a*S*,6*R*,9*S*,11*S*,12*S*,12b*S*)-9-(((2*R*,3*S*)-3-Benzamido-2-((*tert*-butyldimethylsilyl)oxy)-3-phenylpropanoyl)oxy)-12-(benzoyloxy)-4-((4-(6,8-difluoro-7-hydroxy-2-oxo-2*H*-chromene-3-carboxamido)butanoyl)oxy)-11-hydroxy-4a,8,13,13-tetramethyl-5-oxo-3,4,4a,5,6,9,10,11,12,12a-decahydro-1*H*-7,11-methanocyclodeca[3,4]benzo[1,2-*b*]oxete-6,12b(2a*H*)-diyl diacetate (2-14). To a solution of piperidine (20%) in DMF (1 mL) was added **2-11** (30 mg, 0.024 mmol). The mixture was stirred at 22 °C for 10 min followed by complete removal of piperidine under reduced pressure. To this crude intermediate in DMF (1 mL) was added Pacific Blue-NHS ester, prepared as previously described (10 mg, 0.028 mmol), and DIEA (12 µL, 0.069 mmol). After stirring for 16 h, the reaction was concentrated under reduced pressure. The crude product was dissolved in DMSO (2 mL) and purified by preparative reverse phase HPLC (gradient: 90/10 H_2O/MeCN to 100% MeCN over 20 min with 0.1% TFA added; retention time = 19 min) to yield **2-14** (26 mg, 87%) as a yellow solid. ^{1}H NMR (500 MHz, $CDCl_3$) δ 8.79-8.69 (m, 2H), 8.15-8.07 (m, 2H), 7.78-7.69 (m, 2H), 7.62-7.56 (m, 1H), 7.54-7.27 (m, 11H), 7.16 (dd, *J* = 9.3, 2.0 Hz, 1H), 7.10 (d, *J* = 8.9 Hz, 1H), 6.33-6.24 (m, 2H), 5.79-5.58 (m, 3H), 4.97 (dd, *J* = 9.5, 2.0 Hz, 1H), 4.68 (d, *J* = 2.4 Hz, 1H), 4.34 (d, *J* = 8.5 Hz, 1H), 4.20 (d, *J* = 8.5 Hz, 1H), 3.97 (d, *J* = 6.8 Hz, 1H), 3.60-3.43 (m, 2H), 2.69-2.52 (m, 4H), 2.53-2.29 (m, 3H), 2.23-2.12 (m, 4H), 2.02-1.85 (m, 6H), 1.85-1.75 (m, 4H),

1.22 (s, 3H), 1.16 (s, 3H), 0.80 (s, 9H), –0.03 (s, 3H), –0.30 (s, 3H); ^{13}C NMR (126 MHz, CDCl3) δ 202.2, 172.3, 171.6, 170.1, 169.3, 167.5, 167.0, 161.5, 160.1, 148.9 (d, *J* = 243.2 Hz, 3.78 Hz), 147.6, 141.0, 140.8 (d, *J* = 7.56 Hz), 139.4 (m), 139.2 (dd, *J* = 226.8, 5.04 Hz), 138.2, 134.1, 133.9, 132.8, 132.1, 130.3, 129.1, 129.0, 128.91, 128.89, 128.2, 127.2, 126.54, 126.49, 117.0, 110.6 (d, *J* = 10.08 Hz), 109.9 (m), 84.2, 81.1, 78.8, 76.6, 75.4, 75.3, 74.6, 71.5, 71.4, 56.2, 55.9, 47.0, 43.5, 39.3, 35.7, 33.5, 31.4, 26.5, 25.7, 24.2, 23.2, 21.5, 20.9, 18.3, 14.8, 11.1, –5.0, –5.7; HRMS (ESI+) m/z 1299.4524 ($M+Na^+$, $C_{67}H_{74}F_2N_2O_{19}SiNa$ requires 1299.4521).

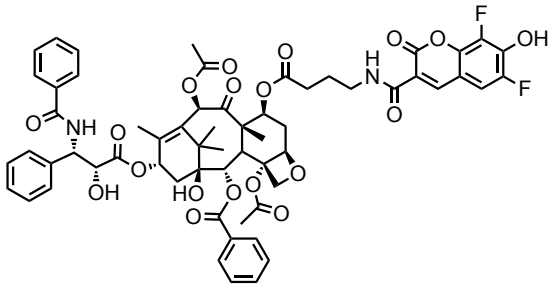

PB-GABA-Taxol
2-7

(2a*R*,4*S*,4a*S*,6*R*,9*S*,11*S*,12*S*,12b*S*)-9-(((2*R*,3*S*)-3-Benzamido-2-hydroxy-3-phenylpropanoyl)oxy)-12-(benzoyloxy)-4-((4-(6,8-difluoro-7-hydroxy-2-oxo-2*H*-chromene-3-carboxamido)butanoyl)oxy)-11-hydroxy-4a,8,13,13-tetramethyl-5-oxo-3,4,4a,5,6,9,10,11,12,12a-decahydro-1*H*-7,11-methanocyclodeca[3,4]benzo[1,2-*b*]oxete-6,12b(2a*H*)-diyl diacetate (PB-GABA-Taxol, 2-7). Following general procedure B, **2-14** (16 mg, 0.013 mmol) yielded compound **2-7** (13 mg, 86%) as a yellow solid. ^{1}H NMR (500 MHz, $CDCl_3$) δ 8.81 (t, *J* = 6.0 Hz, 1H), 8.73 (d, *J* = 1.5 Hz, 1H), 8.11–8.05 (m, 2H), 7.80–7.73 (m, 2H), 7.63–7.56 (m, 1H), 7.53–7.28 (m, 11H), 7.16 (dd, *J* = 9.4, 2.0 Hz, 1H), 6.19 (s, 1H), 6.18-6.13 (m, 1H), 5.79 (dd, *J* = 9.0, 2.9 Hz, 1H), 5.65 (d, *J* = 6.8 Hz, 1H), 5.54 (dd, *J* = 10.4, 7.2 Hz, 1H), 4.92 (dd, *J* = 9.6, 2.0 Hz, 1H), 4.81 (d, *J* = 2.9 Hz,

1H), 4.30 (d, *J* = 8.5 Hz, 1H), 4.17 (d, *J* = 8.5 Hz, 1H), 3.89 (d, *J* = 6.7 Hz, 1H), 3.53–3.39 (m, 2H), 2.64-2.50 (m, 1H), 2.46 (dt, *J* = 17.3, 7.2 Hz, 1H), 2.36 (s, 3H), 2.31–2.26 (m, 3H), 2.17 (s, 3H), 2.00–1.84 (m, 2H), 1.81 (s, 3H), 1.79 (s, 3H), 1.36–1.23 (m, 2H), 1.19 (s, 3H), 1.15 (s, 3H); HRMS (ESI-) m/z 1161.3683 ($M\text{-}H^+$, $C_{61}H_{59}F_2N_2O_{19}$ requires 1161.3680).

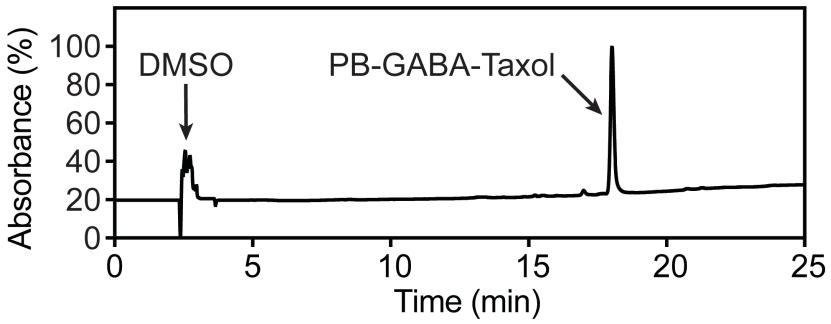

Figure 2.14 Analytical HPLC profile of PB-GABA-Taxol (**2-7**) after preparative HPLC. Retention time = 18.0 min monitored by UV absorbance at 254 nm. Purity >97% by HPLC.

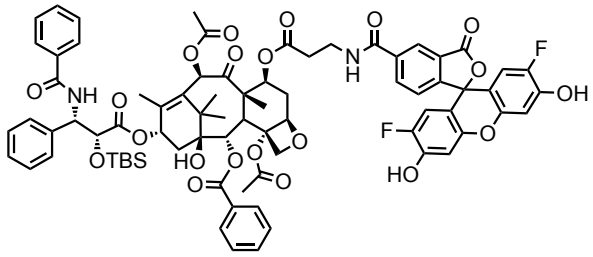

2-15

5-((3-(((2a*R*,4*S*,4a*S*,6*R*,9*S*,11*S*,12*S*,12b*S*)-6,12b-Diacetoxy-9-(((2*R*,3*S*)-3-benzamido-2-((*tert*-butyldimethylsilyl)oxy)-3-phenylpropanoyl)oxy)-12-(benzoyloxy)-11-hydroxy-4a,8,13,13-tetramethyl-5-oxo-2a,3,4,4a,5,6,9,10,11,12,12a,12b-dodecahydro-1*H*-7,11-methanocyclodeca[3,4]benzo[1,2-*b*]oxet-4-yl)oxy)-3-oxopropyl)carbamoyl)-2-(2,7-difluoro-6-hydroxy-3-oxo-3*H*-xanthen-9-yl)benzoic acid (2-15). To a solution of piperidine (20%) in DMF (2 mL) was added **2-8** (10 mg, 0.010 mmol). The mixture was stirred at 22 °C for 10 min followed by complete removal of piperidine under reduced

pressure. To this crude intermediate in DMF (2 mL) was added Oregon Green 488 Carboxylic Acid, Succinimidyl Ester, 5-isomer (Thermofisher Scientific, 5 mg, 0.011 mmol) and DIEA (5 µL). After stirring for 16 h, the reaction was concentrated under reduced pressure. The crude product was dissolved in DMSO (2 mL) and purified by preparative reverse phase HPLC (gradient: 90/10 H_2O/MeCN to 100% MeCN over 20 min with 0.1% TFA added; retention time = 18 min (488 nm)) to afford **2-15** as an orange solid (6 mg, 43%). HRMS (ESI+) m/z 1431.4731 ($M+Na^+$, $C_{77}H_{78}F_2N_2O_{21}SiNa$ requires 1455.4732).

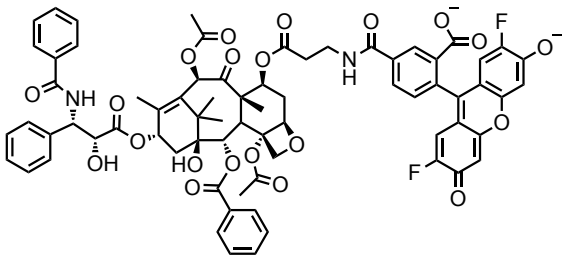

Flutax-2
(β-Ala variant, **2-3**)

5-((3-(((2a*R*,4*S*,4a*S*,6*R*,9*S*,11*S*,12*S*,12b*S*)-6,12b-Diacetoxy-9-(((2*R*,3*S*)-3-benzamido-2-hydroxy-3-phenylpropanoyl)oxy)-12-(benzoyloxy)-11-hydroxy-4a,8,13,13-tetramethyl-5-oxo-2a,3,4,4a,5,6,9,10,11,12,12a,12b-dodecahydro-1*H*-7,11-methanocyclodeca[3,4]benzo[1,2-*b*]oxet-4-yl)oxy)-3-oxopropyl)carbamoyl)-2-(2,7-difluoro-6-hydroxy-3-oxo-3*H*-xanthen-9-yl)benzoic acid (Flutax-2 (β-Ala), 2-3). This compound is commercially available from Thermo Fisher Scientific (cat# P22310), but was synthesized for these studies as follows: using general procedure B, **11** (4 mg, 0.0028 mmol) yielded Flutax-2 (β-Ala) (3 mg, 82%) as an orange solid. HRMS (ESI+) m/z 1319.4038 ($M+H^+$, $C_{71}H_{65}F_2N_2O_{21}$ requires 1319.4048).

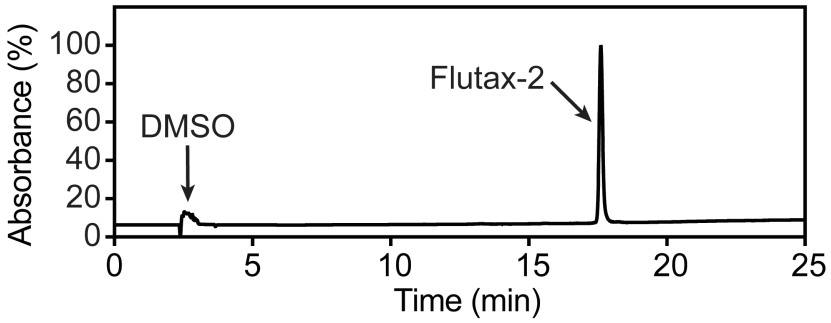

Figure 2.15 Analytical HPLC profile of synthetic Flutax-2 (β-Ala) after preparative HPLC. Retention time = 17.6 min monitored by UV absorbance at 254 nm. Purity >99% by HPLC.

2.11 References

1. Wani, M. C.; Taylor, H. L.; Wall, M. E.; Coggon, P.; McPhail, A. T. Plant antitumor agents. VI. Isolation and structure of taxol, a novel antileukemic and antitumor agent from Taxus brevifolia. *J. Am. Chem. Soc.* **1971,** 93, 2325-2327.

2. Rohena, C. C.; Mooberry, S. L. Recent progress with microtubule stabilizers: new compounds, binding modes and cellular activities. *Nat. Prod. Rep.* **2014,** 31, 335-355.

3. Nogales, E.; Wolf, S. G.; Downing, K. H. Structure of the αβ tubulin dimer by electron crystallography. *Nature* **1998,** 391, 199-203.

4. Mitchison, T.; Kirschner, M. Dynamic instability of microtubule growth. *Nature* **1984,** 312, 237-242.

5. Alushin, G. M.; Lander, G. C.; Kellogg, E. H.; Zhang, R.; Baker, D.; Nogales, E. High-resolution microtubule structures reveal the structural transitions in alphabeta-tubulin upon GTP hydrolysis. *Cell* **2014,** 157, 1117-1129.

6. Jordan, M. A.; Wilson, L. Microtubules as a target for anticancer drugs. *Nat. Rev. Cancer* **2004,** 4, 253-265.

7. Schiff, P. B.; Horwitz, S. B. Taxol stablilizes microtubules in mouse fibroblast cells. *Proc. Natl. Acad. Sci. U.S.A.* **1980,** 77, 1561-1565.

8. Horwitz, S. B.; Lothstein, L.; Manfredi, J. J.; Mellado, W.; Parness, J.; Roy, S. N.; Schiff, P. B.; Sorbara, L.; Zeheb, R. Taxol: mechanisms of action and resistance. *Ann. N. Y. Acad. Sci.* **1986,** 466, 733-744.

9. Mitchison, T. J. The proliferation rate paradox in antimitotic chemotherapy. *Mol. Biol. Cell* **2012,** 23, 1-6.

10. Komlodi-Pasztor, E.; Sackett, D.; Wilkerson, J.; Fojo, T. Mitosis is not a key target of microtubule agents in patient tumors. *Nat. Rev. Clin. Oncol.* **2011,** 8, 244-250.

11. Barasoain, I.; Díaz, J. F.; Andreu, J. M. Fluorescent Taxoid Probes for Microtubule Research. *Methods Cell Biol.* **2010,** 95, 353-372.

12. Barasoain, I.; Garcia-Carril, A. M.; Matesanz, R.; Maccari, G.; Trigili, C.; Mori, M.; Shi, J. Z.; Fang, W. S.; Andreu, J. M.; Botta, M.; Diaz, J. F. Probing the pore drug binding site of microtubules with fluorescent taxanes: evidence of two binding poses. *Chem. Biol.* **2010,** 17, 243-253.

13. Bgloglu, E.; Kingston, D. G. I.; Patel, P.; Chatterjee, S. K.; Bane, S. L. Synthesis and microtubule binding of fluorescent paclitaxel derivatives. *Bioorg. Med. Chem. Lett.* **2001,** 11, 2249-2252.

14. Diaz, J. F.; Barasoain, I.; Souto, A. A.; Amat-Guerri, F.; Andreu, J. M. Macromolecular accessibility of fluorescent taxoids bound at a paclitaxel binding site in the microtubule surface. *J. Biol. Chem.* **2005,** 280, 3928-3937.

15. Diaz, J. F.; Strobe, R.; Engelborghs, Y.; Souto, A. A.; Andreu, J. M. Molecular recognition of taxol by microtubules. Kinetics and thermodynamics of binding of fluorescent taxol derivatives to an exposed site. *J. Biol. Chem.* **2000,** 275, 26265-26276.

16. Duchi, S.; Dambruoso, P.; Martella, E.; Sotgiu, G.; Guerrini, A.; Lucarelli, E.; Pessina, A.; Cocce, V.; Bonomi, A.; Varchi, G. Thiophene-based compounds as fluorescent tags to study mesenchymal stem cell uptake and release of taxanes. *Bioconjug. Chem.* **2014,** 25, 649-655.

17. Guy, R. K.; Scott, Z. A.; Sloboda, R. D.; Nicolaou, K. C. Fluorescent taxoids. *Chem. Biol.* **1996,** 3, 1021-1031.

18. Han, Y.; Chaudhary, A. G.; Chordia, M. D.; Sackett, D. L.; Perez-Ramirez, B.; Kingston, D. G. I.; Bane, S. Interaction of a fluorescent derivative of paclitaxel (Taxol) with microtubules and tubulin-colchicine. *Biochemistry* **1996,** 35, 14173-14183.

19. Li, X.; Barasoain, I.; Matesanz, R.; Diaz, J. F.; Fang, W. S. Synthesis and biological activities of high affinity taxane-based fluorescent probes. *Bioorg. Med. Chem. Lett.* **2009,** 19, 751-754.

20. Lukinavicius, G.; Reymond, L.; D'Este, E.; Masharina, A.; Gottfert, F.; Ta, H.; Guther, A.; Fournier, M.; Rizzo, S.; Waldmann, H.; Blaukopf, C.; Sommer, C.; Gerlich, D. W.; Arndt, H. D.; Hell, S. W.; Johnsson, K. Fluorogenic probes for live-cell imaging of the cytoskeleton. *Nat. Methods* **2014,** 11, 731-733.

21. Sengupta, S.; Boge, T. C.; I., G. G.; Himes, R. H. Interaction of a fluorescent paclitaxel analogue with tubulin. *Biochemistry* **1995,** 34, 11889-11894.

22. Souto, A. A.; Acuna, A. U.; Andreu, J. M.; Barasoain, I.; Abal, M.; Amat-Guerri, F. New fluorescent water-soluble taxol derivatives. *Angew. Chem. Int. Ed. Engl.* **1995,** 34, 2710-2712.

23. Melan, M. A. Use of fluorochrome tagged Taxol to produce fluorescent microtubules in solution. *BioTechniques* **1998,** 25, 188-192.

24. Martin, C.; Walker, J.; Rothnie, A.; Callaghan, R. The expression of P-glycoprotein does influence the distribution of novel fluorescent compounds in solid tumour models. *Br. J. Cancer.* **2003,** 89, 1581-1589.

25. Gao, B.; Russell, A.; Beesley, J.; Chen, X. Q.; Healey, S.; Henderson, M.; Wong, M.; Emmanuel, C.; Galletta, L.; Johnatty, S. E.; Bowtell, D.; Australian Ovarian Cancer Study, G.; Haber, M.; Norris, M.; Harnett, P.; Chenevix-Trench, G.; Balleine, R. L.; deFazio, A. Paclitaxel sensitivity in relation to ABCB1 expression, efflux and single nucleotide polymorphisms in ovarian cancer. *Sci. Rep.* **2014,** 4, 4669.

26. Patwardhan, G.; Gupta, V.; Huang, J.; Gu, X.; Liu, Y. Y. Direct assessment of P-glycoprotein efflux to determine tumor response to chemotherapy. *Biochem. Pharmacol.* **2010,** 80, 72-79.

27. Di Maio, I. L.; Barbier, P.; Allegro, D.; Brault, C.; Peyrot, V. Quantitative analysis of tau-microtubule interaction using FRET. *Int. J. Mol. Sci.* **2014,** 15, 14697-14714.

28. Lipinski, C. A.; Lombardo, F.; Dominy, B. W.; Feeney, P. J. Experimental and computational approaches to estimate solubility and permeability in drug discovery and development settings. *Adv. Drug. Deliv. Rev.* **1997,** 23, 3-25.

29. Bhal, S. K.; Kassam, K.; Peirson, I. G.; Pearl, G. M. The Rule of Five revisited: applying log D in place of log P in drug-likeness filters. *Mol Pharm* **2007,** 4, 556-560.

30. Sun, W.; Gee, K. R.; Klaubert, D. H.; Haugland, R. P. Synthesis of fluorinated fluoresceins. *J. Org. Chem.* **1997,** 62, 6469-6475.

31. Sun, W.; Gee, K. R.; Haugland, R. P. Synthesis of novel fluorinated coumarins: excellent UV-light exicitable fluorescent dyes. *Bioorg. Med. Chem. Lett.* **1998,** 8, 3107-3110.

32. Lee, M. M.; Peterson, B. R. Quantification of Small Molecule-Protein Interactions using FRET between Tryptophan and the Pacific Blue Fluorophore. *ACS Omega* **2016,** 1, 1266-1276.

33. Xiao, X.; Wu, J.; Trigili, C.; Chen, H.; Chu, J. W.; Zhao, Y.; Lu, P.; Sheng, L.; Li, Y.; Sharom, F. J.; Barasoain, I.; Diaz, J. F.; Fang, W. S. Effects of C7 substitutions in a high affinity microtubule-binding taxane on antitumor activity and drug transport. *Bioorg. Med. Chem. Lett.* **2011,** 21, 4852-4856.

34. Gibson, J. D.; Khanal, B. P.; Zubarev, E. R. Paclitaxel-functionalized gold naoparticles. *J. Am. Chem. Soc* **2007,** 129, 11653-11661.

35. Trott, O.; Olson, A. J. AutoDock Vina: improving the speed and accuracy of docking with a new scoring function, efficient optimization, and multithreading. *J. Comput. Chem.* **2010,** 31, 455-461.

36. Buey, R. M.; Calvo, E.; Barasoain, I.; Pineda, O.; Edler, M. C.; Matesanz, R.; Cerezo, G.; Vanderwal, C. D.; Day, B. W.; Sorensen, E. J.; Lopez, J. A.; Andreu, J. M.; Hamel, E.; Diaz, J. F. Cyclostreptin binds covalently to microtubule pores and lumenal taxoid binding sites. *Nat. Chem. Biol.* **2007,** 3, 117-125.

37. Jang, S. H.; Wientjes, M. G.; Au, J. L.-S. Kinetics of P-glycoprotein-mediated efflux of paclitaxel. *J. Pharmacol. Exp. Ther.* **2001,** 298, 1236-1242.

38. Aller, S. G.; Yu, J.; Ward, A.; Weng, Y.; Chittaboina, S.; Zhuo, R.; Harrell, P. M.; Trinh, Y. T.; Zhang, Q.; Urbatsch, I. L.; Chang, G. Structure of P-glycoprotein reveals a molecular basis for poly-specific drug binding. *Science* **2009,** 323, 1718-1722.

39. Tsuruo, T.; Iida, H.; Tsukagoshi, S.; Sakurai, Y. Overcoming of vincristine resistance in P388 leukemia in vivo and in vitro through enhanced cytotoxicity of vincristine and vinblastine by verapamil. *Cancer Res.* **1981,** 41, 1967-1972.

40. Lebedeva, I. V.; Pande, P.; Patton, W. F. Sensitive and specific fluorescent probes for functional analysis of the three major types of mammalian ABC transporters. *PLoS ONE* **2011,** 6, e22429.

41. Eckford, P. D. W.; Sharom, F. J. ABC efflux pump-based resistance to chemiotherapy drugs. *Chem. Rev.* **2009,** 109, 2989-3011.

42. van Brussel, J. P.; Van Steenbrugge, G. J.; Romijn, J. C.; Schröder, F. H.; Mickisch, G. H. J. Chemosensitivity of prostate cancer cell lines and expression of multidrug resistance-related proteins. *Eur. J. Cancer* **1999,** 35, 664-671.

43. Pétriz, J.; Gottesman, M. M.; Aran, J. M. An MDR-EGFP gene fusion allows for direct cellular localization, function and stability assessment of p-glycoprotein. *Curr. Drug. Deliv.* **2004,** 1, 43-56.

44. Forster, S.; Thumser, A. E.; Hood, S. R.; Plant, N. Characterization of rhodamine-123 as a tracer dye for use in in vitro drug transport assays. *PLoS ONE* **2012,** 7, e33253.

Chapter 3 - Photochemical depolarization of mitochondria of living cells mediated by a fluorinated pyronin fluorophore

3.1 Introduction

As described in Chapter 1, mitochondria play crucial roles in metabolism, production of ATP, and specific signal transduction pathways.[1] These functions rely on the integrity of the negative membrane potential across the mitochondrial inner membrane ($\Delta\psi m$ = -120 to -180 mV, shown in Figure 3.1).[2] If this membrane is depolarized, the production of ATP ceases, leading to cell death. Consequently, many diseases are associated with abnormal mitochondria, including cancer, obesity, cardiomyopathies and neurodegeneration.[3-5] Hyperpolarized mitochondria are often observed in cancer, providing a potential target for therapeutics (shown in Figure 3.1).

Due to the negatively charged environment within mitochondria, lipophilic cations are prone to permeate across the mitochondrial membrane and accumulate in the mitochondrial matrix. Because of this driving force, many lipophilic cationic fluorescent probes including rhodamines, pyronins, and others, have been used to study these organelles.[6, 7] Whereas rhodamine derivatives have been widely investigated in vitro,[6, 8, 9] in vivo,[10, 11] and as fluorescent chemosensors,[12, 13] studies of analogues of pyronin B are more limited. However, pyronins have been used for cell cycle analysis,[14] bioimaging,[15] as sensors of pH,[16] nerve agents,[17] cellular peroxynitrite,[18] heavy metals,[19] ATP dynamics,[20] proteases,[21] and protein-protein interactions,[22]

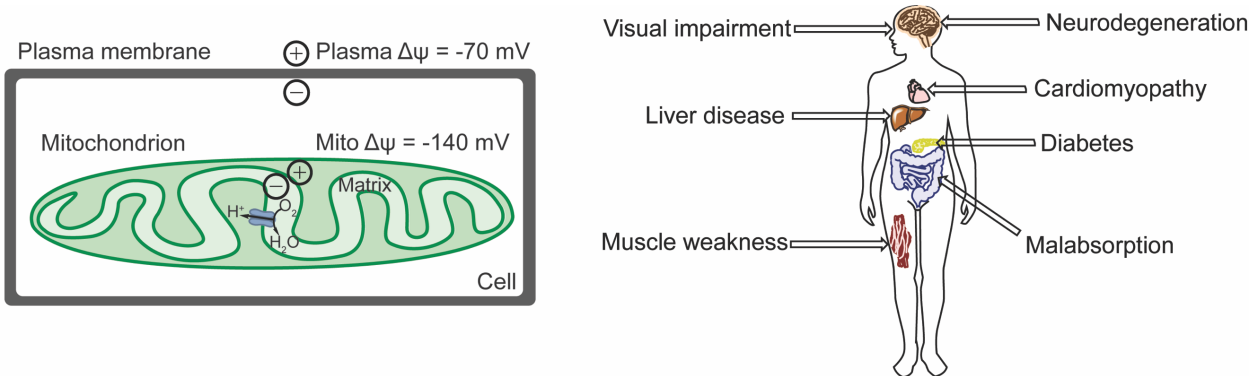

Figure 3.1. The mitochondrial membrane potential is more negative than the potential across the plasma membrane of mammalian cells. Abnormal mitochondria have been associated with diseases in multiple different tissues.

Small molecules that uncouple the electron chain of mitochondria, or that otherwise depolarize mitochondrial membranes, are important molecular probes with potential therapeutic applications.[23] Compounds that use photochemistry to depolarize mitochondrial membranes are of substantial interest because they provide novel tools to study fundamental mitochondria biology.[24, 25] However, existing photoactivatable probes rely on either UV-mediated cleavage of a nitrobenzyl group to release the uncoupler DNP from a mitochondria-targeting triphenylphosphonium salt[25] or the production of reactive oxygen species by near-IR laser radiation of mitochondria-targeted silica-carbon nanoparticles.[26]

In an effect to create more drug-like probes to study mitochondria, we synthesized a series of pyronin B derivatives (**69**-**72** in Figure 3.2). Studies of the biological properties of these compounds were used to identify 2,7-difluoropyronin B (**69**) as a small molecule capable of depolarizing mitochondrial membranes upon irradiation with visible blue light.

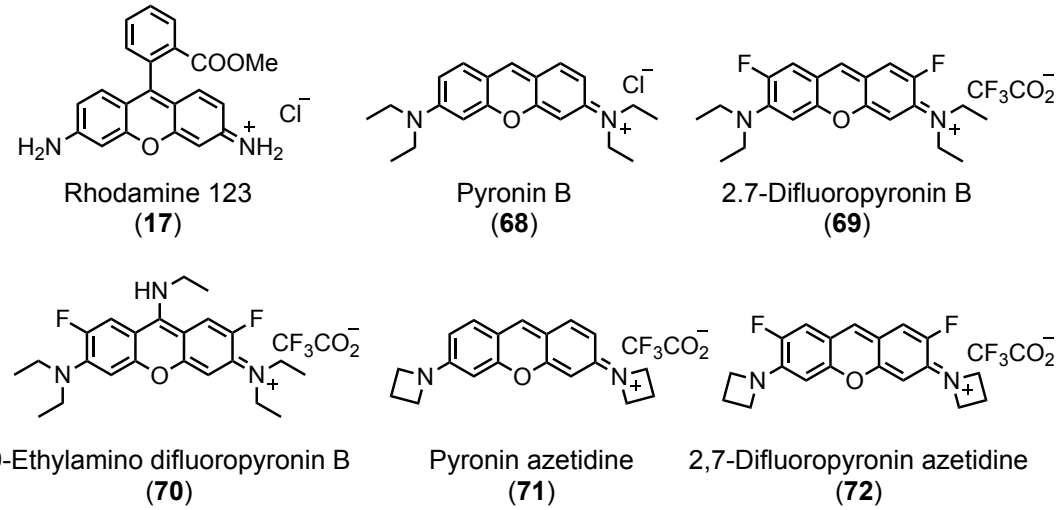

Figure 3.2. Chemical structures of the known fluorophores rhodamine 123 (**17**) and pyronin B (**68**) compared with the novel compounds 2,7-difluoropyronin B (**69**), 9-ethylamino difluoropyronin B (**70**), pyronin azetidine (**71**), and 2,7-difluoropyronin azetidine (**72**).

3.2 Synthesis of pyronins

To design novel analogues of pyronin shown in Figure 3.2, we proposed to incorporate fluorine in compounds **69**, **70**, and **72** because this modification has been widely used to improve the chemical and biological properties of therapeutics and fluorescent probes.[27] Among other effects, fluorination can profoundly affect drug metabolism and chemical reactivity. When incorporated into fluorophores such as Pennsylvania Green, fluorine has been shown to confer enhanced photostability and fluorescence in acidic environments compared to the non-fluorinated analogue Tokyo Green.[28] A similar improvement of photostability is observed in the fluorinated coumarin Pacific Blue compared to its non-fluorinated parent compound.[29] Additionally, substitution of alkyl chains with cyclic azetidine analogues has been used to improve brightness and other photophysical properties of fluorophores, and **71** and **72** were designed to explore this modification.[30, 31] The synthesis of these analogues of pyronin B is shown in Scheme

3.1. This route is based on a previously published method for the preparation of difluoroxanthones.[32] Briefly, the inexpensive benzophenone starting material **73** is converted to difluoroxanthone (**74)** by nucleophilic aromatic substitution with diethylamine followed by cyclization under basic conditions. The intermediate **74** was reduced with borane dimethylsulfide (BH_3-SMe_2) and oxidized with 2,3-dichloro-5,6-dicyanobenzoquinone (DDQ), followed by precipitation with trifluoroacetic acid (TFA) to provide 2,7-difluoropyronin B (**69**) as the TFA salt. 2,7-Difluoropyronin azetidine (**72**) was prepared from using a similar method with azetidine. To make 9-ethylamino difluoropyronin B (**70**), the intermediate **74** was first triflated with trifluoromethanesulfonic anhydride (Tf_2O), substituted by ethylamine, and the desired product precipitated with TFA.

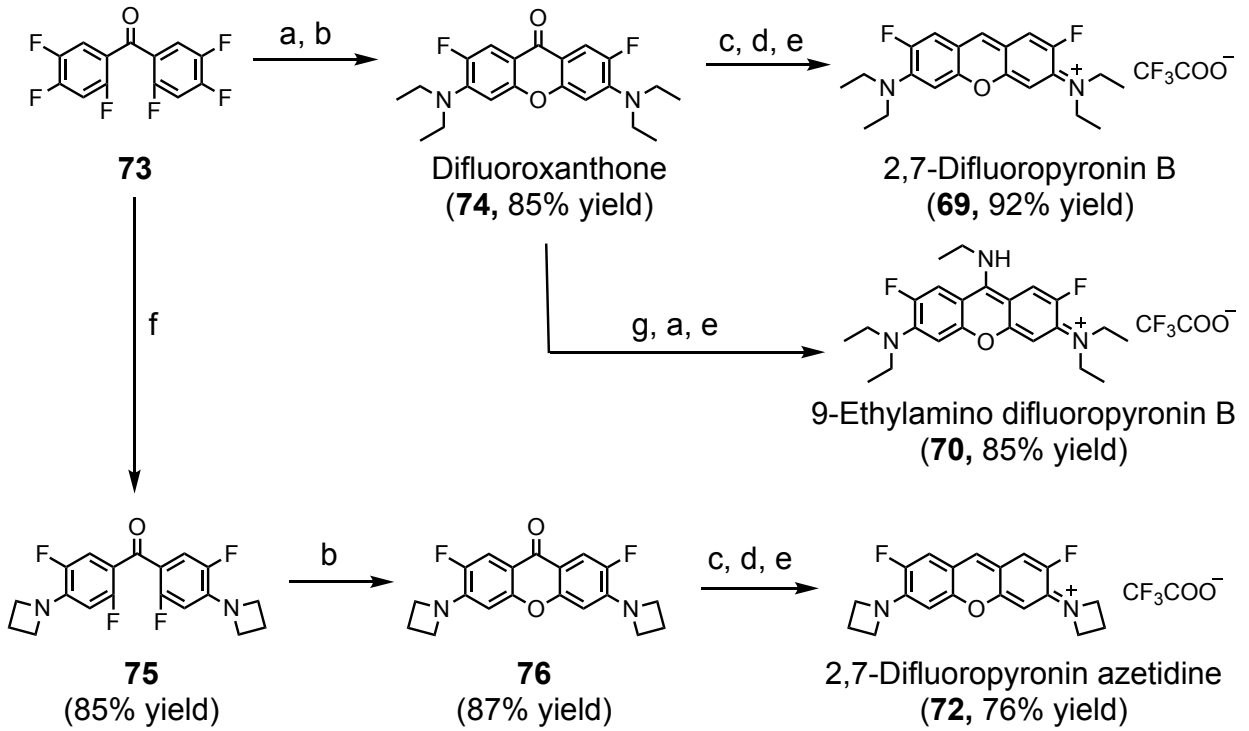

Scheme 3.1. Synthesis of 2,7-difluoropyronin B (**69**), 2,7-difluoropyronin azetidine (**72**), and 9-ethylamino difluoropyronin B (**70**). Reaction conditions: a) Et_2NH, 90 °C. b) KOH, DMSO, Reflux. c) BH_3-SMe_2. d) DDQ. e) TFA. f) Azetidine, DIEA, MeCN, 100 °C. g) Tf_2O.

Synthesis of the pyronin azetidine (**71**) required an alternative route involving triflation of xanthone **77** with Tf_2O to provide intermediate **78**, followed by substitution with azetidine to give xanthone **79**. This compound was reduced with BH_3-SMe_2, oxidized with DDQ, and precipitated with TFA to form the pyronin azetidine salt.

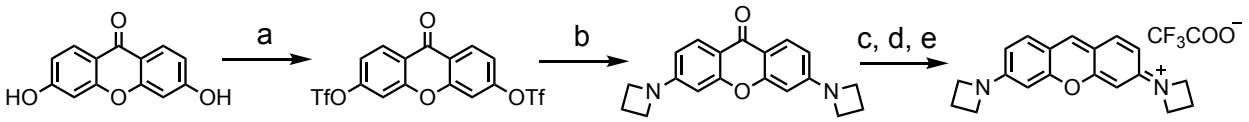

77 **78** (82% yield) **79** (21% yield) Pyronin azetidine (**71**, 47% yield)

Scheme 3.2. Synthesis of pyronin azetidine. Reaction conditions: a) Tf_2O, pyridine, 90 °C, 12 h. b) Azetidine, DIEA, MeCN, 150 °C, 12 h. c) BH_3-SMe_2 d) DDQ. e) TFA.

3.3 Photophysical properties of pyronins

Pyronin B and its structurally similar *N*, *N*-dimethylamine analogue Pyronin Y are reported to be highly fluorescent. To compare new pyronin analogues with parent compounds, absorbance and emission spectra in ethanol were acquired. As shown in Figure 3.3 A, the maximal absorbance and emission of **71** and **72** are similar to the parent compound **68**, with the maximum absorbance of ca. 553 nm, whereas the maximum emission is ca. 574 nm. The maximal absorbance and emission of difluoropyronin B (**69**) was somewhat red shifted. In contrast, the spectra of ethylaminopyronin (**70)** were largely blue-shifted, with maximal absorbance at 443 nm and emission at 531 nm.

The extinction coefficients of pyronins were determined at the maximum absorbance wavelength in ethanol as shown in Figure 3.3 B. In comparison to the non-fluorinated pyronin B **68** (ε = 64360 $M^{-1}cm^{-1}$) and azetidine pyronin **71** (ε = 72740 $M^{-1}cm^{-1}$), the fluorinated **69** and **72** exhibited slightly decreased extinction coefficients of 61610 $M^{-1}cm^{-1}$ and 67740 $M^{-1}cm^{-1}$, respectively. Additionally, the azetidine analogues **71** (ε = 72740 $M^{-1}cm^{-1}$) and **72** (ε = 67740 $M^{-1}cm^{-1}$) showed higher extinction coefficients than **68**

(ε = 64360 $M^{-1}cm^{-1}$) and **69** (ε = 61610 $M^{-1}cm^{-1}$), as expected. The blue shifted fluorophore **70** exhibited a lower extinction coefficient (ε = 43390 $M^{-1}cm^{-1}$) compared to the parent fluorophore **68**.

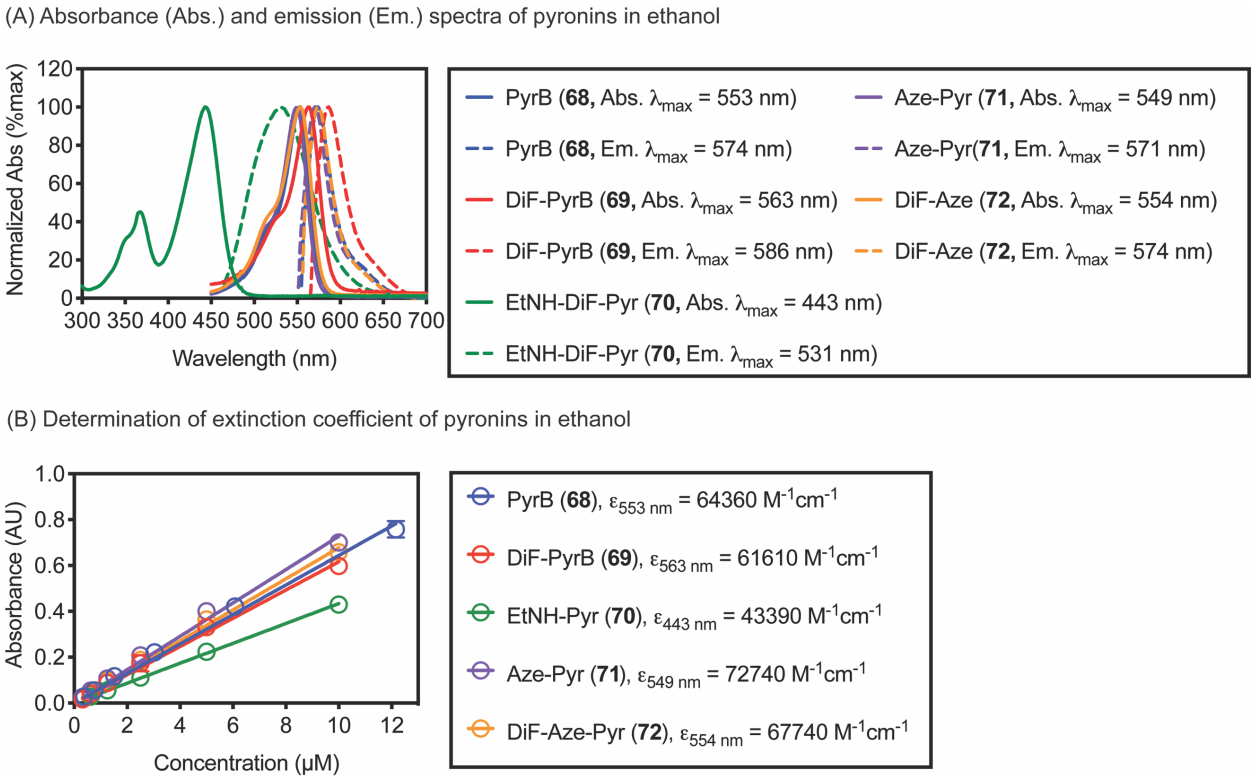

Figure 3.3. Normalized absorbance (Abs.) and emission (Em.) spectra of pyronins in ethanol (A) and determination of extinction coefficients at absorbance λ_{max} (B).

3.4 Accumulation of pyronins in cells

To examine the subcellular distribution of pyronin analogues, HeLa cervical cancer cells were treated with concentrations of 2 μM or 10 μM (1 h). Confocal images were obtained upon excitation with 405 nm, 488 nm, and 532 nm lasers. The fluorescence emission was collected using blue (425-550 nm), green (500-650 nm) and yellow (550-650 nm) channels as shown in Figure 3.4. Based on their absorbance and emission spectra, pyronins, **68**, **69**, **71** and **72** were proposed to be excited at 488 nm or 532 nm

detected with the green and yellow channels. The blue shifted fluorophore **70** should be excited at 405 nm or 488 nm and detected with the blue and green channels. As expected, **68**, **69** and **71** were observed with the both green and yellow channels, whereas **70** observed mainly with the blue channel. Surprisingly, despite the high in vitro fluorescence of compound **72**, it didn't exhibit cellular fluorescence. No significant uptake was observed in cells even after treatment with a concentration of 10 μM, suggesting that the enhanced electrophilicity in this particular pyronin due to the combination of fluorination and the strained azetidine ring might result in rapid reactivity toward cellular nucleophiles and abolishment of fluorescence.

Similar to the positive control Rhodamine 123, a hydrophobic cation known to be localized in mitochondria, **68**, **70** and **71** (2 μM) were observed to accumulate in tubular organelles. This same localization pattern was observed for **69** (10 μM), suggesting that these compounds specifically accumulate in mitochondria. Interestingly, **70** also appeared to label vesicles in the cytosol.

(A) Rhodamine 123 (**17**, 2 μM, 1 h)

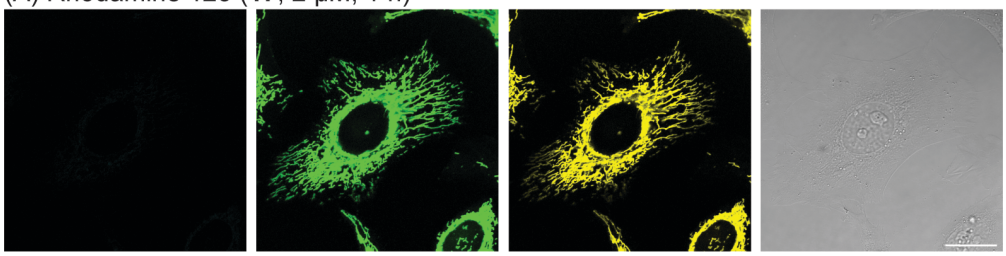

(B) Pyronin B (**68**, 2 μM, 1 h)

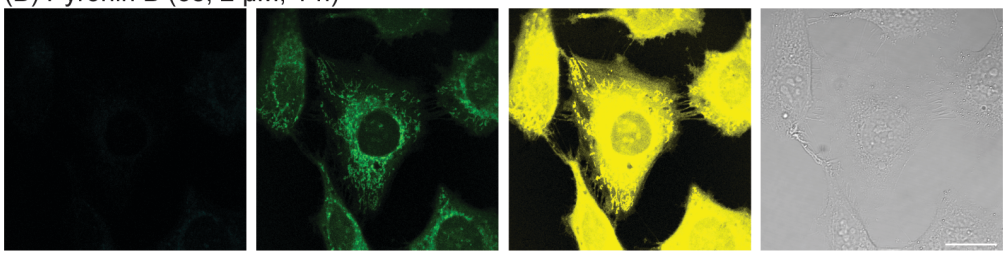

(C) 2,7-Difluoropyronin B (**69**, 10 μM, 1 h)

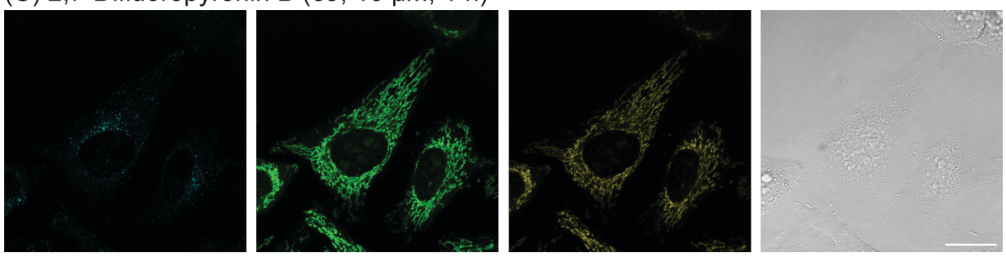

(D) 9-Ethylamino difluoropyronin B (**70**, 2 μM, 1 h)

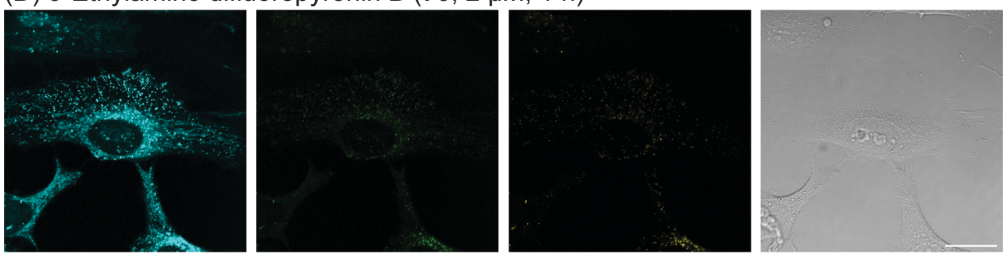

(E) Pyronin azetidine (**71**, 2 μM, 1 h)

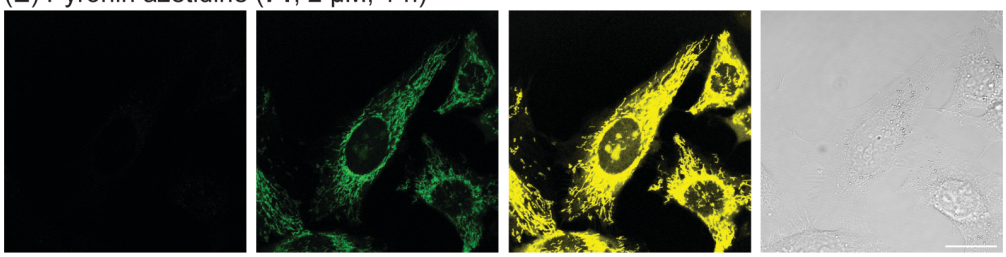

(F) 2,7-Difluoropyronin azetidine (**72**, 10 μM, 1 h)

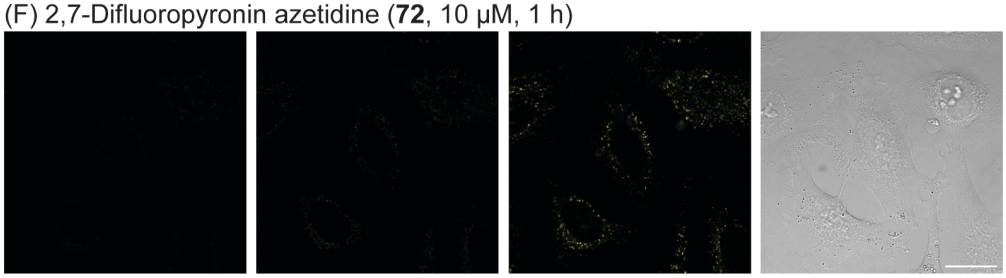

Ex. 405 nm Em. 425-550 nm	Ex. 488 nm Em. 500-650 nm	Ex. 532 nm Em. 550-650 nm	DIC

Figure 3.4. Confocal fluorescence and DIC micrographs of HeLa cells treated with **17, 68-72**. Cells were washed with media prior to imaging. Scale bar = 25 μm.

To further confirm that pyronins **69** and **71** specifically localize in mitochondria, we treated HeLa cells with these compounds and Mitochondria Deep Red FM (**32**, MTDR, 100 nM). This commercially available fluorophore is spectrally orthogonal to these pyronins and specifically labels mitochondria. After incubation, confocal images were obtained with excitation at 488 nm and 532 nm. These images revealed that **69** (10 μM, 1 h) or **71** (10 μM, 1 h) acquired in the green channel overlaid (shown in yellow) with MTDR (100 nM, 5 min) acquired in the red channel, indicating that **69** and **71** specifically accumulate in mitochondria (Figure 3.5, A and D). Compound **70** was also observed to localize in mitochondria under these conditions (shown in Figure 3.5 B). However, this compound also labels lysosomes in cells, as evidenced by yellow overlaid vesicles upon co-treatment with **70** (10 μM, 1 h) and spectrally orthogonal lysotracker red (1 μM, 30 min, Figure 3.5 C).

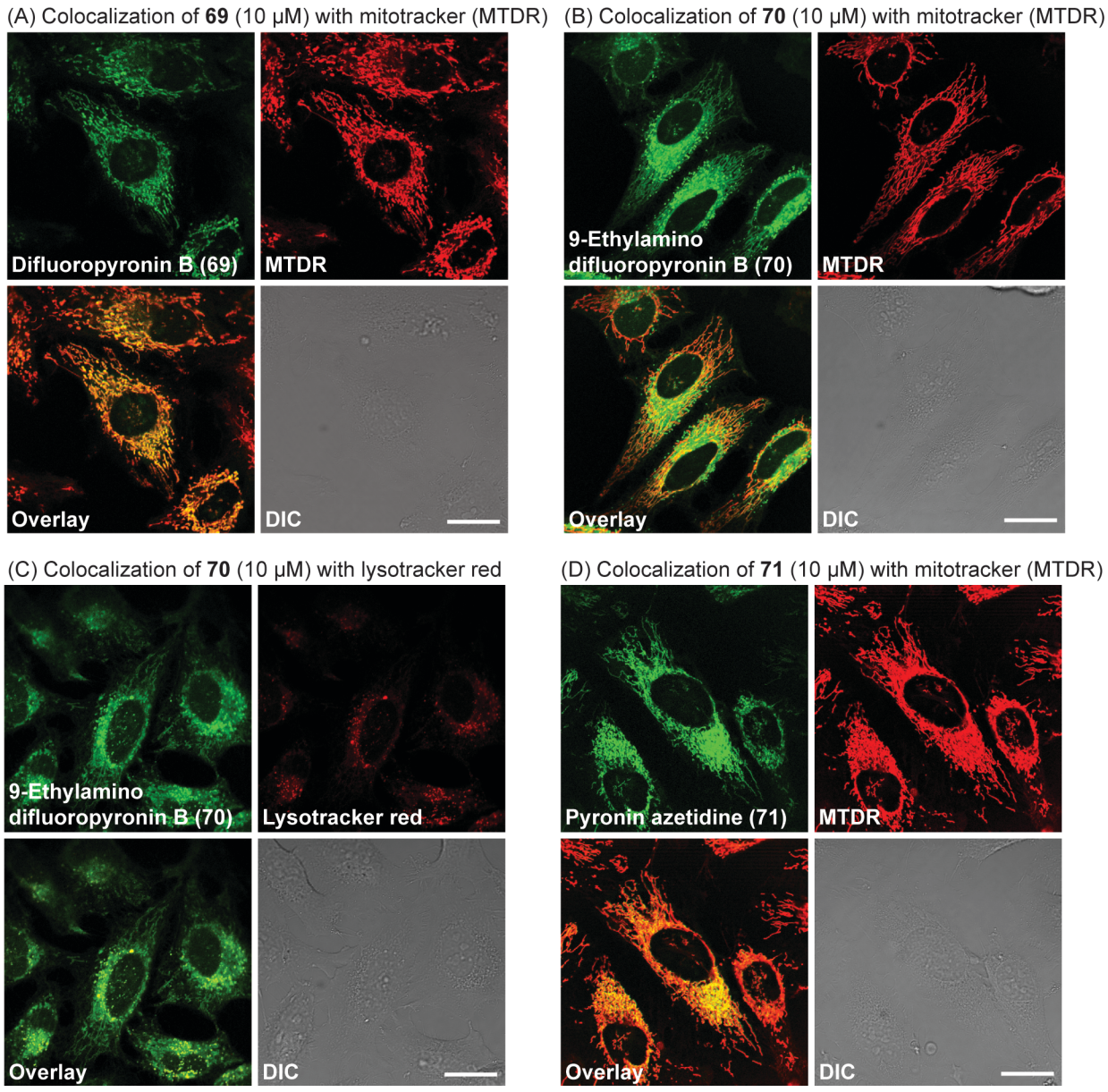

Figure 3.5. Colocalization assay of probes **69**, **70**, and **71** with organelle markers respectively by confocal microscopy. (A) Cells treated with **69** (10 μM, 1 h) and mitotracker deep red (MTDR, 100 nM, 5 min). (B) Cells treated with **70** (10 μM, 1 h) and MTDR (100 nM, 5 min). (C) Cells treated with **70** (10 μM, 1 h) and lysotracker red (1 μM, 30 min). (D) Cells treated with **71** (10 μM, 1 h) and MTDR (100 nM, 5 min). Cells were imaged without washing. Scale bar = 25 μm. The emission of **69**, **71** and **72** was detected at 500-650 nm after excitation at 488 nm. The emission of MTDR was detected at 650-750 nm after excitation at 635 nm. The emission of Lysotracker Red was detected at 600-650 nm after excitation at 532 nm. The emission of **70** was detected at 425-550 nm after excitation at 405 nm.

The mitochondrial membrane potential is commonly elevated in cancer cells.[33] Hence, in principle, selectivity for cancer cells over normal cells might be obtained by treatment with probes that are dependent on this membrane potential. To explore this concept, we dosed two different cell lines, the cervical cancer cell line HeLa, and the normal kidney cell line CV-1, which has a lower mitochondrial membrane potential. As expected, uptake of the positive control rhodamine 123 (**17**, 2 μM, 1 h) was less in CV-1 cells compared with HeLa cells (Figure 3.6 D and C), suggesting that the mitochondrial membrane potential of CV-1 is lower than HeLa. When both cells were treated with **69** (10 μM, 1 h), low fluorescence was observed in CV-1 in comparison to HeLa, suggesting that **69** depends on the membrane potential to accumulate in mitochondria. Additionally, these results suggest that one could gain selectivity for targeting of cancer cells using **69**.

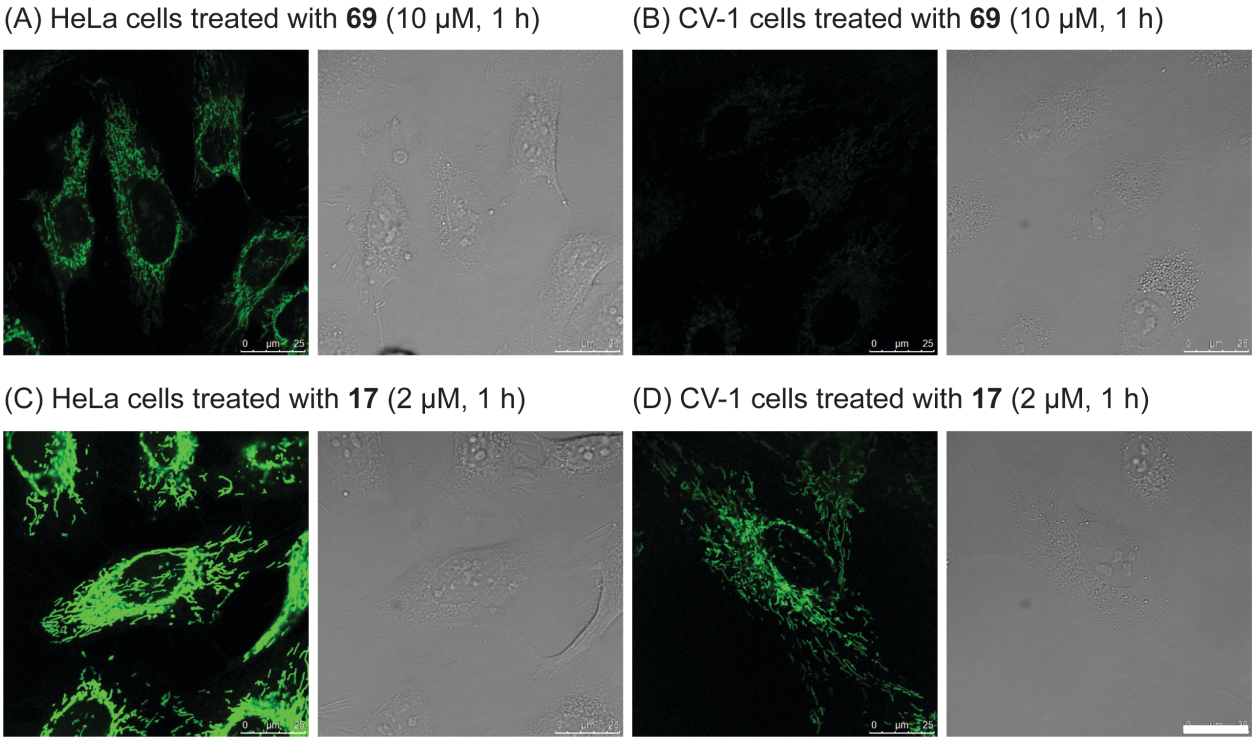

Figure 3.6. Confocal images of HeLa (A, C) and CV-1 (B, D) cells. Cells were treated with **69** (10 μM, 1 h) or rhodamine 123 (2 μM, 1 h). Emitted photons were collected at 500-600 nm upon excitation at 488 nm. Scale bar = 25 μm

3.5 Photochemical depolarization of mitochondrial membranes mediated by 69

In contrast to **68**, the subcellular localization of **69** was substantially altered after imaging for an extended period of time. Initially, **69** accumulates only in mitochondria of living cells, similar to the parent compound **68**. However, after irradiation for 60 seconds at 488 nm, the fluorescence was observed to diffuse from mitochondria into the cytoplasm and nucleus, where it further accumulated in nucleoli (shown in Figure 3.7 A, B, D and E). Because other pyronins are reported to bind with RNA in nucleoli of fixed cells that lack polarized mitochondria, these results suggested that the blue (488 nm) laser enables **69** to depolarize mitochondria. To test this hypothesis, we treated cells with **69** (10 μM, 1 h) and CCCP (10 μM, 5 min, Figure 3.7 F), a uncoupler known to depolarize mitochondria membrane, for comparison with cells treated only with **69** (10 μM, 1 h). After irradiation with blue light (60 s, Figure 3.7 E), essentially identical phenotypes of diffusion of fluorescence from mitochondria to cytosol and nuclei were observed, suggesting that **69** can trigger mitochondrial depolarization upon irradiation with visible blue light. For comparison, we also treated cells with the parent compound **68** (10 μM, 1 h) and irradiated with blue light (60s, Figure 3.7 B) or treated with CCCP (10 μM, 5 min, Figure 3.7 C). A similar phenotype was observed upon treatment with CCCP but not irradiation, indicating that the fluorine substituents on **69** are critical for the observed light-mediated depolarization of mitochondria.

(A) Pyronin B (**68**, 10 μM, 1 h)

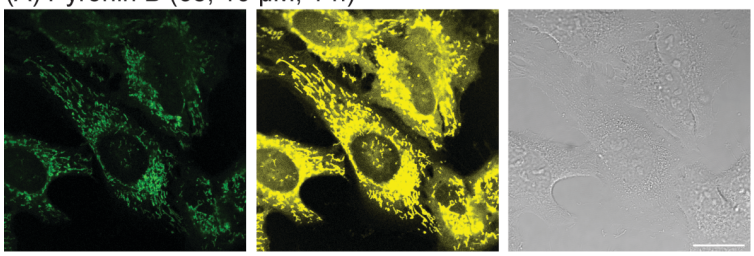

(B) Pyronin B (**68**, 10 μM, 1 h, followed by irradiation at 488 nm for 60 s)

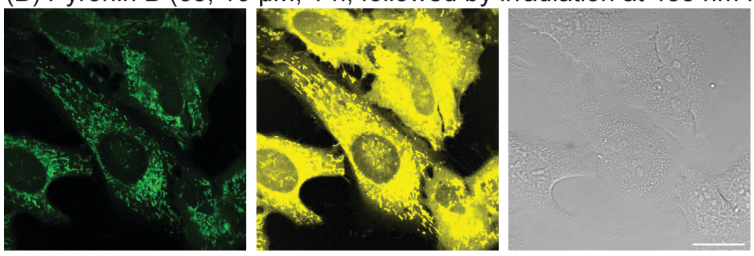

(C) Pyronin B (**68**, 10 μM, 1 h, followed by treatment with CCCP (**80**,10 μM, 5 min))

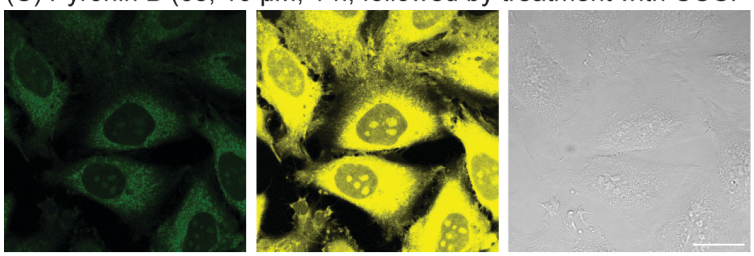

(D) 2,7-Difluoropyronin B (**69**, 10 μM, 1 h)

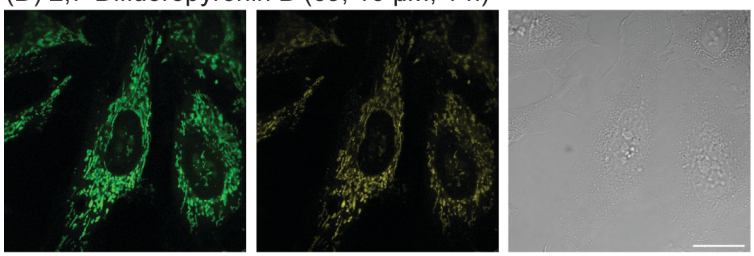

(E) 2,7-Difluoropyronin B (**69**, 10 μM, 1 h, followed by irradiation at 488 nm for 60 s)

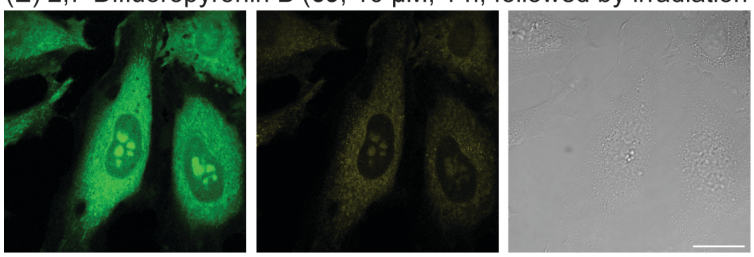

(F) 2,7-Difluoropyronin B (**69**, 10 μM, 1 h, followed by treatment with CCCP (**80**,10 μM, 5 min))

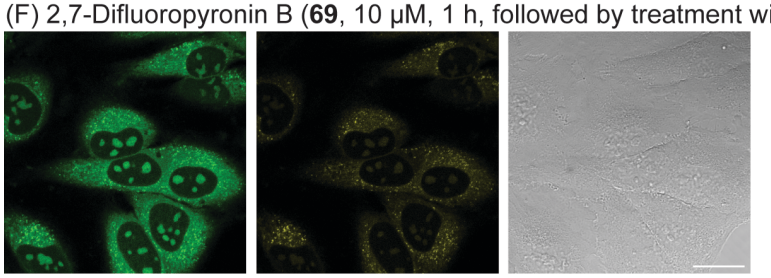

Ex. 488 nm
Em. 500-650 nm

Ex. 532 nm
Em. 550-650 nm

DIC

Figure 3.7. Effects of blue light or the mitochondrial decoupler CCCP on fluorescence of **68** and **69** in HeLa cells. Cells were imaged by confocal microscopy without washing. Scale bar = 25 μm.

Pyronin Y, a dye with a structure similar to **69**, has been widely used as a fluorescent marker for RNA.[14, 34, 35] To examine whether RNA is a target of **69** in cells, we removed RNA from cells by fixation with paraformaldehyde and digestion with RNase (10 μg/mL or 30 μg/mL), followed by treatment with **69** (10 μM, 1 h). Living cells treated with **69** (10 μM, 1 h) provided a control. As shown in Figure 3.8 (A and B), nuclear fluorescence was observed only in fixed cells (B) but not in living cells (A) due to the lack of a mitochondrial membrane potential in fixed cells, further indicating that accumulation of **69** in mitochondria is a dependent on this membrane potential. Upon treatment with RNase, this nuclear fluorescence dramatically decreased in a dose-dependent manner, providing evidence that RNA is a target of **69** or its metabolites after release from mitochondria.

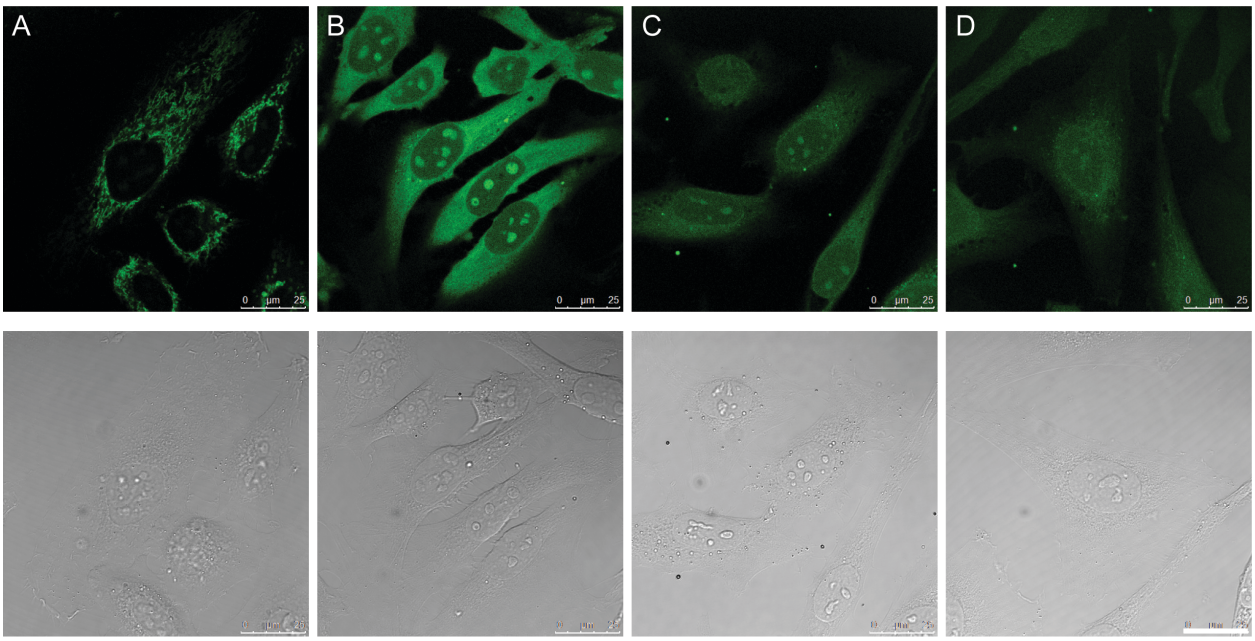

Figure 3.8. Confocal images of living HeLa cells (A) or fixed HeLa cells (B) treated with **69** (10 μM, 1 h). Images of fixed cells treated with RNase (10 μg/mL, C or 30 μg/mL, D) following **69** (10 μM, 1 h) by confocal microscopy. Scale bar = 25 μm.

3.6 Investigation of the mechanism of action of photochemical depolarization of mitochondria mediated by difluoropyronin B

We hypothesized that the unique chemical reactivity of **69** might be responsible for its ability to uniquely cause depolarization of mitochondria upon irradiation with blue light. Fluorination of this pyronin ring was predicted to generate a more electrophilic pyronin compared to the non-fluorinated parent compound. To investigate its potential reactivity, we measured absorbance spectra in aqueous solution upon addition of nucleophilic amines such as reduced glutathione (GSH), lysine (Lys), and bovine serum albumin (BSA). As shown in Figure 3.9, the absorbance spectra of the non-fluorinated pyronin **68** was unchanged upon addition of amines, whereas **69** was observed to react with GSH, Lys and BSA. These results indicate that the fluorination of **68** to generate **69** enables reactivity towards these compounds, and this suggests that this increased reactivity might be responsible for this unique phenotype of cellular mitochondrial depolarization.

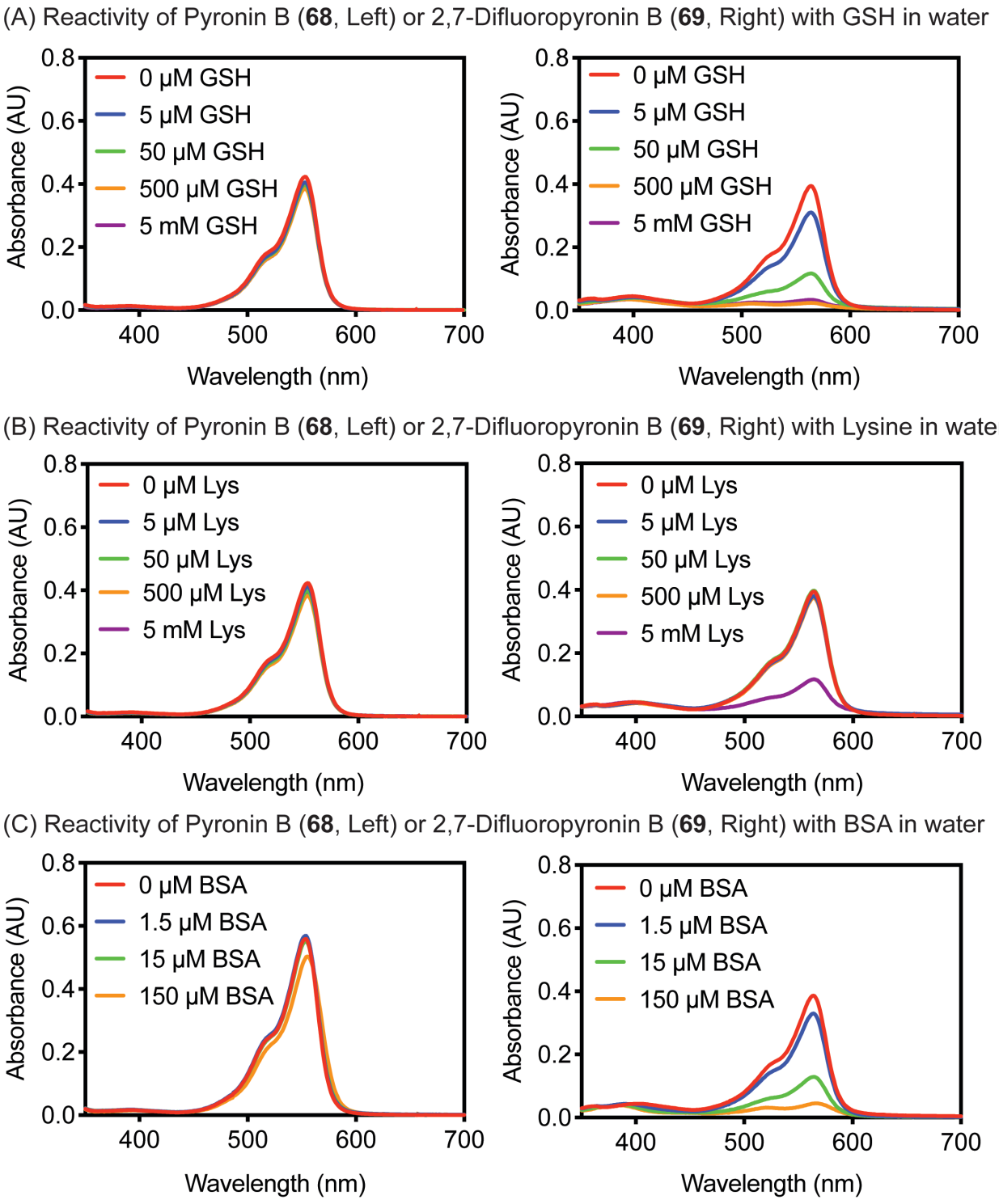

Figure 3.9. Absorbance spectra of **68** (10 μM) or **69** (10 μM) with addition of GSH (0, 5, 50, 500, 5000 μM), Lys (0, 5, 50, 500, 5000 μM) and BSA (0, 1.5, 15, 150 μM) respectively in water by UV-Vis.

To identify whether **69** forms products upon irradiation with blue light, we acquired emission spectra using a highly sensitive fluorimeter. We hypothesized that spermine, a polyamine found in mitochondria at a high concentrations of approximately 1 mM,[36] might be a target of **69**. Mixing 100 μM spermine with 10 μM **69** in phosphate buffer resulted in loss of fluorescence (Shown in Figure 3.10 A), indicated that **69** likely reacts with spermine to form a non-fluorescent adduct. Moreover, upon irradiation of this solution with a blue LED light for 10 min, a new peak appears with a maximum emission wavelength around 540 nm. This peak is approximately 50 nm blue shifted compared to **69**, which exhibits maximum emission wavelength at 588 nm in this buffer. This blue-shifted emission is very similar to ethylamino pyronin **70**, suggesting that the new fluorescent species might be an aminopyronin formed by photooxidation of the non-fluorescent adduct. It has been previously reported that depletion of spermine by transduction of cells with adenovirus encoding spermine acetyltransferase 1 causes loss of the mitochondrial membrane potential,[37] indicating that reaction of **69** with spermine in mitochondria might result in depolarization.

The reactivity of other amines commonly found in cells with **69** and blue light irradiation was also examined. The photochemical generation of aminopyronin products was also observed with glycine, GSH, lysine, Nα-Ac-lysine, Nε-Ac-lysine and glutamine (Shown in Figure 3.10 B). When compared to other pyronins (**68**, **71** and **72**), only **69** formed aminopyronins upon irradiation of BSA as a model protein, further demonstrating its unique reactivity (Shown in Figure 3.10 C).

The degree of labeling (DOL) towards BSA by **69** was additionally examined. Labelled BSA was isolated by size-exclusion chromatography after its reaction with

pyronins. Measurement of absorbance by UV-Vis spectroscopy was used to calculate the dye concentration, protein concentration, and the DOL. As shown in Figure 3.10 D, consistent with Figure 3.10 C, only **69** was shown to label BSA. However, given that BSA has 59 lysine residues, where 30–35 are known to exhibit reactivity towards electrophiles (Thermo Scientific BSA product literature), a measured DOL of approximately 0.2 suggests that **69** exhibits limited reactivity with this protein under these conditions.

Furthermore, to determine whether the unique reactivity of **69** could be observed in living cells, we generated emission spectra of cells treated with **69** (10 μM, 1 h) by spectral scanning on a confocal microscope. As shown in Figure 3.10 E, fluorescence of cells treated with **69** has a maximum emission wavelength close to 540 nm whereas the control with **68** emits maximally at 580 nm. Consistent with the in vitro reactivity assay, **69** is converted into aminopyronins in cells. Essentially, all of the signal detected in cells treated with **69** is derived from product aminopyronins. Additionally, we analyzed the fluorescence of the supernatant after treatment of cells with **68** and **69**. Similar to the lambda scan confocal microscopy, **69** was able to converted into aminopyronins by cells resuspended in phosphate buffer, suggesting that after aminopyronins are formed in cells, they can rapidly diffuse across cellular plasma membranes and can be readily detected, indicating that a major cellular amine target of **69** is likely to be abundant small molecule, possibly reduced glutathione (GSH).

To examine the potential for formation of an aminopyronin derived from GSH, we used LCMS to identify the MS of products from **69** reacting with this small molecule amine in vitro (Figure 3.10 G). In the absence of cells, a product was detected with MS of 664, supporting the formation of an oxidized GSH adduct. Thiopyronins that might be

generated by reaction of **69** with GSH or other thiols are predicted to be substantially more red-shifted[38] than aminopyronins, and the fluorescence emission spectra were consistent with exclusive modification of the amine. To further confirm this amine target, future studies will attempt to identify this product by LC-MS after generation in cells resuspended in buffer.

(A) Reactivity of **69** with Spermine under light

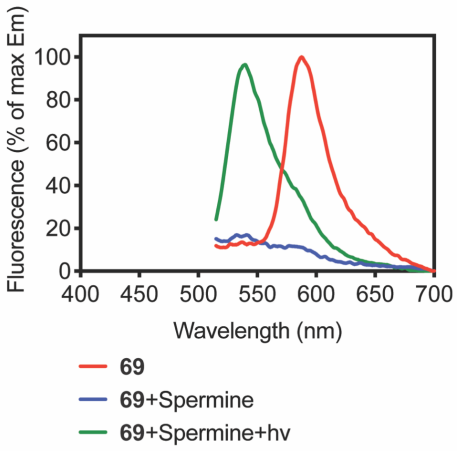

(B) Reactivity of **69** with various amines under light

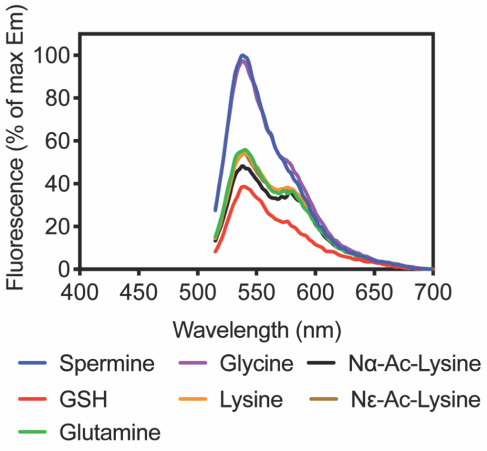

(C) Reactivity of pyronins with BSA

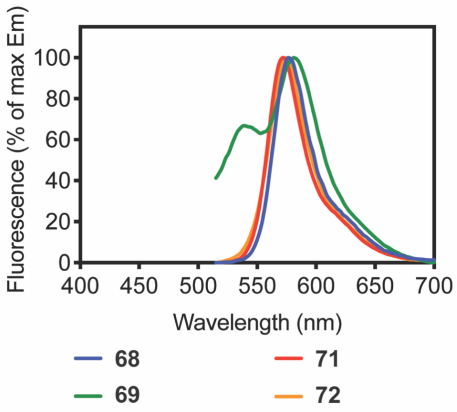

(D) Absorbance spectra of labelled BSA

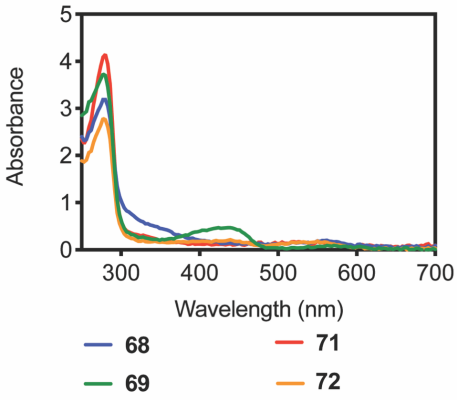

(E) Lamda scan of **69** and **68** in HeLa cells

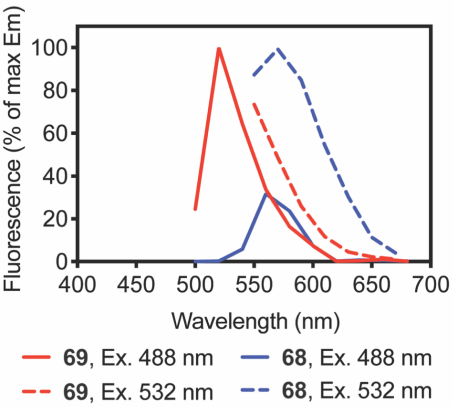

(F) Emission spectra of supernatant from HeLa cells treated with **69** and **68**

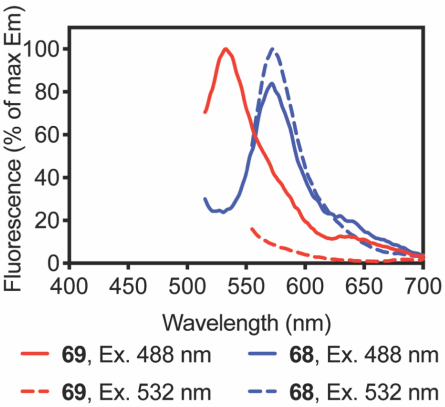

(G) LCMS analysis of **69** reacting with GSH

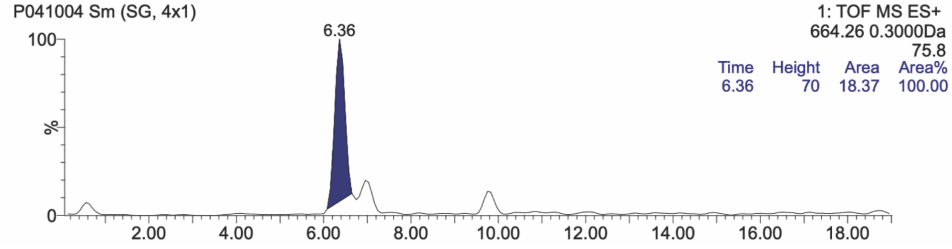

Figure 3.10. Reactivity of **69** towards amines with and without irradiation by a blue LED (10 min). Fluorescence emission spectra (Ex. 488 nm) after treatment of **69** with amines in vitro: (A, B) spermine, glutathione, glutamine, glycine, lysine, Nα-Ac-lysine and Nε-Ac-lysine in phosphate buffer (10 mM, pH = 7.4); (C) BSA protein in H_2O. (D) Absorbance spectra of BSA after treatment with **68**–**72**. (E) Fluorescence emission spectra (Ex. 488 nm) of HeLa cells treated with **68** and **69** by lambda scan confocal microscopy. (F) Analysis of supernatant from cells treated with **68** and **69** by fluorimetry. (E) LCMS analysis of products resulting from reaction of **69** with glutathione after additional irradiation with blue light.

3.7 Irradiation of 69 in cells with blue light generates reactive oxygen species

Depolarization of mitochondrial membranes is always associated with increased reactive oxygen species (ROS) in cells. To examine whether irradiation of **69** with blue light generates ROS that might be involved in oxidization of amine adducts to fluorescent aminopyronins, we performed a dihydroethidium (DHE) assay that detects production of ROS in live cells by a change in fluorescence. Upon reaction with ROS, the weak fluorophore DHE becomes oxidized to ethidium and 2-hydroxyethidium, which further bind to nucleic acids to emit strong fluorescence. Changes in the fluorescence of the cell nucleus can be quantified by confocal microscopy. Quantification of intensity is done by drawing a region of interest around the nucleus and averaging data from more than 10 cells for each treatment. As shown in Figure 3.11, no fluorescence was detected for negative controls, including cells treated only with DHE (5 μM), **68** (2 μM) and **69** (2 μM) separately. Antimycin A, an inhibitor of electron transport in mitochondria that induces generation of ROS was used as a positive control. A significant increase of fluorescence was observed when cells treated with DHE (5 μM) and antimycin A (20 μM), providing validation for this assay. When cells were treated with DHE and each pyronin, followed by irradiation for 1 min or 2 min, enhancement of fluorescence was observed for **69**,

whereas no change in fluorescence for the parent compound **68**, indicating **69** selectively induces formation of ROS over time under blue light irradiation.

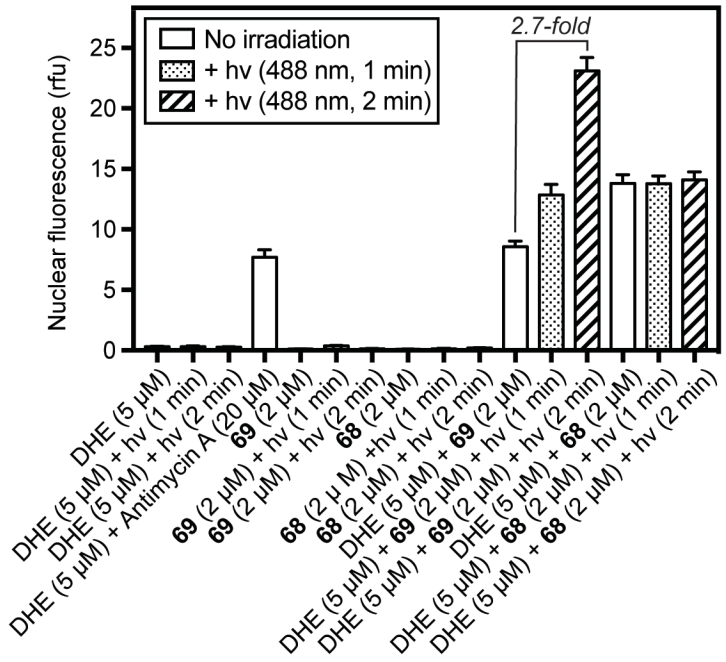

Figure 3.11. Effects of **68** and **69** on reactive oxygen species (ROS) in HeLa cells. Cells were treated with pyronins (2 µM) or the positive control compound antimycin A (20 µM) for 1 h followed by the ROS sensor dihydroethidium (DHE, 5 µM) for an additional 1 h. Fluorescence of individual cell nuclei was measured by image analysis of confocal micrographs (N ≥ 10).

3.8 Cytotoxicity of pyronin analogues

We further measured the cytotoxicity of pyronins towards HeLa cells and Jurkat lymphocytes by flow cytometry after treatment for 48 h. As shown in Figure 3.12, HeLa cells were more resistant to toxic effects of these compounds. Additionally, the parent compound **68** ($IC_{50,\ Hela}$ = 2 µM, $IC_{50,\ Jurkat}$ = 0.07 µM) was substantially more toxic than **69** ($IC_{50,\ Hela}$ = 9 µM, $IC_{50,\ Jurkat}$ = 0.96 µM) towards both cell lines. This reduced cytotoxicity might be due to increased hydrolysis of **69** to the weakly toxic difluoroxanthone product ($IC_{50,\ Hela}$ = 51 µM, $IC_{50,\ Jurkat}$ = 17 µM). Additionally, **72** ($IC_{50,\ Hela}$ = 15 µM, $IC_{50,\ Jurkat}$ = 0.87 µM) was less toxic than non-fluorinated **71** ($IC_{50,\ Hela}$ = 2 µM, $IC_{50,\ Jurkat}$ = 0.07 µM), further

supporting decreased cytotoxicity associated with fluorination. This is consistent with the cellular uptake assay, where no fluorescence was observed upon treatment **72**, which could be a consequence of high reactivity of **72** towards biomolecules.

(A) Cytotoxicity towards HeLa cells (48 h)

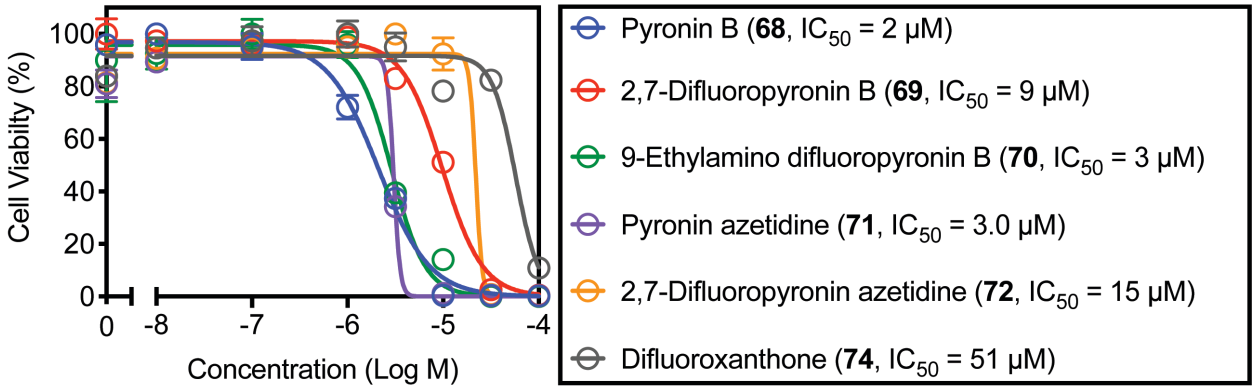

(B) Cytotoxicity towards Jurkat cells (48 h)

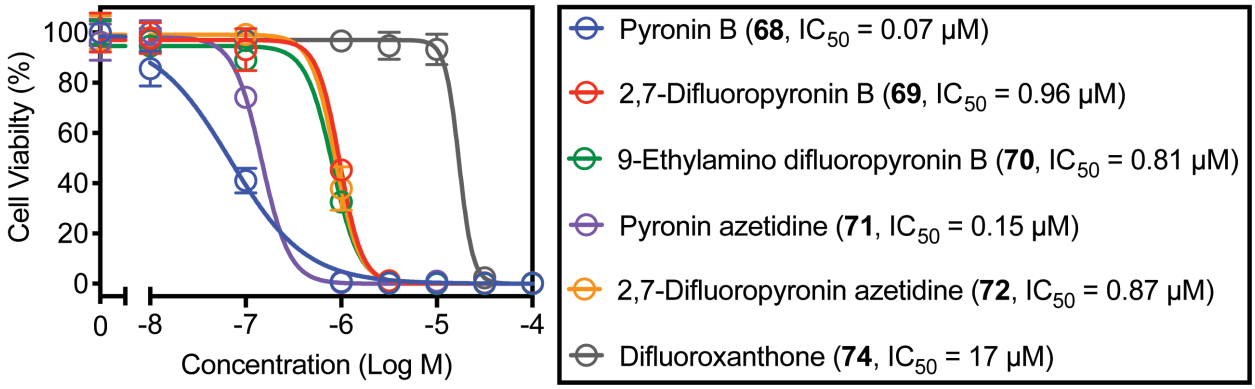

Figure 3.12. Cytotoxicity of pyronins (**68**, **69**, **70**, **71** and **72**) and difluoroxanthone (**74**) towards HeLa cells (A) and Jurkat lymphocytes (B) after 48 h treatment.

3.9 Efflux of pyronin analogues

To assess whether pyronins might form stable fluorescent adducts with biomolecules in cells, we measured the half-life of each pyronin along with the positive

control Rhodamine 123 in Jurkat lymphocytes, a suspension cell line that is easy to analyze by flow cytometry. Cells were treated with each probe for 1 h followed by washing with fresh media to allow efflux of small molecules. Cellular fluorescence was immediately measured by flow cytometry. Analysis of fluorescence after different time points was used to generate kinetics data and half-lives were calculated using prism. As shown in Figure 3.13, the positive control Rhodamine 123 strongly retained in mitochondria and exhibited a very long half-life of over 17 h. In contrast, the fluorescence of the pyronins was substantially lost over 1 h, especially **68** ($t_{1/2}$ = 6 min) and **69** ($t_{1/2}$ = 12 min), suggesting the rapid efflux of pyronins and their metabolites from cells. The longer half-life of 9-ethylamino pyronindifluoropyronin B (**70**, $t_{1/2}$ = 60 min) might be due to its retention in lysosomes as observed by confocal microscopy.

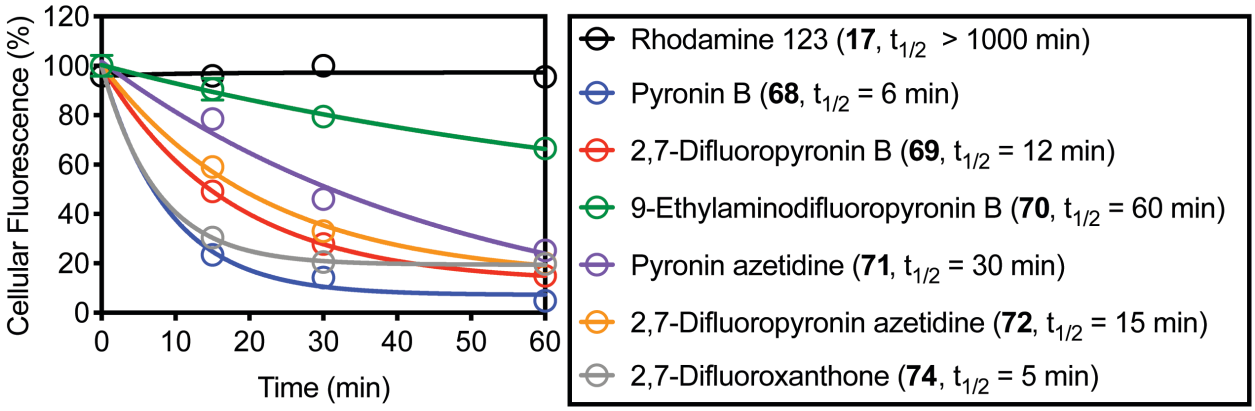

Figure 3.13. Efflux of pyronins and Rhodamine 123 from Jurkat lymphocytes as quantified by flow cytometry. Cells were treated with probes (10 μM) for 1 h (37 °C). At each time point shown, cells were washed with fresh complete media prior to analysis of cellular fluorescence (Ex. 405 nm or 488 nm) by flow cytometry. Standard errors are estimated as ± 5 min.

3.10 Conclusion

We synthesized four analogues of pyronin B (**68**) including 2,7-difluropyronin B (**68**), 9-ethylamino difluoropyronin (**70**), pyronin azetidine (**71**) and 2,7-difluoropyronin

azetidine (**72**) by either fluorination on pyronin ring or replacement of alkyl side chains with azetidine. One particular compound, 2,7-difluoropyronin B, exhibited unique biological activity resulting from its increased reactivity towards nucleophilic amines. In living cells, this compound accumulates in mitochondria but likely reacts with amines, such as spermine, GSH and proteins, to form adducts that can be further oxidized to fluorescent aminopyronins or hydrolyzed to generate a difluoroxanthone as shown in Figure 3.14. This formation of aminopyronins is enhanced by visible blue light. Irradiation by blue light also increases production of cellular ROS, and rapid depolarization of the mitochondrial membrane potential is observed. Aminopyronins diffuse from mitochondria into cytosol and bind to RNA in nuclei. The unique reactivity of **69** offers a novel tool for photochemical control of depolarization of mitochondria.

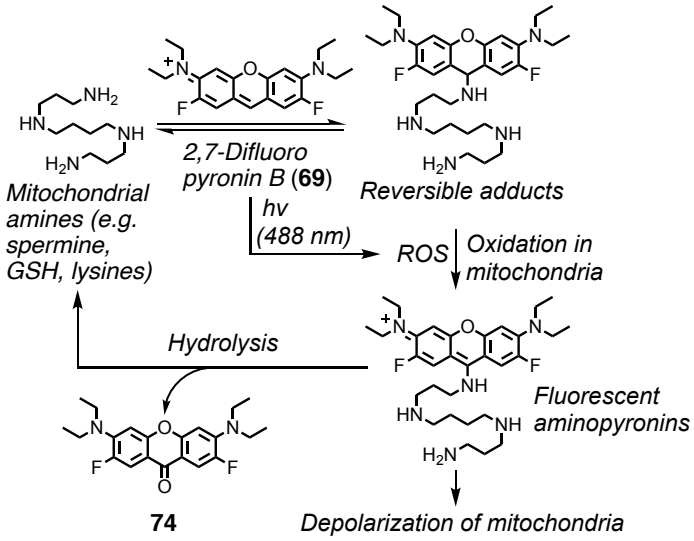

Figure 3.1 Proposed mechanism of photochemical depolarization of mitochondria by 2,7-Difluoropyronin B (**69**) with visible blue light.

3.11 Future Plans

Photochemical depolarization of mitochondria has been proposed as a strategy to improve cancer chemotherapy using nanoparticles that target these organelles.[26] In this

approach, the activity of the ATP-dependent efflux pump P-gp is decreased upon depolarization of mitochondria. P-gp is a major mechanism of drug resistance, and methods for the inhibition of P-gp overexpressed cancer cells could lead to increased exposure of these cells to anticancer agents such as Taxol. To investigate whether DiF-PyrB might exhibit similar effects on P-gp, it would be interesting to evaluate whether irradiation of cells treated with DiF-PyrB might enhance uptake of taxoids such as PB-Gly-Taxol, a fluorescent mimic of taxol described in chapter 2. Preliminary data suggests that this approach might be successful, but additional studies are necessary to confirm these results.

3.12 Experimental Section

Determination of molar extinction coefficients and quantum yields

Molar extinction coefficients (ε) were calculated using Beer's Law: $A = \varepsilon bc$ (A is absorbance, b is path length and c is the concentration). Absorbance spectra were obtained from solutions of dry powders, and maximal absorbance versus concentration was analyzed by linear regression (including a zero intercept) with GraphPad Prism 7 software (slope = ε).

Relative quantum yields (Φ_F) were calculated as: $Q_x = Q_R \times \frac{A_R}{A_x} \times \frac{E_x}{E_R} \times \frac{n_x^2}{n_R^2}$ where Q is the quantum yield, A is the absorbance, E is the area under curve (AUC) of the emission spectra, and n is the refractive index of the solution. Subscripts X and R refer to the sample and reference compound, respectively. The absorbance was extrapolated to yield values at low concentrations. Emission spectra were obtained with a fluorescence

spectrometer, and emission AUC values were calculated with GraphPad Prism 7. Extrapolated absorbance was plotted versus AUC and fitted by linear regression to provide the slope as $\frac{Ex}{Ax}$ of the tested compound. The reference compound provided $\frac{A_R}{E_R}$.

Cell culture: Cell culture: HeLa cells (CCL-2) and CV-1 (CCL-70) were purchased from ATCC, and cultured in Dulbecco's Modified Eagle Medium (DMEM, Sigma D6429). Jurkat lymphocytes (TIB152) were obtained from ATCC and cultured in RPMI-1640 medium (Sigma R8758). Media was supplemented with fetal bovine serum (FBS, 10%, Fisher Scientific, NC0924828), penicillin (100 units/mL), and streptomycin (100 µg/mL, Sigma P4333). Cells were maintained in a humidified 5% CO_2 incubator at 37 °C.

Confocal microscopy: Cells were added to an 8-well cover glass slide (Ibidi µ-Slide, 300 µL, 20,000 cells/well) and allowed to proliferate for 24 h prior to addition of compounds. Compounds in DMSO stock solutions were serially diluted 1,000-fold in complete medium (final concentration of 0.1% DMSO) prior to addition to cells. Cells were treated with compounds at 37 °C for indicated length of time before imaging with a Leica SPE2 confocal laser-scanning microscope (63X oil-immersion objective).

Flow cytometry. Cells were analyzed with a Beckman Coulter Cytoflex S (B2-R0-V2-Y2) flow cytometer. Fluorophores were excited with 405 nm, 488 nm, and or 638 nm diode lasers and emitted photons were collected through 450/45 nm BP (Pacific Blue), 525/40 nm BP (sensors), or 690/50 nm BP (PI) filters (FSC threshold = 500,000, flow speed =

fast, mixing time = 5 s, backflush time = 5 s, and cells were collected until 10,000 cells were counted).

Analysis of efflux of small molecules from Jurkat cells by flow cytometry: Jurkat lymphocytes (300,000 cells/mL) in complete media were aliquoted into Eppendorf tubes (600 µL per tube before treatment). Fluorescent probes in DMSO stock solutions were added to each tube to achieve concentrations of 10 µM (0.1% DMSO) in triplicate. The resulting cells were incubated in Big Shot III Hybridization Oven at 37 °C for 1 h. Cells were centrifuged at 2000 rpm for 2 min to pellet. The supernatant was removed by aspiration, the cell pellets were washed once with fluorophore-free media (600 µL), and the cells were resuspended in media (600 µL). Cells in media (100 µL) were removed and analyzed by flow cytometry (t=0 min). The remaining cell suspension (500 µL) was incubated (37 °C) for an additional 30 min. Cells were centrifuged, washed, and analyzed by flow cytometry. Time points were recorded at 30, 60, 120, and 240 min. To keep the cell density constant, the media added for each round was 100 µL less than that of the previous cycle. Fluorescence was recorded on a cytoflex S flow cytometer and was normalized to the intensity observed at 0 min. Cellular fluorescence was analyzed with GraphPad Prism 7 using one phase exponential decay model.

Analysis of ROS with DHE: HeLa cells were seeded on 8-well cover glass slides (Ibidi µ-Slide, 300 µL, 20,000 cells/well) and allowed to proliferate for 16 h prior to addition of compounds. Cells were treated with **69** or **68** (2 µM, 1 h, 37 °C), followed by addition of DHE (5 µM, 1 h). Cells were washed twice with complete media (300 µL) before imaging

by confocal microscopy. Cells subjected to irradiation were scanned with a 488 nm laser at 25% power. To quantify differences in nuclear fluorescence, regions of interest (ROI) were drawn around this organelle. Mean fluorescence values were generated and analyzed with GraphPad Prism 7. Antimycin A (20 μm) was used as a positive ROS-generating control. Cells treated only with the pyronin were used to confirm that the signal from the nucleus originated only from DHE and its metabolites.

Analysis of cytotoxicity: Cells were seeded on a 96-well plate in complete medium at 8,000 cells / 200 μL per well 16 h prior to treatment. All compounds were serial diluted in DMSO and added to complete medium to achieve a 1:1000 dilution factor (0.1% DMSO in each well). The original media was removed from all wells by aspiration and replaced with the treatment media (200 μL) at the concentrations indicated. Plates were incubated for 48 h at 37 °C and cells were analyzed in triplicate. Following this incubation period, for HeLa cells, the media was aspirated and wells were washed with PBS (phosphate-buffered saline, pH 7.4). Cells were then detached with a solution of trypsin and EDTA (50 μL) at 37 °C for 5 min followed by treatment with complete medium (100 μL). The total cell-count for each well was determined by flow cytometry, using a Beckman Coulter Cytoflex S flow cytometer, and populations of live cells were identified by light scattering. For Jurkat lymphocytes, cells were directly counted with the Cytoflex. Counts of viable cells for each treatment in triplicate were used to generate dose-response curves. These curves were fitted by non-linear regression with an inhibitor vs. response variable slope 4-parameter model (GraphPad Prism 7) to determine IC_{50} values (Figure S7). Based on curve fitting, standard errors for cytotoxic IC_{50} values were ≤ 10%.

General experimental section. Chemicals were purchased from Sigma Aldrich, Alfa Aesar. ^{1}H and ^{13}C NMR spectra were acquired on Avance AVIII (500 MHz) or Varian VNMRS (400 MHz) instruments. Chemical shifts (δ) are reported in ppm referenced to $CDCl_3$ (7.22 ppm for ^{1}H and 77.0 ppm for ^{13}C) or DMSO-d_6 (2.50 ppm for ^{1}H, 39.5 ppm for ^{13}C). ^{1}H coupling constants (J_{HH}, Hz) and ^{13}C coupling constants (J_{CF}, Hz) are reported as: chemical shift, multiplicity (br = broad, s = singlet, d = doublet, t = triplet, q = quartet, m = multiplet, dd = doublet of doublets, ddd = doublet of doublet of doublets, dq = doublet of quartets, dt = doublet of triplets, ddt = doublet of doublet of triplets), coupling constant, and integration. High Resolution Mass Spectra (HRMS) were obtained at the Mass Spectrometry Laboratory at the University of Kansas on a Micromass LCT Premier. Thin layer chromatography (TLC) was performed on EMD aluminum-backed (0.20 mm) silica plates (60 F-254) and visualized with a UV lamp. Flash chromatography used ICN silica gel (200-400 mesh). Preparative HPLC was performed with an Agilent 1290 Infinity II instrument equipped with a Hamilton PRP-1 reverse phase column (250 mm length, 21.2 mm ID, 7 μm particle size) with detection of absorbance at 215 and 254 nm. All non-aqueous reactions were carried out using flame- or oven-dried glassware under an atmosphere of dry argon or nitrogen. Absorbance spectra were obtained using a semimicro (1.4 mL) UV quartz cuvette (Sigma-Aldrich, Z27667-7) on an Agilent 8452A diode array spectrometer. Fluorescence spectra were acquired using a SUPRASIL ultra-micro quartz cuvette (PerkinElmer, B0631079) on a Perkin-Elmer LS55 Fluorescence Spectrometer (10 nm slit width). Melting points were acquired using a Bibby scientific SMP10 melting point apparatus and are uncorrected. Infrared spectra (IR) were recorded

with a Shimadzu GladiATR 10 Single Reflection ATR accessory. All commercial reagents and solvents were used as received unless otherwise noted. Yields are reported based on isolated material. Pyronin B (**68**) was purchased from Combi-Blocks as the HCl salt. 3,6-Bis(diethylamino)-2,7-difluoro-9*H*-xanthen-9-one (**74**),[39] 2,2',4,4',5,5'-hexafluorobenzophenone (**73**),[39] and 3,6-bis(trifluoromethanesulfonate)xanthone (**78**)[40] were synthesized as previously reported.

Synthetic procedures and compound characterization data

General procedure A

The corresponding 3,6-diaminosubstituted benzophenone (9.00 mmol), KOH (10 M, 12.0 mL, 120 mmol), and DMSO (12 mL) were refluxed at 120 °C for 12 h. The resulting mixture was cooled to room temperature and subsequently placed in an ice bath for 1 h. The contents were further diluted with ice cold water (100 mL), and the resulting solid was collected by vacuum filtration. The crude solid was purified via recrystallization with CH_2Cl_2/hexanes.

General Procedure B

Step 1 - The corresponding 3,6-diaminosubstituted xanthone (0.314 mmol), 3.33 equivalents of borane dimethyl sulfide (1.04 mmol), and THF (5.00 mL) were added to a round bottom flask and refluxed at 70 °C until starting material was consumed by TLC. When the reaction was complete, the flask was allowed to cool to room temperature. Methanol (5 mL) was added to quench the reaction. The solvent was removed under reduced pressure and the contents of the flask were passed through a silica gel plug (25

g of silica) in which the silica gel had been pretreated with a mixture of 25 mL CH_2Cl_2, and 2 mL trimethylamine using CH_2Cl_2 containing trimethylamine (0.1%) as the eluent. The solvent was removed under reduced pressure and placed under high vacuum (0.1 mmHg) to remove all residual volatiles. The resulting solid material (xanthene) is unstable and slowly decomposes into the pyronin product, a process which is considerably accelerated by the use of DDQ as described in step 2.

Step 2 -The solid material from the previous step was dissolved in CH_2Cl_2 (7 mL) and treated with DDQ (0.377 mmol). The resulting mixture was stirred at 26 °C and monitored by TLC. Upon completion, trifluoroacetic acid (1 mL) was added to the reaction mixture and the resulting mixture was stirred for an additional 5 min. Volatiles were removed under reduced pressure. CH_2Cl_2 (7 mL) was added and the crude pyronin was stirred at room temperature for 1 h. The slurry was filtered under vacuum and the solid residue was washed with CH_2Cl_2 (5 mL). The filtrate was concentrated under reduced pressure. The residue was crystallized/recrystallized using toluene. During this process, the compound was vacuum filtered while dissolved in hot toluene to remove any insoluble impurities. The toluene filtrate was reheated to dissolve all solid material, slowly cooled, and allowed to stand at room temperature for 24-48 h before the pure pyronin crystals were recovered by vacuum filtration.

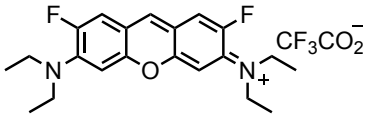

2.7-Difluoropyronin B
(**69**)

***N*-(6-(Diethylamino)-2,7-difluoro-3*H*-xanthen-3-ylidene)-*N*-ethylethanaminium 2,2,2-trifluoroacetate** (**2,7-Difluoropyronin B trifluoroacetate**, **69**). Using general

procedure B with a reaction time of 1.5 h for step 1 and 1.5 h for step 2, xanthone **73** was converted into pyronin **69**. Pure crystals of **3** (147 mg, 92%) were obtained. m.p. 53-35 °C; ^{1}H NMR (400 MHz, $CDCl_3$) δ 8.61 (s, 1H), 7.54 (d, *J* = 14.3 Hz, 2H), 6.93 (d, *J* = 7.4 Hz, 2H), 3.67 (q, *J* = 7.0 Hz, 8H), 1.36 (t, *J* = 7.1 Hz, 12H); ^{13}C NMR (101 MHz, $CDCl_3$) δ 160.3 (d, $J_{C, F}$ = 38 Hz, ArC_2-F, ArC_7-F), 155.1, 151.9, 149.4, 147.9 (d, $J_{C, F}$ = 11 Hz, ArC_6-N), 145.4, 117.59, 116.4 (d, $J_{C, F}$ = 26 Hz, ArC_8), 114.7, 114.4 (d, $J_{C, F}$ = 10 Hz, ArC_1), 99.9 (d, $J_{C, F}$ = 5.4 Hz, ArC_4, ArC_5), 48.4, 13.2; IR (thin film) 2985, 2870, 1728, 1605, 1466, 1281, 1134, 1072 cm^{-1}; HRMS (ESI) m/z 359.1915 (M^+, $C_{21}H_{25}F_2N_2O$ requires 359.1935).

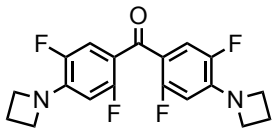

75

Bis(4-(azetidin-1-yl)-2,5-difluorophenyl)methanone (75). 2, 2', 4, 4', 5, 5'-hexafluorobenzophenone (**73**, 2.50 g, 8.61 mmol), azetidine hydrochloride (2.34 g, 25.0 mmol), *N*,*N*-diisopropylethylamine (5.23 mL, 30.0 mmol), and acetonitrile (15 mL), were combined in a sealed tube and heated at 100 °C for 12 h. The resulting solution was concentrated under reduced pressure and the residue dissolved in CH_2Cl_2 (50 mL) and extracted with aq. HCl (1 M, 3 x 50 mL). The organic fraction was dried (anhydrous Na_2SO_4) and the solvent was removed under reduced pressure. The residue was recrystallized using CH_2Cl_2/hexane to provide 2.78 g (85%) of colorless crystals of benzophenone **75**. m.p. 155-157 °C; ^{1}H NMR (400 MHz, $CDCl_3$) δ 7.27 (dd, *J* = 13.0, 6.0 Hz, 2H), 5.97 (dd, *J* = 11.7, 7.2 Hz, 2H), 4.22–4.10 (m, 8H), 2.53–2.26 (m, 4H); ^{13}C NMR (101 MHz, $CDCl_3$) δ 185.3 (C=O), 158.8 (d, $J_{C, F}$ = 249 Hz, ArC_6-F), 147.5 (d, *J* = 238 Hz,

ArC_2-F), 143.8 (m, ArC_4-F), 117.3 (dd, $J_{C,F}$ = 22, 4.5 Hz, ArC_5-F), 115.8 (m, ArC_1-F), 99.5 (dd, $J_{C,F}$ = 29, 5.1 Hz, ArC_3-F), 53.6 (NCH_2), 17.6 (CH_2); IR (thin film) 2949, 2876, 1618, 1589, 1450, 1375, 1159, 895, 742 cm^{-1}; HRMS (ESI) m/z 387.1070 ($M+Na^+$, $C_{19}H_{16}F_4N_2ONa$ requires 387.1096).

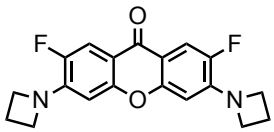

76

3,6-Di(azetidin-1-yl)-2,7-difluoro-9H-xanthen-9-one (76). Using general procedure A, benzophenone **75** was converted into **76.** After recrystallization, colorless crystals (2.68 g, 87%) of xanthone **76** were collected. m.p. 261-263 °C; ^1H NMR (400 MHz, $CDCl_3$) δ 7.69 (d, *J* = 12.6 Hz, 2H), 6.09 (d, *J* = 7.3 Hz, 2H), 4.23–4.00 (m, 8H), 2.51–2.27 (m, 4H); ^{13}C NMR (101 MHz, $CDCl_3$) δ 174.2 (C=O), 154.0 (ArC-O), 149.1 (d, $J_{C,F}$ = 242 Hz, ArC_2-F, ArC_7-F), 144.6 (d, $J_{C,F}$ = 14 Hz, ArC_3-N, ArC_6-N), 111.6 (d, $J_{C,F}$ = 6.3 Hz, ArC_1, ArC_8), 111.21 (d, $J_{C,F}$ = 21 Hz, ArC_{8a}, ArC_{10a}), 98.9 (d, $J_{C,F}$ = 4.8 Hz, ArC_4, ArC_5), 53.7, 17.6; IR (thin film) 2953, 2884, 1618, 1530, 1464, 1352, 1252, 775 cm^{-1}; HRMS (ESI) m/z 365.1084 ($M+Na^+$, $C_{19}H_{16}F_2N_2O_2Na$ requires 365.1078).

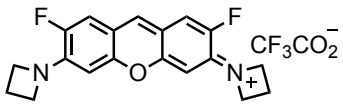

2,7-Difluoropyronin azetidine
(**72**)

1-(6-(Azetidin-1-yl)-2,7-difluoro-3*H*-xanthen-3-ylidene)azetidin-1-ium 2,2,2-trifluoroacetate (**2,7-Difluoropyronin azetidine trifluoroacetate**, **72**). Using general procedure B with a reaction time of 84 h for step 1 and 4 h for step 2, xanthone **76** was converted into pyronin **72**. Pure crystals (114 mg, 76%) of **72** were obtained. m.p. >

300 °C; ^{1}H NMR (400 MHz, $CDCl_3$) δ 8.41 (s, 1H), 7.35 (d, *J* = 11.6 Hz, 2H), 6.39 (d, *J* = 7.0 Hz, 2H), 4.75–4.11 (br, 8H), 2.76–2.40 (m, 4H); ^{13}C NMR (101 MHz, $CDCl_3$) δ ^{13}C NMR (101 MHz, Chloroform-*d*) δ 160.5 (d, $J_{C, F}$ = 37 Hz, ArC_2-F, ArC_7-F), 154.8, 151.5, 149.0, 147.7 (d, $J_{C, F}$ = 15 Hz, ArC_6-N), 145.6, 114.8 (d, $J_{C, F}$ = 21 Hz, ArC_8), 114.0 (d, $J_{C, F}$ = 9.3 Hz, ArC_1), 96.8 (d, $J_{C, F}$ = 5.4 Hz, ArC_4, ArC_5), 17.1, 1.0; IR (thin film) 3047, 2951, 2874, 1659, 1614, 1504, 1362, 1287, 1180, 621 cm^{-1}; HRMS (ESI) m/z 327.1292 (M^+, $C_{19}H_{17}F_2N_2O$ requires 327.1309).

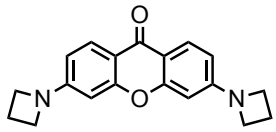

79

3,6-Di(azetidin-1-yl)-9H-xanthen-9-one (79). Acetonitrile (10 mL), KOH (10 M, 0.95 mL, 9.5 mmol), azetidine hydrochloride salt (0.936 g, 10.0 mmol), and 3,6-bis(trifluoromethanesulfonate)xanthone (**78**, 0.492 mg, 1.00 mmol)[40] were combined in a sealed tube vessel and heated to 180 °C for 12 h. Once cooled to 70 °C, the resulting slurry was filtered while hot under vacuum and the solid residue was washed with of MeOH in CH_2Cl_2 (1:9, 50 mL). The combined filtrate was concentrated under reduced pressure and the resulting residue was purified via column chromatography (3% MeOH in CH_2Cl_2 as the eluent). After removal of solvent under reduced pressure, the solid residue was recrystallized from DMSO; the crystals were washed with of cold water (50 mL) to remove trace amounts of DMSO. Colorless needle crystals of pure **79** (64 mg, 21%) were collected; ^{1}H NMR (400 MHz, $CDCl_3$) δ 7.91 (d, *J* = 8.7 Hz, 2H), 6.22 (dd, *J* = 8.7, 2.2 Hz, 2H), 6.01 (d, *J* = 2.2 Hz, 2H), 3.97–3.81 (m, 8H), 2.41-2.20 (m, 4H); ^{13}C NMR (101 MHz, $CDCl_3$) δ 175.8, 158.0, 155.3, 127.4, 111.8, 107.9, 95.4, 51.4, 16.3; IR (thin

film) 3047, 2963, 2855, 1597, 1435, 1343, 1258, 1088, 1018, 795 cm^{-1}; HRMS (ESI) m/z 307.1458 ($M+H^+$, $C_{19}H_{19}F_2N_2O_2$ requires 307.1447).

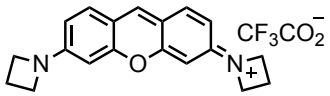

Pyronin azetidine
(**71**)

1-(6-(Azetidin-1-yl)-3*H*-xanthen-3-ylidene)azetidin-1-ium 2,2,2-trifluoroacetate (Pyronin azetidine trifluoroacetate, 71). Using general procedure B, the xanthene intermediate was formed after a reaction time of 3 h for step 1. To avoid decomposition of the final pyronin, it is imperative the xanthene intermediate is recrystallized in CH_2Cl_2/hexanes prior to step 2. The purified xanthene was converted to pyronin **71** using a reaction time of 12 h for step 2. Further purification by reverse phase HPLC provided pure crystals of **71** (65 mg, 47%); ^{1}H NMR (500 MHz, DMSO-d) δ 8.66 (s, 1H), 7.80 (d, *J* = 8.9 Hz, 2H), 6.75 (dd, *J* = 8.9, 2.0 Hz, 2H), 6.46 (d, *J* = 2.1 Hz, 2H), 4.27 (t, *J* = 7.6 Hz, 8H); ^{13}C NMR (126 MHz, DMSO-d) δ 156.9, 156.4, 146.1, 133.4, 113.7, 112.5, 99.8, 51.8, 15.4; HRMS (ESI) m/z 291.1487 (M^+, $C_{19}H_{19}N_2O$ requires 291.1497).

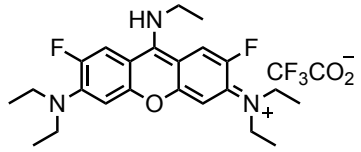

9-Ethylamino difluoropyronin B
(**70**)

N-(6-(diethylamino)-9-(ethylamino)-2,7-difluoro-3H-xanthen-3-ylidene)-N-ethylethanaminium 2,2,2-trifluoroacetate (9-Ethylamino difluoropyronin B, 70). To a flame dried round bottom flask was added xanthone 7 (200 mg, 0.540 mmol). The flask was sealed and placed under argon. Acetonitrile (5.0 mL) was added and the resulting

suspension was treated dropwise with trifilate anhydride (110 µL, 0.650 mmol). The dark purple mixture was stirred for 20 min, during which all of the remaining solid solubilized. A solution of aqueous ethylamine (70% w/w, 1.00 mL, 12.6 mmol) was added dropwise. The mixture was stirred for 10 min and the resulting yellow/green solution was diluted with CH_2Cl_2 (20 mL) and extracted with H_2O (3 x 20 mL). The resulting organic fraction was dried (anhydrous Na_2SO_4) and concentrated under reduced pressure. The remaining viscous yellow oil was passed through a plug of silica gel using CH_2Cl_2 to remove any nonpolar impurities followed by TFA:MeOH:CH_2Cl_2 (1:10:89) to elute the product. The solvent was removed under reduced pressure and the residue was crystallized using CH_2Cl_2/Hexanes to provide 237 mg of pure 4 (85%). m.p. 117-118 °C; ^{1}H NMR (400 MHz, DMSO-*d*) δ 9.54 (d, *J* = 5.9 Hz, 1H), 8.30 (d, *J* = 17 Hz, 1H), 7.94 (d, *J* = 17 Hz, 1H), 7.08-6.58 (m, 1H), 4.21–3.89 (m, 2H), 3.70–3.36 (m, 8H), 1.42 (t, *J* = 7 Hz, 3H), 1.20 (d, *J* = 7 Hz, 12H); ^{13}C NMR (126 MHz, DMSO-*d*) δ 158.1 (d, $J_{C,F}$ = 35 Hz, ArC_7-F), 153.91, 153.23, 151.28, 149.3 (d, $J_{C,F}$ = 178 Hz, ArC_2-F), 147.3 (d, $J_{C,F}$ = 176 Hz, ArC_6-N), 143.8 (d, $J_{C,F}$ = 29 Hz, ArC_3-N), 114.8 (d, $J_{C,F}$ = 28 Hz, ArC_8), 111.2 (d, $J_{C,F}$ = 28 Hz, ArC_1), 102.5, 100.0, 46.3, 42.8, 14.2, 12.9; IR (thin film) 3303, 2984, 2941, 1616, 1500, 1198, 799 cm^{-1}; HRMS (ESI) m/z 402.2345 (M^+, $C_{23}H_{30}F_2N_3O$ requires 402.2357).

3.13 Reference

1. Friedman, J. R.; Nunnari, J. Mitochondrial form and function. *Nature* **2014,** 505, 335-343.

2. Logan, A.; Pell, V. R.; Shaffer, K. J.; Evans, C.; Stanley, N. J.; Robb, E. L.; Prime, T. A.; Chouchani, E. T.; Cocheme, H. M.; Fearnley, I. M.; Vidoni, S.; James, A. M.;

Porteous, C. M.; Partridge, L.; Krieg, T.; Smith, R. A.; Murphy, M. P. Assessing the Mitochondrial Membrane Potential in Cells and In Vivo using Targeted Click Chemistry and Mass Spectrometry. *Cell Metab.* **2016,** 23, 379-385.

3. Nunnari, J.; Suomalainen, A. Mitochondria: in sickness and in health. *Cell* **2012,** 148, 1145-1159.

4. Suomalainen, A.; Battersby, B. J. Mitochondrial diseases: the contribution of organelle stress responses to pathology. *Nat. Rev. Mol. Cell Biol.* **2018,** 19, 77-92.

5. Vafai, S. B.; Mootha, V. K. Mitochondrial disorders as windows into an ancient organelle. *Nature* **2012,** 491, 374-383.

6. Johnson, L. V.; Walsh, M. L.; Chen, L. B. Localization of mitochondria in living cells with rhodamine 123. *Proc. Natl. Acad. Sci. U.S.A.* **1979,** 77, 990-994.

7. Meinig, J. M.; Peterson, B. R. Anticancer/antiviral agent Akt inhibitor-IV massively accumulates in mitochondria and potently disrupts cellular bioenergetics. *ACS Chem. Biol.* **2015,** 10, 570-576.

8. Horikoshi, T.; Yoshioka, T.; Kubota, Y.; Yanagisawa, K. Fluorescent dye monitoring of mitochondrial changes associated with malignant cell transformation. *Cell Struct. Funct.* **1987,** 12, 525-537.

9. Forster, S.; Thumser, A. E.; Hood, S. R.; Plant, N. Characterization of rhodamine-123 as a tracer dye for use in in vitro drug transport assays. *PLoS ONE* **2012,** 7, e33253.

10. Mottram, L. F.; Forbes, S.; Ackley, B. D.; Peterson, B. R. Hydrophobic analogues of rhodamine B and rhodamine 101: potent fluorescent probes of mitochondria in living C. elegans. *Beilstein J. Org. Chem.* **2012,** 8, 2156-2165.

11. Deng, X.; Yin, X.; Allan, R.; Lu, D. D.; Maurer, C. W.; Haimovitz-Friedman, A.; Fuks, Z.; Shaham, S.; Kelesnick, R. Ceramide biogenesis is required for radiation-induced apoptosis in the germ line of c. elegans. *Science* **2008,** 322, 110-115.

12. Zheng, H.; Zhan, X. Q.; Bian, Q. N.; Zhang, X. J. Advances in modifying fluorescein and rhodamine fluorophores as fluorescent chemosensors. *Chem. Commun. (Camb.)* **2013,** 49, 429-447.

13. Beija, M.; Afonso, C. A.; Martinho, J. M. Synthesis and applications of Rhodamine derivatives as fluorescent probes. *Chem. Soc. Rev.* **2009,** 38, 2410-2433.

14. Darzynkiewicz, Z.; Kapuscinski, J.; Traganos, F.; Crissman, H. A. Application of pyronin Y(G) in cytochemistry of nucleic acids. *Cytometry A* **1987,** 8, 138-145.

15. Pastierik, T.; Sebej, P.; Medalova, J.; Stacko, P.; Klan, P. Near-infrared fluorescent 9-phenylethynylpyronin analogues for bioimaging. *J. Org. Chem.* **2014,** 79, 3374-3382.

16. Horvath, P.; Sebej, P.; Solomek, T.; Klan, P. Small-molecule fluorophores with large Stokes shifts: 9-iminopyronin analogues as clickable tags. *J. Org. Chem.* **2015,** 80, 1299-1311.

17. Lei, Z.; Yang, Y. A concise colorimetric and fluorimetric probe for sarin related threats designed via the "covalent-assembly" approach. *J. Am. Chem. Soc.* **2014,** 136, 6594-6597.

18. Zhang, H.; Liu, J.; Sun, Y. Q.; Huo, Y.; Li, Y.; Liu, W.; Wu, X.; Zhu, N.; Shi, Y.; Guo, W. A mitochondria-targetable fluorescent probe for peroxynitrite: fast response and high selectivity. *Chem. Commun. (Camb.)* **2015,** 51, 2721-2724.

19. Malek, A.; Thomas, T.; Prasad, E. Visual and Optical Sensing of Hg2+, Cd2+, Cu2+, and Pb2+ in Water and Its Beneficiation via Gettering in Nanoamalgam Form. *ACS Sustainable Chem. Eng.* **2016,** 4, 3497-3503.

20. Kurishita, Y.; Kohira, T.; Ojida, A.; Hamachi, I. Organelle-localizable fluorescent chemosensors for site-specific multicolor imaging of nucleoside polyphosphate dynamics in living cells. *J. Am. Chem. Soc.* **2012,** 134, 18779-18789.

21. Debieu, S.; Romieu, A. Kinetics improvement of protease-mediated formation of pyronin dyes. *Tetrahedron Lett.* **2018,** 59, 1940-1944.

22. Hymel, D.; Woydziak, Z. R.; Peterson, B. R. Detection of protein-protein interactions by proximity-driven S(N)Ar reactions of lysine-linked fluorophores. *J. Am. Chem. Soc.* **2014,** 136, 5241-5244.

23. Childress, E. S.; Alexopoulos, S. J.; Hoehn, K. L.; Santos, W. L. Small Molecule Mitochondrial Uncouplers and Their Therapeutic Potential. *J. Med. Chem.* **2018,** 61, 4641-4655.

24. Tkatch, T.; Greotti, E.; Baranauskas, G.; Pendin, D.; Roy, S.; Nita, L. I.; Wettmarshausen, J.; Prigge, M.; Yizhar, O.; Shirihai, O. S.; Fishman, D.; Hershfinkel, M.; Fleidervish, I. A.; Perocchi, F.; Pozzan, T.; Sekler, I. Optogenetic control of mitochondrial metabolism and Ca(2+) signaling by mitochondria-targeted opsins. *Proc. Natl. Acad. Sci. U.S.A.* **2017,** 114, E5167-E5176.

25. Chalmers, S.; Caldwell, S. T.; Quin, C.; Prime, T. A.; James, A. M.; Cairns, A. G.; Murphy, M. P.; McCarron, J. G.; Hartley, R. C. Selective uncoupling of individual mitochondria within a cell using a mitochondria-targeted photoactivated protonophore. *J. Am. Chem. Soc.* **2012,** 134, 758-761.

26. Wang, H.; Gao, Z.; Liu, X.; Agarwal, P.; Zhao, S.; Conroy, D. W.; Ji, G.; Yu, J.; Jaroniec, C. P.; Liu, Z.; Lu, X.; Li, X.; He, X. Targeted production of reactive oxygen species in mitochondria to overcome cancer drug resistance. *Nat. Commun.* **2018,** 9, 562.

27. Gillis, E. P.; Eastman, K. J.; Hill, M. D.; Donnelly, D. J.; Meanwell, N. A. Applications of Fluorine in Medicinal Chemistry. *J. Med. Chem.* **2015,** 58, 8315-8359.

28. Mottram, L. F.; Boonyarattanakalin, S.; Kovel, R. E.; Peterson, B. R. The Pennsylvania Green fluorophore: a hybrid of Oregon Green and Tokyo Green for the construction of hydrophobic and pH-insensitive molecular probes. *Org. Lett.* **2006,** 8, 581-584.

29. Sun, W.; Gee, K. R.; Haugland, R. P. Synthesis of novel fluorinated coumarins: excellent UV-light exicitable fluorescent dyes. *Bioorg. Med. Chem. Lett.* **1998,** 8, 3107-3110.

30. Grimm, J. B.; English, B. P.; Chen, J.; Slaughter, J. P.; Zhang, Z.; Revyakin, A.; Patel, R.; Macklin, J. J.; Normanno, D.; Singer, R. H.; Lionnet, T.; Lavis, L. D. A general method to improve fluorophores for live-cell and single-molecule microscopy. *Nat. Methods* **2015,** 12, 244-250, 243 p following 250.

31. Grimm, J. B.; Muthusamy, A. K.; Liang, Y.; Brown, T. A.; Lemon, W. C.; Patel, R.; Lu, R.; Macklin, J. J.; Keller, P. J.; Ji, N.; Lavis, L. D. A general method to fine-tune fluorophores for live-cell and in vivo imaging. *Nat. Methods* **2017,** 14, 987-994.

32. Woydziak, Z. R.; Fu, L.; Peterson, B. R. Synthesis of fluorinated benzophenones, xanthones, acridones, and thioxanthones by iterative nucleophilic aromatic substitution. *J. Org. Chem.* **2012,** 77, 473-481.

33. Chen, L. B. Mitochondrial membrane potential in living cells. *Ann. Rev. Cell Biol.* **1988,** 4, 155-181.

34. Cowden, R. R.; Curtis, S. K. Supravital experiments with pyronin Y, a fluorochrome of mitochondria and nucleic acids. *Histochemistry* **1983,** 77, 535-542.

35. Kapuscinski, J.; Darzynkiewicz, Z. Interactions of pyronin Y(G) with nucleic acids. *Cytometry A* **1987,** 8, 129-137.

36. Hoshino, K.; Momiyama, E.; Yoshida, K.; Nishimura, K.; Sakai, S.; Toida, T.; Kashiwagi, K.; Igarashi, K. Polyamine transport by mammalian cells and mitochondria: role of antizyme and glycosaminoglycans. *J. Biol. Chem.* **2005,** 280, 42801-42808.

37. Mandal, S.; Mandal, A.; Park, M. H. Depletion of the polyamines spermidine and spermine by overexpression of spermidine/spermine N(1)-acetyltransferase 1 (SAT1) leads to mitochondria-mediated apoptosis in mammalian cells. *Biochem. J.* **2015,** 468, 435-447.

38. Wu, L.; Burgess, K. Fluorescent amino- and thiopyronin dyes. *Org. Lett.* **2008,** 10, 1779-1782.

39. Woydziak, Z. R.; Fu, L.; Peterson, B. R. Synthesis of fluorinated benzophenones, xanthones, acridones, and thioxanthones by iterative nucleophilic aromatic substitution. *J. Org. Chem.* **2012,** 77, 473-481.

40. Stacko, P.; Sebej, P.; Veetil, A. T.; Klan, P. Carbon-carbon bond cleavage in fluorescent pyronin analogues induced by yellow light. *Org. Lett.* **2012,** 14, 4918-4921.

Appendix A

NMR Spectra

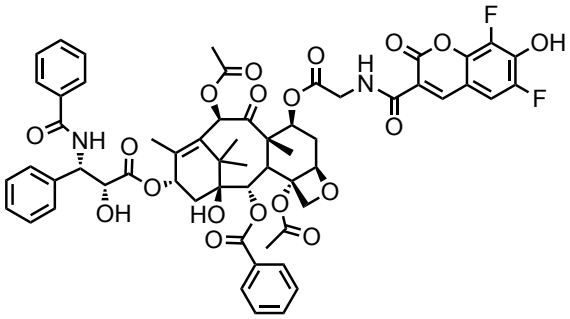

PB-Gly-Taxol
56

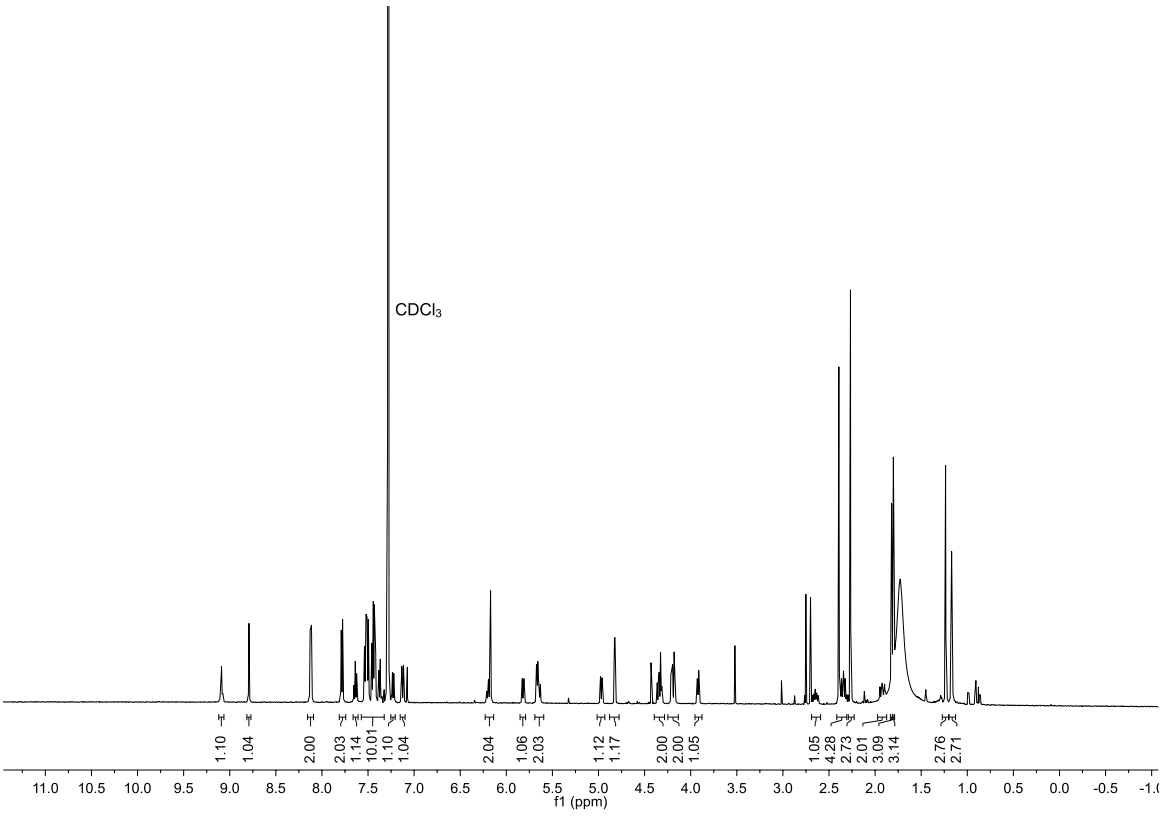

Figure S1. ^{1}H NMR (500 MHz, $CDCl_3$) spectrum of PB-Gly-Taxol (**56**).

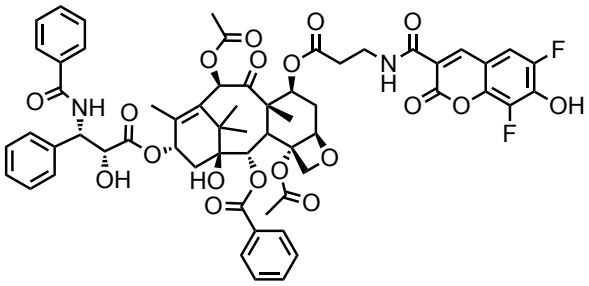

PB-βAla-Taxol
57

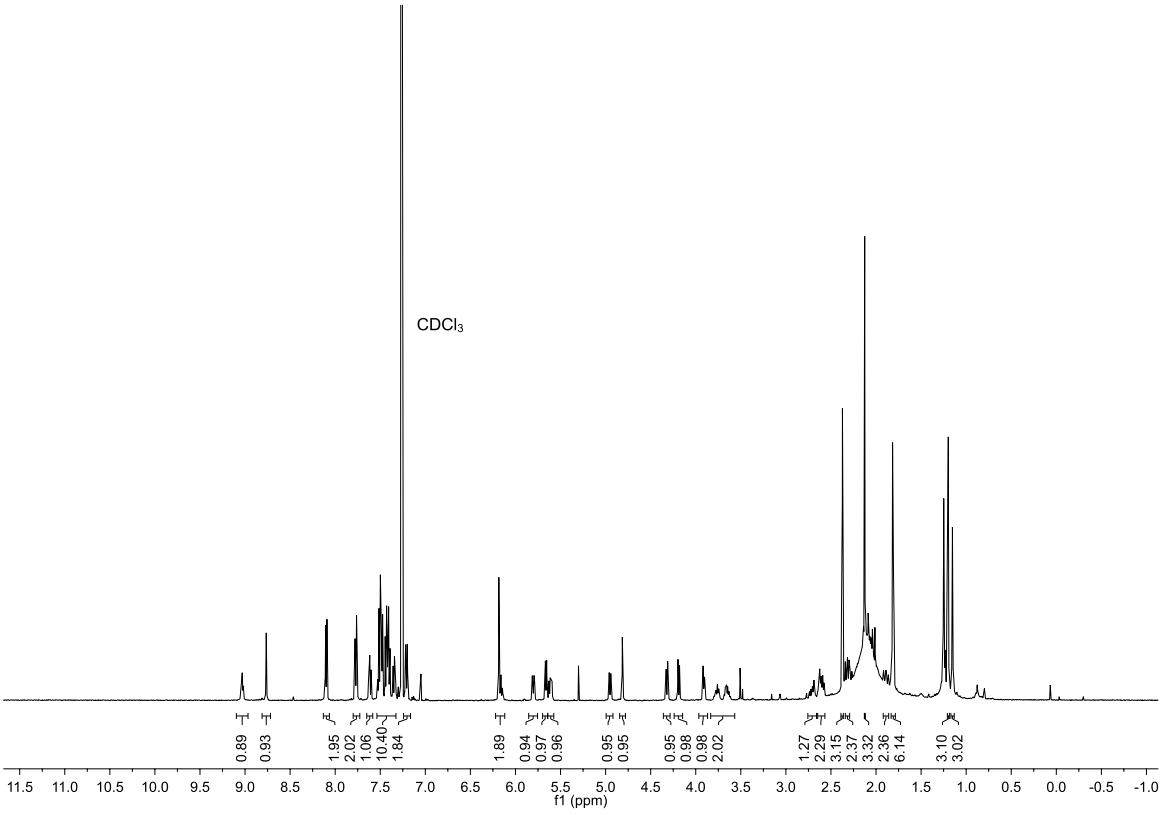

Figure S2. ^{1}H NMR (500 MHz, $CDCl_3$) spectrum of PB-β-Ala-Taxol (**57**).

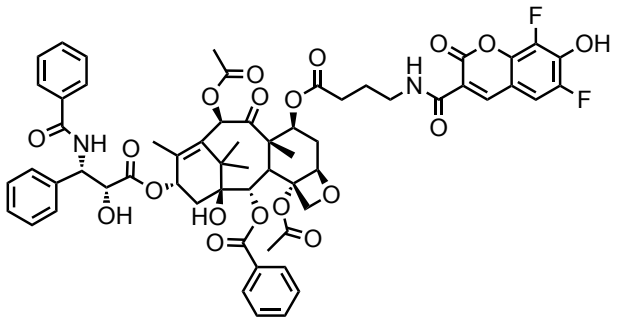

PB-GABA-Taxol
58

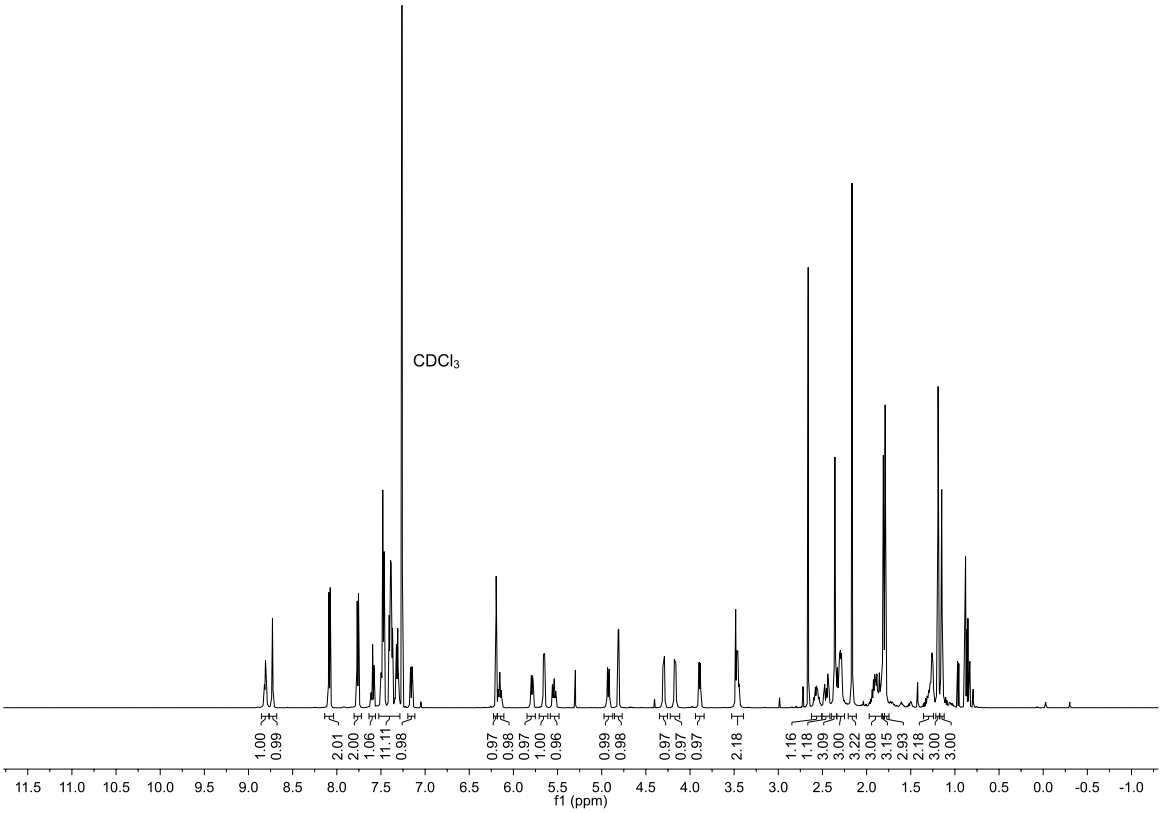

Figure S3. ^{1}H NMR (500 MHz, $CDCl_3$) spectrum of PB-GABA-Taxol (**58**).

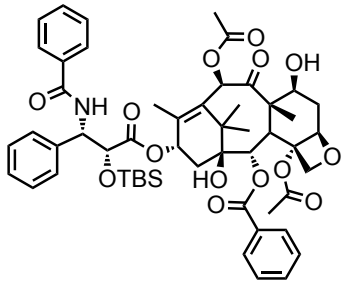

59

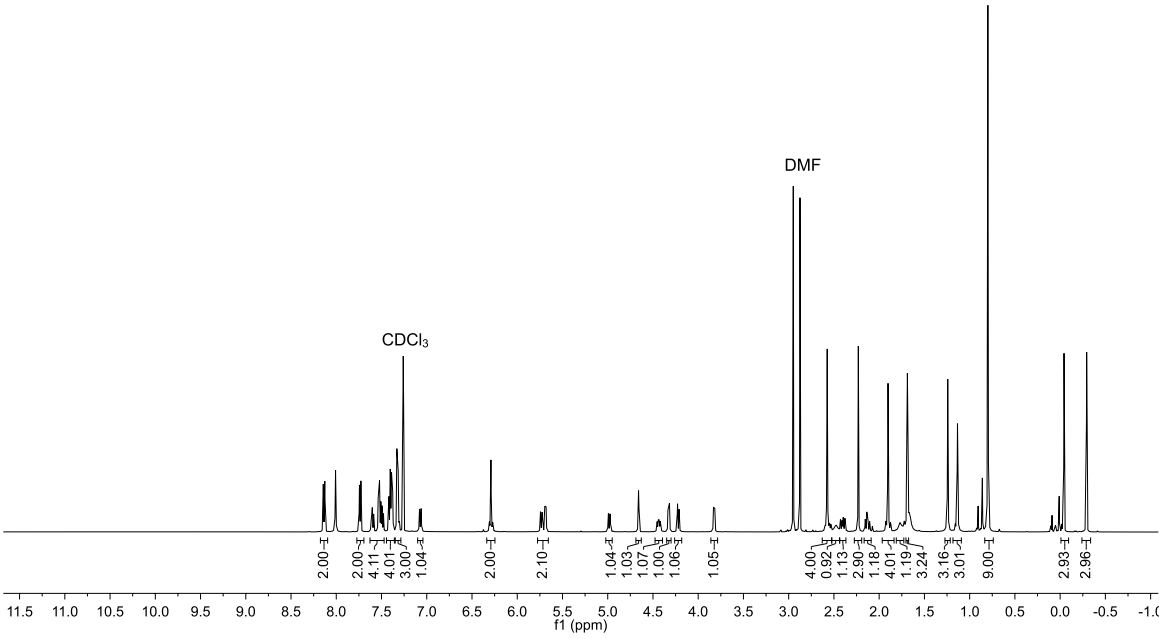

Figure S4. ^{1}H NMR (500 MHz, $CDCl_3$) spectrum of **59**.

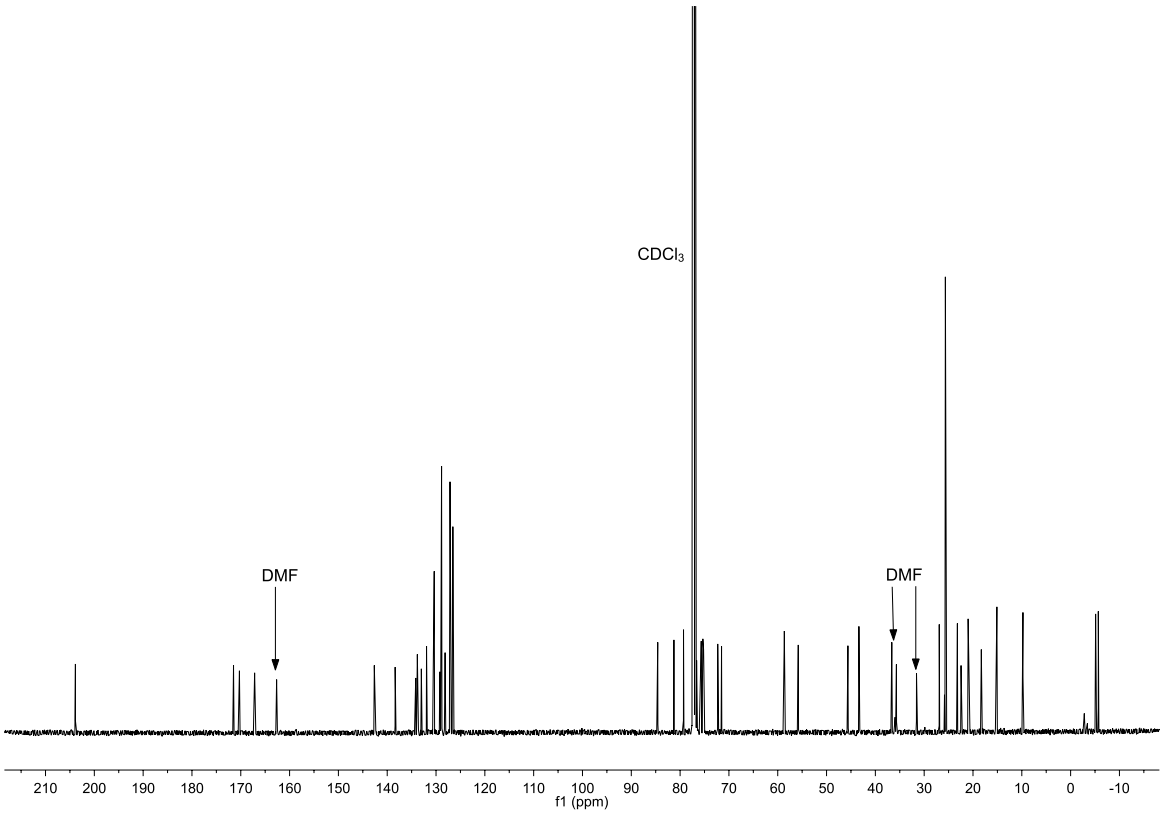

Figure S5. ^{13}C NMR (126 MHz, $CDCl_3$) spectrum of **59**.

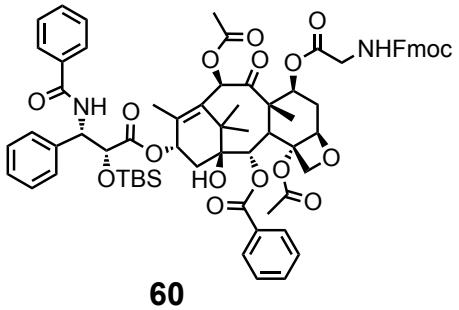

60

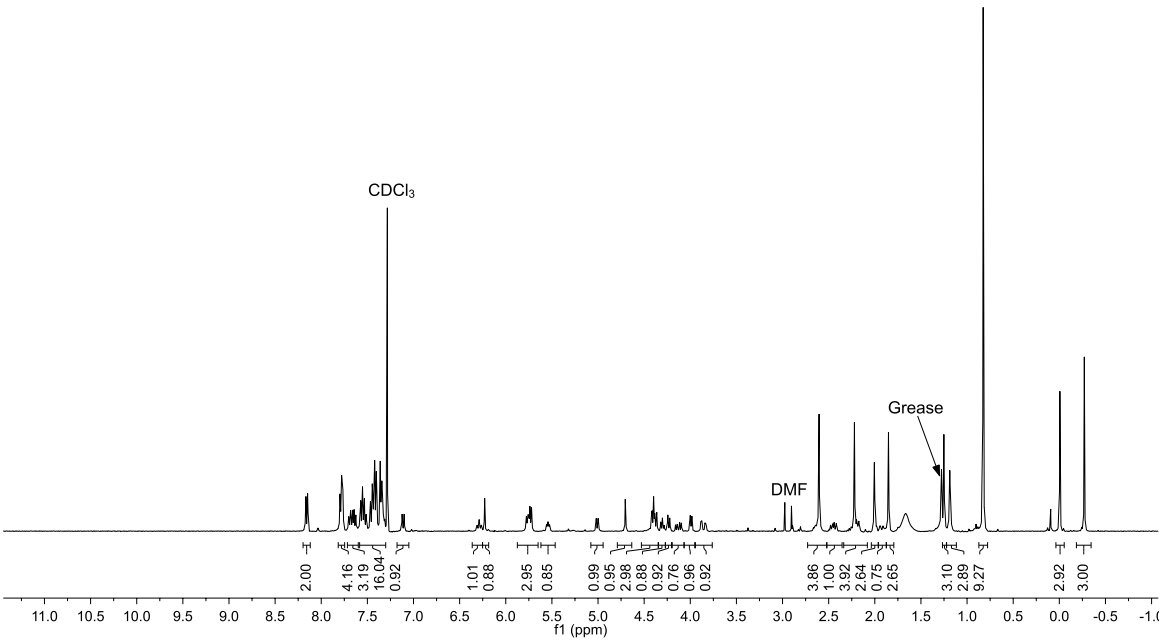

Figure S6. ^{1}H NMR (500 MHz, $CDCl_3$) spectrum of **60**.

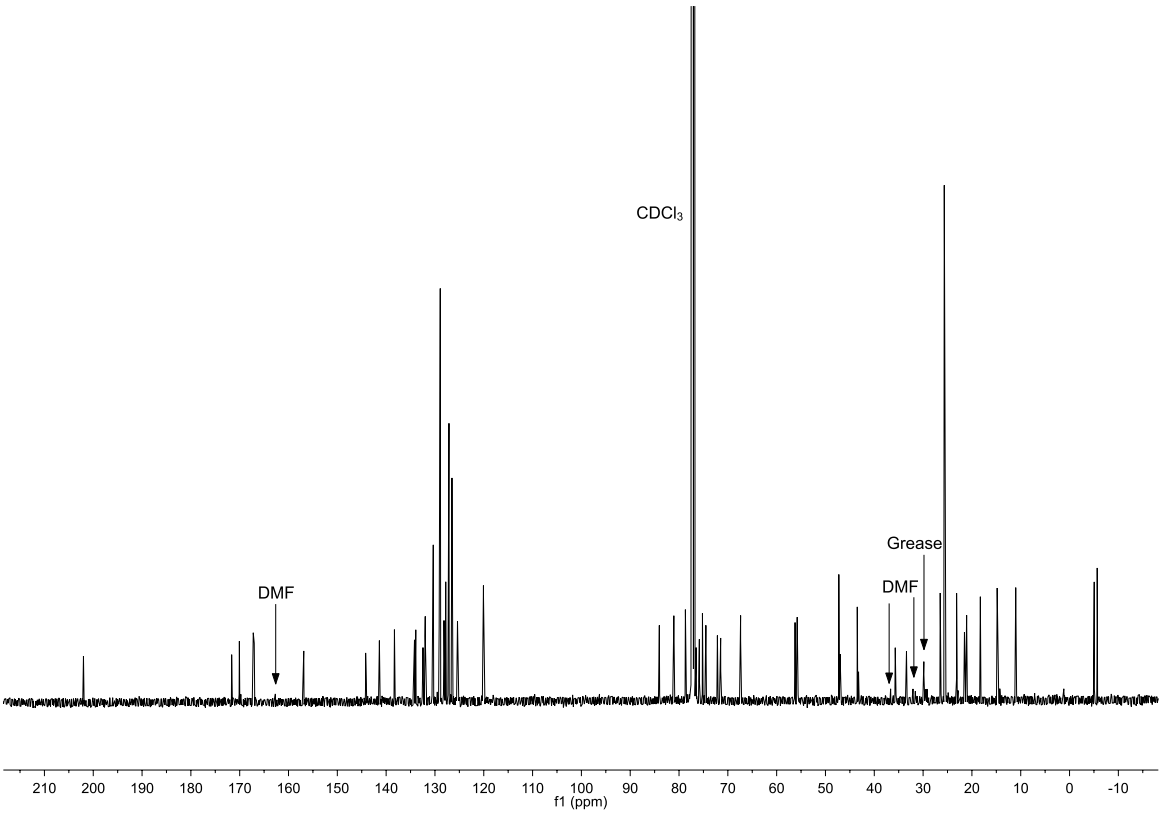

Figure S7. ^{13}C NMR (126 MHz, $CDCl_3$) spectrum of **60.**

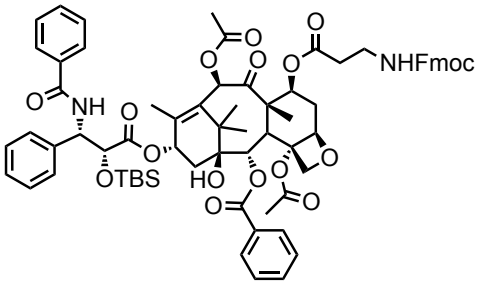

61

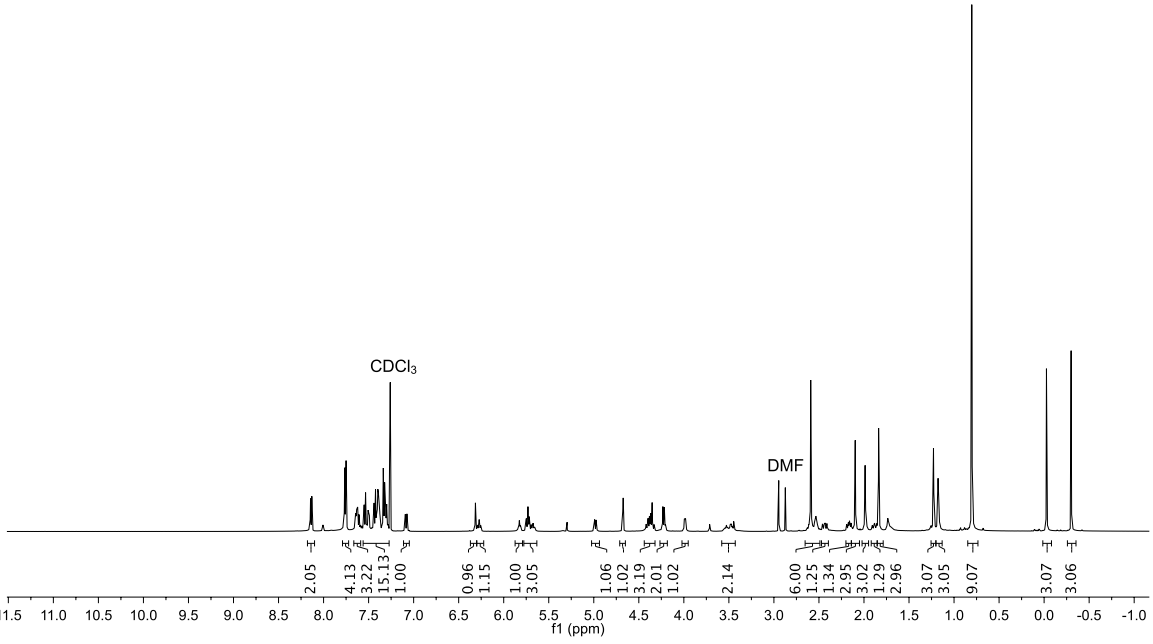

Figure S8. ^{1}H NMR (500 MHz, $CDCl_3$) spectrum of **61**.

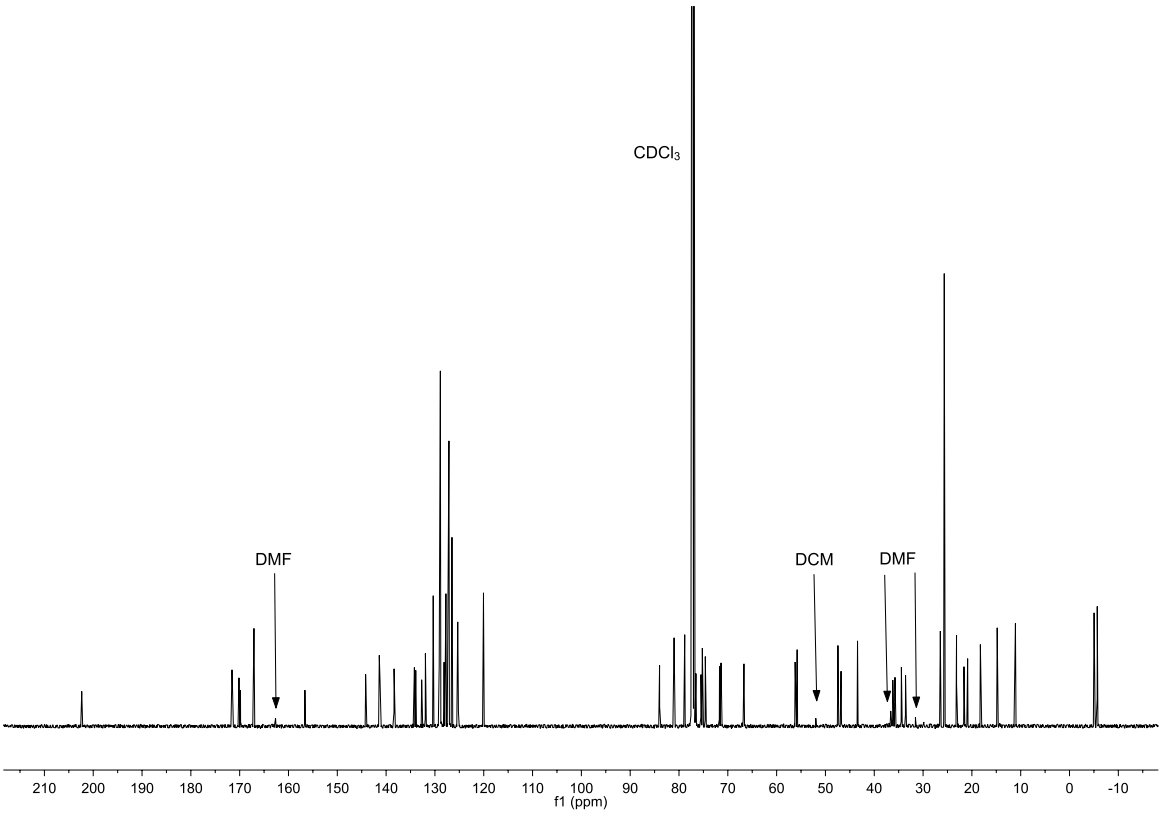

Figure S9. ^{13}C NMR (126 MHz, $CDCl_3$) spectrum of **61**.

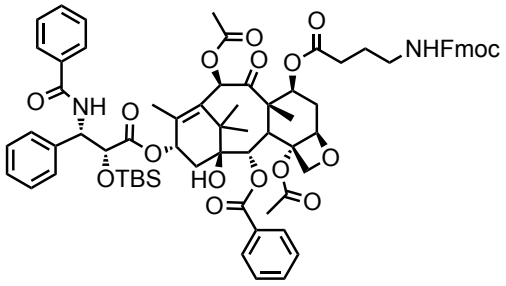

62

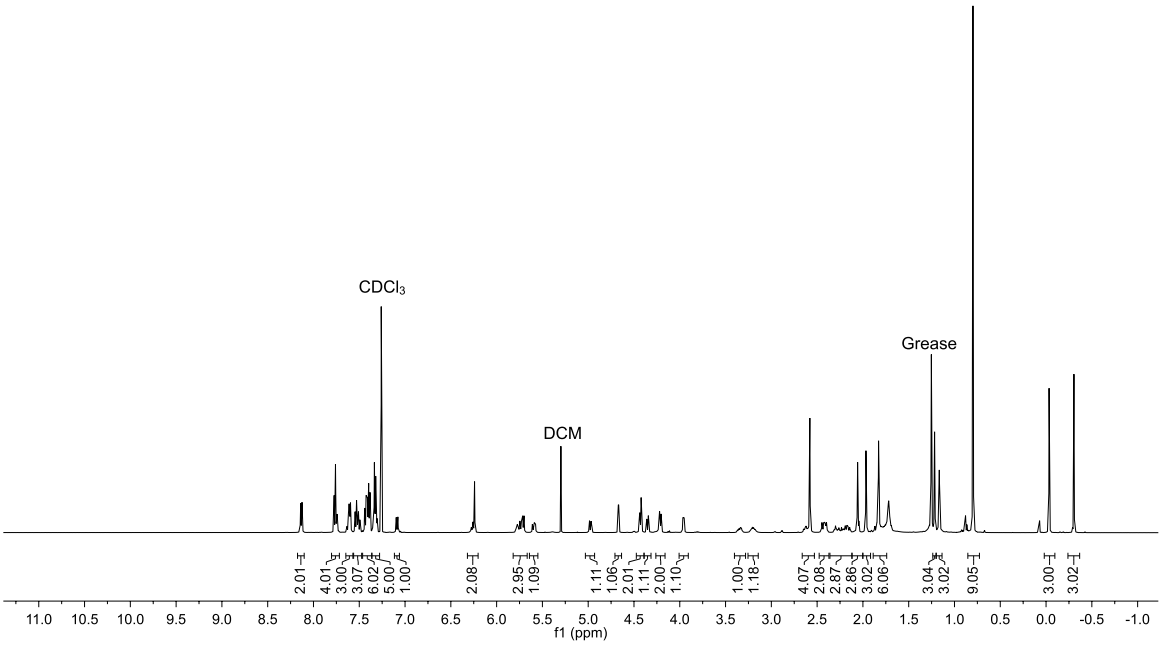

Figure S10. ^{1}H NMR (500 MHz, $CDCl_3$) spectrum of **62**.

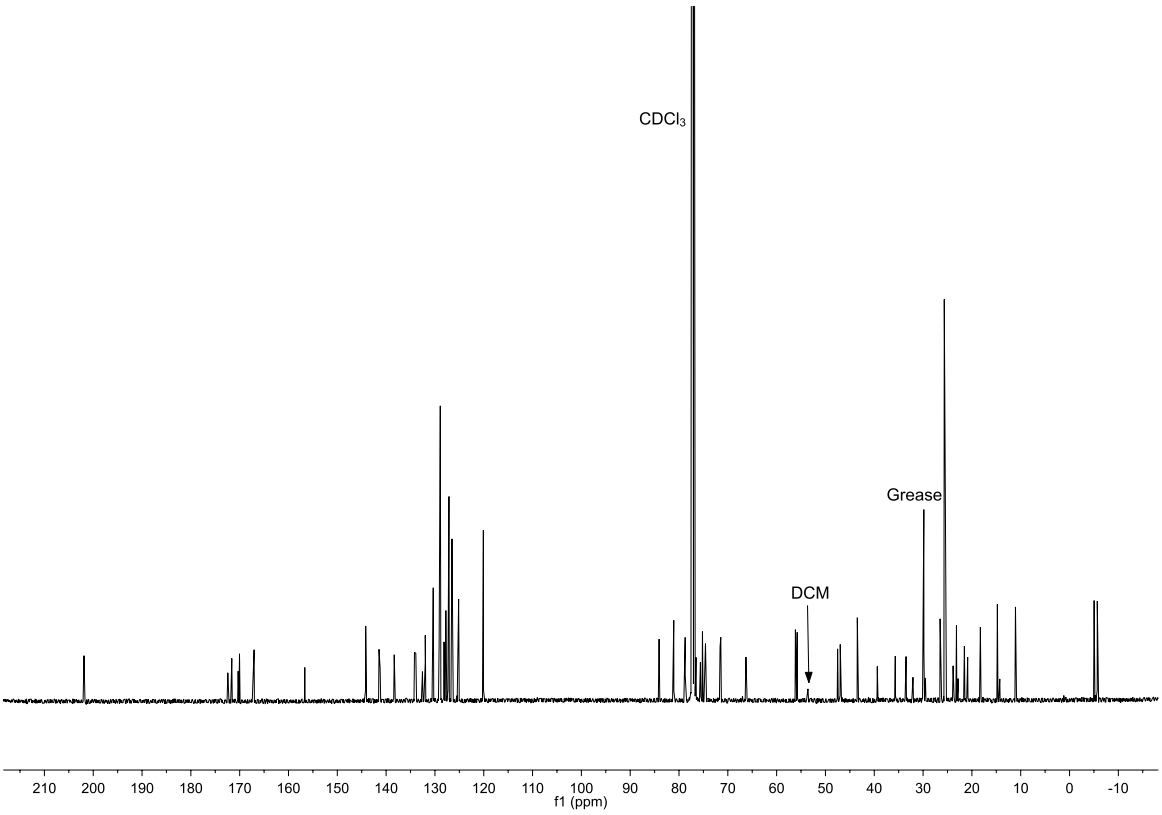

Figure S11. ^{13}C NMR (126 MHz, $CDCl_3$) spectrum of **62**.

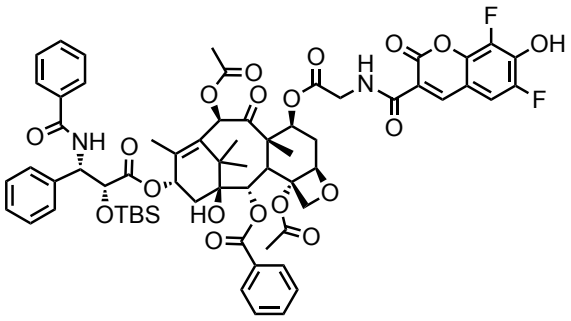

63

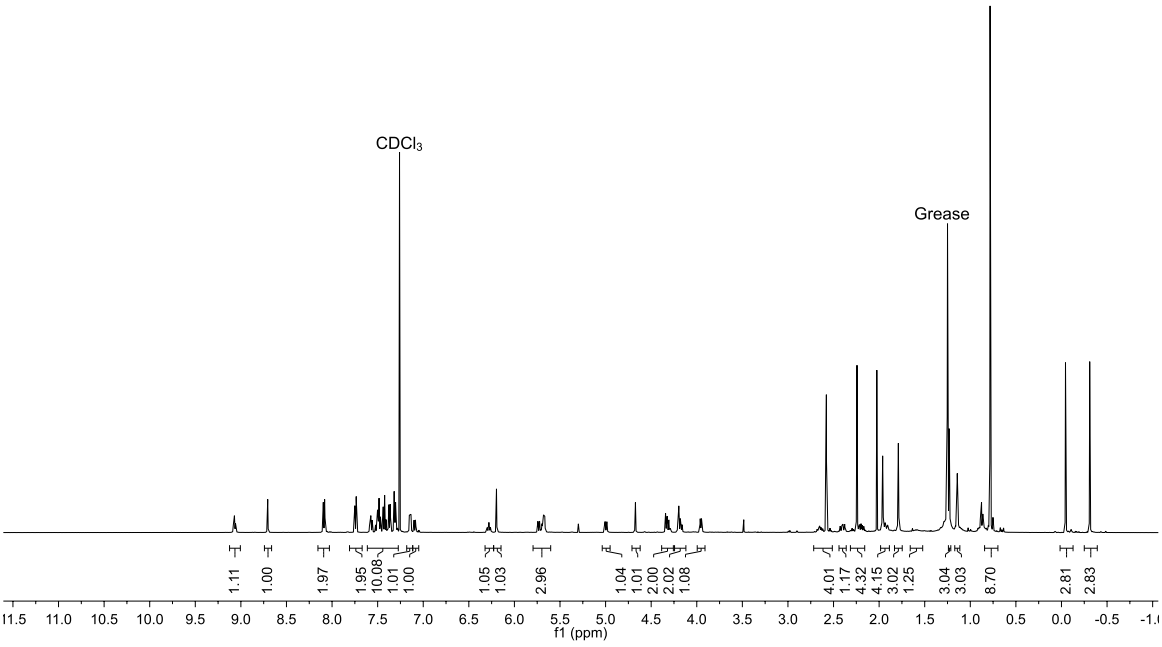

Figure S12. ^{1}H NMR (500 MHz, $CDCl_3$) spectrum of **63**.

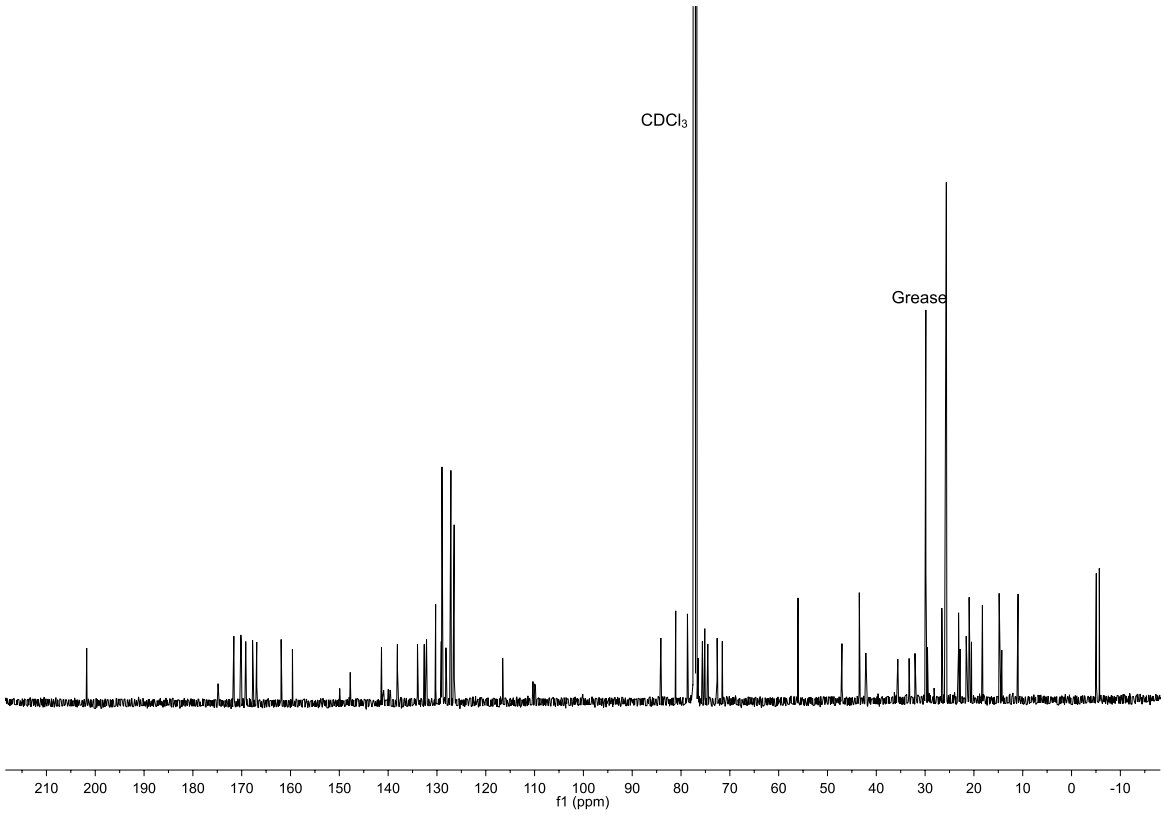

Figure S13. ^{13}C NMR (126 MHz, $CDCl_3$) spectrum of **63**.

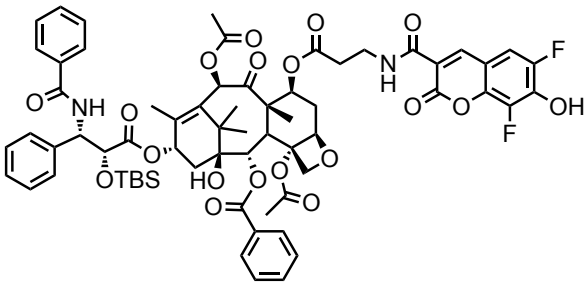

64

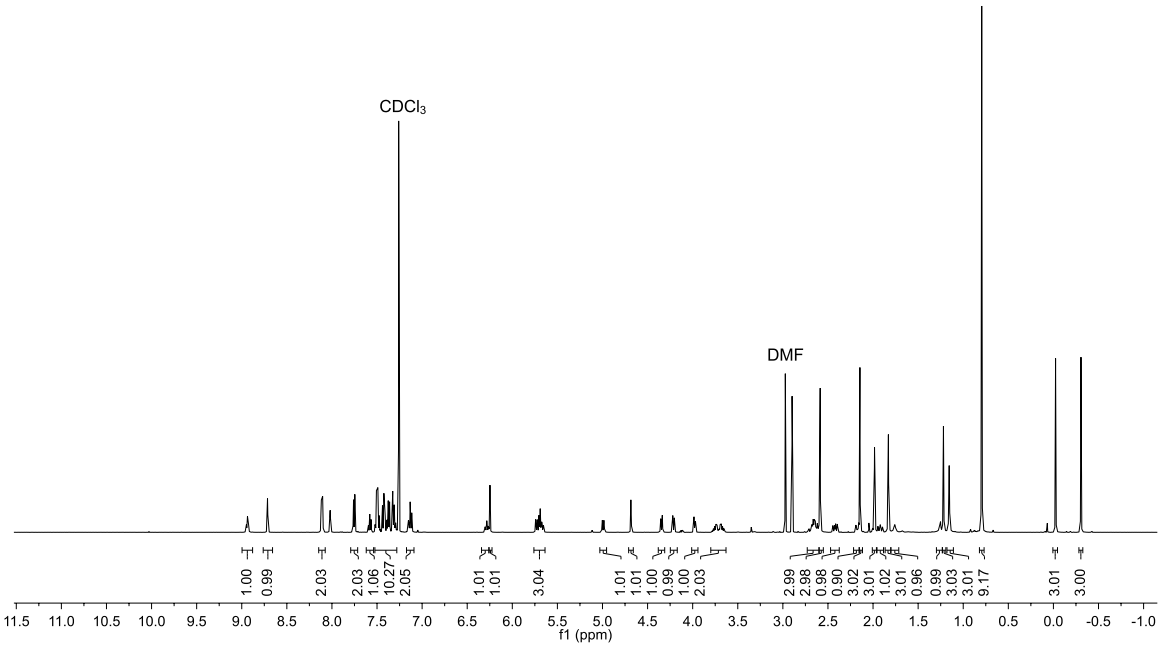

Figure S14. ^{1}H NMR (500 MHz, $CDCl_3$) spectrum of **64**.

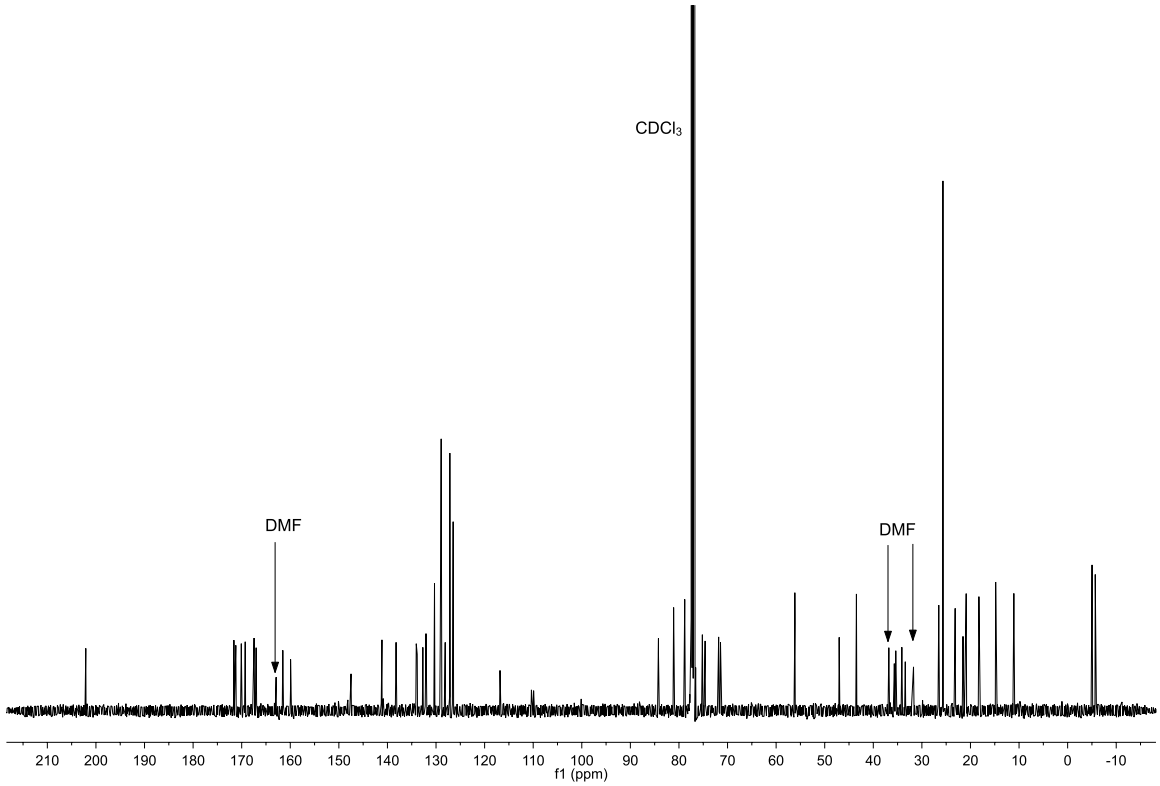

Figure S15. ^{13}C NMR (126 MHz, $CDCl_3$) spectrum of **64**.

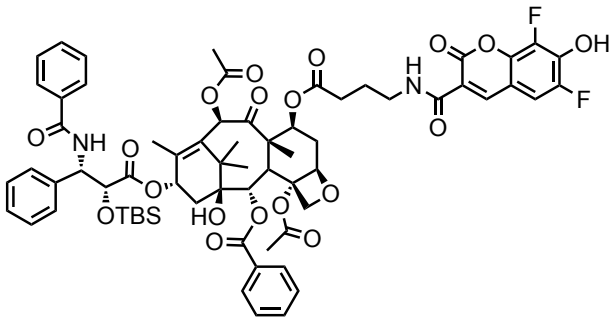

65

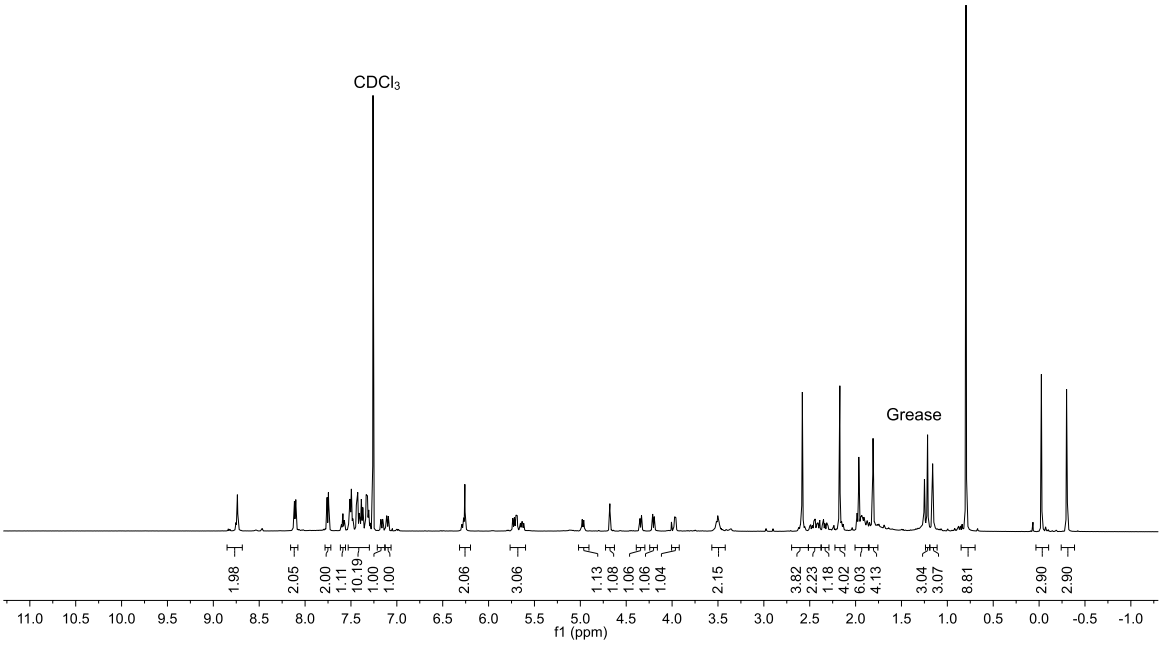

Figure S16. ^{1}H NMR (500 MHz, $CDCl_3$) spectrum of **65**.

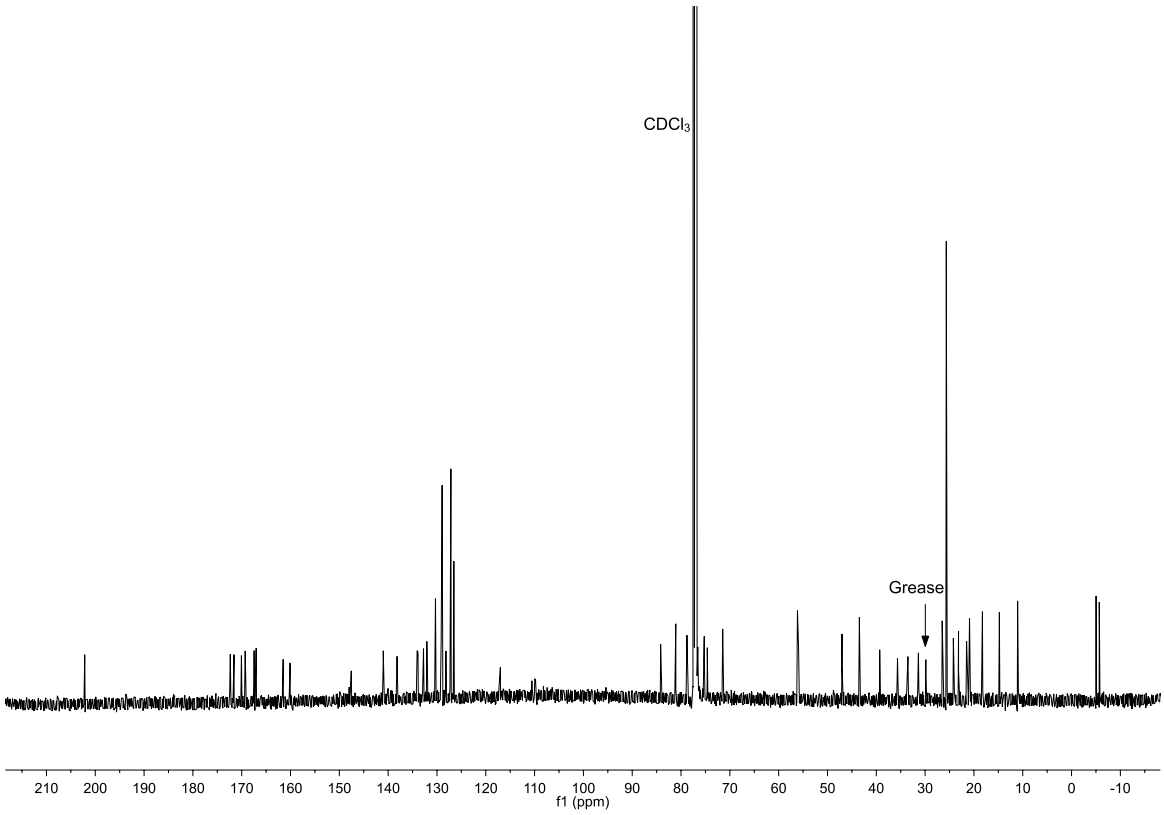

Figure S17. ^{13}C NMR (126 MHz, $CDCl_3$) spectrum of **65**.

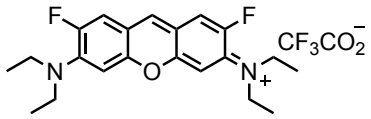

2.7-Difluoropyronin B
(**69**)

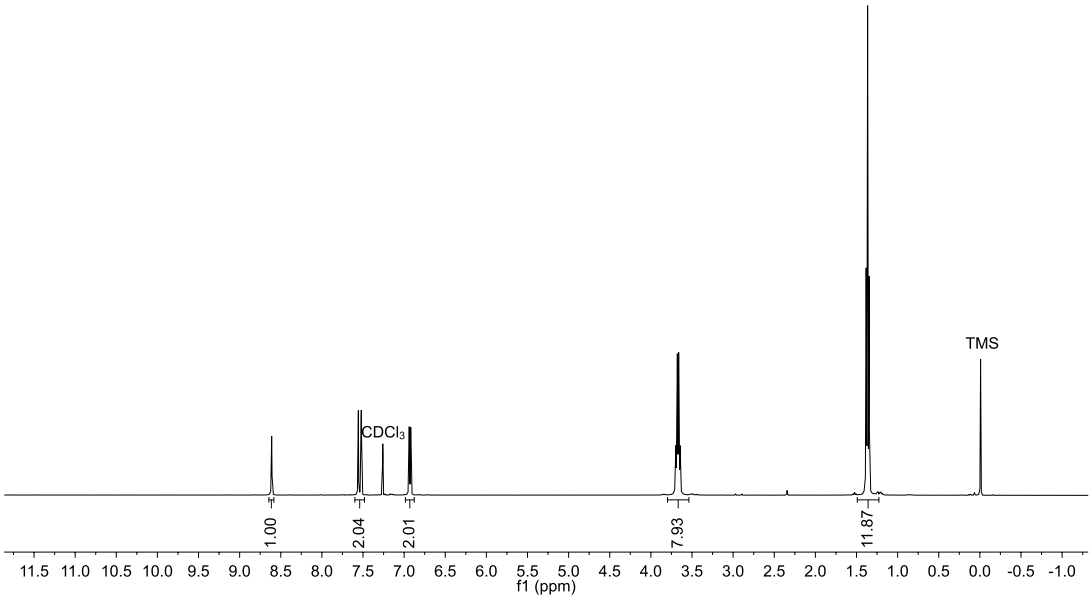

Figure S18. ^{1}H NMR (400 MHz, $CDCl_3$) spectra of **69**.

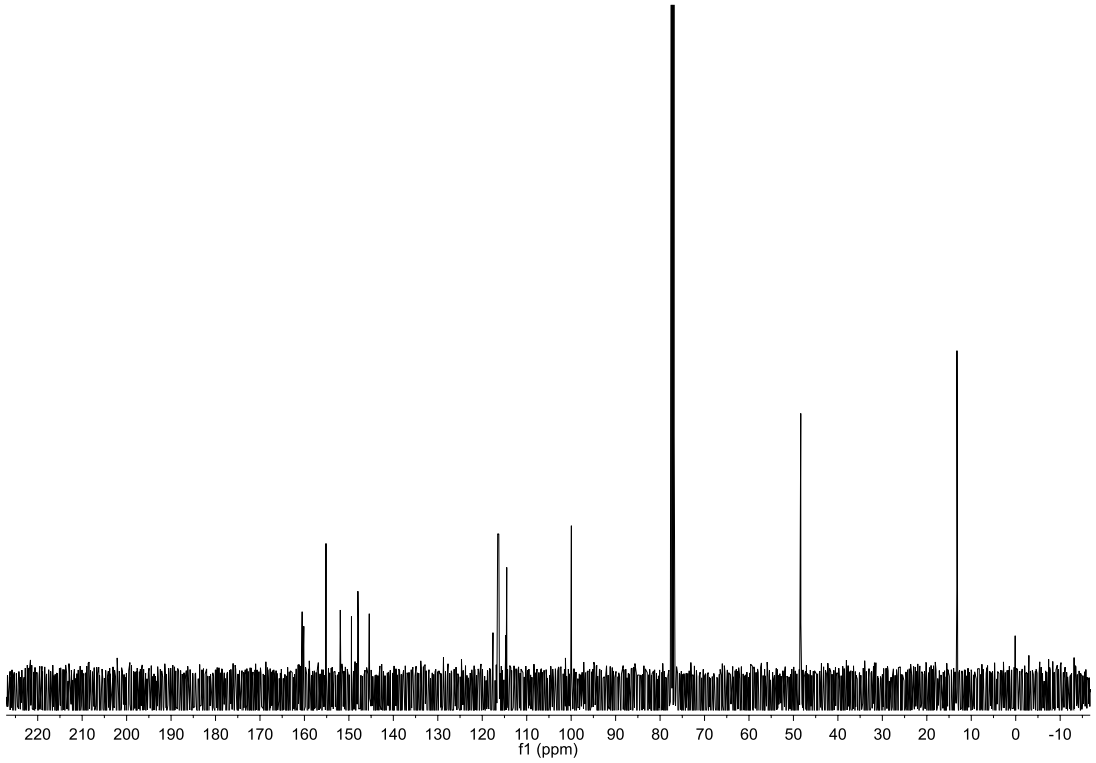

Figure S19. ^{13}C NMR (101 MHz, $CDCl_3$) spectra of **69**.

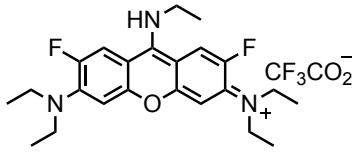

9-Ethylamino difluoropyronin B
(**70**)

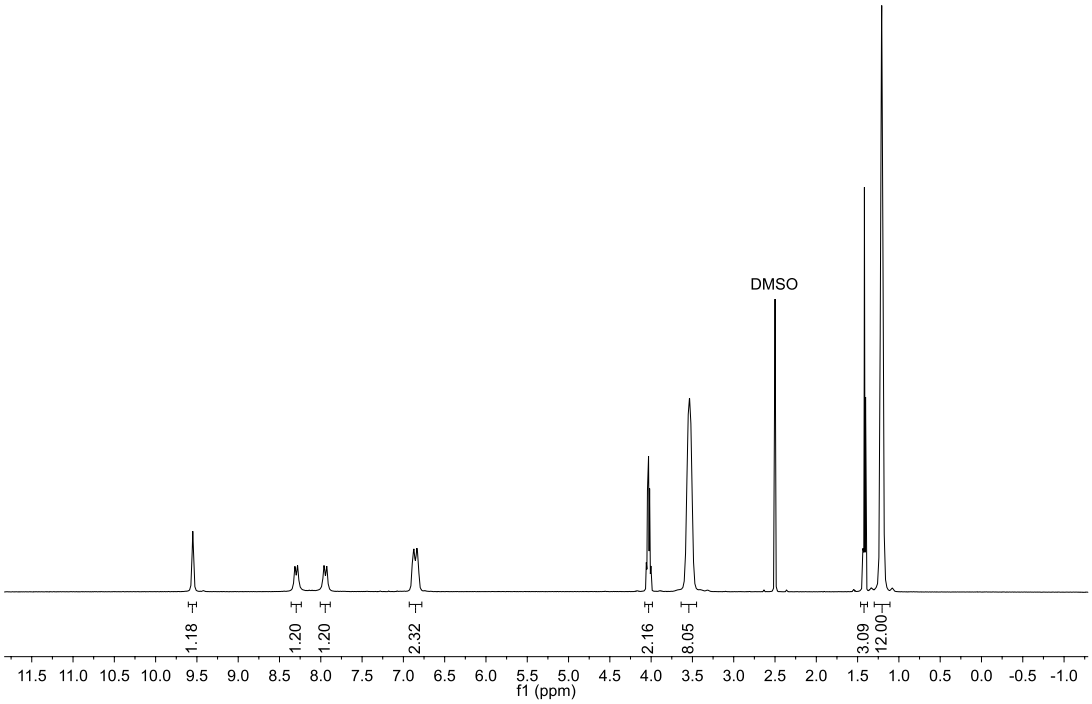

Figure S20. ^{1}H NMR (500 MHz, DMSO-d6) spectra of **70**.

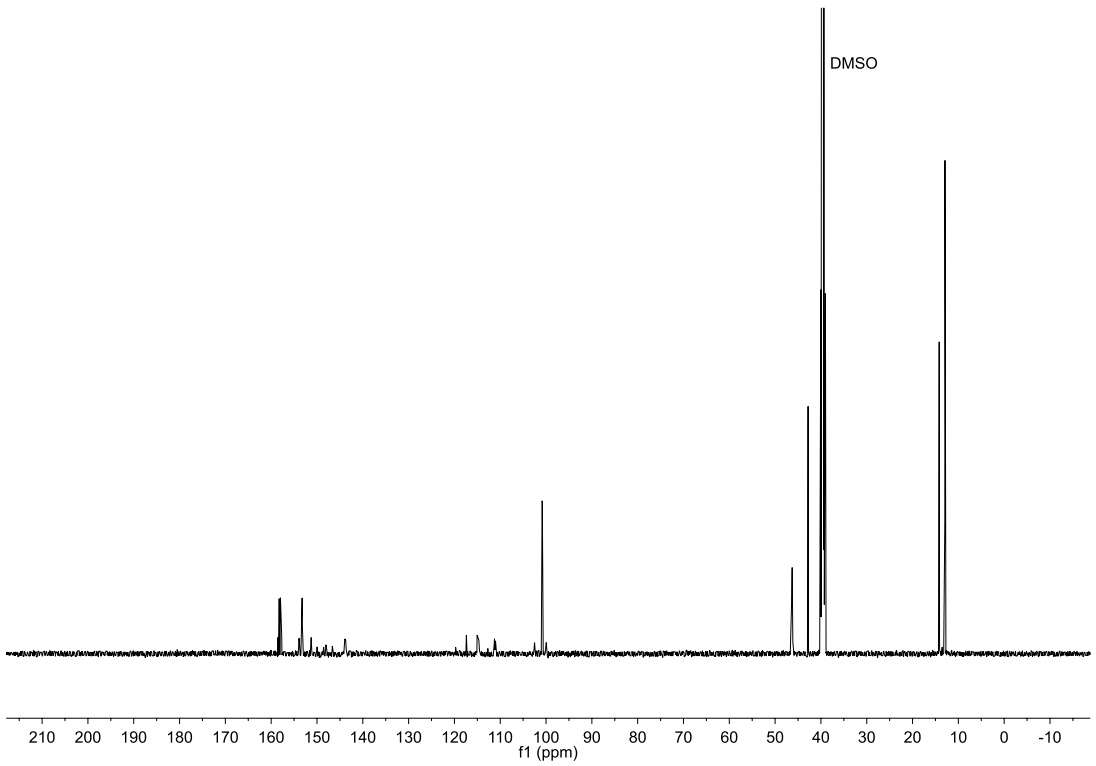

Figure S21. ^{13}C NMR (126 MHz, DMSO-d6) spectra of **70**.

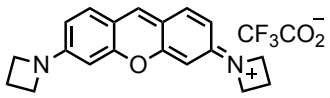

Pyronin azetidine
(**71**)

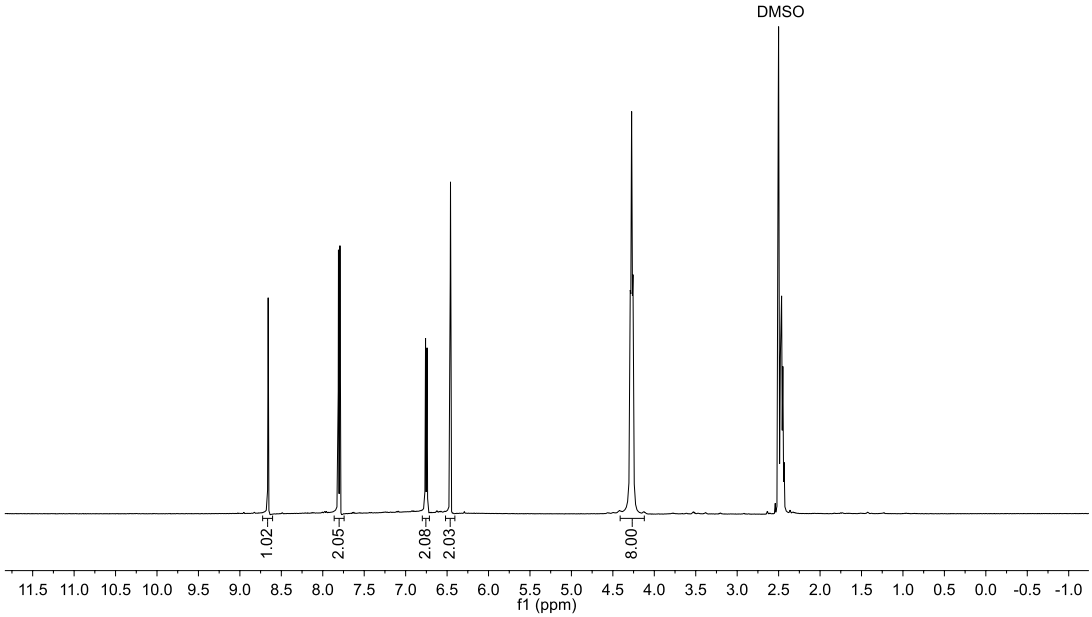

Figure S22. ^{1}H NMR (500 MHz, DMSO-d6) spectra of **71**.

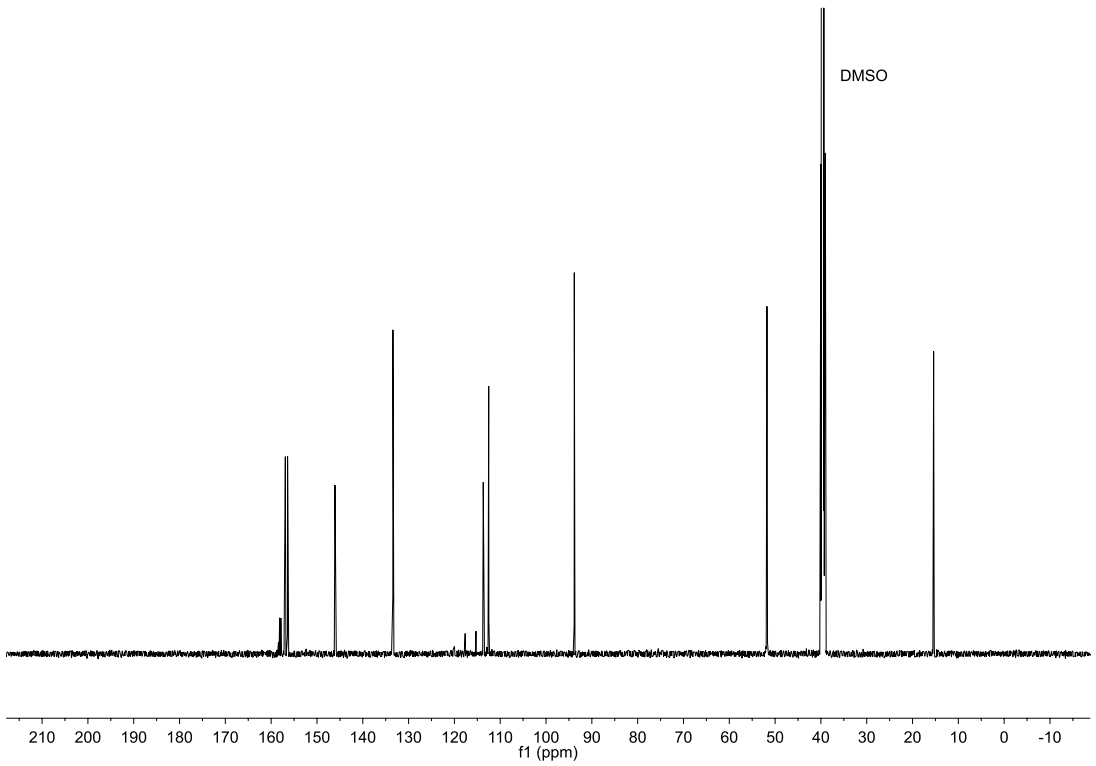

Figure S23. ^{13}C NMR (126 MHz, DMSO-d6) spectra of **71**.

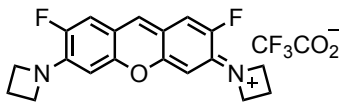

2,7-Difluoropyronin azetidine
(**72**)

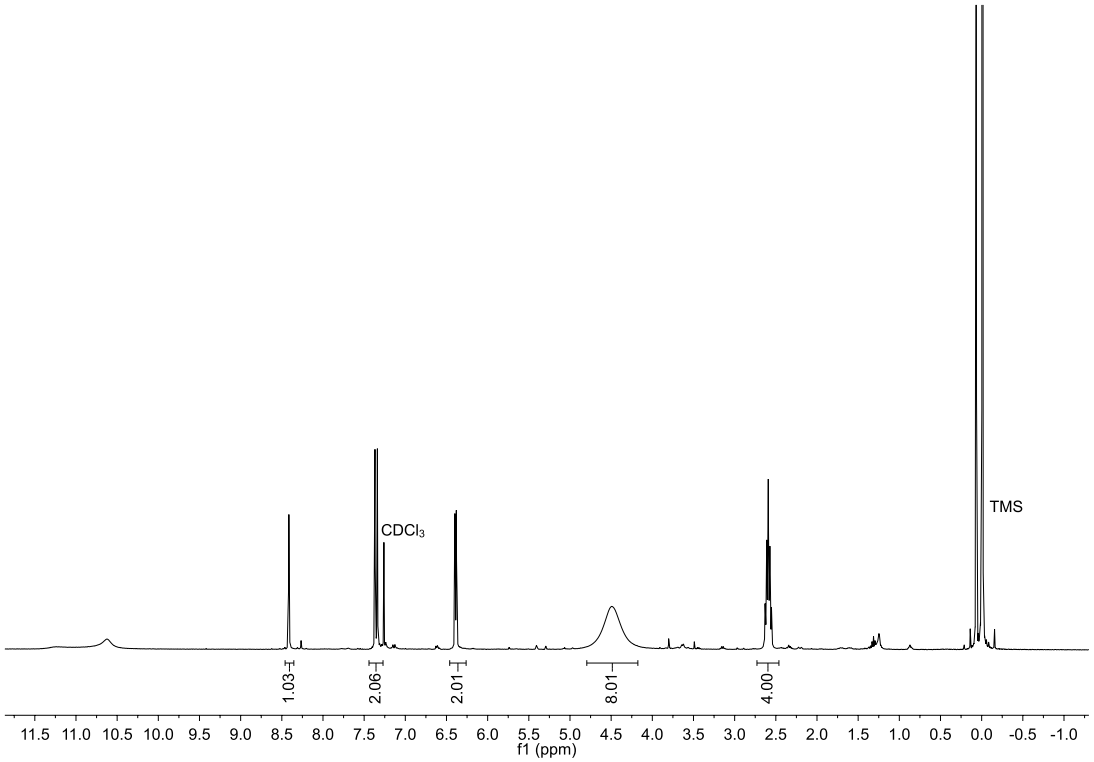

Figure S24. ^{1}H NMR (400 MHz, $CDCl_3$) spectra of **72**.

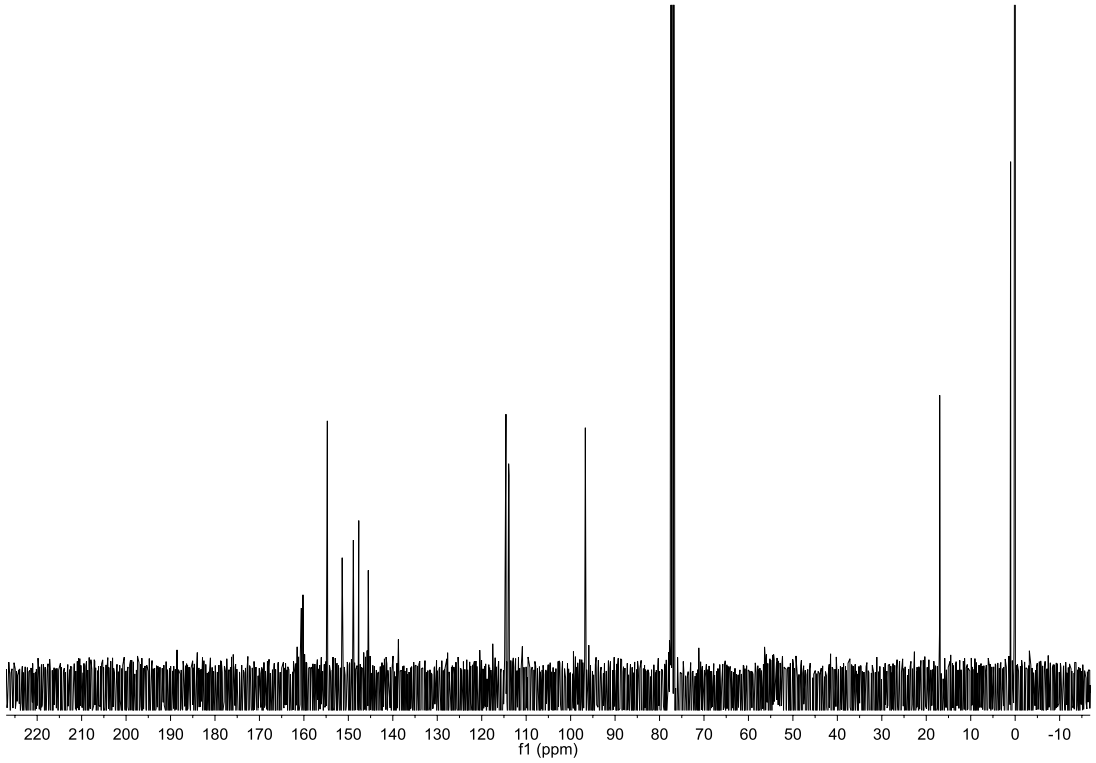

Figure S25. ^{13}C NMR (101 MHz, $CDCl_3$) spectra of **72**.

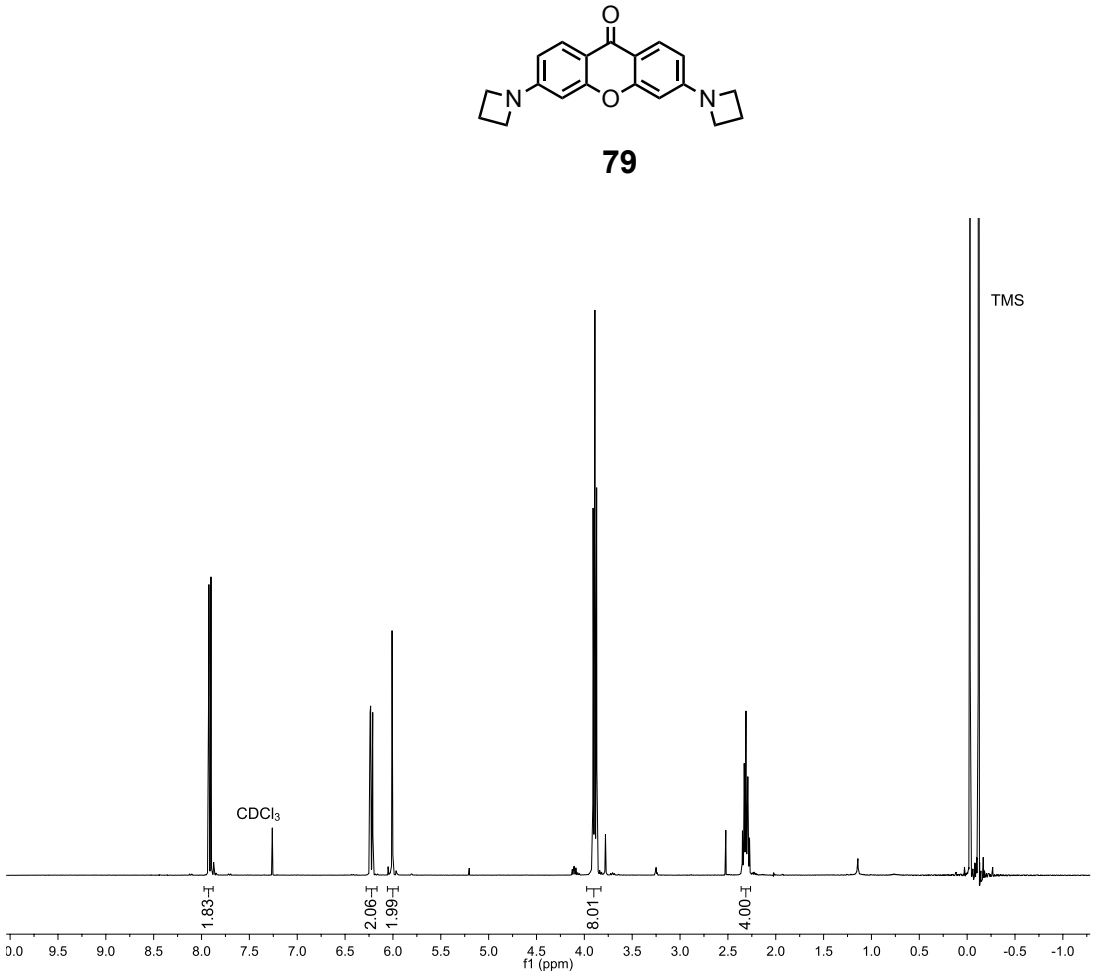

Figure S26. ^{1}H NMR (400 MHz, $CDCl_3$) spectra of **79**.

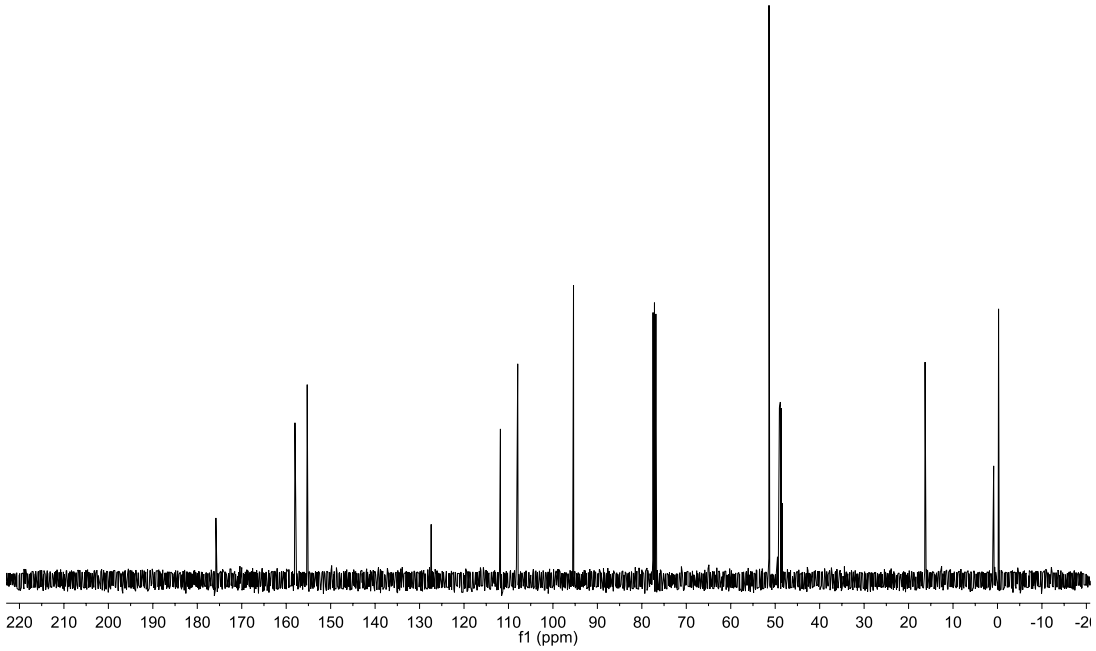

Figure S27. ^{13}C NMR (101 MHz, $CDCl_3$) of **79**.

75

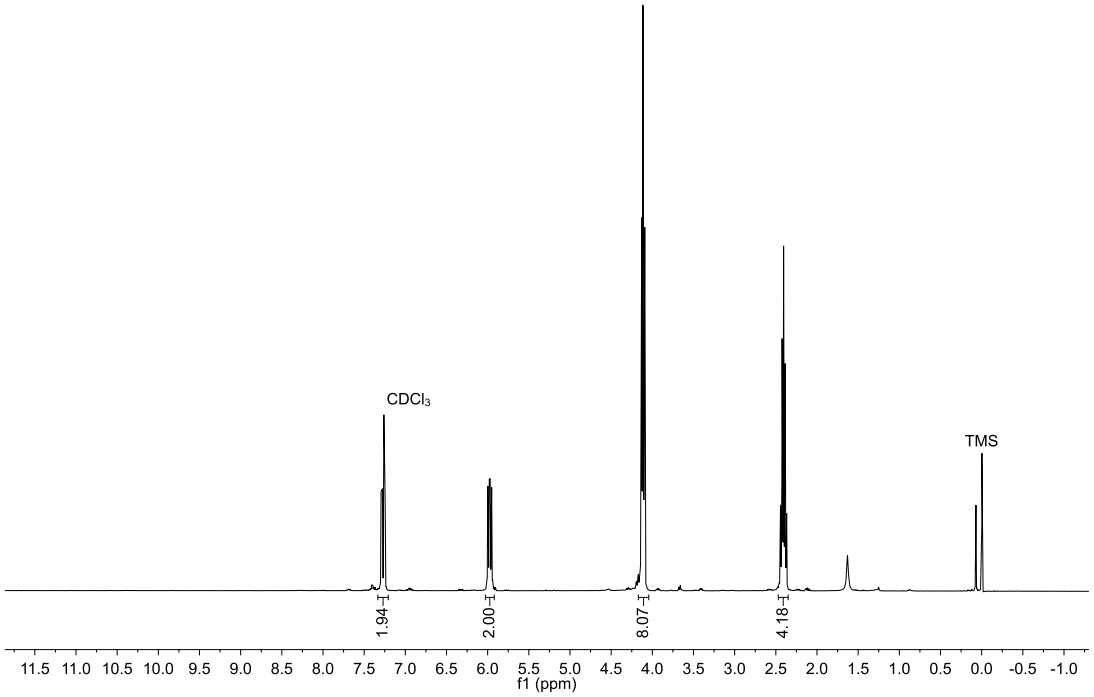

Figure S28. ^{1}H NMR (400 MHz, $CDCl_3$) spectra of **75**.

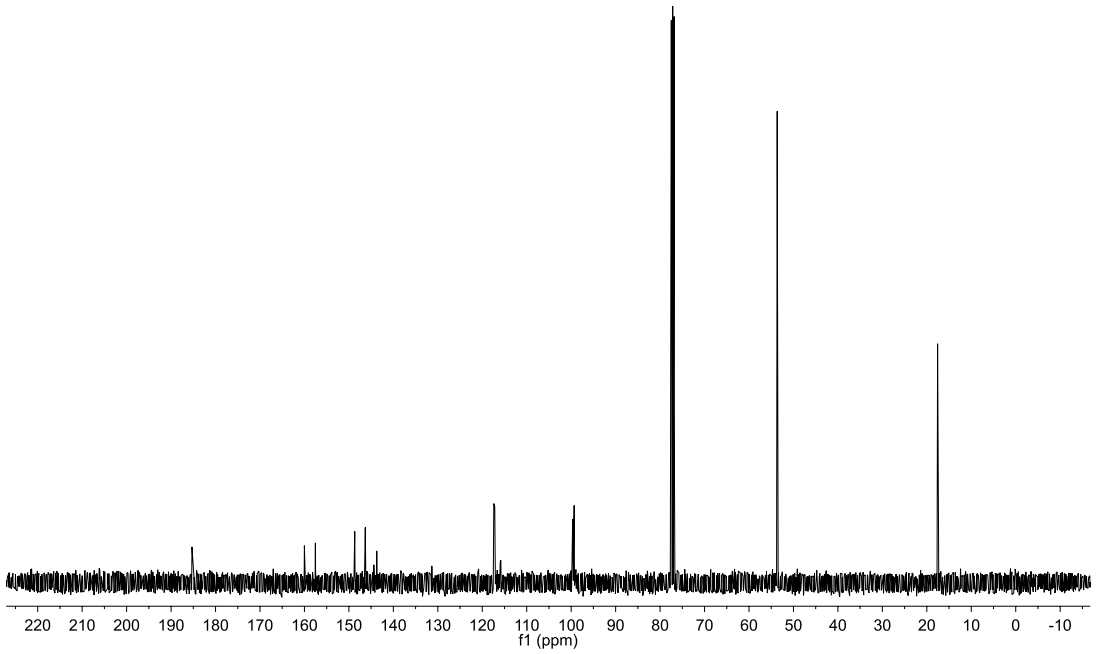

Figure S29. ^{13}C NMR (101 MHz, $CDCl_3$) spectra of **75**.

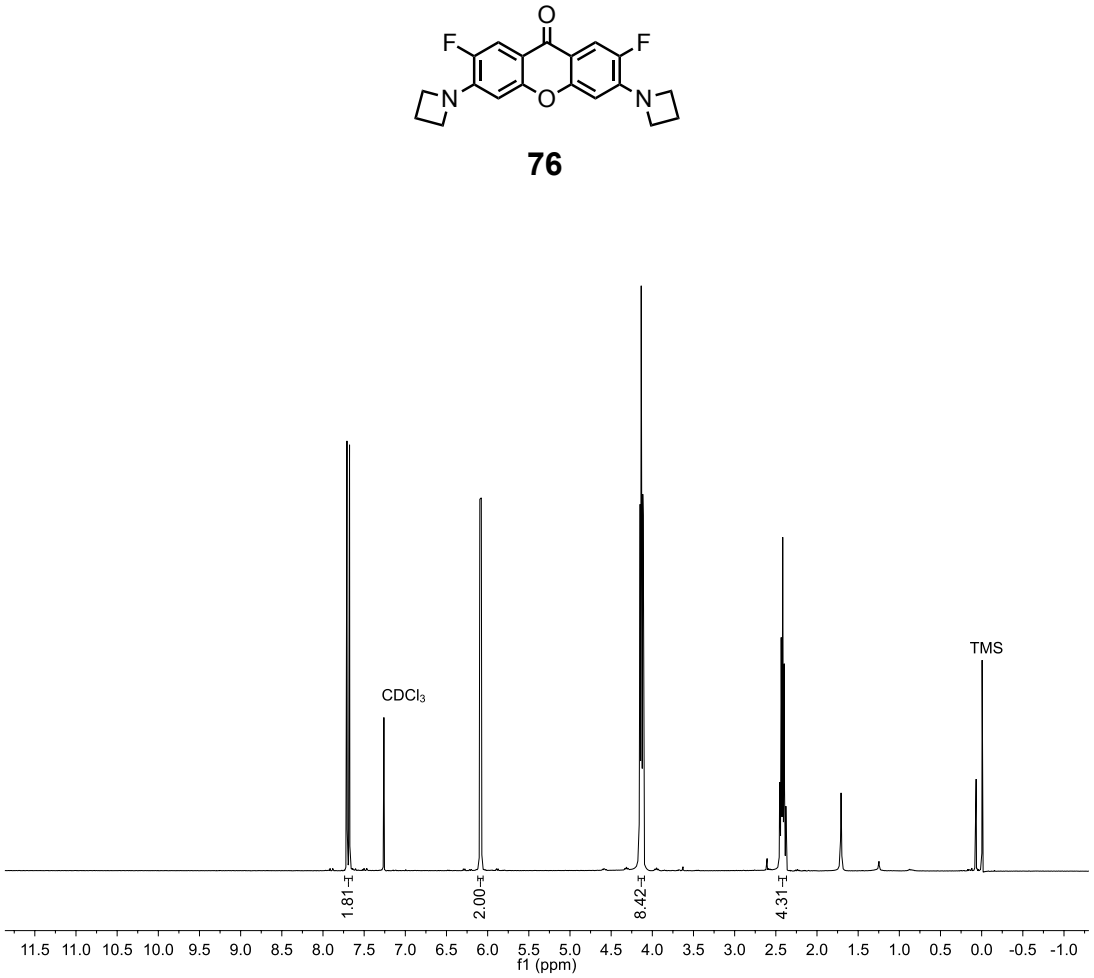

Figure S30. ^{1}H NMR (400 MHz, $CDCl_3$) spectra of **76**.

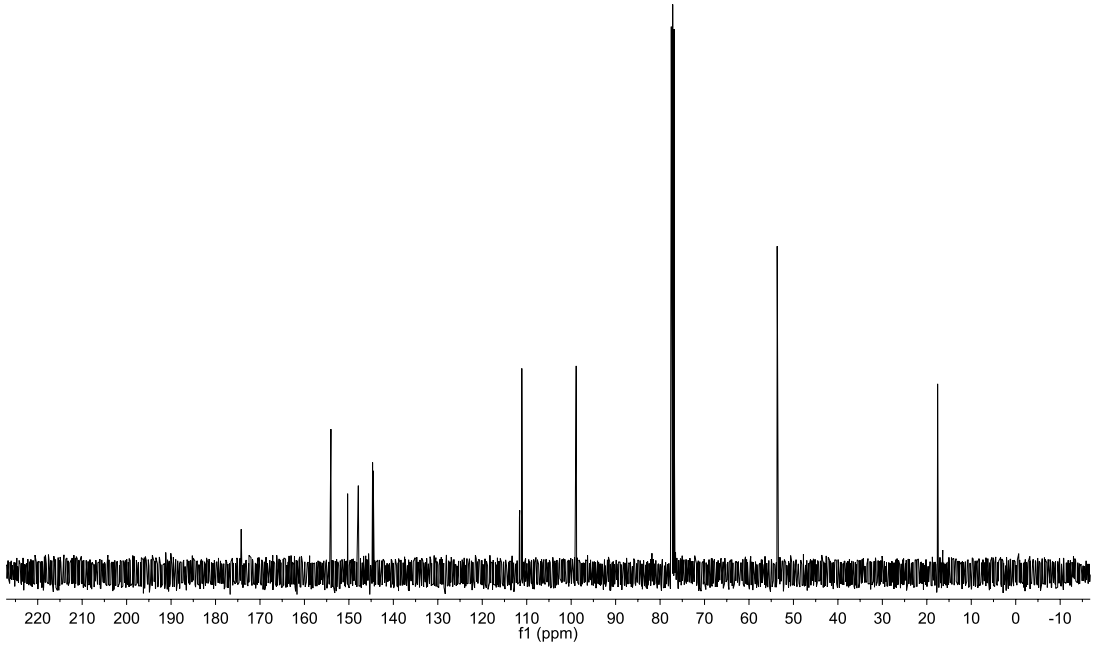

Figure S31. ^{13}C NMR (101 MHz, $CDCl_3$) spectra of **76**.

Appendix B

List of cell lines used

Cell line	Source	Tissue	Growth	Media
HeLa	ATCC #CCL-2	Cervical	Adherent	DMEM
PC-3	Dr. Matthew Levy	Prostate	Adherent	DMEM/F12
Jurkat	ATCC # TIB-152	Lymphocyte	Suspension	RPMI 1640
HCT-15	Dr. Liang Xu	Colon	Adherent	RPMI 1640
CV-1	ATCC #CCL-70	Kidney	Adherent	DMEM

List of plasmids used

Name	Source	Bacterial resistance	Vector backbone	Gene product
pHaMDR-EGFP	Dr. Michael Gottesman	Ampicillin	pHa	Human P-glycoprotein-EGFP
mCerulean-ER-5	Addgene #55366	Kanamycin	mCerulean	Calreticulin-Cerulean-KDEL
DsRed2-ER-5	Addgene #55836	Kanamycin	DsRed2	Calreticulin-DsRed2-KDEL
mCerulean3-Golgi-7	Addgene #55420	Kanamycin	mCerulean3	β-1,4-galactosyltransferase 1-mCerulean3
mEmerald-Golgi-7	Addgene #54108	Kanamycin	mEmerald	β-1,4-galactosyltransferase 1-mEmerald
mDsRed-Golgi-7	Addgene #55832	Kanamycin	mDsRed	β-1,4-galactosyltransferase 1-mDsRed
perbB1-Citrine	Addgene #40266	Kanamycin	pEYFP-N3	EGFR-Citrine
pGFP-Cytochrome C	Addgene #41181	Kanamycin	pEGFP-C1	GFP-cytochrome C
pAcGFP-C2-hSphK2	Addgene #84370	kanamycin	pAcGFP-C2	pAcGFP-Sphingosine kinase2
pDONR223-SPHK1	Addgene #23704	Spectinomycin	pDONR223	Sphingosine kinase1